LA-10500-MS

Los Alamos National Laboratory is operated by the University of California for the United States Department of Energy under contract W-7405-ENG-36.

COMPACT REVERSED-FIELD PINCH REACTORS (CRFPR):

FUSION-POWER-CORE INTEGRATION STUDY

a framework study

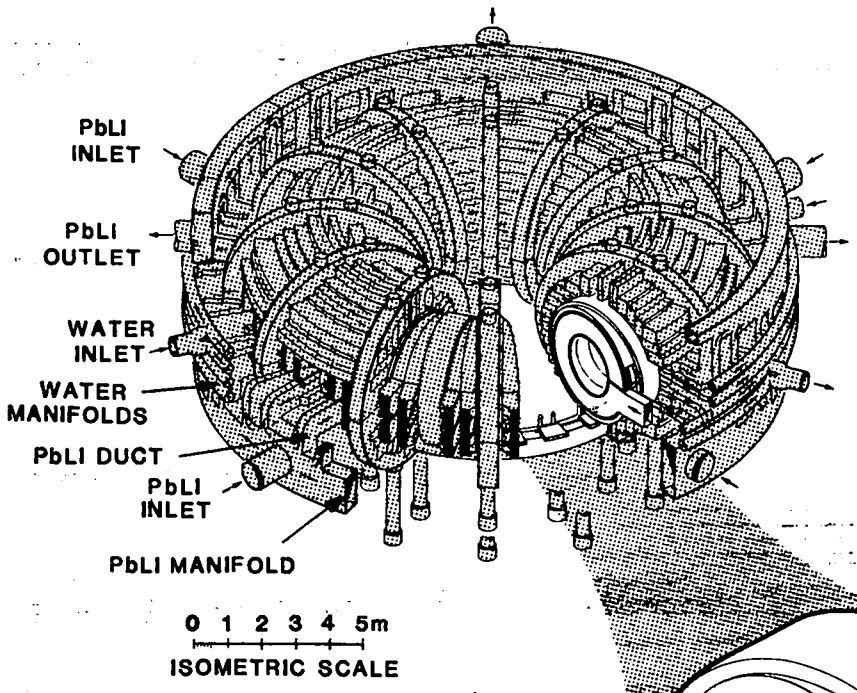

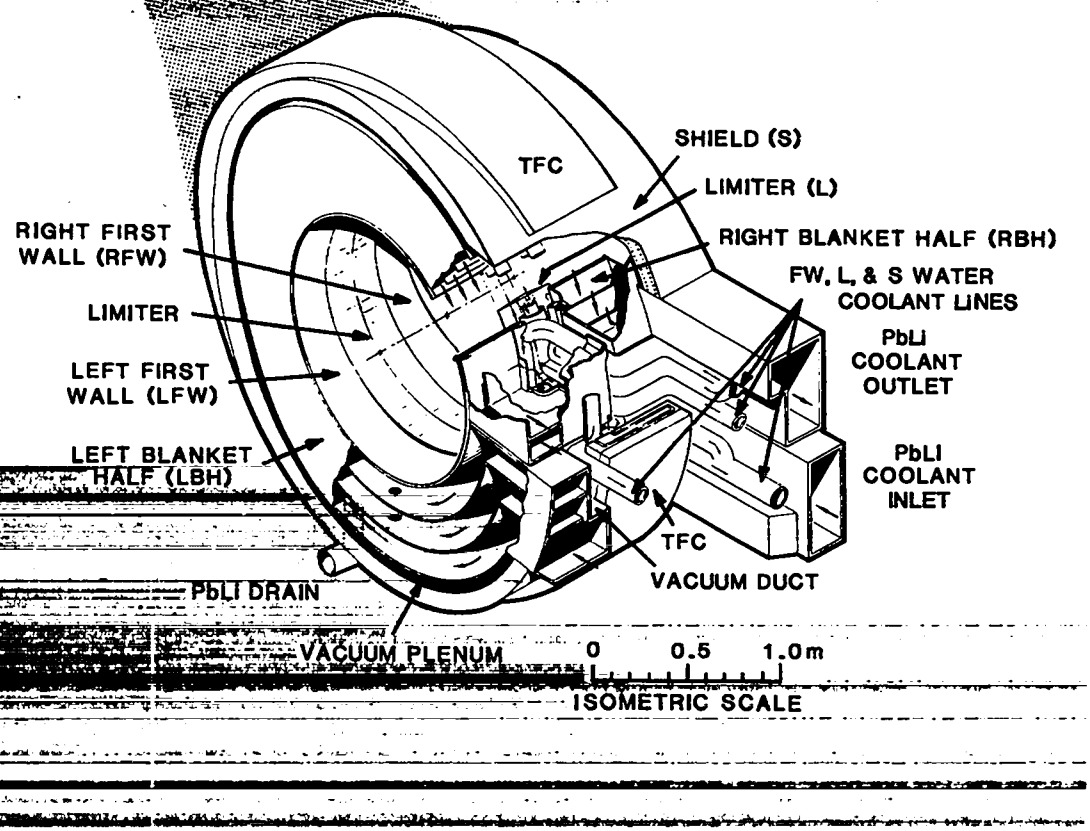

Los Alamos
Los Alamos National Laboratory
Los Alamos, New Mexico 87545

This work was supported by the US Department of Energy, Office of Fusion Energy.

Prepared by Marion Clark, Group CTR-12

LA-10500-MS

UC-20d
Issued: August 1985

Compact Reversed-Field Pinch Reactors (CRFPR):

Fusion-Power-Core Integration Study

C. Copenhaver
R. A. Krakowski
N. M. Schnurr
R. L. Miller
C. G. Bathke
R. L. Hagenson*
C. R. Mynard
A. D. Chaffee
C. Cappiello
J. W. Davidson

*Consultant at Los Alamos. Phillips Petroleum Company, Bartlesville, OK 74004.

Los Alamos Los Alamos National Laboratory
Los Alamos, New Mexico 87545

TABLE OF CONTENTS

COMPACT REVERSED-FIELD PINCH REACTORS (CRFPR): FUSION-POWER-CORE INTEGRATION STUDY

by

C. Copenhaver, R. A. Krakowski, N. M. Schnurr, R. L. Miller,
C. G. Bathke, R. L. Hagenson, C. R. Mynard, A. D. Chaffee,
C. Cappiello, J. W. Davidson

ABSTRACT

Using detailed two-dimensional neutronics studies based on the results of a previous framework study (LA-10200-MS), the fusion-power-core (FPC) integration, maintenance, and radio-activity/afterheat control are examined for the Compact Reversed-Field Pinch Reactor (CRFPR). While maintaining as a base case the nominal 20-MW/m^2 neutron first-wall loading design, CRFPR(20), the cost and technology impact of lower-wall-loading designs are also examined. The additional detail developed as part of this follow-on study also allows the cost estimates to be refined. The cost impact of multiplexing lower-wall-loading FPCs into a ~ 1000-MWe(net) plant is also examined. The CRFPR(20) design remains based on a PbLi-cooled FPC with pressurized-water used as a coolant for first-wall, pumped-limiter, and structural-shield systems. Single-piece FPC maintenance of this steady-state power plant is envisaged and evaluated on the basis of a preliminary layout of the reactor building. This follow-on study also develops the groundwork for assessing the feasibility and impact of impurity/ash control by magnetic divertors as an alternative to previously considered pumped-limiter systems. Lastly, directions for future, more-detailed power-plant designs based on the Reversed-Field Pinch are suggested.

1. INTRODUCTION

1.1. Background

Recent studies[1,2] of the principal fusion concepts as electric power plants indicate costs of electricity [COE(mills/kWeh)] that are at least 1.5-2.0 times greater than alternative nuclear energy sources. Since a majority of the total direct cost for these designs is projected to lie in the Reactor Plant Equipment cost account (i.e., Account 22., 56% of total direct cost for STARFIRE[1] and 64% for MARS[2]), compared to 25-30% for a light-water fission reactor,[3] the most significant and direct reductions in cost can be made by reducing the size (mass) and complexity of the fusion power core (FPC, i.e., plasma chamber, first wall, blanket, shield, magnets, and structure) and related support equipment. Typically, the FPC "mass utilization" (e.g., FPC mass divided by gross thermal power) for STARFIRE and MARS is, respectively, 5.7 and 6.8 tonne/MWt, compared to ~ 0.3-0.4 for Pressurized-Water Fission Reactors (PWRs), and reductions in this figure of merit by at least a factor of 2-3 for a 1000-MWe(net)-class device are deemed necessary for competitive fusion power.[4,5]

A recent investigation[6] into the role of FPC power density, mass utilization or "mass power density," has concluded that for the latter parameter a value above ~ 100 kWe(net)/tonne would give fusion a competitive position with respect to PWRs, where the latter ratio of net electric power to FPC mass has recently been suggested[6] as a measure of FPC performance. Both "mass utilization" and "mass power density" are used in this report, with a preference for the former because of a decoupling from quantities such as thermal-conversion efficiency and recirculating power fraction, which are not entirely related to the FPC. Within limits, nevertheless, both quantities are useful indicators of device performance.[6]

The reduction in development cost and the enhanced probability for success because of a more flexible, affordable development path have also been suggested[6] as reasons for pursuing low-mass-utilization or high-mass-power-density systems, particularly if such systems can be developed at low unit powers. Although these benefits are not easily quantified at present, the capability to extend learning curves for both physics and technology and to build rapidly and less expensively an operational database with which to assess the critical issue of plant availability also are strong reasons for emphasizing low-unit-power, high-mass-power-density approaches.

A number of preconceptual and framework studies of high-mass-power-density fusion systems have been reported.[7-10] Because of an ability to confine stable, high-beta plasma by self-generated poloidal fields, the Reversed-Field Pinch (RFP) offers a route to improved FPC mass power density, mass utilization, and cost based on an encouraging but developing physics database.[10,11] The Ref. 10 Compact RFP Reactor (CRFPR) designs used each of two relatively independent elements in the prescription for low-mass-utilization or high-mass-power-density FPCs: a) increased plasma power density or fusion-neutron first-wall loading, and b) reduced blanket, shield, and coil mass (and volume) allowed by the use of resistive (copper-alloy) coils. The potential for significant shrinkage of the FPC physical size, mass, and cost by using resistive copper coils without recirculating a large fraction of the gross electric power generated to supply ohmic losses in those coils is generally characteristic of poloidal-field-dominated confinement systems[12] like the RFP.

The qualities of the RFP that permit efficient plasma confinement by resistive coils positioned outside a thin tritium-breeding, heat-recovering blanket and (nominal) shield also allow high engineering beta (i.e., plasma pressure normalized to the magnetic field pressure at the confining coils). Central to maintaining this high engineering beta throughout the DT burn is the postulate of a low-frequency ($\sim$ 10s Hz) oscillating-field drive for sustaining the large plasma currents against ohmic dissipation; the close coupling of toroidal and poloidal circuits through the plasma projects a unique current-drive mechanism for the RFP, called "F-Θ pumping" after the $F = B_\phi(r_p)/\langle B_\phi \rangle$ and $\Theta = B_\theta(r_p)/\langle B_\phi \rangle$ parameters commonly used to define the Taylor near-minimum-energy state.[13,14] In these expressions, the toroidal field is B_ϕ, the poloidal field is B_θ, r_p is the plasma minor radius, and $\langle\rangle$ denotes an average over the plasma volume. Although partial tests of F-Θ pumping are encouraging,[11,15] clear demonstration of this non-intrusive current drive must await improved (i.e., higher-current, hotter, less-resistive) RFPs. Lastly, the plasma current density in RFPs is sufficient to give ohmic heating to DT ignition, thereby eliminating the need for auxiliary heating.

The RFP characteristics that give high-β, plasma-physics-decoupled aspect ratio, F-Θ pumping current drive, ignition by ohmic heating alone, and low-field/low-current coils combine to offer a potential for improved FPC design that, if needed, can far exceed the threshold for improvement suggested in Refs. 4 and 6. Figure 1-1 summarizes these RFP characteristics in the form of a

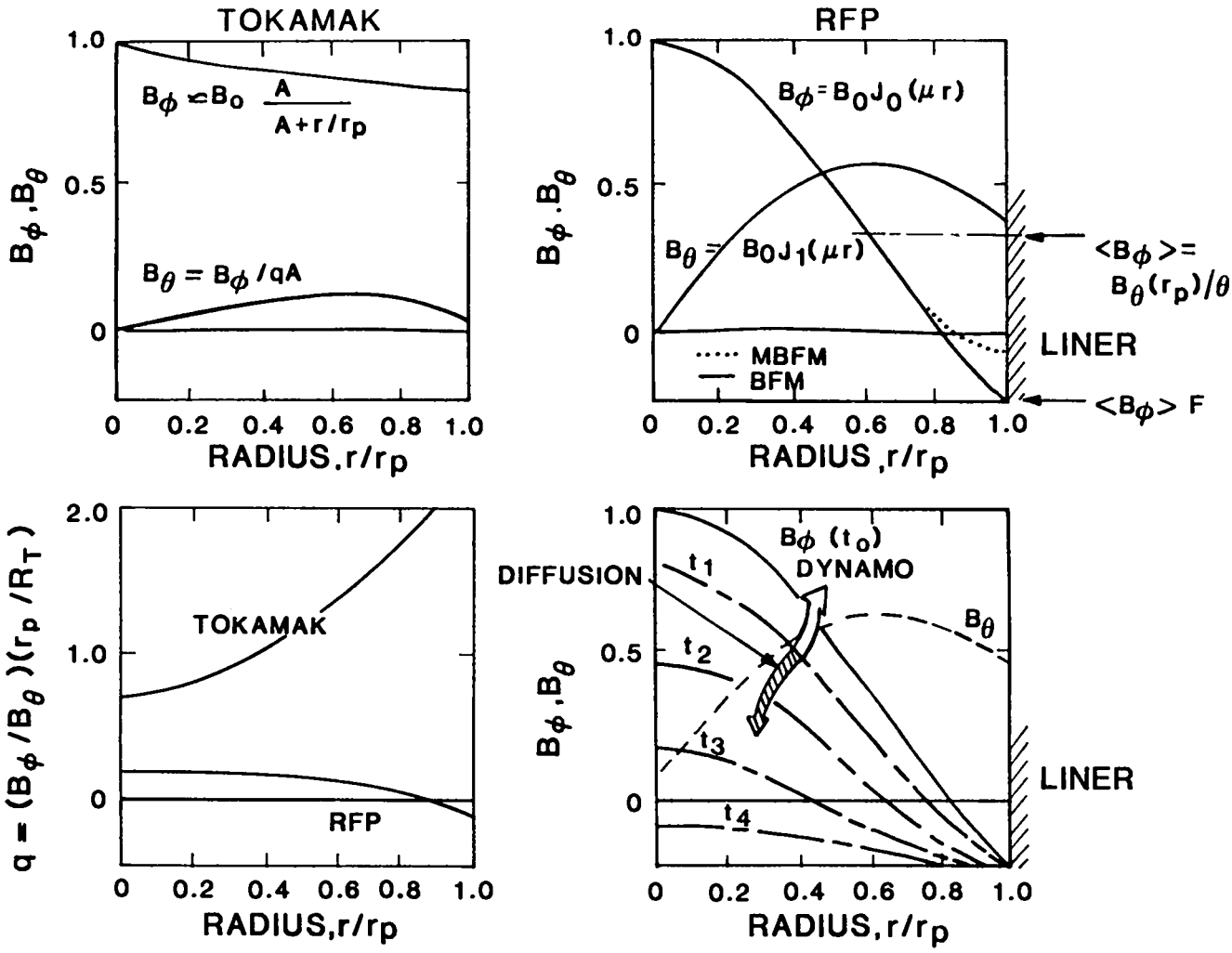

Fig. 1-1. Comparison of magnetic-field and $q = (B_\phi/B_\theta)(r_p/R_T)$ profiles in the minor radial dimension for the RFP and the tokamak. Shown also is an illustration of the natural tendency of B_ϕ to decay resistively to $B_\phi(r > r_p)$ being counteracted by the RFP dynamo.

comparison of field profiles with the tokamak. As noted previously, many of these characteristics are shared with or are positive extensions of other poloidal-field-dominated systems,[12] such as the spheromak compact torus.[16]

1.2. Scope

The compact, higher-power-density options for fusion power may have to accommodate higher heat fluxes, increased fusion-neutron currents, increased blanket power density, and in some cases[7-9] high magnetic fields in order that reduced FPC mass utilization (< 1-2 tonne/MWt), increased FPC power density (> 5 MWt/m^3 compared to 0.3-0.5 MWt/m^3 for MARS and STARFIRE), or increased FPC mass power density [> 100 kWe(net)/tonne][4,6] are achieved in systems that generate no more than ~ 1000 MWe(net) and ideally less. The CRFPR framework study reported in Ref. 10 addressed key design issues for this ~ 1100-tonne, 1000-MWe(net) FPC that would operate with a fusion-neutron first-wall loading of $I_w \simeq 20$ MW/m^2. Although only a ~ 15% cost-of-electricity (COE) reduction is projected in increasing I_w from 5 MW/m^2 to the minimum-COE $I_w \simeq 20$ MW/m^2 design value, the higher-wall-loading case was selected as a base case in Ref. 10 in order a) to maintain physical compactness from the viewpoints of single-piece (batch) FPC maintenance and reduced nuclear envelope within the power plant and b) to quantify the technology needs and COE tradeoffs for the higher-wall-loading case. From the viewpoint of heat-transport and stress, the $I_w \simeq 20$ MW/m^2 design, termed CRFPR(20), was estimated at the onset of the Ref. 10 study as representing a maximum limit while preserving acceptable engineering design safety margins. The COE tradeoffs anticipated for the low-mass-utilization FPC are directly related to a balance between a significant reduction in capital cost compared to the possibility of somewhat reduced thermal conversion efficiency (i.e., lower coolant/structural temperatures), increased recirculating power, and a yet-to-be-determined tradeoff between power density and overall availability.

As addressed in Ref. 10, the CRFPR(20) framework study and the FPC integration that ensued were based on a one-dimensional neutronics model requiring modification to accommodate two-dimensional effects that emerged as the FPC design detail evolved (i.e., coolant headers and manifolds, vacuum gaps, pumped limiters, finite coils, fluid ducts, etc.). The required two-dimensional neutronics calculations were conducted and reported at the closure of the Ref. 10 framework study with indications being that the changes required to achieve two-dimensional tritium-breeding ratios (TBRs) above unity were modest perturbations to the original Ref. 10 design. These results are given in Sec. 2.1., with the updated models used to perform the FPC integration also being described in Sec. 2. Section 3. updates and extends the FPC integration

originally reported in Sec. III.L. of Ref. 10. The present follow-on report extends the CRFPR(20) framework study to include in Sec. 4. a better resolution of the FPC maintenance approach and in Sec. 5. a quantified assessment of the radioactivity-disposal and afterheat-control issues anticipated for these higher-wall-loading, high-power-density systems. Although the focus of these studies remains on the CRFPR(20) design, the impact beyond increased cost and difficulty of single-piece maintenance as the neutron first-wall loading is decreased to $I_w \simeq 5$ MW/m^2 [i.e., CRFPR(5)] is also examined. Modifications to the costing procedure and database that resulted from this follow-on study are also implemented in the RFP parametrics code[10] and used in Sec. 6. to re-examine cost tradeoffs, including multiplexing lower-wall-loading designs into a nominal 1000-MWe(net) power plant. Lastly, Sec. 7. gives a feasibility study of magnetic divertors and the impact on the Ref. 10 framework design of adopting this impurity-control scheme. The directions for a more detailed, multi-institutional conceptional design study of an RFP fusion reactor plant are suggested in Sec. 8., which also summarizes key physics issues related to the RFP reactor.

1.3. Fusion-Power-Core (FPC) Configuration and Standard Conditions

This section gives a brief description of the Ref. 10 CRFPR(20) design. The FPC depicted in Fig. 1-2 consists of the limiters, first wall, second wall, blanket, shield, all coils, and structure. The reactor torus (first wall, blanket, shield, and toroidal-field coils) is comprised of 24 such segments, and a plan layout of these components for a half toroidal sector is shown in Fig. 1-3. The blanket uses a flowing eutectic mixture of 83% lead and 17% lithium, termed hereinafter as "PbLi," as both the tritium breeder and blanket coolant. In addition to the limiter and first wall, the second wall (i.e., first structural wall of the blanket) and shield are also cooled by pressurized water. The 316-stainless-steel shield also serves a major structural function for the FPC. The ohmic and nuclear heating deposited into the toroidal-field coils (TFCs) and poloidal-field coils (PFCs), with the inner PFCs being ohmic-heating coils (OHCs) and the outer PFCs being equilibrium-field coils (EFCs), is removed as waste heat by low-temperature, low-pressure water coolant. Energy from the PbLi and the pressurized-water coolant is transferred directly to a steam power cycle through a steam generator for electrical energy production. Table 1-I summarizes the Ref. 10 plasma conditions, and Table 1-II gives a

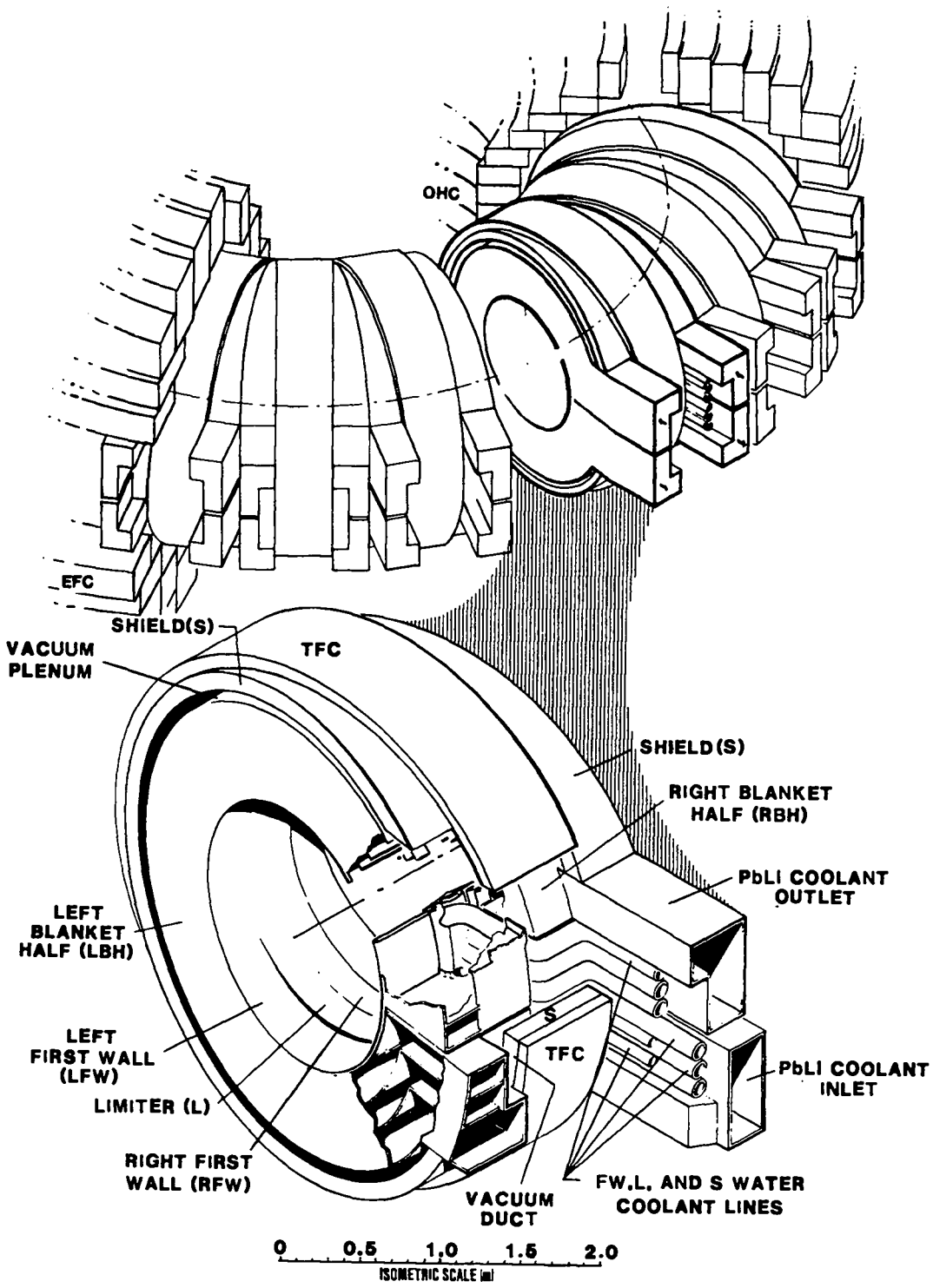

Fig. 1-2. One of 24 sectors that comprise the FPC of the Compact RFP Reactor.[10]

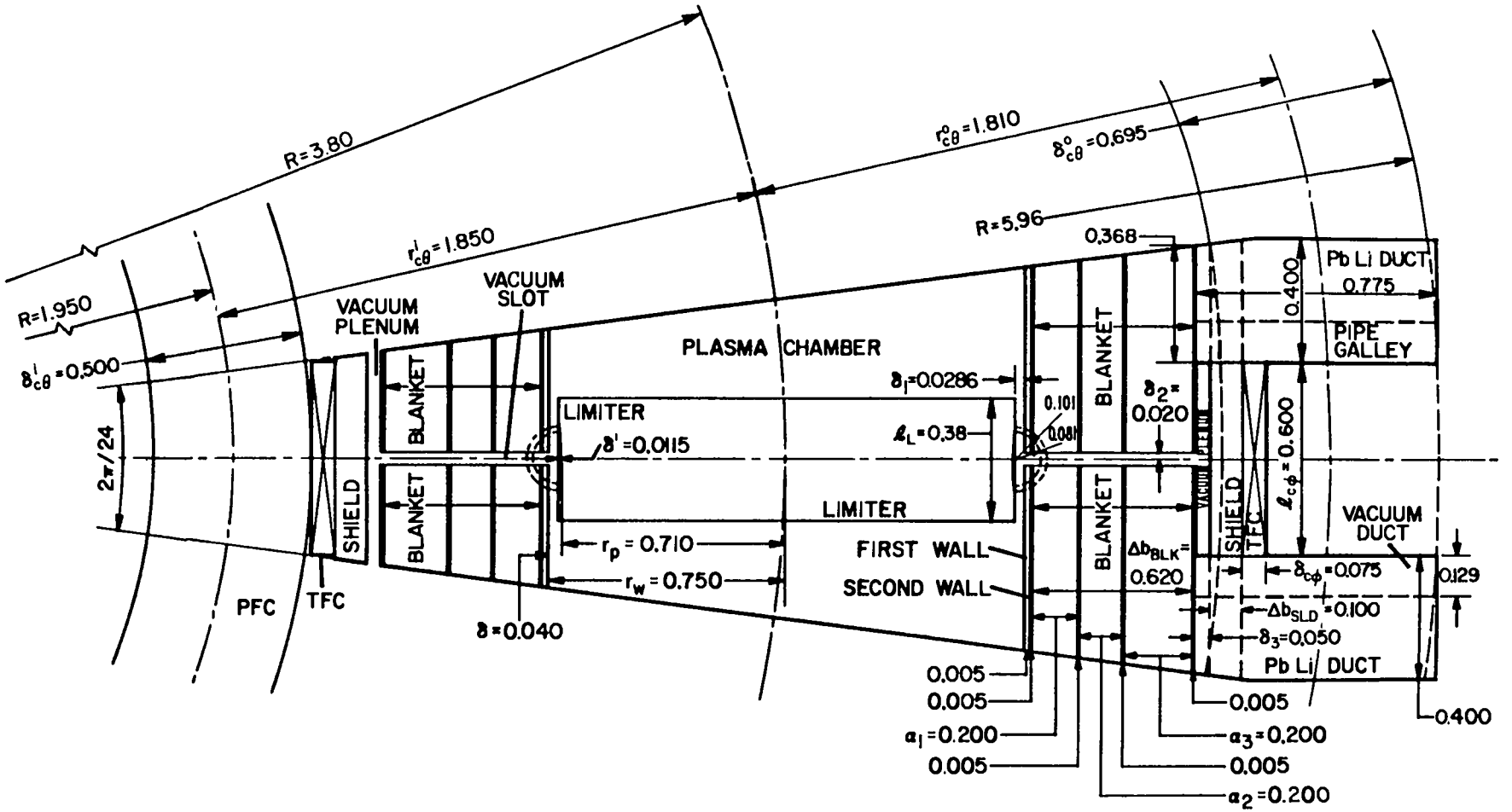

Fig. 1-3. Plan view of one of 24 toroidal sectors used to form the single-piece FPC for the minimum-COE CRFPR(20) design. Dimensions are in meters.

quantitative overview of the Ref. 10 FPC characteristics. Where possible, modifications incurred in the Ref. 10 design resulting from the follow-on study are also given.

As discussed in Sec. 6., the parametric systems model used to identify cost-optimized reactor designs specifies an ignition condition (i.e., $n\tau_E$ for a given plasma temperature and profiles). For a specific net-power output, therefore, the global plasma confinement time required to assure a minimum-COE design, $\tau_E(OPT)$, is dictated. A physics confinement time based on theory[17] or experiment,[11] $\tau_E(PHYS)$, is required to assess the margin for DT ignition [e.g., $\tau_E(PHYS)/\tau_E(OPT)$] and, hence, the physical credibility of achieving a given minimum-COE design. For an ohmically heated plasma, $\tau_E(PHYS) \equiv 3nk_BTV_p/(I_\phi V_\phi)_\Omega$, where $V_p = 2\pi^2 r_p 2R_T$ is the plasma volume and $(I_\phi V_\phi)_\Omega$ is the resistive power deposited into the plasma. With $\eta = V_\phi/I_\phi$ being a plasma resistivity, and expressing pressure balance in terms of the poloidal beta ($2nk_BT \simeq \beta_\theta B_\theta^2/2\mu_o \propto \beta_\theta I_\phi^2/r_p^2$), it follows that $\tau_E(PHYS) \propto \beta_\theta r_p^2/\eta$. The definition of plasma resistivity in an RFP depends on whether an energy or magnetic flux (helicity) basis is adopted.[18] The temperature scaling of η is reported to be classical ($\eta \propto 1/T^{3/2}$).[11]

Relating the $\tau_E(PHYS) \propto \beta_\theta r_p^2/\eta$ scaling to plasma current, I_ϕ, or to an average current density, $j_\phi \simeq I_\phi/\pi r_p^2$, is made ambiguous by the limited data, although the existing database has been advanced significantly over the past few years by a number of groups.[11,19-22] For both constant beta and ratio I_ϕ/N, where $N = n\pi r_p^2$ is the plasma line density, pressure balance predicts $T \propto I_\phi$, which for $\eta \propto 1/T^{3/2}$ gives $\tau_E(PHYS) \propto I_\phi^3/2r_p^2$ and $n\tau_E \propto I_\phi^{5/2}$. The dependence of both $\tau_E(PHYS)$ and $n\tau_E$ on I_ϕ for the ZT-40M experiment[11] is shown in Fig. 1-4. It is emphasized that the dependence of τ_E on r_p, as well as the constancy of I_ϕ/N, is uncertain. For the purposes of this study, $\tau_E(PHYS) = C_1 f(\beta_\phi) r_p^2 I_\phi^\nu$ is adopted, where for a given ν the data given in Fig. 1-4 are used to determine the fitting constant, C_1. The empirical relationship between ν and C_1 is given in Table 1-III. The function, $f(\beta_\theta) = (\beta_{\theta c}/\beta_\theta)^2$, decreases $\tau_E(PHYS)$ if $\beta_\theta > \beta_{\theta c} \simeq 0.13$ and is otherwise unity. These data fits are used to compare $\tau_E(PHYS)$ with the confinement time required for the minimum-COE confinement time, $\tau_E(OPT)$. Generally, $\tau_E(PHYS)$ is equated to an electron energy confinement time, τ_{ce}, with the ion confinement taken as $\tau_{pi} \simeq 4\tau_{ce}$, in estimating a global energy confinement time with which to compare $\tau_E(OPT)$ and assess ignition margins.

TABLE 1-I

SAMPLE COMPACT RFP REACTOR DESIGN POINTS
FOR THE MINIMUM-COE 1000-MWe(net) CASE AND
A CASE OF LOWER FUSION NEUTRON FIRST-WALL LOADING

DEVICE	CRFPR(20)[a]	CRFPR(5)
Neutron first-wall loading, I_w(MW/m^2)	19.5	5.0
Net electrical power, P_E(MWe)	1,000.	1,000.
Total thermal power, P_{TH}(MWt)	3,365.	3,609.
Recirculating power fraction, $1/Q_E$	0.185	0.208
Plasma minor radius, r_p(m)	0.71	1.42
Plasma major radius, R_T(m)[b]	3.8	7.6
Plasma volume, V_p(m^3)	37.8	302.5
Plasma power density, P_F/V_p(MW/m^3)	72.4	9.6
Plasma temperature, T(keV)	10.0	10.0
Plasma density, n(10^{20}/m^3)	6.3	2.3
Average beta, β_θ[c]	0.23	0.23
Plasma energy confinement time, τ_E(s)	0.23	0.70
Plasma thermal diffusivity,[d] χ_E(m^2/s)	0.41	0.54
Field at plasma, B_θ(T)	5.2	3.0
Peak field at coil, $B_{\theta c}$(T)	4.5	2.6
Plasma current, I_ϕ(MA)	18.4	21.6
Plasma current density, j_ϕ(MA/m^2)	11.2	3.41
FPC volume, V_{FPC}[e](m^3)	285.	1,042.
FPC mass, M_{FPC}(tonne)	1,105.	2,000.
FPC power density, P_{TH}/V_{FPC}(MWt/m^3)	11.8	3.5
FPC mass utilization, M_{FPC}/P_{TH}(tonne/MWt)	0.33	0.55
FPC mass power density, 1000 P_E/M_{FPC}(kWe/tonne)	905.0	500.0
FPC cost as fraction of total direct cost[f]	0.045	~0.05
Unit Direct Cost, UDC ($/kWe)[g]	1,007.	1,169.
Cost of Electricity, COE(mills/kWeh)[g]	48.4	55.5

[a] Values reported are derived from a parametric systems code and differ somewhat from final design values derived from conceptual subsystem design and plasma simulations, as reported in Ref. 10 and subsequently modified by this follow-on study (see Appendix B and Sec. 6.3.3.).

[b] Plasma aspect ratio preserved at $A = R_T/r_p = 5.35$, which is a minimum-COE value, but this minimum is very shallow. Blanket design adjustments driven by this follow-on study increased A to 5.5 (see Sec. 6.3.3.).

[c] Includes ~ 0.03 for steady-state alpha-particle pressure, total (volume-average) beta is ~ 0.12.

[d] Taken as ~ $(3/16)r_p^2/\tau_E$ for a parabolic temperature and flat density profile.

[e] Fusion power core, includes plasma chamber, first-wall/limiters, blanket, shield, and coils; excludes coolants.

[f] Compared to 0.255 for STARFIRE[1] and 0.201 for MARS.[2]

[g] 1980 dollars, with COE given as a "then-current" value and Ref. 10 cost database used (see Appendix B and Sec. 6.1. for impact of cost database refinements).

TABLE 1-II

KEY CRFPR ENGINEERING PARAMETERS AND CHARACTERISTICS
FOR THE I_w = 19.5 MW/m^2, CRFPR(20) DESIGN FROM REF. 10[a]

Net/gross electrical power, P_E(MWe)/P_{ET}(MWe)	1000./1227.[1000./1256.]
Total thermal power, P_{TH}(MWt)	3365.[3473.]
Gross power-conversion efficiency, η_{TH}	0.365[0.369]
Recirculation power fraction, ε	0.185[0.204]
Overall plant availability, p_f	0.75 (15 MWyr/m^2 FPC life)
Major/minor plasma radius, R_T/r_p(m)	3.8[3.9]/0.71
Plasma volume, V_p(m^3)	37.8[38.8]
First-wall area, A_{FW}(m^2)	112.[115.]
Neutron first-wall loading, I_w(MW/m^2)	19.5[19.0]
Number of toroidal sectors, N	24.[b]
Maximum field at magnet, $B_{\theta c}$ (T)	4.5[c]
Field at plasma axis/edge, $B_\phi(0)/B_\theta(r_p)$(T)	9.5/5.2
Average poloidal/total beta, β_θ/β	0.23/0.12
Average DT ion density/temperature, n(10^{20}/m^3)/T(keV)	6.6/10.0
Plasma burn mode	Continuous/ignited[d]
Plasma heating method (startup)	Ohmic (246 V-s total, 26 V-s, ohmic)
Plasma current/ohmic power (MA/MW)	18.4/25.3
Plasma impurity-control method	Poloidal pumped limiter (24, 38% first wall)
First-wall/limiter materials	MZC copper alloy (water-cooled)
Blanket/shield structural material	HT-9 steel (water-cooled second wall)
Tritium-breeding medium	PbLi(35 MW/m^3 average), TBR = 1.06
Primary coolant	PbLi (poloidal flow, 0.5[0.6]-m-thick)
Shield	Tungsten/B_4C[stainless steel] (0.1-m-thick, water-cooled)
Thermal-conversion method	Dual-medium (~40% H_2O, ~60% PbLi) steam
FPC Masses (tonne; 306 m^3, 3.34 tonne/m^3, 11.0 MWt/m^3, 0.3 tonne/MWt)	
• Limiters[e]	7.64[8.4]
• First wall	2.88[1.8]
• Second wall[e]	8.39[9.9]
• Blanket[f]	72.41[48.2]
• Shield	50.60[159.6]
• TFC (Subtotal)	77.4 (190.3)[76.2(304.)]
• OHC	411. [400.]
• EFC	421. [413.]
Total	1022. [1117.]

(a)Values in brackets correspond to changes made during this follow-on study.
(b)For off-site fabrication purposes only, single-piece or batch FPC maintenance is envisaged for this system that weighs ~ 190[304] tonne (first wall, blanket, shield, toroidal-field coils), to which is added a separate 832[813]-tonne poloidal-field coil set and ~ 925[943] tonne of PbLi coolant.
(c)At the OHC during the burn, 9.2 T during startup. Peak field at the TFC is 0.7 T, with the plasma dynamo providing a major part of the toroidal flux during startup. TFC/OHC/EFC power consumption is 12.6/73.0/53.5 MWe, with the OHC power going to zero upon initiation of "F-Θ pumping" current drive.
(d)Based on "F-Θ pumping" at 50 Hz with $\delta\Phi/\Phi \leq 0.01$ toroidal flux swing, $\delta V_\phi/\langle I_\phi R_p\rangle \simeq 200$, $\delta I_\phi/I_\phi \leq 0.0042$ plasma current swing.
(e)Includes manifolds and headers.
(f)Includes inlet/outlet ducts, but not 925-tonne PbLi coolant.

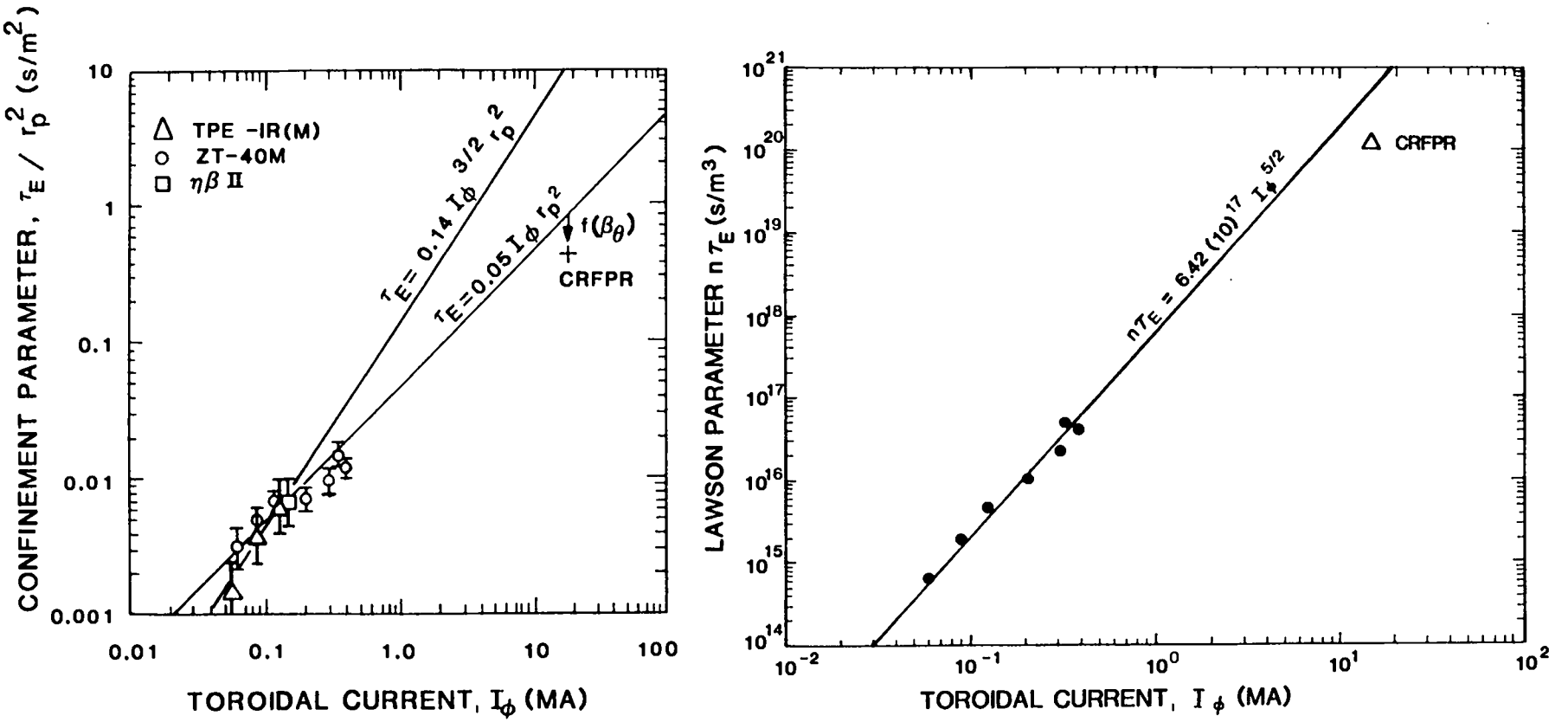

Fig. 1-4. Dependence of confinement time on plasma current for the ZT-40M reversed-field-pinch experiment.[11] The Ref. 10 CRFPR(20) design point is also indicated.

TABLE 1-III

FITTING PARAMETERS FOR THE CONFINEMENT-TIME DATA GIVEN IN FIG. 1-4

Current exponent, ν	$C_1(s/m^2/MA^\nu) = \tau_E(PHYS)/r_p^2 I_\phi^\nu$
0.90	0.040
1.00	0.050
1.10	0.062
1.25	0.082
1.50	0.140

A summary of size (r_p), neutron-wall-loading (I_w), COE, and physics [i.e., $\tau_{ce} \propto f(\beta_\theta) I_\phi^\nu r_p^2$, $\tau_{pi} \simeq 4\tau_{ce}$] scalings and tradeoffs, as reported in Ref. 10, is depicted in Fig. 1-5, which shows the CRFPR(20) minimum-COE 1000-MWe(net) design point. The constant-ν curves depicted in Fig. 1-5 correspond to an ignited margin of unity [$\tau_E(OPT) = C_1 f(\beta_\theta) r_p^2 I_\phi^\nu / (1 + \tau_{ce}/\tau_{pi})$, with $\tau_{ce}/\tau_{pi} \simeq 1/4$]. The COE and scaling impacts of the CRFPR(5) design are depicted in Fig. 1-5 as two extrema: a) fixed P_E = 1000-MWe(net) doubles the FPC size (mass) and increases cost by $\sim$ 15%; b) fixed FPC size decreases net electric power to $P_E \simeq$ 250 MWe and increases COE by a factor of $\sim$ 2.5 unless N $\simeq$ 3-4 such FPC units are multiplexed to drive a nominal $P_E \simeq$ 1000-MWe plant. The COE for this N $\simeq$ 4 multiplexed case is estimated in Sec. 6.3.2. to be 30-40% more than the CRFPR(20) base case.

Generally, the size-invariant CRFPR(20) FPC is used to describe thermal/hydraulic aspects of the CRFPR(5) in subsequent sections because blanket and magnet redesign for the single-unit 1000-MWe(net) CRFPR(5) case is beyond the scope of this follow-on study. Although the latter case is larger than the minimum-COE CRFPR(20) core, the system nevertheless remains one of low mass utilization or high mass power density.

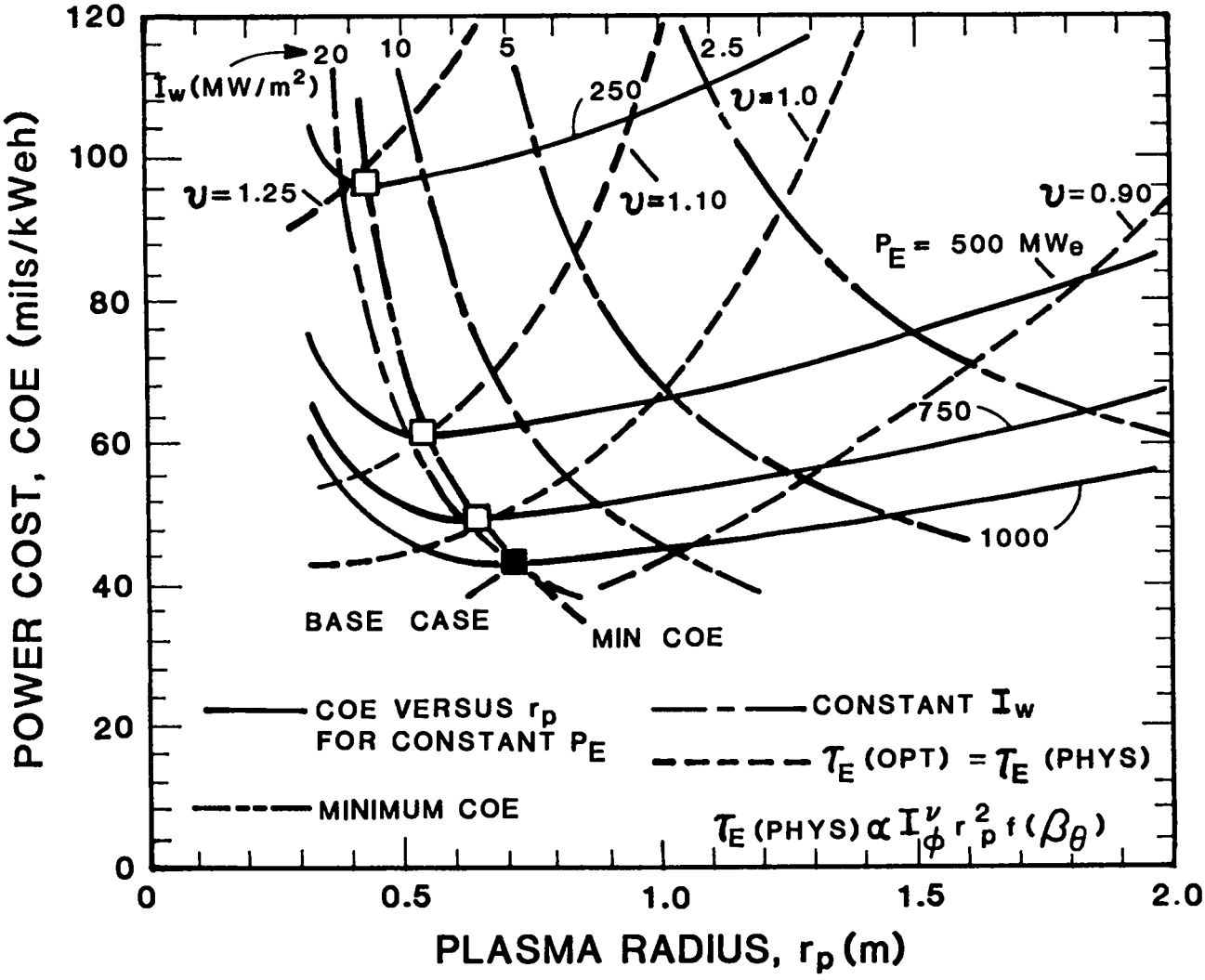

Fig. 1-5. Dependence of COE on plasma radius, r_p, for a range of net electric powers, P_E. The cost optimization gives an optimum plasma confinement time, τ_E(OPT), dictated by cost considerations only. A physics scaling based on electron conduction time, τ_{ce}, and an ion particle confinement time, $\tau_{pi} = r\tau_{ce}$, is used to determine the ignition margin [i.e., τ_E(OPT) = τ_E(PHYS)] for a range of current exponents, ν. Also shown are lines of constant neutron first-wall loading, I_w.

2. FUSION-POWER-CORE MODELS

2.1. Two-Dimensional Neutronics

The neutronics performance of the first wall, second wall, blanket, and shield used to evaluate the Ref. 10 design was based on the results of a one-dimensional, discrete-ordinates code, ONEDANT.[23] A 30-neutron/12 gamma-ray group library based on ENDF/B-IV cross-section data was used. Inclusion of the limiter, vacuum ducts, manifolds, and headers that evolved from the Ref. 10 design, however, gave significant two-dimensional characteristics to the FPC model. A two-dimensional analysis, therefore, was performed after completion of the Ref. 10 study. These two-dimensional effects on the blanket performance serve as a basis for this follow-on study.

Of particular interest is the tritium-breeding ratio (TBR); the one-dimensional calculation for the Ref. 10 FPC model predicted a TBR value of 1.108. The two-dimensional neutronics model adapted to the Fig. 1-3 layout is shown in Fig. 2-1, which also gives geometric details for the limiter, the first-wall/second-wall, and associated manifold regions. The manifold regions and the first-wall/second-wall regions were homogenized into zones composed of metal, water, and void. The two-dimensional neutronics calculations were performed with a combination of computer codes: the two-dimensional, discrete-ordinate codes TRIDENT-CTR,[24] TWODANT,[25] the Monte Carlo code MCNP,[26] and the one-dimensional discrete-ordinates code ONEDANT.[23] This combination of codes was needed both to benchmark the various calculations[27] against each other and to utilize the particular assets of each (i.e., spatial resolution versus running time).

A TRIDENT-CTR calculation applied to the reference FPC model[10] yielded a TBR of 0.785 compared to the value of 1.108 for the ONEDANT model and the highly homogenized "canonical" blanket used to initiate the Ref. 10 study. The effects of various design and material changes were subsequently examined[10,27] with a series of TWODANT calculations, which were selectively benchmarked with TRIDENT-CTR calculations.

The effect of thickening the blanket was examined by replacing the 50-mm-thick vacuum region behind the blanket with PbLi. The 20-mm-thick copper-alloy first wall used in Ref. 10 was decreased to 3 mm (2-mm-thick copper-alloy and water region followed by 1-mm-thick copper alloy). The effect of relocating the first-wall/second-wall coolant manifold (Fig. 2-1) was estimated by shifting the homogenized material representing this manifold to the rear of the blanket.

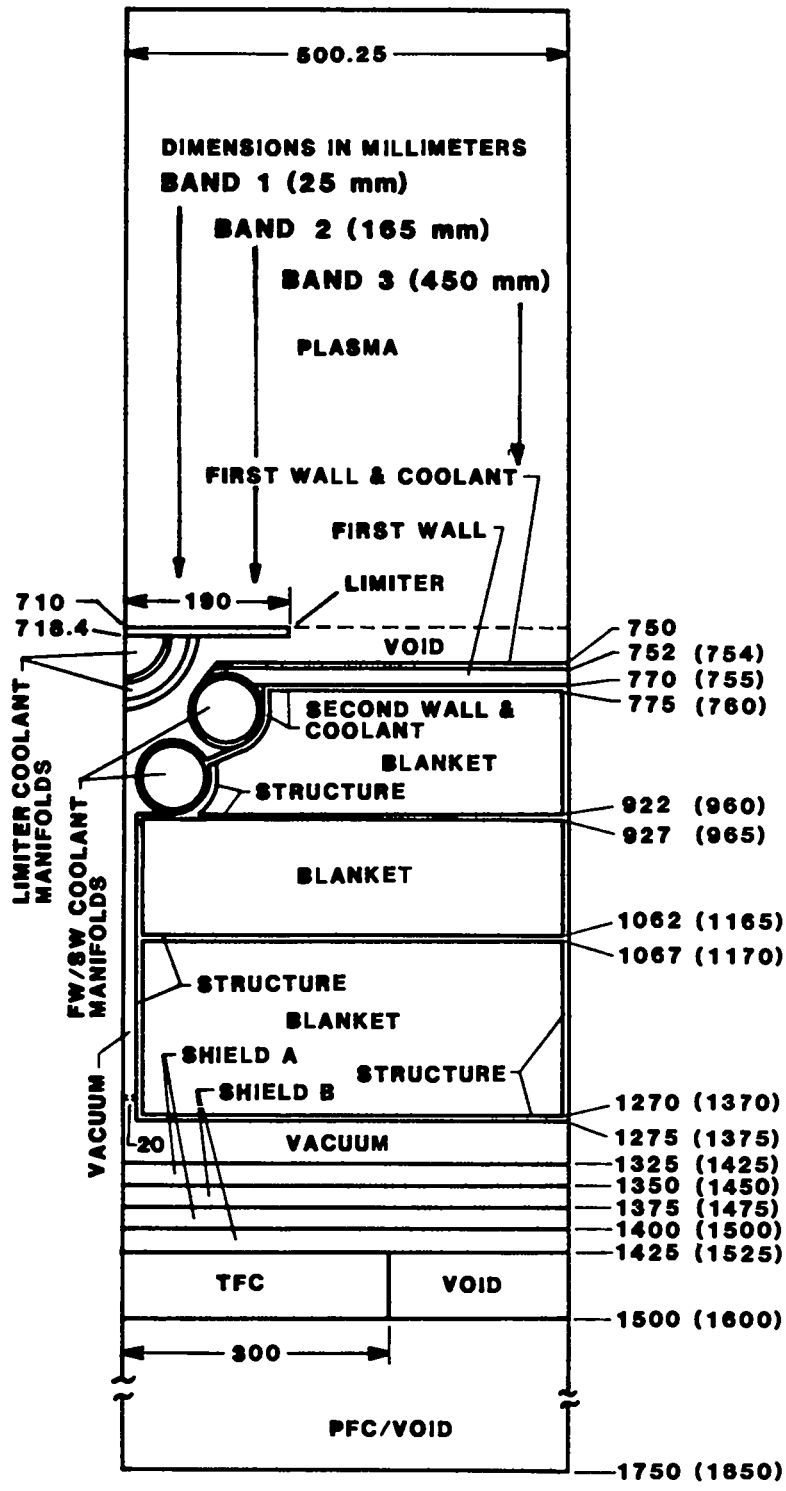

Fig. 2-1A. First-wall/second-wall/limiter/blanket/shield/coil model used in two-dimensional TRIDENT-CTR[24] neutronics re-assessment of CRFPR(20) fusion power core, including pressurized-water coolant manifolds/headers. Values given in parentheses indicate updates resulting from neutronics reoptimization described in Ref. 10 and summarized in Sec. 2.1.

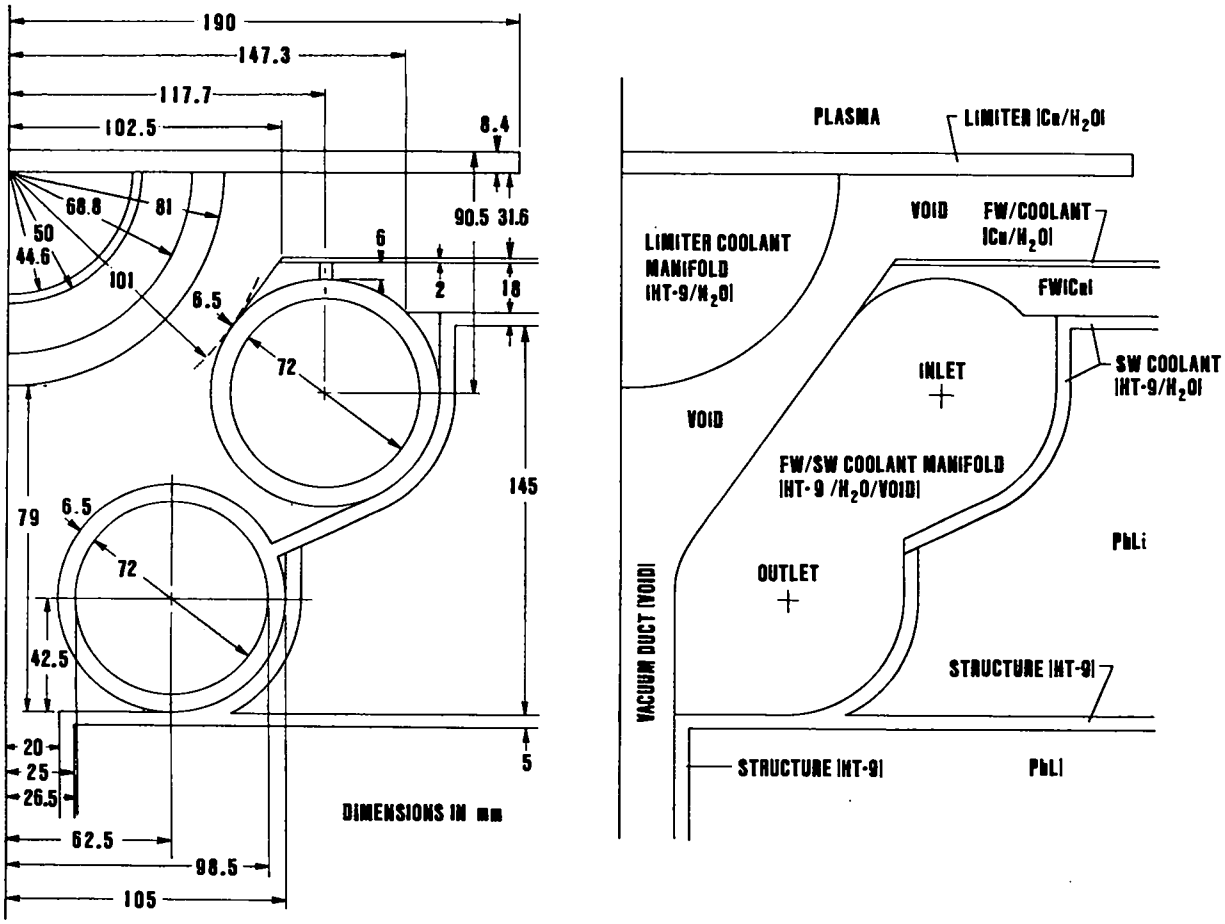

Fig. 2-1B. Detailed view of first wall, second wall, limiter, and associated coolant manifolding used in the two-dimensional TRIDENT-CTR model.

The region previously occupied by the manifold was then replaced by PbLi, while the volume of the regions was conserved. In addition, the effects of using D_2O as a first-wall/second-wall and limiter coolant and increasing the ^6Li enrichment from 60% to 80% were investigated. The values for the TBR calculated by the TRIDENT-CTR and TWODANT codes for these design changes are summarized in Table 2-I. All cases reported correspond to the first-wall/second-wall coolant manifolds located near the first wall.

A 5-mm-thick first wall (4-mm-thick copper and water followed by a region of 1-mm-thick copper) was adopted as part of the modified reference design. The TRIDENT-CTR calculation of the 5-mm-thick first wall gave a TBR of 0.899, while a value of 0.892 was calculated by TWODANT. The MCNP calculations were also performed for this model and yielded a TBR of 0.870 ±0.010, which agrees with the discrete-ordinates calculations.

In order to assess the effects of ^6Li enrichment, TWODANT calculations were made for 80% and 90% ^6Li enrichments. Calculations were also performed with D_2O coolant for a range of ^6Li enrichments. The resulting TBRs are plotted in Fig. 2-2. An approximately linear variation in TBR with ^6Li enrichment for both H_2O and D_2O coolants is observed. The H_2O/90%-^6Li case was also calculated with MCNP, which gave a TBR of 0.939 ± 0.005.

The 0.10-m-thick shield adopted in Ref. 10 consisted of alternating 25-mm-thick layers of 80% tungsten and 80% B_4C; each layer also contains 10% structure [primary candidate alloy, stainless steel (PCASS)] and 7.9% H_2O coolant. Replacement of this shield with a good reflector was expected to improve the TBR. Calculations were performed with 90%-enriched ^6Li in which all four shield layers were a) taken as the W/PCASS/H_2O mixture described above, b) replaced with pure tungsten, or c) replaced with 90% PCASS and 10% H_2O. The TBR values calculated using TWODANT for these three cases are 0.979, 0.992 and 1.006 respectively. An MCNP calculation was made for the 90% PCASS/10% H_2O case and gave a TBR value of 0.978 ±0.009. Hence, added enhancement of TBR can be achieved by emphasizing the reflecting nature of this thin shield rather than the absorbing nature.

To investigate the possibility of providing a TBR margin with a slightly thicker blanket, TWODANT calculations were performed for the 90%-enriched, PCASS-reflected model with 50-mm and 100-mm thicknesses of additional PbLi in the blanket region. Radii of all regions and boundaries behind the blanket were correspondingly increased. These calculations yielded TBR values of 1.033 and

TABLE 2-I

TRITIUM-BREEDING RATIOS CALCULATED FOR DESIGN AND MATERIAL VARIATIONS ON THE REF. 10 MODEL

Coolant	^{6}Li Enrichment (%)	Design Variation	TBR	
			TWODANT	TRIDENT-CTR
H_2O	60	Reference	0.786	0.785
H_2O	60	Add 50 mm to PbLi blanket	0.818	-
H_2O	60	Relocate manifold to rear of blanket	1.033	-
H_2O	60	Reduce first-wall thickness from 20 mm to 3 mm	0.898	0.901
H_2O	80	Reference	0.842	-
H_2O	80	Reduce first-wall thickness from 20 mm to 3 mm	0.955	0.959
D_2O	60	Reference	0.989	-
D_2O	60	Reduce first-wall thickness from 20 mm to 3 mm	1.125	1.113

1.058, respectively, and are plotted in Fig. 2-3. The latter case was also calculated with the MCNP code, giving a TBR of 1.035 ± 0.008 and consistency with previous results.

In summary, the effects of the two-dimensional neutronics analysis resulted in an FPC design that is modified somewhat from the ONEDANT-based design presented in Ref. 10. The principal changes in the modified design are listed as follows and represent the starting point for this follow-on study:

- Decreasing first-wall thickness from 20 mm to 5 mm gives a TBR = 0.899.
- Increasing ^{6}Li enrichment from 60% to 90% gives TBR = 0.939 ±0.005.
- Reoptimizing neutron-absorbing shield (W/PCASS/H_2O/B_4C) to function more as a reflector (PCASS/H_2O) gives TBR = 0.978 ±0.009.
- Adding 100 mm of PbLi thickness to the blanket gives TBR = 1.058.

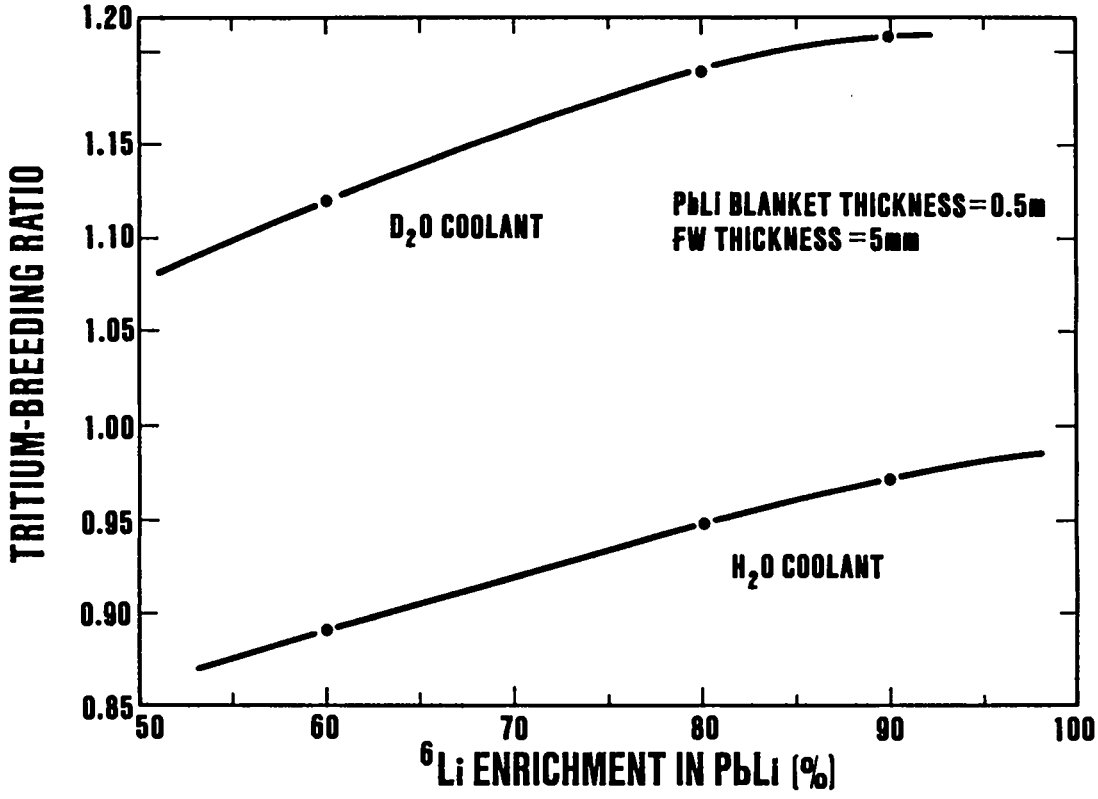

Fig. 2-2. Dependence of TBR on ^{6}Li enrichment for both D_2O and H_2O coolants when the first-wall thickness is reduced from 20 mm to 5 mm.

These design changes are also represented in Fig. 2-1 and are minor. The major changes upon which this follow-on study is based are embodied in a better resolution of the distribution of the local heating rates, FPC energy balance, and magnetic-field profiles, all of which are used to perform an improved thermal-hydraulic and thermal-mechanical reoptimization of the FPC.

An alternative or supplemental approach towards improved TBR values would relocate the first-wall/second-wall coolant manifold to the rear of the blanket but inboard of the shield region. This option provides large TBR margins and allows ^{6}Li enrichments significantly below 90%, should a lithium-enrichment cost issue arise. Moving the manifolds away from the first-wall region would also increase the plant thermal efficiency somewhat, since the fraction of neutron energy delivered to PbLi relative to water is increased. Lastly, as indicated in Fig. 2-2, use of D_2O coolant in the first-wall/second-wall and limiter regions would give a strong increase in TBR margin although the complexity and added expense of a heavy-water coolant loop remains unknown. Major design

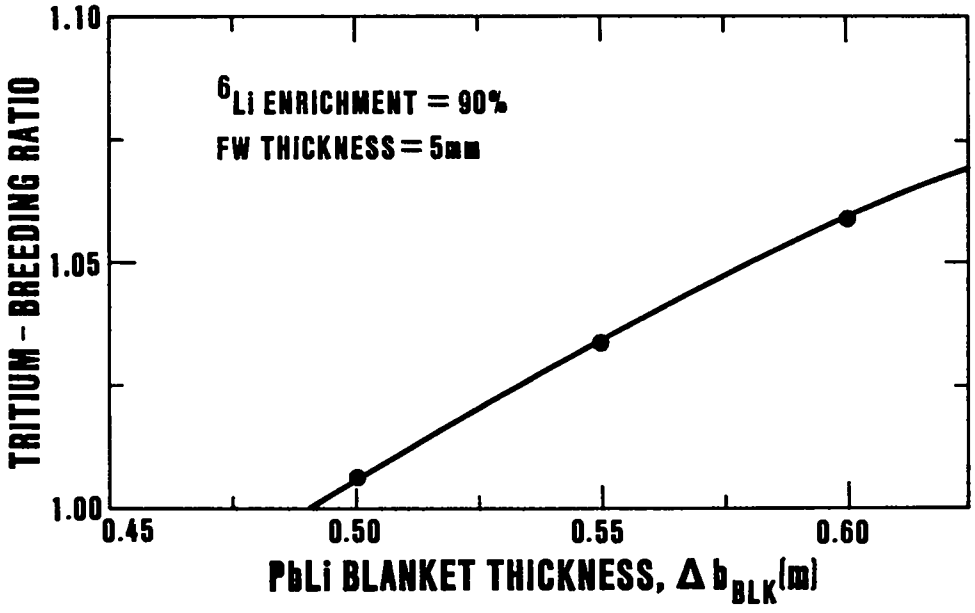

Fig. 2-3. Dependence of TBR on increased PbLi blanket thickness for 90%-enriched ^{6}Li, a reduced 5-mm first-wall thickness, and H_2O-cooled first-wall, second-wall, and limiter systems.

changes that replace the pumped limiters with magnetic divertors, and/or decrease the neutron first-wall loading (i.e., eliminate a separately cooled first wall) would generally improve the TBR margin, although the amount of blanket lost to the divertors remains to be fully assessed (Sec. 7.).

The TRIDENT-CTR edits for fluxes, heating rates, dpa, gas production, and radioactivity production (including afterheat) were used as an updated database with which to reoptimize and integrate the FPC. Figure 2-4 gives the spatial distribution of neutron and gamma-ray heating rates along the three radial bands identified in Fig. 2-1, these results being averaged in the toroidal direction for use in the thermal-hydraulic analyses (Sec. 3.2.3.). The TRIDENT-CTR fluxes were also used to estimate radioactivity and afterheat effects in Sec. 5.

2.2. FPC Thermal-Hydraulics Model

The thermal-hydraulic design of the FPC performed in Ref. 10 was based on the results of a one-dimensional neutronics analysis. That analysis could not include the effects of limiter and first-wall manifolds positioned inside the blanket. When calculating the heat transferred from the PbLi in the first blanket coolant channel (Fig. 2-1) to the second-wall coolant, laminar flow and conduction-dominated transport in the flowing PbLi were assumed. Furthermore, only a limited number of design configurations were considered for the blanket channels. The number of configurations considered to model thermal contact between the blanket and second wall was also limited. This follow-on study extends and refines the FPC thermal-hydraulic design model used in Ref. 10 and

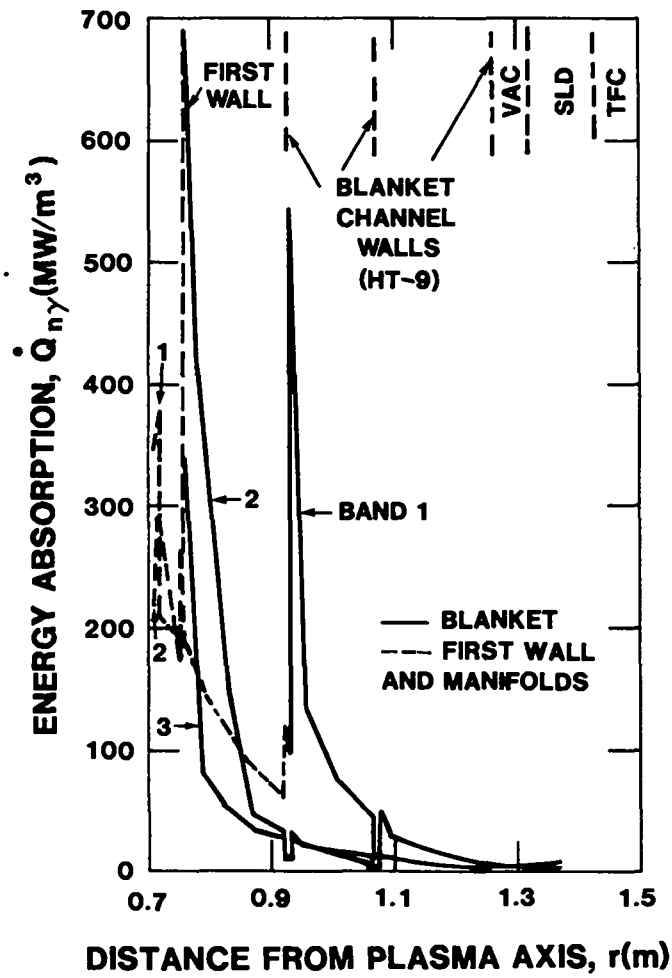

Fig. 2-4. Spatial dependence of heating rates determined from the TRIDENT-CTR redesign and used in subsequent thermal-hydraulic analyses and FPC integration studies. Refer to Fig. 2-1 for band locations.

re-evaluates the CRFPR(20) thermal-hydraulics design based on the more exact two-dimensional neutronics results. The most significant changes in the models are listed as follows:

- The results from a two-dimensional neutronics calculation that includes separately and distinctly the first-wall/second-wall and limiter coolant manifolds are used (Sec. 2.1.).
- A detailed numerical analysis has been used for analyzing thermal convection in the poloidal and radial (inlet) blanket channels. Both laminar and turbulent flow can be analyzed.
- Additional second-wall/blanket interfacial configurations are considered to examine the impact on maximum structural temperature in the PbLi-cooled blanket.
- Restrictions on the geometry of the blanket channels are relaxed to allow consideration of a wider variety of options.

The dual-media coolant system adopted in the Ref. 10 design must be retained, as is depicted in the highly schematic Fig. 2-5. The limiter, first wall, second wall, and shield are each cooled by separate, single-pass pressurized-water circuits that share common input and output headers but have separate manifolds. The first structural wall of the PbLi-cooled blanket serves as the return leg for the first-wall water coolant and, as previously noted, is termed the "second wall." A mechanical separation between the second wall and the containing structure for the PbLi may be possible, depending on achievable contact thermal resistances. Separate cooling of the inside structural wall is necessary for the CRFPR(20) design in order to hold 450-500°C corrosion-related temperature limits[28] at the PbLi/structural interface. The conditions where a mechanical separation can be maintained between this second-wall water coolant and the inner-blanket PbLi coolant are described in Sec. 2.2.1. The conditions under which separate cooling of the blanket structure by pressurized water can be eliminated are addressed in Sec. 3.5. The following subsections separately describe the thermal hydraulic models and conditions for the first-wall/second-wall, limiter, and blanket, paralleling Secs. III.D.2.a., III.D.2.b., and III.E. of Ref. 10. Section 3. then presents a power, thermal-hydraulic, and mechanical integration of the separate FPC components, paralleling Sec. III.L. of the Ref. 10 framework design.

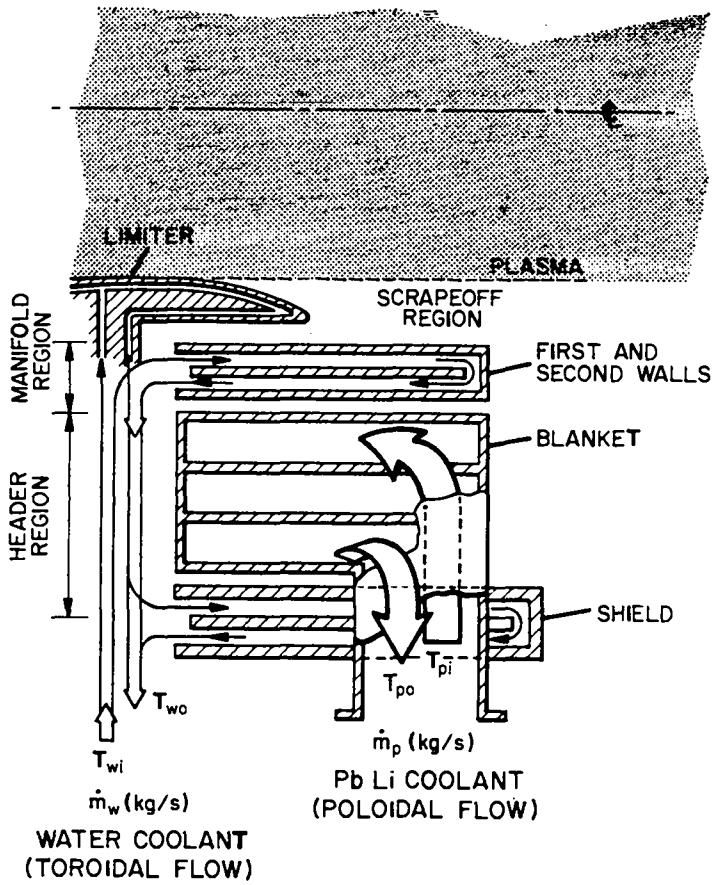

Fig. 2-5. Schematic diagram of dual-media, pressurized-water/flowing-PbLi coolant system for each half of N = 24 CRFPR(20) toroidal sectors. Key notation used throughout the thermal-hydraulic analysis is also shown.

2.2.1. First-Wall/Second-Wall Models

A possible first-wall/second-wall system is shown in Fig. 2-6. The first wall consists of copper-alloy tubes aligned in the toroidal direction. One possible option for the second wall is a 5-mm-thick HT-9 wall containing pressurized-water coolant channels. The chemical composition and selected thermal and mechanical properties for these materials are given in Table 2-II. Other second-wall options are discussed in Sec. 2.2.3.3.

The energy absorption rate for the first wall includes radiation and particle fluxes from the plasma and neutron/gamma-ray volumetric heating. The second-wall energy absorption includes heat conduction from the PbLi in the blanket (possibly through a separating metal/metal interface) and from neutron/gamma-ray volumetric heating. The first and second walls are cooled by high-pressure, subcooled (~ 10 K) water flowing through the first-wall D-tubes and returning through the second-wall channels.

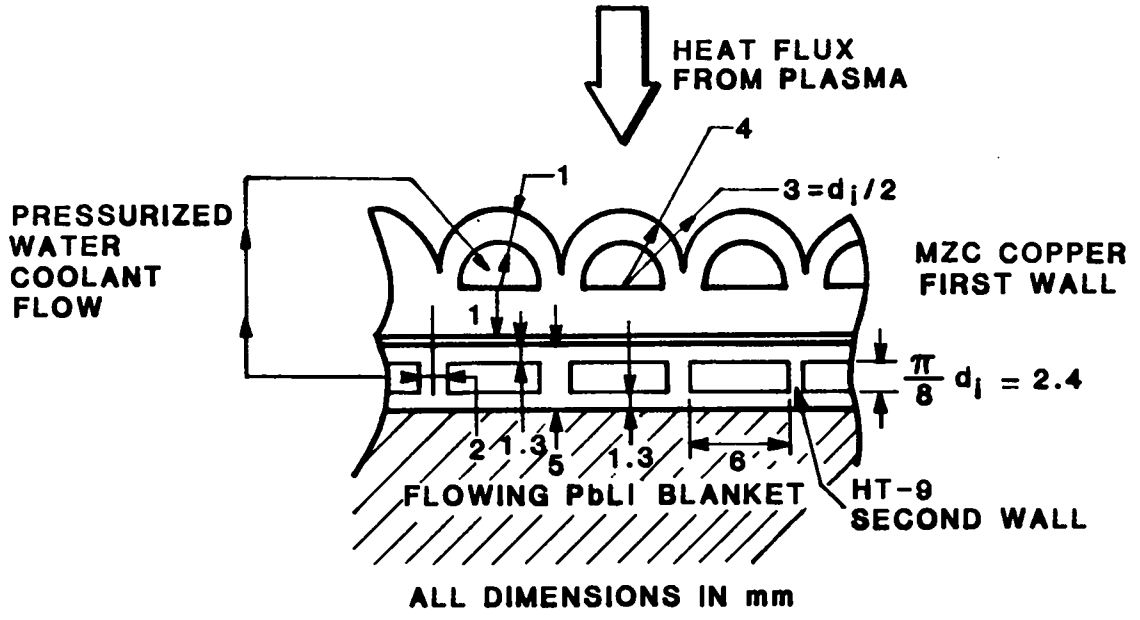

Fig. 2-6. First-wall/second-wall configuration used in thermal analyses, where flow directions are toroidal. Depending on thermal contact resistance, a third structural wall may be placed between flowing PbLi coolant and the HT-9 second wall.

TABLE 2-II

SELECTED PROPERTIES OF STRUCTURAL MATERIALS

	MZC Copper Alloy	HT-9 Ferritic Steel
Composition	0.06% Mg, 0.15% Zr, 0.4% Cr	12% Cr, 1% Mo
Density (kg/m^3)	8880.	7800.
Melting point (^oC)	1075.	1420.
Specific heat (J/kg K)[a]	394.	680.
Thermal conductivity (W/m K)[a]	324.	29.5
Emissivity[b]	0.4	0.5
Young's modulus (GPa)	138.	170.
Poisson's ratio	0.33	0.27
Thermal-expansion coefficient ($10^{-6}/K$)	18.4	12.7
Yield strength at 500°C (MPa)	416.4	200.

(a) At 400°C.

(b) Values quoted for nominally roughened surfaces.

The design parameters for the first-wall/second-wall cooling system include the water pressure, inlet and exit temperatures, and the geometry/dimensions of the coolant passages. The optimum design ultimately gives the maximum net electrical power output from the reactor. Achieving this optimum requires the maximum temperatures for all coolants without exceeding stress and temperature limits of the materials. Generally, the exit conditions for the pressurized-water coolant limit the overall plant efficiency.

2.2.1.1. First-Wall Structural Analysis

A detailed structural analysis for the first wall (and limiter) would require a two-dimensional finite-element model that includes the effects of fatigue, creep, sputtering erosion at the surface, and possibly non-uniform heat loads. Because of the scoping nature of the CRFPR design, a simpler approach was adopted that uses a steady-state one-dimensional stress calculation and applies a large factor of safety. The total stress for a thin-walled tube is given by

$$\sigma = P_w d_i/(2\delta) + \alpha E q_w \delta/[2k(1 - \nu)] \ , \qquad (1)$$

where P_w is the coolant pressure (w for water versus p for PbLi), d_i is the inside tube diameter, δ is the tube-wall thickness, α is the thermal expansion coefficient, E is Young's modulus, q_w is the wall heat flux, k is the thermal conductivity, and ν is Poisson's ratio. The two terms on the right side of Eq. (1) correspond to the pressure (primary) stress and the thermal (secondary) stress, respectively. The stress is required to be less than a design value, σ_D, which is taken to be the yield strength (Table 2-II) reduced by a factor of safety of 5. The wall thickness for a given tube diameter may be calculated from Eq. (1) for $\sigma = \sigma_D$, giving

$$\delta_{\pm} = C_1/2 \pm [C_1^2 - 4C_2]^{1/2}/2 \ , \qquad (2)$$

where $C_1 = 2\sigma_D k(1 - \nu)/(\alpha E q_w)$, $C_2 = P_w d_i k(1 - \nu)/(\alpha E q_w)$, and the plus(minus) sign gives the thick(thin)-wall solutions.

A solution to Eq. (2) exists only if

$$d_i < d_{iMAX} = \sigma_D^2 k(1 - \nu)/(P_w \alpha q_w E). \quad (3)$$

This condition provides an upper limit on d_i. For a given value of d_i, a wall thickness exists that gives the minimum stress. This wall thickness is obtained by setting the derivative of σ with respect to δ equal to zero, and is given by

$$\delta_{OPT} = [P_w k(1 - \nu) d_i/(\alpha E q_w)]^{1/2} . \quad (4)$$

The final selection of δ and d_i also depends on the results of a thermal analysis, the safety factor selected, and constraints imposed on coolant velocity and exit coolant conditions (Sec. 3.2.2). Figure 2-7 plots Eq. (1) for conditions that are close to the optimum design developed in Sec. 3.2.2. Also shown is the variation of coolant bulk velocity, V(m/s), and number of coolant tubes per sector, N_T. The minimum-stress thickness is chosen for further optimization.

A stress analysis for the pressurized rectangular coolant channels in the second wall gives

$$\sigma = (P_w/2)(w/\delta)^2 + P_w w/(2\delta) , \quad (5)$$

where w is the channel width and δ is the wall thickness. The terms on the right side of Eq. (5) represent the bending and shear stresses, respectively. Thermal stress is negligible in the second wall because of the lower heat fluxes. The minimum allowable value of δ is estimated from Eq. (5) for a given value of w by setting $\sigma = \sigma_D$.

2.2.1.2. First-Wall Thermal-Hydraulic Analysis

A numerical analysis was used for the thermal-hydraulic design of the first and second walls. The inside diameter of the first-wall D-tubes (Fig. 2-6), d_i, the inlet water temperature, T_{wi}, and the inlet water pressure, P_{wi}, are treated

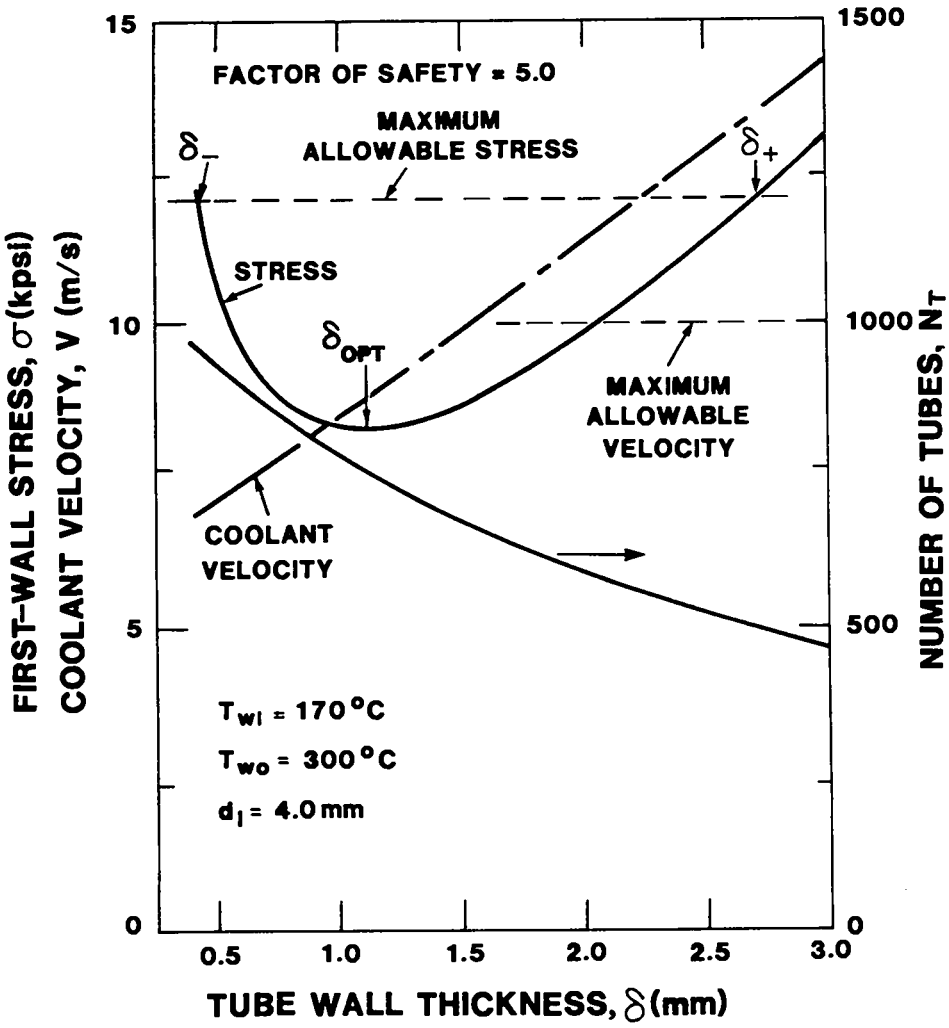

Fig. 2-7. Dependence of first-wall stress, coolant velocity, and coolant-tube number on tube wall thickness.

as design variables. The stress calculations described in Sec. 2.2.1.1. are used to determine an appropriate tube-wall thickness, δ.

The number of first-wall (and second-wall) tubes, N_T, is then determined from the following expression:

$$N_T = 2N[2\pi r_w/(d_i + 2\delta)] \quad , \tag{6}$$

where r_w is the minor radius of the first wall. The factor 2N = 48 corresponds to N = 24 toroidal sectors that comprise the reactor torus, each sector having manifolds at the sector center and coolant tubes at both sides (Fig. 1-3).

Given values for the inlet and exit coolant-water temperatures, the mass flow rate for a single tube is computed from

$$\dot{m}_w = \frac{P'_{FW/SW}}{N_T \Delta i} \quad , \tag{7}$$

where $P'_{FW/SW}$ is the total cooling rate for the first-wall/second-wall system (excludes manifolds, includes surface plus volumetric heating) and Δi is the change in coolant-water specific enthalpy. The average fluid velocity is

$$V = 8\dot{m}_w/(\pi d_i^2 \rho_w) \quad , \tag{8}$$

where ρ_w is the density of the coolant water and $\dot{m}_w$ is the mass flow rate.

The inside tube-wall temperature at the tube exit is

$$T_{si} = T_{wo} + q_w/h \quad , \tag{9}$$

where q_w is the heat flux at the inner surface of the tube wall and h is the local film coefficient. The heat flux is determined by dividing total cooling rate for the first wall (excluding manifolds), P'_{FW}, by the total effective area of the inside surface of the tubes. The film coefficient is calculated from the following expression:

$$h = 0.0155(k_w/d_H)Pr^{0.5}Re^{0.83} \quad , \tag{10}$$

where k_w is the thermal conductivity of water, d_H is the hydraulic diameter, Pr is the Prandtl number, and Re is the Reynolds number. The temperature at the outside surface of the tubes (maximum material temperature) is calculated by a one-dimensional steady-state conduction analysis according to

$$T_{so} = T_{si} + \dot{Q}_{m\gamma}[\delta/h + \delta^2/(2k)] + q_w(1/h + \delta/k) \quad , \tag{11}$$

where $\dot{Q}_{m\gamma}$ is the volumetric heating from neutrons and gamma rays and k is the thermal conductivity of the tube material.

The following criteria are selected to define a satisfactory first-wall/second-wall thermal-hydraulic design.

- The bulk fluid velocity must not be so large as to cause excessive erosion. A value of 10 m/s is selected as the nominal upper limit.
- The maximum temperature at the inside surface of the coolant tubes must be less than the saturation temperature of water by a specified amount. A difference of 10 K is selected for design purposes.
- The maximum material temperature must be less than a specified value. One-half the melting temperature is selected as the upper limit.

The hydraulic pressure drop for the first-wall coolant tubes of length ℓ is estimated from

$$\Delta P = f_F(\ell/d_H)\rho_w V^2/2 \quad , \tag{12}$$

where the friction factor is computed from

$$f_F = 0.184/Re^{0.2} \quad . \tag{13}$$

The procedures used to calculate thermal-hydraulic conditions for the second wall are the same as those used for the first wall except for differences in channel geometry and heating rates. The cooling rates are significantly lower in the second wall because of the absence of the radiative and convective energy fluxes from the plasma. Conduction from the PbLi in the blanket to the second-wall coolant is included, however, thereby coupling the second-wall analysis to the blanket analysis (Sec. 2.2.3.).

The thermal-hydraulic calculations for the first and second walls are performed by a numerical marching procedure that solves the equations in finite-difference form. Calculation of the heat transfer and pressure drops in the inlet and exit manifolds are also included.

2.2.2. Limiter

The Ref. 10 edge-plasma conditions assume $f_{RAD} = 0.9$ of the total energy shed by the plasma (25.3 MW of ohmic dissipation and 546.5 MW of alpha-particle heating) is radiated uniformly over the first-wall and limiter surfaces [$A_{FW} = (2\pi)r_w^2 R_T$], with the N = 24 poloidal limiters occupying ~ 38% of A_{FW} in order to assure that the peak heat load of $q_D = 6$ MW/m^2 is not exceeded. Hence, the cooling requirements for the pumped limiter are similar to those for the first wall. Copper alloy is also proposed for use for the pumped-limiter surfaces facing the plasma. As seen from Figs. 1-2 and 1-3, as well as the more detailed view given in Fig. 2-8, the orientation of the limiter relative to the first wall is poloidal. The shape of the outer surface of the limiter was determined by an edge-plasma model similar to that used for tokamaks[29] and discussed in Ref. 10. The limiter radial thickness is made as small as possible consistent with the inclusion of coolant-water channels of sufficient size to provide adequate cooling at acceptable coolant velocities and pumping power while maximizing the limiter-slot area for purposes of particle pumping.

A thermal-hydraulic analysis similar to that used for the first-wall coolant tubes was used along with a structural analysis to determine suitable coolant-channel dimensions for the pumped limiter. As seen from Fig. 2-8, pressurized-water coolant is supplied to each limiter by concentric poloidal manifolds that direct coolant to the limiter in the toroidal direction. The key design parameters are coolant inlet and exit temperature, channel height and width, thickness of material between the channels and the limiter surface, and spacing between coolant channels. An optimal design requires the highest coolant temperatures that are compatible with maintaining the limiter at an acceptable operating temperature. The coolant channel configuration proposed for the limiter is shown in Fig. 2-9, which gives both heat fluxes and steady-state temperature distribution. It is noted that, although both neutronic and thermal-hydraulic analyses assumed the limiter to be copper alloy, in principle only the high-heat-flux surface need be this material, with the bulk being a steel alloy. Cooling rates, heat fluxes, and geometric parameters for the limiters are summarized in Table 2-III.

The limiter coolant in each of 24 toroidal sectors flows in series with the shield/reflector coolant (86.5 MW). The thermal-hydraulic analysis is incorporated into a computer code which analyzes a total coolant circuit

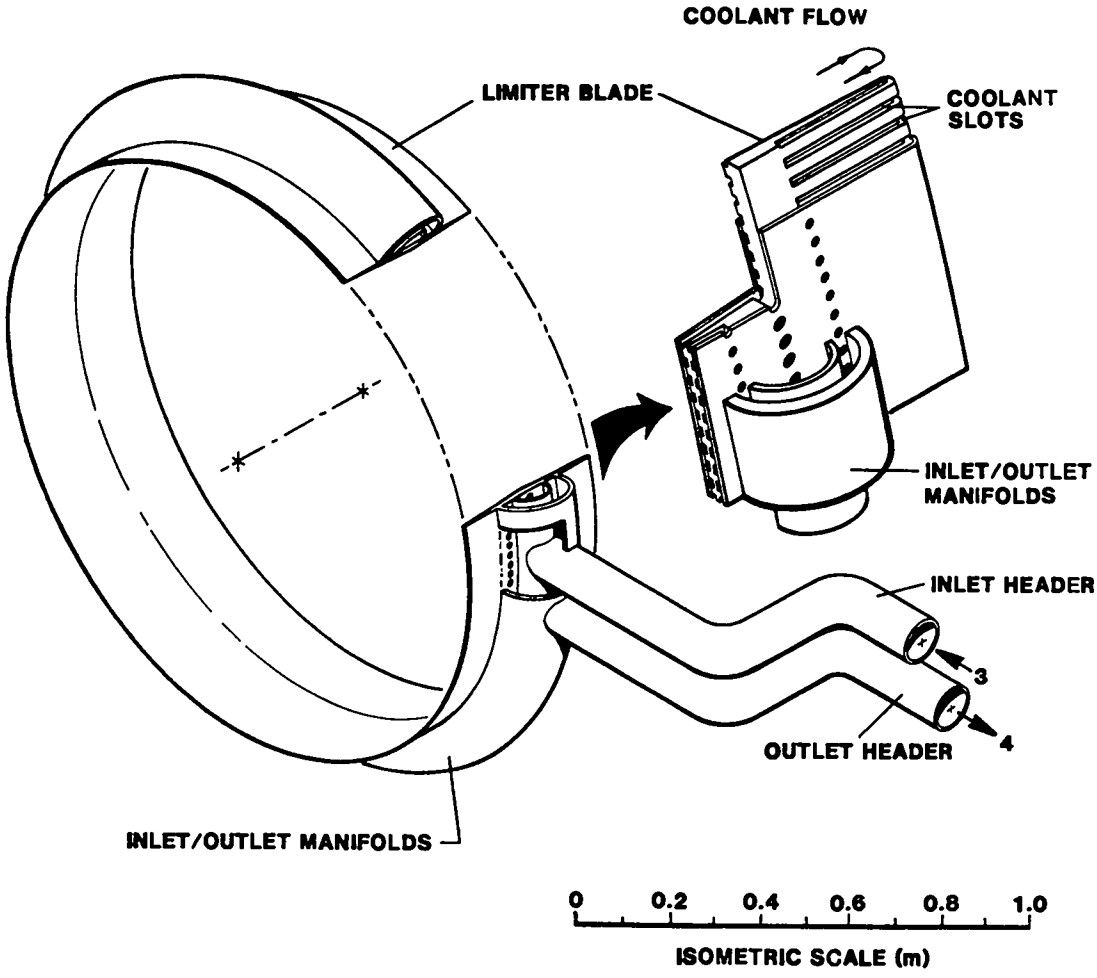

Fig. 2-8. Detailed view of one of N = 24 pumped poloidal limiters and accompanying pressurized-water coolant circuits (see Fig. 1-3).

containing the inlet manifold, limiter outlet manifold, and shield coolants. That code is used in the integrated FPC design discussed in Sec. 3.2.

A critical cooling problem occurs at the limiter tip. The surface of the limiter facing the plasma receives both a radiation flux and a (unresolved) particle flux. The surface is shaped so that the combined energy flux incident

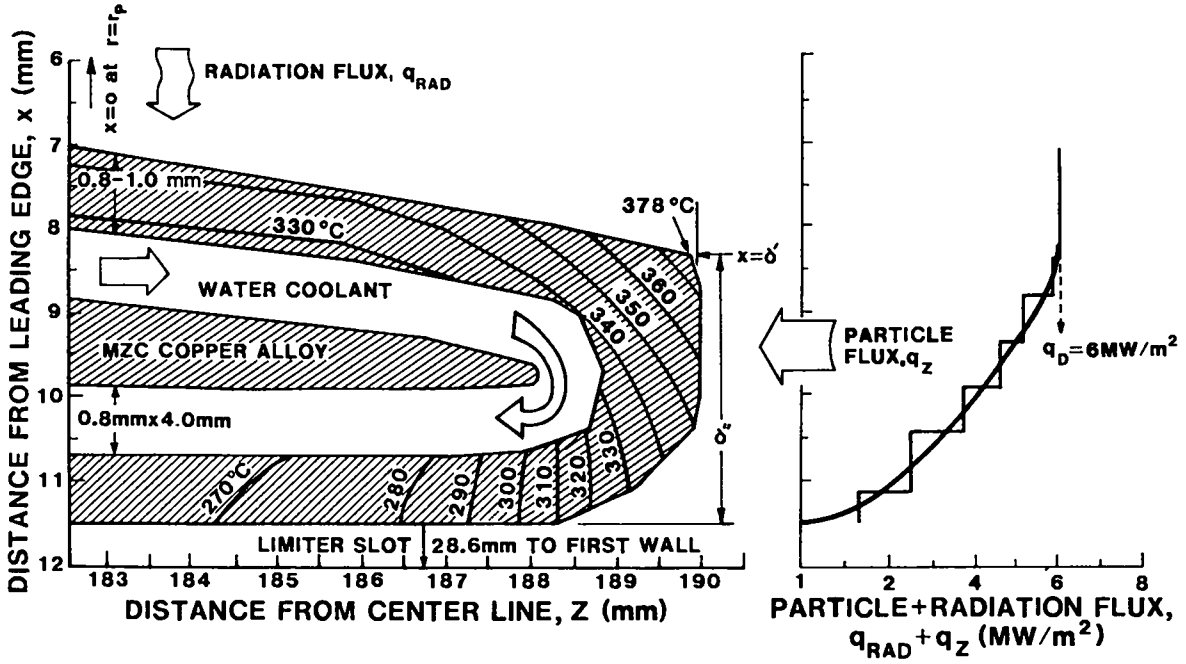

Fig. 2-9. Limiter-tip temperature and heat-flux distribution based on design developed in Ref. 10.

on the limiter surface is uniform and does not exceed a nominal design limit of q_D = 6 MW/m^2. The point where the scrapeoff particle energy flux in the toroidal or z-direction falls below q_D (Fig. 2-9) determines the toroidal extent of the limiter, $z = \pm \ell/2$, which in turn determines the radial extent, $x = \delta'$. The x-z coordinate system is defined by the limiter leading edge (plasma radius, r_p) for x = 0 and the toroidal center, z = 0. The distance $r_w - r_p - \delta'$ determines the limiter-slot (radial) thickness available for pumping as well as the fraction, f_p, of the particles diffusing in the scrapeoff that enter the limiter slot. The resulting thickness δ', as seen from Fig. 2-9, is not sufficient to support cooling channels, and structure material of thickness δ' is added to the underside of the limiter.[10]

The pressurized-water coolant leaves the limiter at 257°C and 10 m/s, which gives a local film coefficient of 100,000 W/m^2 K.[30] These coolant properties, the heat fluxes in Fig. 2-9, the thermal-physical properties in Table 2-II, and the volumetric heat generation of 324.8 MW/m^3 were used to calculate the temperature distribution in Fig. 2-9. The temperature at the limiter tip (378°C) is within the creep limits for this alloy.[31] The slight increase in temperature from that reported in Ref. 10 (378°C versus 371°C) reflects the much larger volumetric heat generation (327.8 MW/m^3 versus 222 MW/m^3), this

TABLE 2-III

PUMPED-LIMITER THERMOHYDRAULIC DESIGN PARAMETERS

Heat Flux and Total Power	
• Heat flux[a] (MW/m^2)	6.2
• Neutron energy absorption (MW)	110.6
• Power absorbed by limiter coolant[b] (MW)	363.4
• Percent of total thermal output[b]	10.5
• Design stress safety factor, σ_Y/σ_D	6.3[c]
Geometry	
• Number of limiters	24.
• Number of channels per limiter side	942.
• Channel length (m)	0.38
• Channel width (mm)	4.0
• Channel height (mm)	0.8
• Wall thickness (mm)	1.0[d]

(a)The plasma side of the limiter would be shaped to maintain a nominally constant plasma heat flux.

(b)In addition, 204.8 MW of neutron and gamma-ray heating is deposited into the inlet/outlet manifolds, giving a total of 568.0 MW or 16.4% of the total thermal power.

(c)Based only on pressure stress applied to a beam-like geometry. Preliminary estimates indicate that the thermal stress is small by comparison.

(d)Although satisfactory from a stress viewpoint, this thickness allows no sputtering margin. Graphite tiles or Be coatings would be used.

difference resulting largely from the two-dimensional limiter-specific neutronics calculations compared to the Ref. 10 one-dimensional estimates. Nuclear heating within the limiter now accounts for 22% of the total energy received by the limiter blade. The temperature contours at the limiter edge (top) reflect the $q_D = 6\ MW/m^2$ design heat flux, while the contours at the bottom of the limiter show flow from the limiter tip toroidally to the bulk limiter material, since the heat flux at the limiter underside is nearly zero for the scrapeoff model used.[10]

Although the limiter temperatures are well within the acceptable range set by creep for the configuration shown, the relatively thin sections required allow little design margin for significant net sputter erosion. The improvements needed to analyze better these important plasma-wall interactions,

including self-consistent calculation of sputtering rates, redeposition, and radiation fractions, represent an important area of future work.

2.2.3. Blanket

The CRFPR(20) blanket consists of liquid PbLi flowing poloidally through channels constructed of HT-9 ferritic steel. The PbLi serves as both the breeding material and coolant. Neutron and gamma-ray heating in the blanket was computed by the TRIDENT-CTR code[24] in two dimensions for the half segment shown in Fig. 2-1. Variations of energy in the toroidal direction are small compared to radial variations. Averaged values of energy absorption given in Fig. 2-4 were calculated for each radial location. These averaged results are shown in Fig. 2-10 and are used in the blanket thermal analysis.

Several concepts for coolant-channel design were originally considered.[10] Two variations of the design adopted in Ref. 10 are shown in Fig. 2-11. The thicknesses of the i^{th} poloidal channel, $w_{\theta i}$, are uniform in both cases. Option A depicted on Fig. 2-11 has radial channels that vary in thickness from $w_{\theta i}$ at the inside to w_{Ri} at the outside. The radial channels in Option B have uniform thickness, w_{Ri}. The blanket design is based on thermal, hydraulic, and one-dimensional MHD analyses of the PbLi flow in each individual channel.

2.2.3.1. Blanket Hydraulic Analysis

Eddy currents are induced when an electrically conducting fluid of viscosity η and electrical conductivity σ flows between parallel plates of separation 2a with a velocity V perpendicular to a magnetic field. These eddy currents interact with the magnetic field and produce a pressure gradient given by [32]

$$dP_M/dx = - \eta V/a^2\left[(H^2 \tanh(H))/(H - \tanh(H)) + H^2 C/(1 + C)\right] , \qquad (14)$$

where $H = aB(\sigma/\eta)^{1/2}$ is the Hartmann number, B is the strength of the transverse magnetic field, and $C = (\sigma_w t_w)/(\sigma a)$ is the ratio of conductivity-thickness products of the channel walls and the flowing fluid.

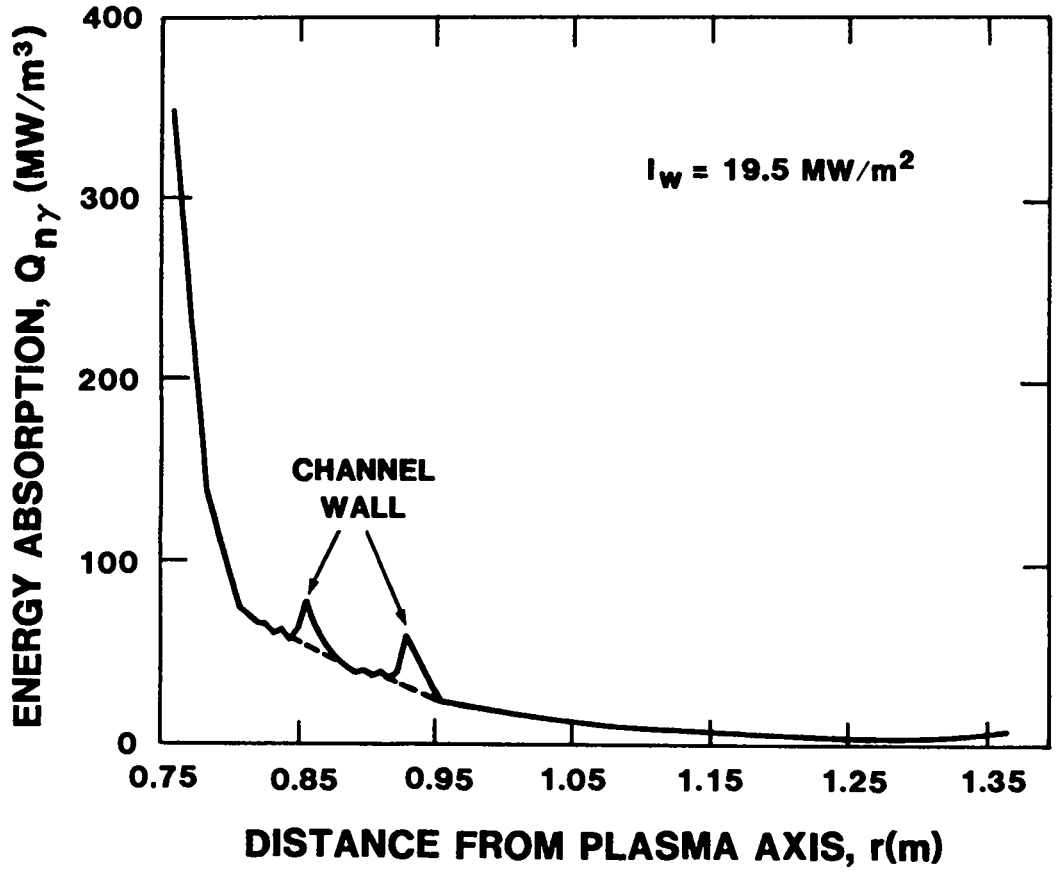

Fig. 2-10. Toroidal averages of the neutron and gamma-ray heating rates shown in Fig. 2-4 for the TRIDENT-CTR calculations and used in all blanket thermal hydraulics analyses. Remanent heating peaks at channel-wall positions were averaged. Channel walls were shifted somewhat from the positions used in the TRIDENT-CTR calculations by subsequent thermal-hydraulic analyses (Sec. 3.2.3.).

The thermal power deposited in the PbLi blanket, P_{BLK}, is computed by numerical integration of the power distribution obtained from the neutronics analysis (Fig. 2-10) over the radial extent of a given channel. If inlet and exit PbLi temperatures, T_{po} and T_{pi}, are specified, the PbLi mass flow rate can be calculated from $\dot{m}_p = P_{BLK}/[c_p(T_{po} - T_{pi})]$.

Equation (14) is then integrated for specified channel geometry, flow rate, and fluid properties to give the MHD pressure drop, ΔP_M. The spatial variations of the poloidal and toroidal fields, B_θ and B_ϕ, within the blanket and coil regions are approximated[10] by the following expressions:

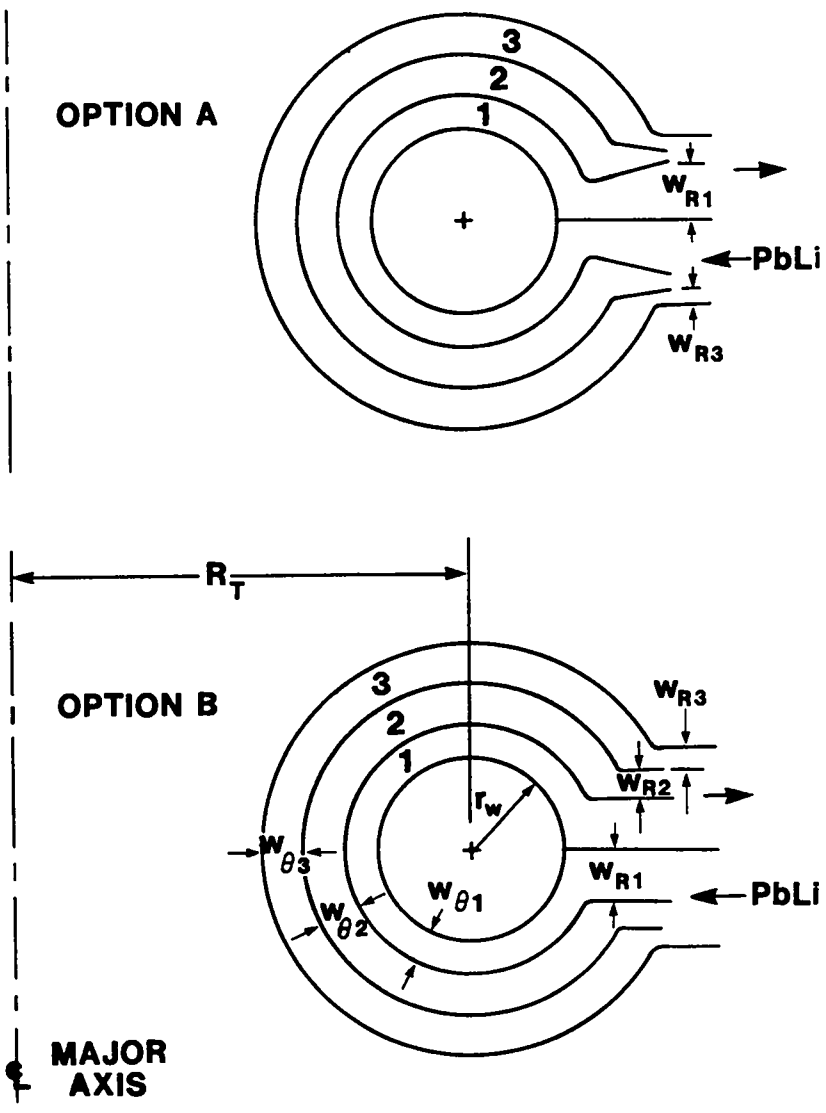

Fig. 2-11. Two variations on the parallel poloidal-channel concept suggested for the PbLi blanket in Ref. 10, both being based on inlet/outlet coolant access at the outboard equatorial plane of the FPC. The radial channel thickness, w_{Ri}, and poloidal channel thickness, $w_{\theta i}$, of the i^{th} coolant channel are noted. The design of w_{Ri} is important, in that the majority of the MHD pressure drop occurs at that location.

$$B_\phi(T) = 1.52/R = 1.52/(R_T + r \cos\theta) \quad \text{(inside the TFC)}, \quad (15A)$$

$$B_\phi(T) = 0 \quad \text{(outside the TFC)}, \quad (15B)$$

and

$$B_\theta(T) = 4.25/r - 0.8r - 0.2 \quad , \quad (16)$$

where R_T is a major radius and r is a minor radius. The viscous or frictional pressure drop, $\Delta P_F = (f_F \rho V^2)/(8a)$, is added to the magnetic pressure drop to obtain the total pressure drop, $\Delta P = \Delta P_M + \Delta P_F$. The pumping power is then computed from

$$P_{pump} = \dot{m}_p \Delta P/(\rho_p \eta_{pump}) \quad , \quad (17)$$

where η_{pump} is the pump efficiency, which is taken as 75%. This power dissipation is not assumed to enter the coolant stream as added thermal power.

The pressure drop calculated from Eq. (14) does not include local losses that may occur in regions where the flow direction, velocity, channel dimensions, or magnetic fields are rapidly changing. An accurate determination of those losses would require the simultaneous solution of the Navier-Stokes and Maxwell equations in three dimensions and was not within the scope of this study. When properly taken into account, the actual pressure drop and pumping power are therefore expected to be somewhat higher than those computed here when these effects are properly taken into account.[33] Specifically, the blanket designs considered in this study require the fluid to turn from a direction normal to a large magnetic field to a parallel direction. When MHD effects are present, the pressure drop will depend on the detailed manifolding geometry, the presence of insulators, and wall-thickness distributions. The semi-empirical correlation for a single conduit[32] with a bend may not give an accurate description of the actual pressure drop; the latter will depend on the details of the actual configuration and needs to be calculated using three-dimensional

MHD effects.[33] In most PbLi blanket designs, the flow is laminar and slug flow is generally assumed. The relevant transition numbers are $Re_T = 500H_\perp = 390{,}000$ and $Re_T = 60H_\parallel = 463{,}000$ for this study; since Re > 10^6 for the present design, the flow is expected to be turbulent.

2.2.3.2. Blanket Thermal Analysis

The temperature distribution within the PbLi in the blanket channels is determined by a numerical solution of the energy equation

$$\frac{\partial T}{\partial x} = \left[\frac{k_{eff}}{\rho c_p v}\right] \frac{\partial^2 T}{\partial y^2} + \frac{\dot{Q}_{m\gamma}}{\rho c_p v} \quad , \tag{18}$$

where x is the poloidal distance, k_{eff} is the effective PbLi thermal conductivity, and v is the local velocity. The total energy generation rate for the channel, $\dot{Q}_{m\gamma}$, is obtained by numerical integration of the neutron and gamma-ray absorption results given in Fig. 2-10. The mass flow rate and average velocity in the channel are then computed for specified values of bulk PbLi inlet and exit temperature, T_{pi} and T_{po}, respectively.

The flow regime depends on the Reynolds number and the Hartmann number. The magnetic field tends to suppress turbulence, with the transition Reynolds number given by[32] $Re_T = 500H$. Neglecting fluid property variations, the velocity distribution can be approximated by

$$v = v_{MAX}(y/a)^{1/n} \quad , \tag{19}$$

where n is 2 for laminar flow and 7 for turbulent flow, y is the distance from the nearest wall, a is the channel half-thickness, and v_{MAX} is the centerline velocity. The effective thermal conductivity for turbulent flow includes the molecular thermal conductivity of the PbLi and an eddy conductivity resulting from turbulent mixing. The effective conductivity is related to the effective viscosity by $k_{eff} = \eta_{eff} c_p / Pr_{eff}$, where the effective Prandtl number, Pr_{eff}, is approximately 0.9 for confined flows. The effective viscosity, η_{eff}, is based

on the Prandtl mixing length theory, with the VanDriest hypothesis[34] being assumed to apply at the wall. Specifically,

$$\eta_{eff} = \eta + \rho(\kappa y)^2 \left[1 - \exp\left(-y(\tau\rho)^{1/2}/(\eta A^+)\right)\right]^2 |dv/dy| \quad , \tag{20}$$

where $\kappa = 0.435$ and $A^+ = 26$ are empirical constants. The shear stress is approximated by $\tau = \eta(dv/dy)$ evaluated at the wall.

The thermal boundary condition at the inside structural wall of the blanket depends on the second-wall configuration. The four configurations shown in Fig. 2-12 were considered and are summarized as follows:

- Option A: Single barrier between second-wall water coolant and PbLi coolant (Ref. 10 case).
- Option B: Double barrier between second-wall water coolant and PbLi coolant with no thermal contact resistance (oxide layers).
- Option C: Same as Option B with infinite thermal contact resistance (only radiation).
- Option D: No water-cooled first-wall/second-wall system.

The boundary condition at the second wall is obtained by combining an algebraic solution of the one-dimensional heat-conduction equation for the second-wall material (including neutron and gamma-ray heating within the wall) with the energy equation at the blanket nodes near the second wall. The coolant-water temperature and film coefficient calculated in the first-wall/second-wall analysis are used in the boundary condition for the blanket analysis; the first-wall/second-wall and blanket analyses, therefore, are coupled.

Temperature distributions in the flowing PbLi coolant predicted at the downstream end of a poloidal section of inner-blanket channel are shown in Fig. 2-13 for a $w_{\theta 1} = 0.2$-m channel and inlet and exit PbLi bulk temperatures of $T_{pi} = 350^oC$ and $T_{po} = 500^oC$, respectively. A corrosion constraint placed on the Ref. 10 blanket design requires that the PbLi temperature in contact with HT-9 steel structure should be less than 500^oC. Option A is preferred from a thermal standpoint. Option B may be satisfactory if the PbLi outlet temperature, the channel thickness, or both are reduced. Options C and D are not feasible unless a) the neutron first-wall loading is reduced by a factor of ~ 3-4 from

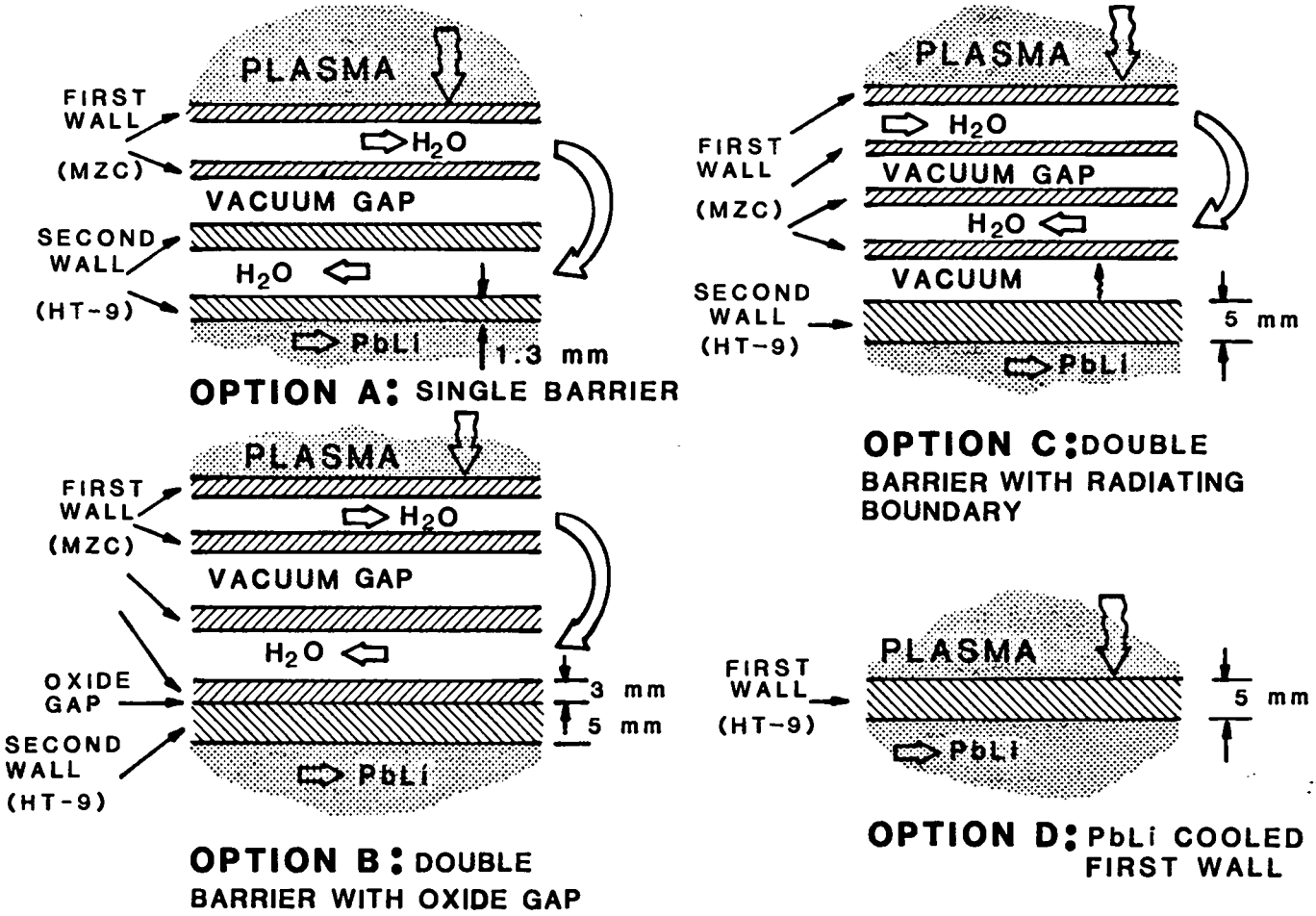

Fig. 2-12. Four inner-blanket-wall/second-wall/first-wall configurations considered in modeling the heat back-leakage boundary conditions between the PbLi coolant and first-wall/second-wall pressurized-water coolant.

I_w = 20 MW/m^2, or b) the channel width is reoptimized for operation at higher PbLi pressure while accepting reduced overall plant efficiency. Directions for Option D (i.e., no first-wall water coolant) are explored further in Sec. 2.2.3.3. and are examined quantitatively in Sec. 3.5.

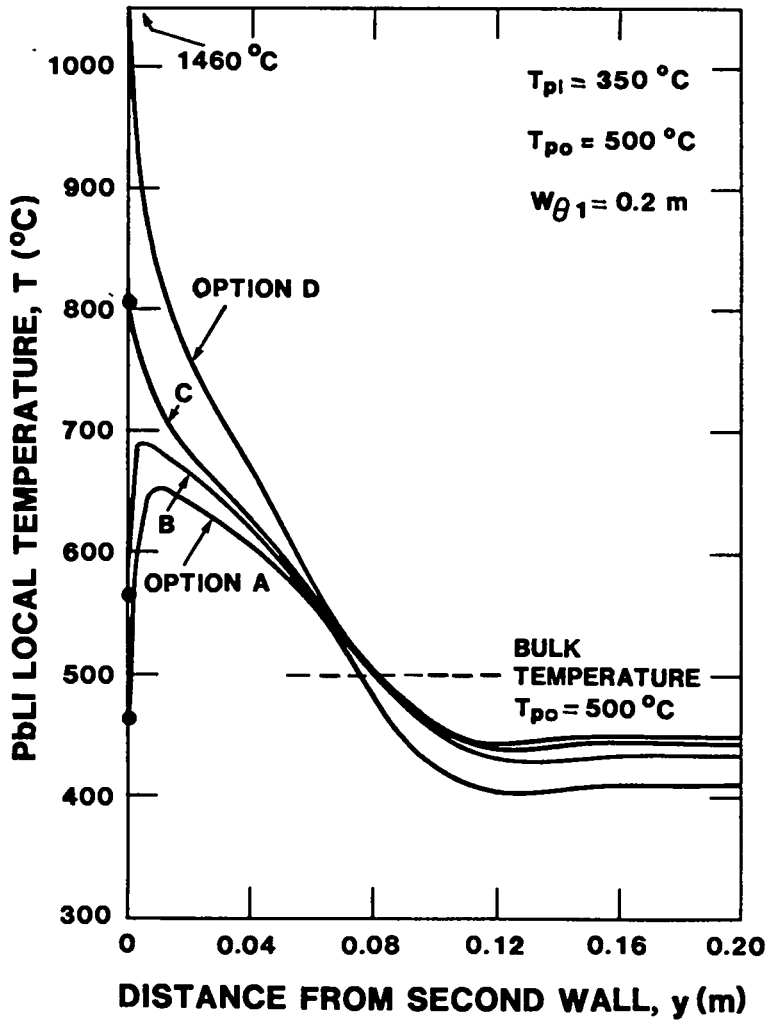

Fig. 2-13. Radial temperature distributions in PbLi coolant for the four first-wall/second-wall boundary options depicted in Fig. 2-12.

2.2.3.3. Channel Design

The hydraulic and thermal calculations discussed in Secs. 2.2.3.1. and 2.2.3.2. are combined to perform an integrated blanket optimization and design. Design parameters include the inlet and exit PbLi temperatures, T_{pi} and T_{po}, radial channel configuration (Fig. 2-11), and second-wall/inner-blanket configuration (Fig. 2-12). The thickness of the poloidal section of all channels and the thickness of the first radial (blanket-exit) channel must also be specified. The thermal analysis is used to compute the average velocity and temperature distribution in the first coolant channel, and the pressure drop is calculated using the hydraulic analysis. Flow rates for the remaining channels are calculated using the overall energy balance in conjunction with the thermal

analysis. The thicknesses of the radial channels at the blanket exit are determined while assuring that the pressure drops for all channels are equal (i.e., a continuity condition).

The sensitivity of key design parameters to system performance was examined first. Specifically, the effects of the various second-wall/inner-blanket boundary conditions and design options were investigated. From the standpoint of reliability, the pressurized cooling water required for high-heat-flux surfaces should be well separated from the PbLi coolant. Option B (Fig. 2-12) is preferable in this respect because two layers of metal separate the respective coolants. Option D is safest because no water resides near the PbLi system, except as required to cool the limiter. Option A is best from a thermal and corrosion standpoint, however, because the PbLi temperature at the HT-9 surface is held to a lower level by the cooling water (Fig. 2-13).

These preliminary calculations indicated that Option D (Fig. 2-12) cannot be used for the CRFPR(20) design because of the excessive temperatures at the PbLi/HT-9 interface. A parametric study was performed to estimate the neutron first-wall loadings below which only PbLi coolant is needed to hold the $\sim 500^{o}C$ temperature limit at the structural wall. The results of that study are shown in Fig. 2-14. The PbLi outlet temperature for the cases shown here is $400^{o}C$. The inlet temperature is $150^{o}C$ lower than outlet for the full-power case ($I_w \simeq 19.5\ MW/m^2$) in order to maintain consistency with the Ref. 10 design, which set this temperature difference on the basis of corrosion, blanket pressure, and pumping-power constraints. The PbLi inlet bulk temperature is adjusted for the lower-power cases to maintain a fixed ratio of pumping power to reactor power, ε_{pump}. The PbLi coolant velocity under these constraints decreases with neutron first-wall loading as $I_w^{1/4}$, and the inlet coolant temperature, T_{pi}, is increased. In the limit of very low power, $T_{pi} \rightarrow T_{po}$, the velocity approaches zero. Generally, the interface temperature cannot be held below $500^{o}C$, unless the PbLi exit bulk temperature is well below $500^{o}C$. In addition, the first-wall loading must be reduced to $\sim$ 25% of the CRFPR(20) design level, and the width of the first PbLi-coolant channel must be reduced. Major consequences of these choices are increased coolant pressures and pumping power (less important). It is possible for the overall thermal conversion efficiency to increase, however, because a small fraction of the total fusion power appears in the water coolant. No attempt has been made to optimize the Option D case examined in Fig. 2-14. The tradeoff between first-wall loading

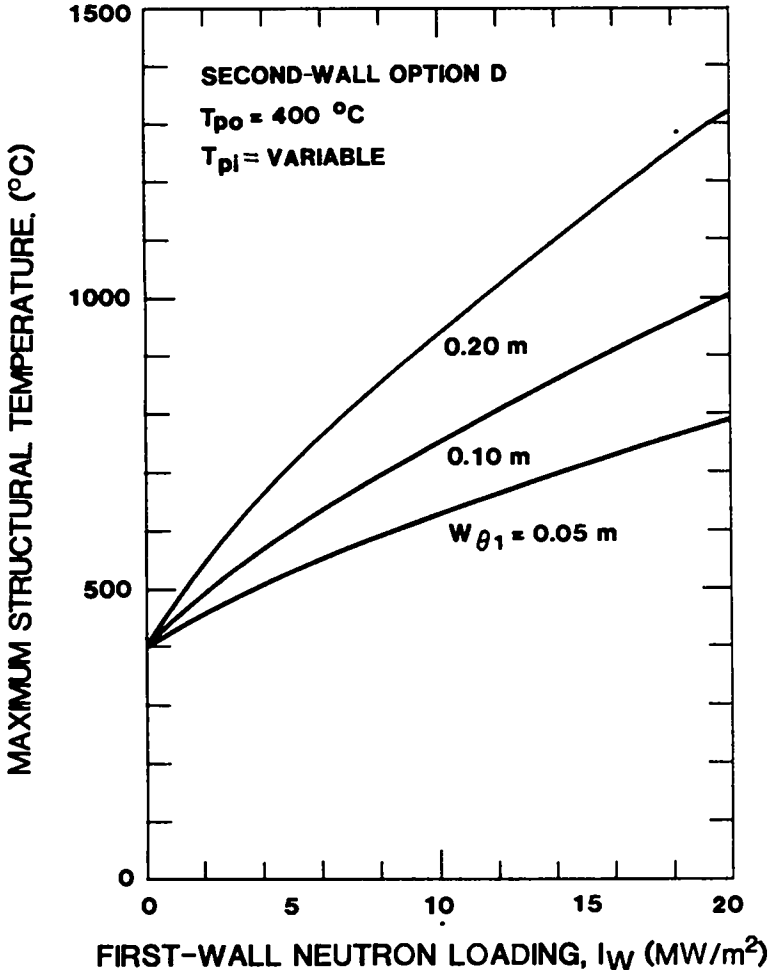

Fig. 2-14. Maximum PbLi temperature versus reduction in first-wall neutron loading relative to the CRFPR(20) design (I_w = 19.5 MW/m^2) for an HT-9 first wall cooled by PbLi (Option D, Fig. 2-12) and a range of thicknesses for the first poloidal-flow channel. For all cases, the recirculating power fraction required by the coolant pump, ε_{pump}, was held constant, and the magnetic fields were scaled as $I_w^{1/4}$, with the CRFPR(20) FPC geometry being maintained.

and overall plant efficiency (i.e., PbLi pressure, pumping power, thermal efficiency, and channel width) for a given maximum structural temperature is examined further in Sec. 3.5.

The results of calculations for first-wall/second-wall Options A and B (Fig. 2-12) are shown in Fig. 2-15 for PbLi inlet and exit bulk temperatures of T_{pi} = 350°C and T_{po} = 500°C. Option A gives HT-9/PbLi interface temperatures less than 500°C for all channel thicknesses considered, with the larger thicknesses being preferred because of lower coolant pressures and pumping power. The maximum PbLi/structure interface temperatures for Option B are too

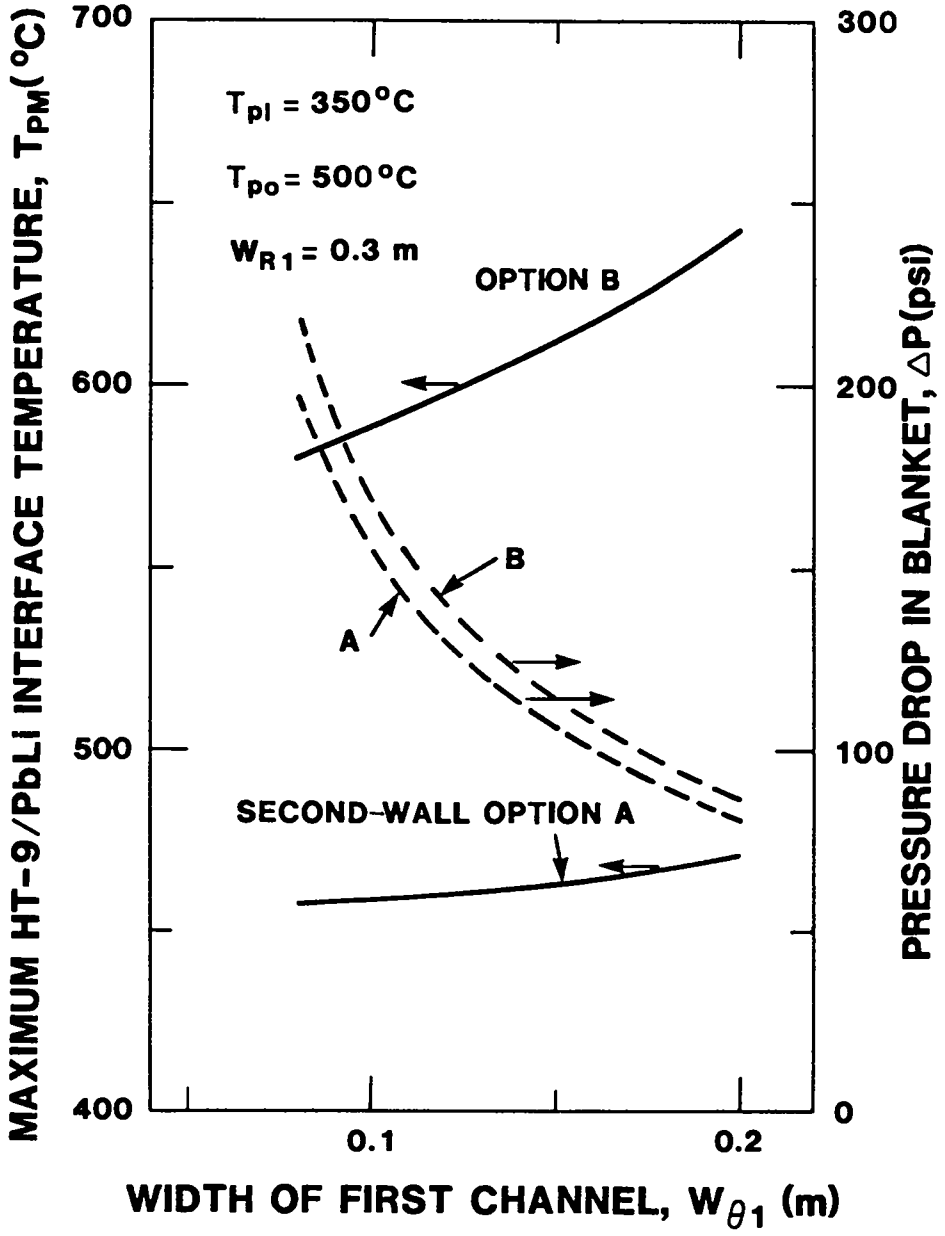

Fig. 2-15. Dependence of maximum blanket structural temperature and PbLi coolant pressure on the thickness of the inner poloidal channel for first-wall/second-wall Options A and B (Fig. 2-12).

high; this temperature can be reduced to acceptable levels if the exit bulk PbLi temperature is lowered with a corresponding decrease in plant efficiency. Results were also calculated for Option C, which give interface temperatures above acceptable levels for all practical combinations of PbLi temperatures and channel thicknesses for the CRFPR(20) design.

The final selection of blanket thermal-hydraulic parameters requires an integrated design of the complete FPC that includes self-consistent studies of tradeoffs between thermal efficiency, exit bulk PbLi temperature, blanket pressure, PbLi pump power, and energy split between water and PbLi coolant streams. That design optimization is discussed in Sec. 3. and represents an update of Sec. III.L. in Ref. 10, as modified by a) the two-dimensional neutronic results with plasma and circuit simulations summarized in Sec. 2.1., and b) the more-complete thermal-hydraulic models described in the present section. Generally, Option A or B (Fig. 2-12) is preferred from a viewpoint of efficiency, although the tradeoffs necessary to achieve a water-free Option D are also explored.

3. FUSION-POWER-CORE INTEGRATION

This section describes the integration of the FPC subsystems using the models and results described in Sec. 2. This integration is performed at three levels: a) power-plant energy balance (Sec. 3.1.), b) thermal-hydraulic design (Sec. 3.2.), and c) mechanical design (Sec. 3.3.). The magnetics design reported in Ref. 10 remains essentially unaltered except for a small radial shift of coils required to accommodate the somewhat thicker blanket suggested by the two-dimensional neutronics calculations (Sec. 2.1.). Accommodation of these changes by the magnet set has preserved the OHC set, leading to a slight increase in plasma aspect ratio. The revised FPC design point is summarized in Sec. 3.4, and derated (lower neutron wall loading) FPC design options and tradeoffs are examined in Sec. 3.5. The material presented in these subsections focuses on the thermal-hydraulic aspect and forms the basis for developing a plant layout to an extent required to assess the single-piece maintenance approach in Sec. 4.

3.1. Power-Plant Energy Balance

The power distribution throughout the FPC is obtained by coupling the neutronics results (Sec. 2.1.) with plasma and circuit simulations[10] and with preliminary designs of key components. The global power-plant energy balance depicted in Fig. 3-1 results. These results are summarized and compared to Ref. 10 values in Table 3-I. The power balance used to complete the FPC integration is based on

- Water-cooled pumped limiter
- Water-cooled first and second walls (Option A or B, Fig. 2-12)
- PbLi-cooled poloidal-flow blanket (Option B, Fig. 2-11)
- Water-cooled structural shield
- Ohmic and nuclear heating in the poloidal-field and toroidal-field coils not used by the thermal-conversion cycle.

The more detailed two-dimensional TRIDENT-CTR neutronics results give a finer breakdown of nuclear heating in various FPC components than was available for the Ref. 10 design. Although the blanket-thickness increase of ~ 0.1 m also increases the coil current centers correspondingly, the Ref. 10 magnetics and global coil parameters were retained. These changes are relatively minor, and

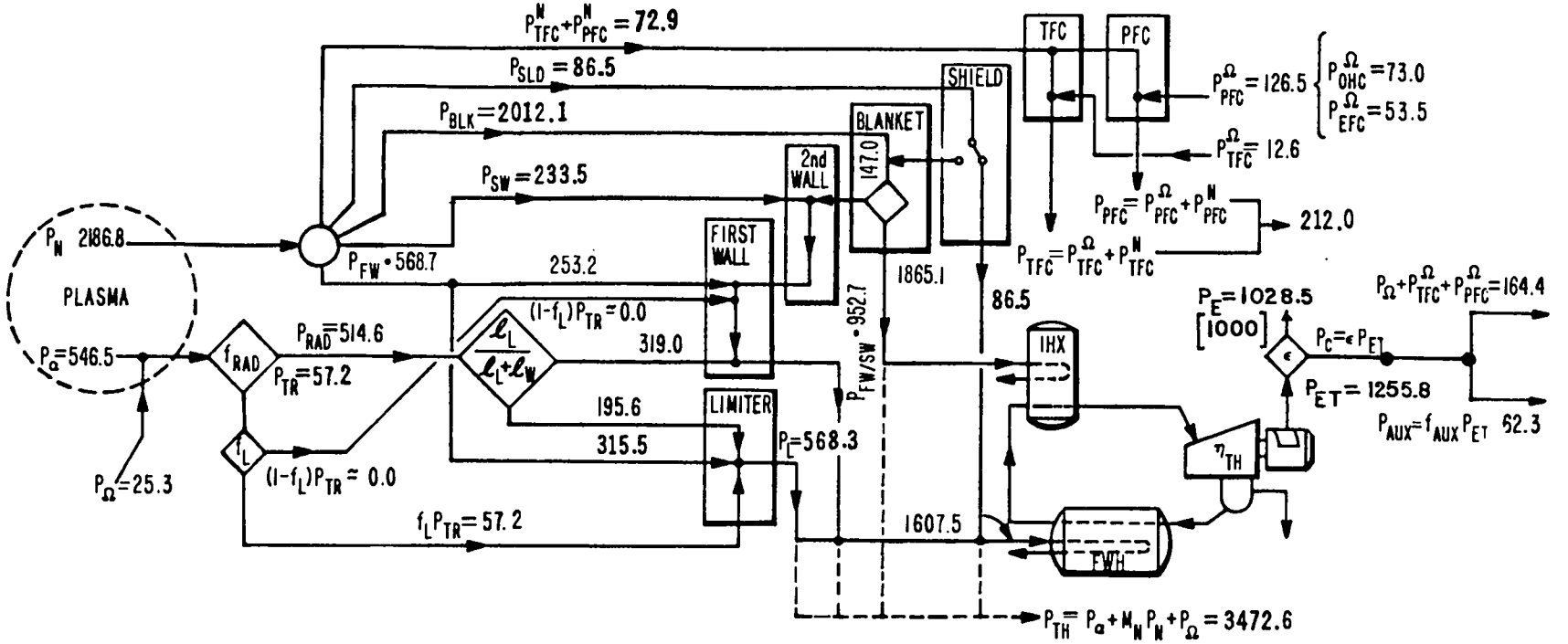

GLOBAL POWER-PLANT
BALANCE FOR CRFPR

$\eta_{TH} = 0.362$ ($\eta_{GEN} = 0.98$)

$\epsilon = 0.181$ [0.204]

$\eta_p = 0.296$ [0.288]

Fig. 3-1. Global power-plant energy balance. Refer to Table 3-I for definitions, notation, and more detailed breakdown. Values in brackets reflect a design point adjustment through the auxiliary power requirement (f_{AUX} increased from 0.05 to 0.07) to retrieve the P_E = 1000 MWe(net) design.

identical coil losses can be maintained between the Ref. 10 case and the minor modification given here by simply shifting conductors while maintaining similar cross-sections and masses of the total coil set.

Under the conditions listed in Table 3-I and Fig. 3-1, 1607.5 MW or 46.3% of the total recoverable thermal power is delivered through the pressurized-water coolant loop. The unrecoverable energy deposited in the coils is 212.0 MW, 66% of which (139.1 MW) results from ohmic dissipation. Hence, 11% of the gross electric power must be recirculated to supply resistive losses in the TFC and PFC sets, and 2.2% is recirculated directly to the plasma, which when combined with an added 7% recirculated to coolant pumps for auxiliary plant needs amounts to a total recirculating power fraction of $\varepsilon = 0.204$. The FPC thermal-hydraulic design and optimization described in the following section give an overall thermal-conversion efficiency of $\eta_{TH} = 0.369$ for this dual-media thermal cycle, which when combined with ε and a generator efficiency of $\eta_{GEN} = 0.98$ gives an overall plant efficiency of $\eta_p = \eta_{GEN}\ \eta'_{TH}(1 - \varepsilon) = P_E/P_{TH} = 0.288$.

3.2. Thermal-Hydraulic Design

The goal of the FPC design is to maximize the overall plant efficiency subject to the design constraints listed for the individual components. Energy is supplied to the CRFPR energy-conversion cycle by two distinct fluid streams at different temperatures. A detailed design of the dual-media steam cycle is not within the scope of this study. The approach taken, therefore, calculates the maximum (ideal) efficiency attainable from such a cycle, as depicted in Fig. 3-2. The expression for this ideal cycle efficiency is[10]

$$\eta_I = 1 - T_E[f_w \ell n(T_{wo}/T_{wi})/(T_{wo} - T_{wi}) + (1 - f_w)\ell n(T_{po}/T_{pi})/(T_{po} - T_{pi})], \quad (1)$$

where T_E is the temperature of the environment to which heat is rejected, f_w is the fraction of total thermal power that is supplied by the pressurized-water coolant, and T designates a bulk fluid temperature. The subscripts are w for water, p for PbLi, and i and o for inlet and outlet, respectively.

A comparison of this equation with predicted or measured efficiencies of other dual- and single-media thermal cycles indicates that approximately 75% of the ideal efficiency can be achieved in a real system. Although uncertainty

TABLE 3-I

CRFPR BASELINE POWER-BALANCE SUMMARY

Parameter	(Ref. 10)	Update[a]
Major toroidal radius, R_T(m)	3.79	3.79
First-wall radius, r_w(m)	0.75	0.75
First-wall area, $A_{FW}(m^2) = (2\pi)2r_wR_T$	112.1	112.1
Major circumference, $2\pi R_T$(m)	23.80	23.80
Fusion neutron first-wall loading, $I_w(MW/m^2)$	19.5	19.5
Fusion neutron power, P_N(MW)	2186.0	2186.8
Alpha-particle power, P_α(MW)	546.5	546.5
Plasma ohmic power,[b] P_Ω(MW)	25.3	25.3
First-wall nuclear heating, $P^N_{FW}(MW) = P_{FWW} + P_{FWM}$	317.0	253.2
• first wall, P_{FWW}(MW)		73.1
• first wall manifold, P_{FWM}(MW)		180.1
Limiter nuclear heating, $P^N_L(MW) = P_{LL} + P_{LM}$	178.1	315.5
• limiter, P_{LL}(MW)		110.6
• limiter manifold, P_{LM}(MW)		204.9
First-wall and limiter nuclear heating, $P^N_{FW} + P^N_L$(MW)	495.1[c]	568.7
Second-wall nuclear heating, $P_{SW}(MW) = P_{SW} + P_{SWM}$	97.1	233.5
• second wall, P_{SWW}(MW)		53.4
• second wall manifold, P_{SWM}(MW)		180.1
Blanket nuclear heating, $P_{BLK}(MW) = P_{BLB} + P_{BLS}$	2057.6	2012.1
• blanket, P_{BLB}(MW)		1959.5
• blanket structure, P_{BLS}(MW)		52.6
Shield nuclear heating, P_{SLD}(MW)	143.3[c]	86.5
Recoverable nuclear heating, $M_NP_N(MW) =$ $P^N_{FW} + P^N_L + P_{SW} + P_{BLK} + P_{SLD}$	2793.1	2900.8
Energy multiplication, M_N	1.28	1.33
Total recoverable thermal power, $P_{TH}(MW) = M_NP_N + P_\alpha + P_\Omega$	3364.9	3472.6
Toroidal-field coil heating, P_{TFC}(MW)	42.6	48.3
• nuclear heating, P^N_{TFC}(MW)	30.0[c]	35.7
• ohmic heating,[d] P^Ω_{TFC}(MW)	12.6	12.6
Poloidal-field coil heating, P_{PFC}(MW)	141.0	163.7
• nuclear heating, P^N_{PFC}(MW)	14.5[c]	37.2
• ohmic heating, [d] P^Ω_{PFC}(MW)	126.5	126.5

TABLE 3-I (cont)

Fraction transport loss to limiter, f_L	~1.0	~1.0
Fraction plasma power radiated, f_{RAD}	0.9	0.9
Fractional limiter coverage, $\ell_L/(\ell_L + \ell_w)$	0.38	0.38
Limiter length (N = 24), ℓ_L(m)	0.38	0.38
Radiated power, $P_{RAD}(MW) = f_{RAD}(P_\alpha + P_\Omega)$	514.6	514.6
Transport power, $P_{TR}(MW) = (1 - f_{RAD})(P_\alpha + P_\Omega)$	57.1	57.1
Power to limiter, $P_L(MW) = f_L P_{TR} + P_L^N + P_{RAD}\ell_L/(\ell_L + \ell_w)$	440.8	568.3
Total power to first wall, $P_{FW}(MW) = (1 - f_L)P_{TR} + P_{FW}^N + P_{RAD}\,\ell_w/(\ell_L + \ell_w)$	626.0	572.2
Power back-leakage from blanket to SW,[e] $P_{BL}(MW)$	96.0	147.0
Total power to FW/SW system, $P_{FW/SW}(MW) = P_{FW} + P_{SW} + P_{BL}$	819.1	952.7
Total power to water-cooled first-wall systems,[f] $P_{THw}(MW) = P_{FW/SW} + P_L$	1259.9	1607.5
Total power to PbLi, $P_{THp} = P_{BLK} - P_{BL}$	1961.6	1865.1
Total power to magnet coolant, $P_{TFC}(MW) + P_{PFC}(MW)$	183.6	212.0
Estimated thermal-conversion efficiency, η'_{TH}	0.365[g]	0.369[g]
Gross electric power, $P_{ET}(MW) = \eta_{GEN}\eta'_{TH}P_{TH}$	1226.7[g]	1255.8[g]
Auxiliary power needs, $P_{AUX}(MW) = f_{AUX}P_{ET}$	62.6	62.8[91.30][g]
Ohmic power to FPC, $P_c^\Omega(MW) = P_{TFC}^\Omega + P_{PFC}^\Omega + P_\Omega$	164.4	164.4
Recirculating power, $P_c(MW) = P_{AUX} + P_c^\Omega$	227.0[g]	227.2[255.7][g]
Recirculating power fraction, $\varepsilon = P_c/P_{ET}$	0.185[g]	0.181[0.204][g]
Plant efficiency, $\eta_p = \eta_{GEN}\eta'_{TH}(1 - \varepsilon)$	0.297[g]	0.296[0.288][g]
Net electrical power, $P_E(MWe) = P_{ET}(1 - \varepsilon)$	1000.[g]	1028.[1000.][g]

(a) The modified CRFPR(20) design presented here has a thinner first wall (5 mm vs 20 mm), higher lithium enrichment (90% vs 60%), and thicker blanket (610 mm vs 495 mm) relative to the Ref. 10 design.
(b) Based on peaked temperature profile, $T(r) \propto J_0(r)$.
(c) Refer to Table III.B-V of Ref. 10.
(d) For the Θ and F values used in the systems code ($B_{R\phi} = -0.68$ T), a continuous TFC would generate 17.6 MW ohmic dissipation. The more-detailed plasma simulations (modified BFM, $\Theta = 1.55$, $F = -0.12$, $\beta_\theta = 0.23$, $B_{R\phi} = 0.4$ T) and the use of discretized coils give the value of $P_{TFC}^\Omega = 53.5$ MW and $P_{OHC}^\Omega = 73.0$, as described in Sec. III.F.2.d. of Ref. 10.
(e) Estimated in Sec. III.E. of Ref. 10 as the penalty incurred when a structural temperature limit of ~ 500°C set by PbLi corrosion limit and amounts to 4.66% of P_{BLK}.
(f) Amounts to 46.2% of P_{TH}.
(g) Values based on thermal-hydraulics optimization and integration study described in Sec. III.L.2. of Ref. 10, and this report. Values in brackets [] reflect an increase in f_{AUX} from 0.05 to 0.07 to force net electric power to equal 1000-MWe(net) as well as consistency with the costing algorithm (Sec. 6.).

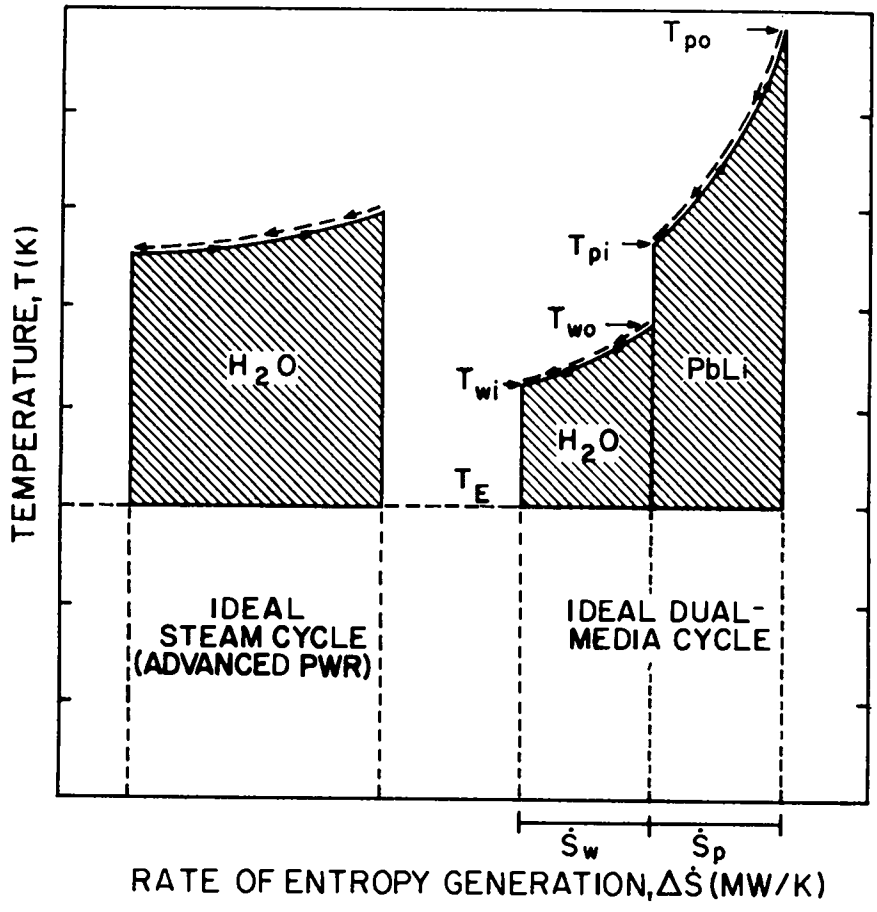

Fig. 3-2. Temperature-entropy diagrams for ideal single-media and dual-media thermal conversion cycles, where in both cases heat is rejected to a common temperature, T_E.

exists in the absolute accuracy of this calculated efficiency, Eq. (1) should accurately reflect the change in cycle efficiency that would be caused by changing fluid temperatures or the fraction of total energy carried by each fluid. For the purposes of this study, therefore, the actual thermodynamic cycle efficiency is approximated as $\eta'_{TH} = 0.75\eta_I$.

The gross electrical energy output is $P_{ET} = \eta'_{TH}\eta_{GEN}P_{TH} = \eta_{TH}P_{TH}$, where P_{TH} is the recoverable thermal power, η_{GEN} is the generator efficiency and $\eta_{TH} \equiv \eta'_{TH}\eta_{GEN}$. The net power output is $P_E = P_{ET} - P_c$, where the recirculating power, P_c, includes magnet and plasma power requirement, the pumping power, and other auxiliary power needs. As indicated in Table 3-I and Fig. 3-1, the magnet and plasma power needs represent a major part of the recirculating power (~ 13%

of P_{ET}), with other needs estimated to require an additional 7% of P_{ET}. The goal of the FPC thermal-hydraulic design integration is to achieve fluid conditions that optimize the thermal efficiency [Eq. (1)] and minimize the pumping power, while holding the following design constraints:

- Primary and secondary stress factor of safety, $\sigma_Y/\sigma_D \geq 5$.
- PbLi blanket pressure, $\leq$ 100 psi.
- Pressurized-water coolant velocity, $V \leq 10$ m/s.
- Maximum copper-alloy high-heat-flux temperature, $\leq 400^{\circ}C$.
- Maximum HT-9 ferritic alloy temperature in contact with PbLi, $\leq 500^{\circ}C$.
- Critical-heat-flux limits for pressurized-water coolant, $\Delta T_{SAT} \geq 10$ K.
- Thermal-conversion efficiency, $\eta_{TH} = 0.75\ \eta_{GEN}\eta_I$ ($\eta_{GEN} = 0.95$, $f_w = 0.46$).
- No structural sputtering margin (coatings, tiles, cold/dense radiating plasma edge required).
- PbLi blanket MHD pressure modeled in one dimension with no sandwiched insulators.

3.2.1. Limiter Analysis

Equation (1) shows that the cycle efficiency increases with increasing fluid temperatures; both the inlet and outlet water temperatures should be as high as possible. Calculations were performed using the limiter model described in Sec. 2.2.2. to determine the velocity and maximum local coolant-water temperature in the limiter channels for various values of inlet and exit bulk temperatures. For all cases considered, the limiter (568.3 MW) and shield (86.5 MW) coolant circuits were operated in series to simplify the manifolding/headering systems. The highest acceptable bulk temperatures correspond to the case where both the velocity and maximum local water temperatures in the limiter channel are equal to the specified limits of $V = 10$ m/s and $T_{SAT} = 10$ K, respectively. This condition corresponds to a bulk coolant-water temperature at the limiter exit of $256^{\circ}C$ and a temperature leaving the shield of $288^{\circ}C$. Results for the limiter/shield coolant design are summarized in Table 3-II.

TABLE 3-II

PUMPED-LIMITER THERMAL-MECHANICAL DESIGN PARAMETERS[a]

PARAMETER	VALUE
Number of limiters, N	24.
Material	MZC Copper
Overall dimensions	
• toroidal extent, ℓ_L(m)	0.38
• maximum radial thickness, δ'(mm)	11.5
• stand-off distance from first wall, δ(mm)	40.
Coolant configuration (toroidal flow)	
• channel height (mm)	0.8
• channel width (mm)	4.0
• wall thickness to outside surface (mm)	0.8
• wall thickness between channels (mm)	1.00
• number of channels per limiter	942.
Limiter thermal rating	
• total cooling rate for all limiters, P_L(MW)	363.4
• manifolds, total thermal power (MW)	204.9
• shield thermal power (MW)	86.5[a]
• total power to limiter/shield circuit (MW)	654.8
• design heat flux, q_D(MW/m^2)	6.0
• maximum limiter temperature (^{o}C)	378.
Coolant properties (pressurized water)	
• inlet temperature, T_{wi}(^{o}C)	170.
• outlet temperature, T_{wo}(^{o}C)	256.
• nominal coolant velocity, V(m/s)	10.0
• total mass flow rate, $\dot{m}_w$(kg/s)	1173.
• pressure drop in channel (MPa)	0.10
Manifold/header properties	
• inlet manifold, ID/OD(mm)	83.7/84.7
• outlet manifold, ID/OD(mm)	122.7/163.8
• inlet header (single radial run), ID/OD(mm)	83.7/112.0
• outlet header (single radial run), ID/OD(mm)	89.5/119.5
• total limiter circuit pressure drop (MPa)	0.30
• limiter pumping power[b] (MW)	0.18
• total limiter circuit pumping power[b] (MW)	0.52

(a) The limiter and shield coolant circuits are operated in series, simplifying the manifolding and headering scheme relative to the Ref. 10 design.
(b) Pump efficiency is $\eta_{pump} = 0.75$.

3.2.2. First-Wall/Second-Wall Analysis

The design of the first-wall/second-wall coolant circuit is coupled to the blanket design because of heat transfer from the flowing PbLi in the inside blanket coolant channel to the pressurized-water coolant. The blanket model, therefore, was evaluated to determine the rate of heat transfer from the blanket to the second wall. The result from that analysis is used as input to the

first-wall/second-wall thermal-hydraulic analysis. Design parameters include the inlet and exit bulk coolant temperatures, first-wall coolant-tube inside diameter and wall thickness, and second-wall configuration. Generally, first-wall/second-wall interface Option A or B (Fig. 2-12) was used, although possible conditions for a water-free first-wall system are examined in Sec. 3.5. From the viewpoint of the steam-power-cycle design, it is convenient to combine the water flows leaving the limiter/shield and first-wall/second-wall circuits to provide a single flow path to a steam generator, while allowing for some use directly in feedwater heating. The coolant water also returns to the FPC as a single stream. The bulk inlet water temperature for both the first-wall/second-wall and limiter/shield circuits, therefore, was selected. The limiting water temperature is taken as the inside wall temperature subcooled by $\Delta T_{SAT} \simeq 10$ K at a pressure of 15.6 MPa (2,200 psi).

A parametric study was performed varying the first-wall tube diameter and the outlet bulk coolant temperature for the first-wall/second-wall circuit and focusing on Option A (Fig. 2-12). The tube-wall thickness was computed from Eq. (2) in Sec. 2. Results are shown in Fig. 3-3. The solid lines represent the maximum local water temperature, and the dashed curves represent the fluid bulk velocity. For low values of d_i (< 2 mm) the flow velocity is sufficient for the region of maximum temperature to move away from the first wall and into the exit coolant manifold/header. The vertical scales on Fig. 3-3 are aligned so that the limiting fluid velocity (10 m/s) and the limiting local water temperature (330°C, boiling at 15.6 MPa) are at the same position. Figure 3-3 can be used to define the tube-diameter design window for any given outlet bulk coolant temperature. This design window is defined as the range of d_i values between the points where the velocity and temperature curves cross the limit lines shown on Fig. 3-3. The maximum acceptable outlet bulk temperature is slightly above $T_{wo} = 320°C$. The tube diameter could be as small as 3.25 mm. The number of tubes per torus sector (N = 24), however, would be more than 1,300. As a practical tradeoff, a nominal value of $T_{wo} = 300°C$ and a tube diameter of $d_i = 4.0$ mm are selected for the canonical design. The cost in overall thermal efficiency amounts to ~ 0.2% in selecting the 300°C design point and higher value of d_i. The values of all first-wall/second-wall coolant-circuit parameters resulting from this choice are given in Table 3-III.

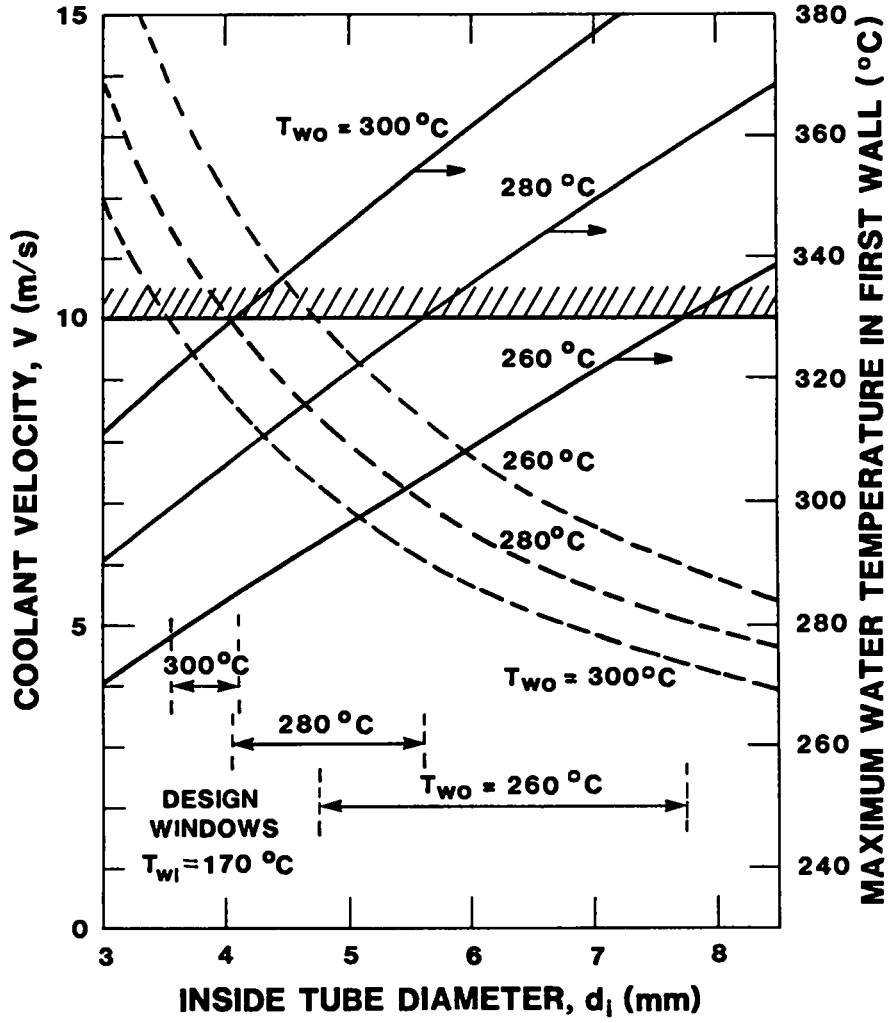

Fig. 3-3. Parametric tradeoff between first-wall/second-wall pressurized-water bulk flow velocity, V, and maximum (local) water temperature in first-wall/second-wall system [T_{BP} = 330°C at P_w = 15.6 MPa(2200 psi)] as a function of first-wall/second-wall coolant-tube inner diameter, d_i, and coolant outlet temperature, T_{wo}. Design windows where V < 10 m/s and $T_{si} < T_{BP}$ are shown as a function of T_{wo}.

3.2.3. Blanket Analysis

The blanket design is performed using the model described in Sec. 2.2.3. This model must be evaluated in conjunction with the first-wall/second-wall model because the boundary condition for the inner blanket coolant channel requires knowledge of the water temperature and film coefficient in the second-wall coolant tubes. The blanket and first-wall/second-wall design models are evaluated iteratively. First, the blanket analysis is performed using estimated second-wall coolant temperatures and film coefficients, and the resulting rate of heat convection to the second-wall coolant is computed. The first-

TABLE 3-III

FIRST-WALL/SECOND-WALL THERMAL-MECHANICAL DESIGN PARAMETERS

PARAMETER	VALUE
Number of segments, N	24.
Material	MZC Copper/HT-9
Overall dimensions of segments	
• toroidal extent, ℓ_w(m) = $2\pi R_T/N$	1.0
• minor radius, r_w(m)	0.75
• major toroidal radius, R_T(m)	3.79
Coolant configuration (toroidal flow)	
• "D-tube" ID/OD(mm)	4.0/6.14
• number of D-tubes per half-segment (inlet or outlet)	767.
• tube-wall thickness, δ(mm)	1.07
• FW/SW flow configuration	single-pass, series
FW/SW thermal rating	
• FW heat flux, I_{Qw}(MW/m^2)	4.55
• FW heat-flux power (MW)	319.1
• FW volumetric nuclear heating (MW/m^3)	260.4
• FW nuclear-heating power (MW)	73.1
• FW total power, P_{FW}(MW)	392.1
• SW nuclear-heating power, P_{SW}(MW)	53.4
• SW back leakage from blanket, P_{BL}(MW)	147.0
• manifolds, total power (MW)	360.2
• total power to FW/SW (MW)	952.7
Coolant properties (pressurized water)	
• coolant inlet temperature, T_{wi}(^{o}C)	197. (to first wall)
• coolant outlet temperature, T_{wo}(^{o}C)	278. (from second wall)
• coolant velocity, V(m/s)	9.0
• coolant mass flow rate, $\dot{m}_w$(kg/s)	1520.7
• peak structural temperature (^{o}C)	328.
Manifold/header Properties	
• inlet manifold, ID/OD(mm)	47.8/56.2
• outlet manifold, ID/OD(mm)	52.5/61.7
• inlet header, ID/OD(mm)	67.6/79.5
• outlet header, ID/OD(mm)	74.2/87.3
• total FW/SW circuit pressure drop (MPa)	0.38
• FW/SW pumping power (MW)	0.174
• total FW/SW circuit pumping power (MW)	0.80

wall/second-wall model is then evaluated using the convection rate predicted from the blanket model, and improved estimates of the coolant temperature and film coefficient are obtained. This iterative process is continued until convergence is obtained for the blanket and first-wall/second-wall thermal results. The design parameters for the blanket include the inlet and exit PbLi temperatures, T_{pi} and T_{po}, the channel geometry, $w_{\theta 1}$, the second-wall configuration (Option A, Fig. 2-12), and the blanket inlet channel configuration (Fig. 2-11).

The PbLi temperatures should be as high as possible, subject to thermal, structural, and corrosion constraints. The exit PbLi bulk temperature is limited to 500°C because of the temperature constraint at the PbLi/HT-9 interface.[28] Calculations were performed to determine the effect of the inlet bulk temperature on plant thermal-cycle efficiency and net electrical power output.

Results of those calculations are shown in Fig. 3-4, where $\eta_{TH} = 0.75\eta_{GEN}\eta_I$ [Eq. (1)]; only the fractional power recirculated to the pumps, ε_{pump}, is used in this tradeoff study in order to enhance the sensitivity of results to changes in coolant conditions. Although the thermal efficiency of the steam power cycle continues to increase with increasing values of T_{pi}, the net efficiency, $\eta_{TH}(1 - \varepsilon_{pump})$, reaches a maximum at $T_{pi} \simeq 400°C$ because of the rapidly increasing pumping power requirements, resulting in the maximum shown in Fig. 3-4. Generally, the blanket-coolant pressure, rather than the pumping power, limits the designs considered. A precise estimate of a blanket-coolant pressure limit would require a detailed structural analysis of the entire blanket, including the design of wall/channel stiffeners. Such an analysis is beyond the scope of this design study. The parametric results depicted in Fig. 3-4 show that the increase in net electrical power is relatively small as inlet bulk PbLi temperature is increased from 350 to 400°C while the pressure difference in the blanket increases rapidly. An inlet PbLi bulk temperature of 350°C, therefore, was selected, which for an inner coolant channel of thickness $w_{\theta 1} \simeq 0.08$ m would pressurize the blanket to 60-70 psi.

The Option A second-wall configuration (Fig. 2-12) was chosen for the canonical design. The preferred radial channel configuration continuously changes the channel thickness (Option A, Fig. 2-11), since this configuration produces a smoother flow pattern. The Option B inlet channel configuration depicted on Fig. 2-11, however, gives lower pumping power for the same manifold size.

A series of analyses was made to determine the effects of channel geometry on pumping power, pressure drop, and maximum interface temperature. Design variables include the thicknesses of the poloidal section of all channels, $w_{\theta i}$, and the thickness of the radial segment of the inside channel, w_{R1}. The thickness of the first poloidal channel is a key parameter, because nuclear heating is most severe in the first channel and the value has a significant effect on the PbLi/HT-9 interface temperature. The radial channel thickness,

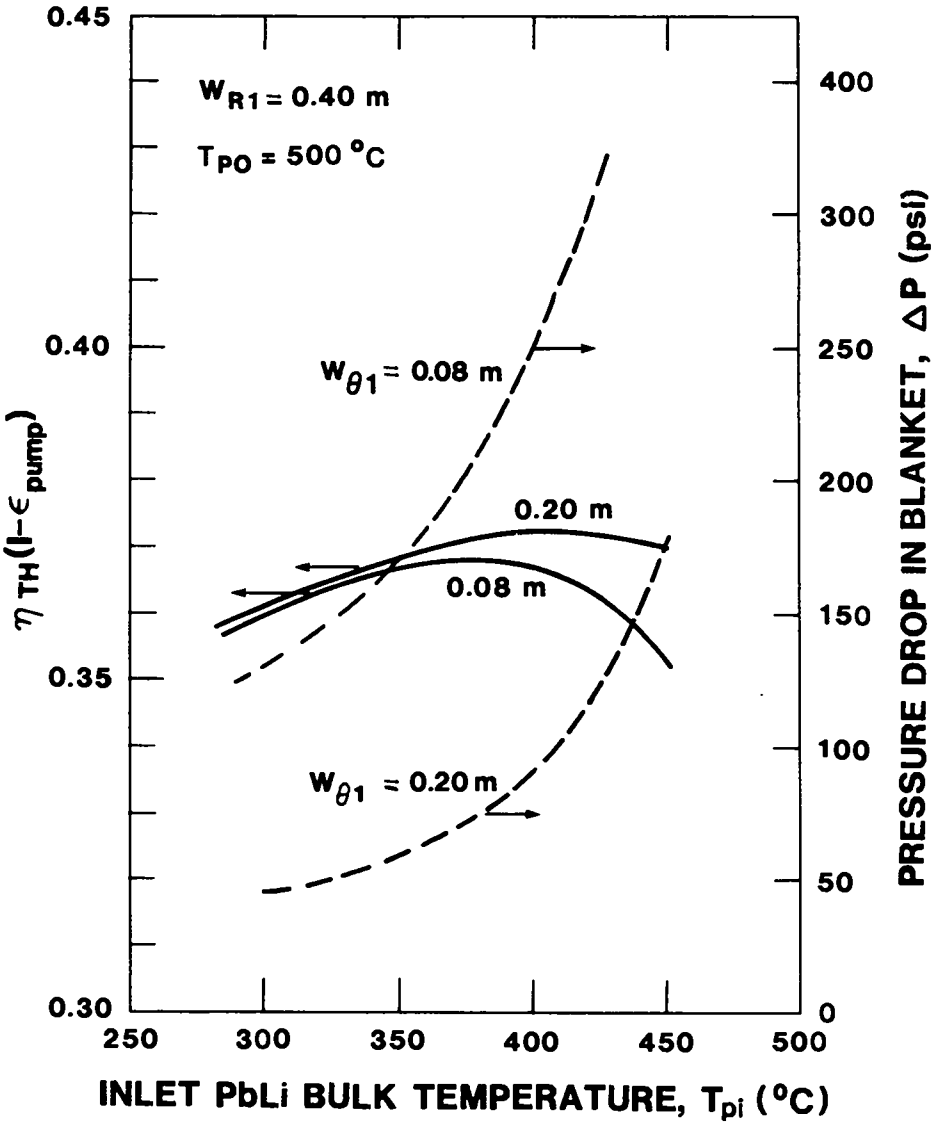

Fig. 3-4. Results of parametric study showing effects of PbLi coolant temperature and inner poloidal coolant-channel thickness on effective plant efficiency and blanket pressure drop.

w_{R1}, primarily controls the pressure drop and pumping power. The dimensions of the remaining channels are of secondary importance to the overall FPC performance.

A series of sensitivity studies was made for a range of w_{R1} and $w_{\theta 1}$ values. Interface temperatures were less than 500°C for $w_{\theta 1} < 0.20$ m. The resulting pressure drops are shown in Fig. 3-5. The dimension w_{R1} is limited to 0.4 m. because of space restrictions on the manifolds as they leave the FPC between the EFCs at the outboard equatorial plane.

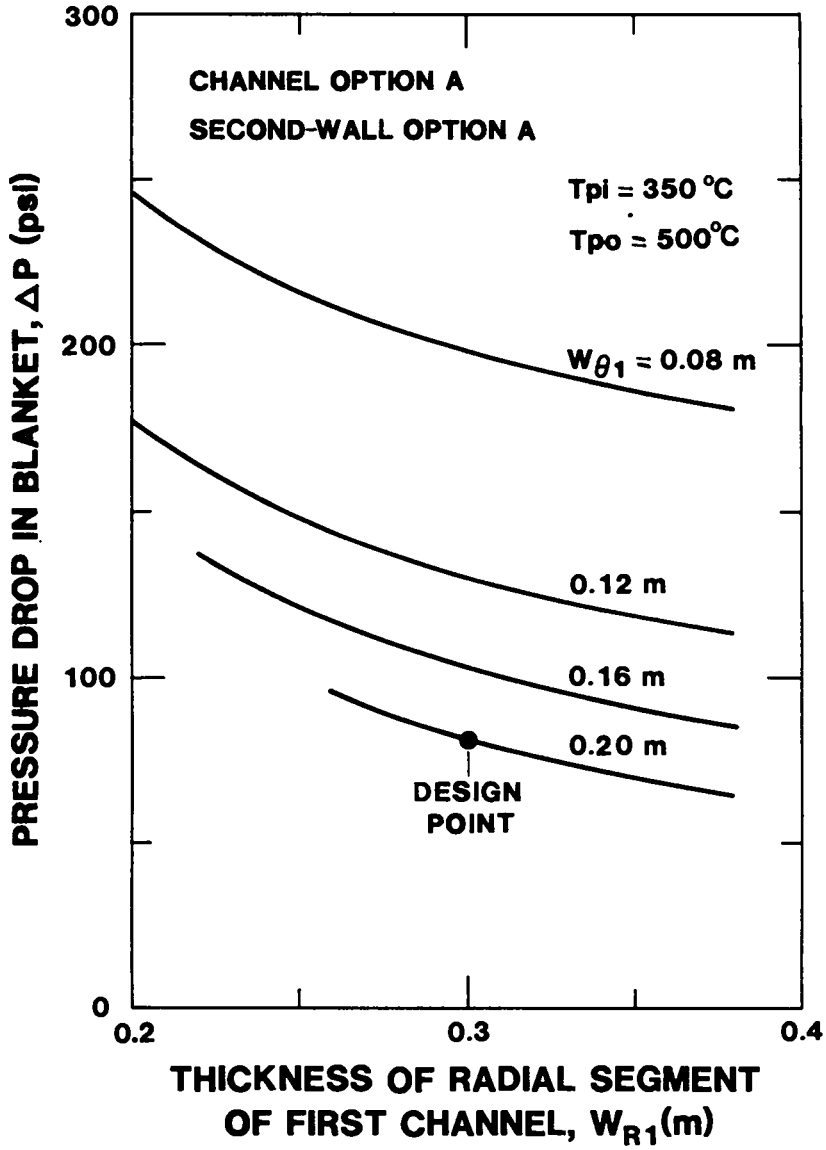

Fig. 3-5. Blanket PbLi pressure drop shown as a function of poloidal and radial channel widths.

The results shown in Fig. 3-4 indicate that $\eta_{TH}(1 - \varepsilon_{pump})$ depends primarily on the T_{po} and T_{pi} and not strongly on channel geometry for the case where T_{po} = 500°C and T_{pi} = 350°C. The selection of geometric parameters is, therefore, governed primarily by the pressure drop in the blanket. A value of $w_{\theta 1}$ = 0.2 m is chosen to minimize pressure levels in the blanket, and w_{R1} = 0.3 m is selected as a compromise between minimizing pressure and keeping the PbLi coolant manifolds as small as possible. A summary of all blanket design parameters is given in Table 3-IV.

TABLE 3-IV

BLANKET THERMAL-MECHANICAL DESIGN PARAMETERS

PARAMETER	VALUE
Number of segments	48.
Material	HT-9/PbLi
Overall dimensions	
• toroidal extent, $\ell_w/2$(m)	0.48
• radial extent, Δb(m)	0.60
• inside radius (m)	0.775
Coolant configuration (poloidal flow, Fig. 2-11)	
• channel thicknesses with increasing radius, $w_{\theta i}$(m)	0.200/0.200/0.200
• channel thicknesses entering manifold, w_{Ri}(m)	0.300/0.062/0.022
• channel wall thickness (mm)	5.0
Blanket thermal rating	
• total cooling rate, $P_{BLK} - P_{BL}$(MW)	1865.1[a]
• peak power density (MW/m^3)	350.
• average power density (MW/m^3)	21.5
• maximum structural temperature (^oC)	500.
Coolant properties	
• inlet temperature, T_{Pi}(^oC)	350.
• outlet temperature, T_{Po}(^oC)	500.
• nominal coolant velocity in channels, V_i(m/s)	1.25/0.35/0.14
• nominal coolant velocity in manifold (m/s)	1.78
• total mass flow rate, $\dot{m}_p$(kg/s)	74,765.
• pressure drop in blanket/manifold (MPa)	0.55
• pumping power (MW)[b]	5.8
Manifold/header properties[c]	
• radial extent beyond blanket (m)	0.47
• height(m)	0.384

(a) Although P_{BLK} = 2012.1 MW is deposited in the blanket, P_{BL} = 147.0 MW leaks back to the first-wall/second-wall water coolant.
(b) Pump efficiency is η_{pump} = 0.75.
(c) Nominal values as PbLi manifolds pass through the PFC set; thereafter, the PbLi main manifolds are sized to maintain a nominal 2-m/s flow speed.

3.2.4. Shield Analysis

The water-cooled 0.1-m-thick 316-stainless-steel shield would serve as a primary structural support for each toroidal sector. Coolant water from the limiter would be used to remove the 86.5 MW from the shield, which operates at a low power density (3.9 MW/m^3) and has moderate cooling requirements. Figure 3-6 illustrates this coolant geometry, and Table 3-V summarizes key thermal-mechanical design parameters. Pressurized water from the limiter enters the shield in the toroidal direction through 10-mm-diameter tubes that are spaced

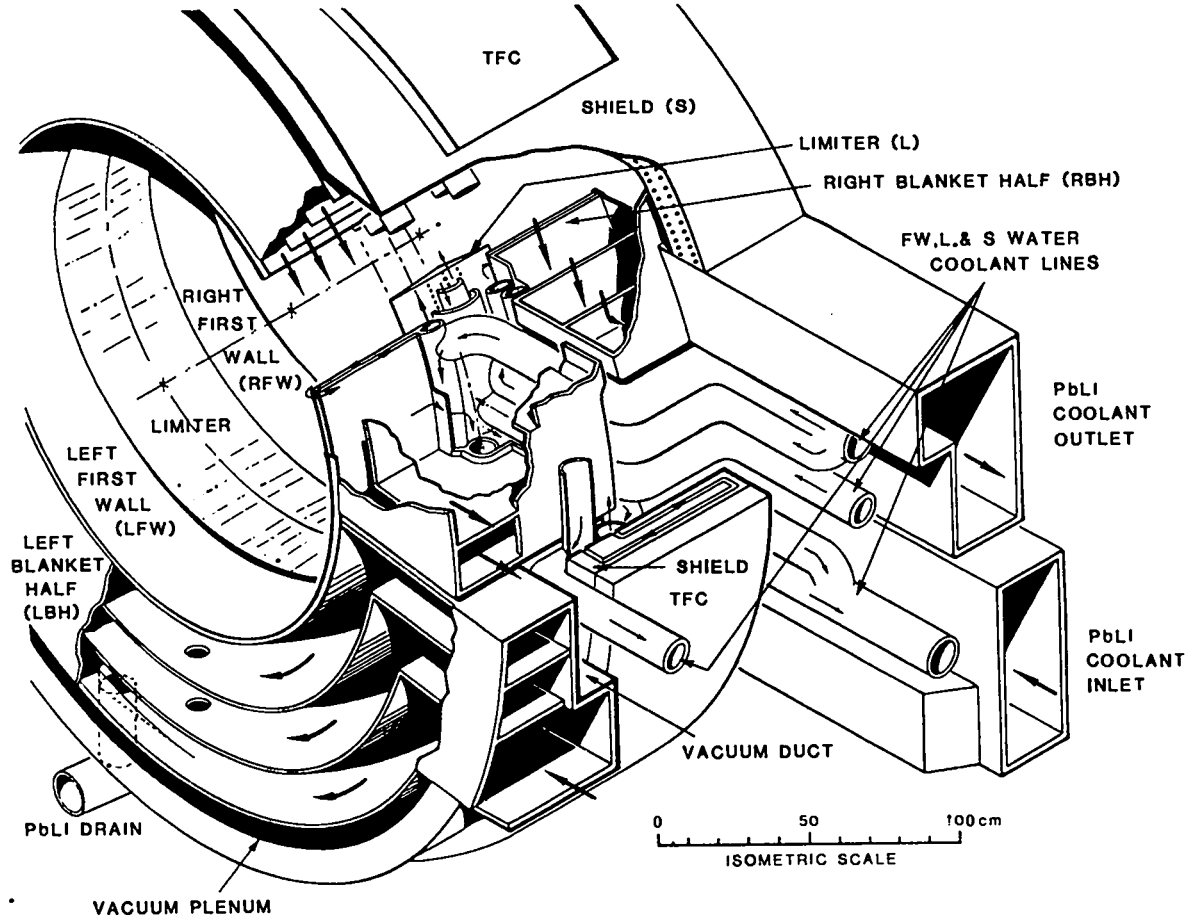

Fig. 3-6. Detailed view of shield cooling geometry and associated manifolding.

25 mm from each other as well as from the edge of the shield mass. The heat-removal requirements on this subsystem are not demanding.

3.2.5. Design Summary

Flow rates, temperatures, and cooling rates are shown in Fig. 3-7 for the design that has emerged from this study. Table 3-I summarizes the key power-handling characteristics of each FPC component, key thermal-hydraulic parameters are given in Table 3-VI, and important properties for the overall CRFPR(20) design are given in Table 3-VII. The sensitivity of this suggested thermal-hydraulics design point is best demonstrated by a plot of curves of $T_{po} - T_{pi}$

TABLE 3-V

SHIELD THERMAL-MECHANICAL DESIGN PARAMETERS

PARAMETER	VALUE
Number of segments	24.
Material	PCASS/H_2O
Overall dimensions	
• toroidal extent, $\ell_w/2$(m)	1.0
• radial extent, (m)	0.10
• inside radius (m)	1.42
Coolant configuration	
• coolant channel diameter (mm)	10.
• coolant channel spacing (mm)	25.
• number of channels per segment	371.
Shield thermal rating	
• total cooling rate, P_{SLD}(MW)	86.5
• peak power density (MW/m^3)	4.7
• average power density (MW/m^3)	3.9
• maximum structural temperature (^oC)	379.
Coolant properties[a]	
• inlet temperature, T_{wi}(^oC)	274.
• outlet temperature, T_{wo}(^oC)	288.
• nominal coolant velocity in channels, V(m/s)	1.7
• total mass flow rate, $\dot{m}_p$(kg/s)	1173.
• pressure drop in blanket/manifold (MPa)	0.01
• pumping power (MW)[b]	0.01

(a)Water coolant exiting limiter at 256°C increases in temperature by 18 K while traversing manifolding/headering and enters the shield at 274°C.
(b)Pump efficiency is $\eta_{pump} = 0.75$.

versus T_{po} that are constrained by a number of physical limitations. Figure 3-8 shows the steam-generator (or IHX) "pinch-point" limits for a 10 K minimum temperature difference between T_{po} and the steam-generator outlet; pinch-point curves for two steam-generator pressures are shown on Fig. 3-8. Lines of constant values of $\eta^*_{TH} \equiv \eta_{TH}(1 - \varepsilon_{PUMP})$ are also plotted on Fig. 3-8 using Eq. (1), $\eta_{TH} \simeq 0.75\eta_{GEN}\eta_I$, and $\eta_{GEN} \simeq 0.98$. When combined with PbLi pressure (stress) and corrosion (temperature) limits, the pinch-point and η^*_{TH} constraints define a global design window. No attempt has been made to optimize the steam cycle, and the pinch-point curves for the respective steam-generator pressures should be viewed only as examples rather than actual constraints. A full thermal-cycle optimization would include the steam-generator dimensions and pressure, and it is likely that first-wall/second-wall and blanket thermal-hydraulic conditions and dimensions different than those selected would result.

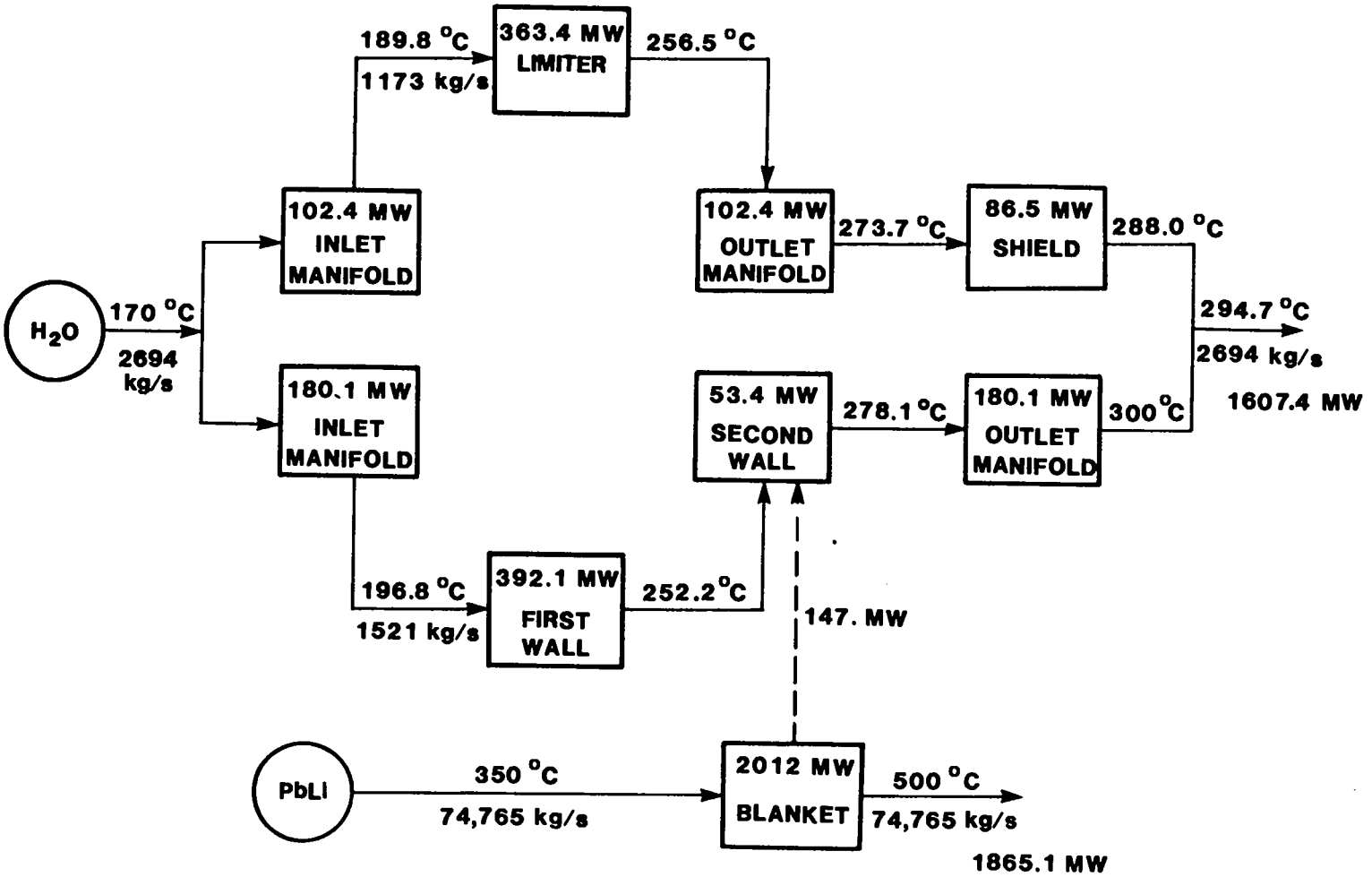

Fig. 3-7. Flow chart showing power ratings, flow rates, and coolant temperatures at various points in the CRFPR(20) power conversion cycle. An optimized steam-cycle design was not performed.

TABLE 3-VI
SUMMARY OF KEY FPC THERMAL-HYDRAULIC PARAMETERS

Subsystem	Limiter	First wall	Blanket	Shield
Material	Copper alloy	Copper alloy	HT-9 Steel	PCASS
Total cooling rate (MW)	363.4[a]	592.5[b]	1865.1	86.5
Design heat flux (MW/m^2)	6.	4.6	~1.3[c]	-
Design power density (MW/m^3)	266.	169.	21.5[d]	3.9
Coolant configuration				
• direction	toroidal	toroidal	poloidal	toroidal
• channel dimensions (mm)	0.8×4.0	4.0 "D-tube"	200./200./200.[e]	10.
• wall thickness (mm)	0.8[f]	1.07[f]	5.0	20.
• channels per unit	942	767	3	371
Peak structural temperature (°C)	378	342	500	379
Coolant properties				
• kind	water	water	PbLi	water
• inlet temperature (°C)	190	197	350	274
• outlet temperature (°C)	256	278[g]	500	288
• bulk velocity (m/s)	10.0	9.0	1.25/0.35/0.14[e]	1.7
• total mass flow rate (kg/s)	1,173.	1,520.	74,765.	1,173.
• pressure drop (MPa)	0.1	0.13	0.55	0.01
• pressure (MPa)	15.6	15.6	0.55	15.6
Total pumping power (MW)	0.52	0.80	5.8	0.01

(a) To this is added 204.9 MW deposited in the manifolds plus 86.5 MW from the shield coupling for a total of 654.8 MW.
(b) To this is added 360.2 MW deposited in the manifolds, but 147.0 MW back leakage from blanket to the second wall as well as 53.4 MW nuclear heating in the second wall is included, for a total of 952.7 MW.
(c) Back-leakage flux to second wall.
(d) 350 MW/m^3 peak in PbLi.
(e) Poloidal Channel Dimensions (velocity) with increasing minor radius.
(f) Does not include sputtering margin, based on factor of safety of 5 relative to yield stress.
(g) Coolant return via HT-9 second wall.

TABLE 3-VII

KEY THERMAL PROPERTIES FOR THE CRFPR CANONICAL DESIGN

PARAMETER	VALUE	
Total recoverable thermal power, P_{TH}(MW)	3472.6	
Pressurized-water coolant		
• power, P_{THw}(MW)	1607.5	
• flow rate, $\dot{m}_w$(kg/s)	2693.7	
• inlet temperature, T_{wi}(^oC)	170.	
• outlet temperature, T_{wo}(^oC)	295.	
• pressure, P_w(MPa/psi)	15.2/2200	
• pumping power (MW)	1.32[a]	
PbLi coolant		
• power, P_{THp}(MW)	1865.1	
• flow rate, $\dot{m}_p$(kg/s)	74,765.	
• inlet temperature, T_{pi}(^oC)	350.	
• outlet temperature, T_{po}(^oC)	500.	
• pressure, P_p(MPa/psi)	0.55/79.8	
• pumping power (MW)	5.8[a]	
Steam-power-cycle efficiency, η'_{TH}	0.369	
Thermal-conversion efficiency, $\eta_{TH} = \eta_{GEN}\eta'_{TH}$	0.362	
Gross electric power, P_{ET}(MW) $= \eta_{GEN}\eta'_{TH}P_{TH}$	1255.8[b]	
Total pump power fraction, ε_{pump}	0.006[c]	
Ohmic power to coils and plasma (MWe)	164.4[d]	
Ohmic power fraction, ε_Ω	0.131	
Auxiliary power fraction		
• f_{AUX} (less pump power)	0.0444	0.067[e]
• $f'_{AUX} = f_{AUX} + \varepsilon_{pump}$	0.050	0.073
Recirculating power fraction, $\varepsilon = f_{aux} + \varepsilon_\Omega + \varepsilon_{pump}$	0.181	0.204
Net plant efficiency, $\eta_p = \eta_{TH}(1 - \varepsilon)$	0.296	0.288
Net electrical power, P_E(MWe)	1028.5	1000.0

(a) Based on $\eta_{PUMP} = 0.75$.
(b) Based on $\eta_{GEN} = 0.98$.
(c) Based on $\eta_{pump} = 0.75$ for all pumps, with PbLi pumping consuming 83% of this power.
(d) Table 2-II, $P_\Omega + P^\Omega_{TFC} + P^\Omega_{PFC}$.
(e) f'_{AUX} is adjusted to give P_E = 1000 MWe(net) considered hereinafter as the base case for purposes of the Appendix A design table.

The slope of the constant pressure curves on Fig. 3-8 results because a complete optimization was not performed for each point and the convection from the PbLi blanket to the second-wall pressurized-water coolant was assumed constant for all cases. At larger values of T_{po} the convection of heat to the second wall increases, and the resulting energy transported by the PbLi coolant would thereby decrease. The coolant flow rate and pressure drop would be correspondingly less, and the constant pressure curves would be more horizontal.

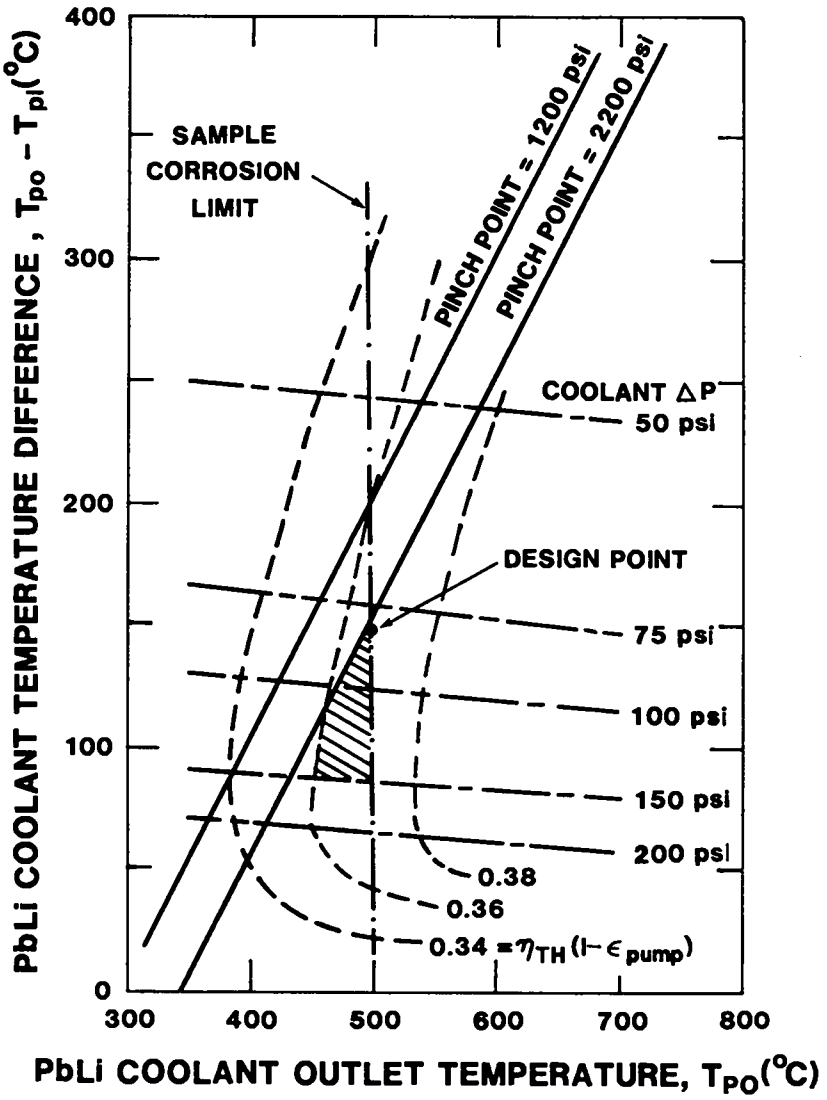

Fig. 3-8. Thermal hydraulic operating window for the PbLi-cooled blanket showing pinch points for a range of steam-generator conditions, effective cycle efficiency (only recirculated pump power shown), blanket pressure, and possible corrosion limits.

Figure 3-8 nevertheless provides a convenient summary of major constraints and the associated margins that define design windows and related tradeoffs.

The canonical design presented above satisfies all of the constraints that can be readily quantified and, therefore, represents an "optimized" preliminary design. Several areas in which additional work is required, however, can be identified. The more important of these are listed as follows:

- Recent work[35,36] indicates a relatively benign reaction between water and hot PbLi, with the interaction mass cooling once the relatively small heat associated with the lithium oxidation is released. Nevertheless, the safety aspects of the first-wall/second-wall/blanket configuration require more-detailed consideration. The separation of pressurized-water coolant from flowing tritium-containing PbLi by a single layer of material is a cause of concern. Alternative configurations can be considered, including multiple barriers (Options B or C, Fig. 2-11) or a second wall cooled by an inert high-pressure gas. Various kinds of safety systems should be investigated, and the effects of various failure modes should be assessed. For instance, leakage of either coolant system for Option B (double barrier) would be sensed before mingling of coolant systems occurs, and appropriate action could be taken.

- A more accurate analysis of PbLi flow in the blanket should be carried out. This analysis may take the form of a two-dimensional (or even three-dimensional) numerical analysis combining solutions of the conservation of mass, energy, and momentum and including the effects of the magnetic field. Two-dimensional effects associated with flow directional changes may be particularly important.[33] The possibility of using ceramic-coated channel walls to reduce the pressure drop and pumping power should be investigated, although the lower fields in the RFP blanket and the dominance of parallel-field coolant flow have been used to great advantage in the present design.

- A structural analysis should be made of the entire blanket, and this analysis should include the effects of (radiation) creep and corrosion. Generally, blanket pressure rather than pump power presents the key constraint in the present design. Furthermore, the corrosion limits[28] to which this blanket has been designed have been set by flow-blockage rather than structural-thinning limits. The considerable reduction in blanket surface area for the CRFPR blanket, as well as the possibility for using better cold-trapping or corrosion inhibitors may allow this $\sim 500^{o}$ C limit to be raised.

- A detailed design of a dual-media steam power cycle should be carried out. This design should include an economic analysis to permit the system to be optimized on the basis of net electrical energy output per unit cost.

3.3. Mechanical Design

The FPC mechanical design described in Ref. 10 and Figs. 1-2 and 1-3 remains largely unchanged by the two-dimensional neutronics analysis and the FPC thermal-hydraulics re-optimization summarized herein. Figures 3-9 and 3-10 give a view of the FPC showing the space allotted in the EFC set to accommodate service penetrations. All fluid lines are positioned at or near the outboard equatorial plane to facilitate pumping, power distribution, FPC disconnects, and vertical or horizontal single-piece FPC removal and replacement (Sec. 4.). Table 3-VIII summarizes the FPC component masses. The dimensional changes resulted in minor PFC and TFC design changes, and the Ref. 10 parameters are

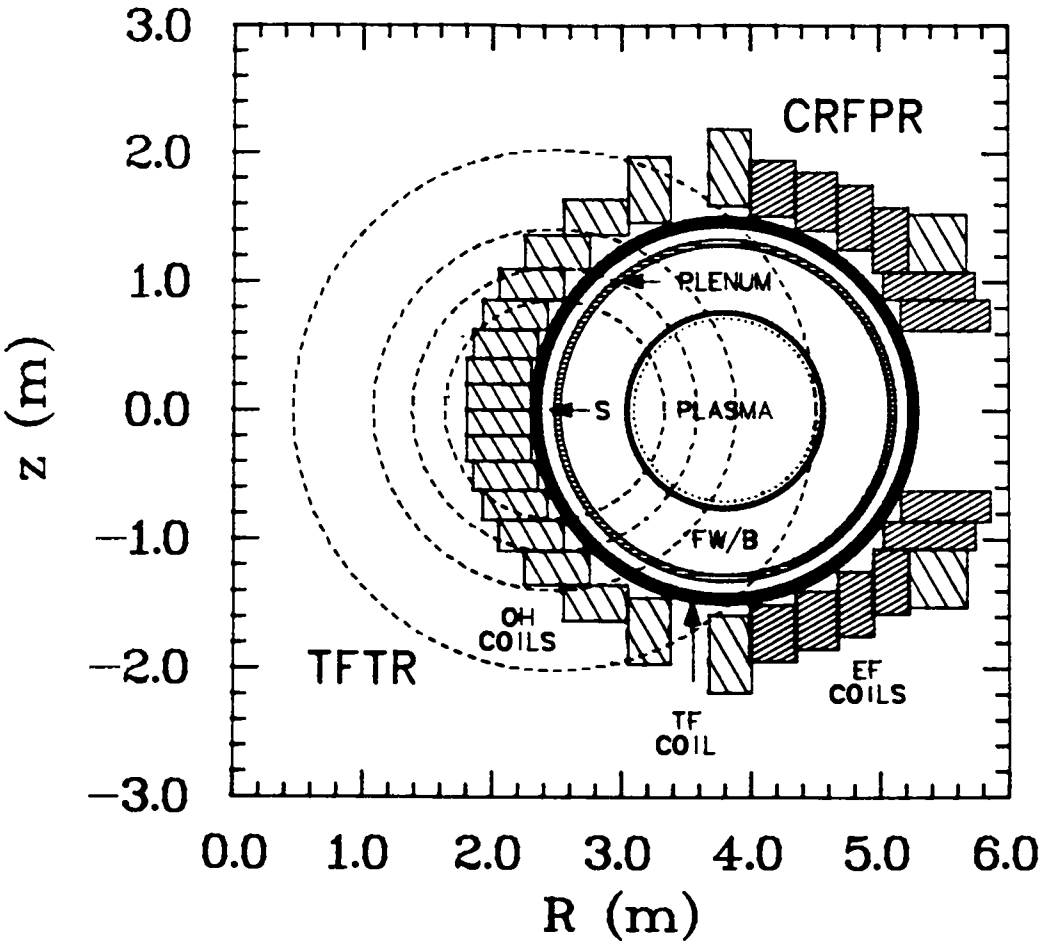

Fig. 3-9. Cross-section view of CRFPR(20) fusion power core showing space allowed in EFCs to accommodate coolant manifolds.

retained for the purposes of this analysis. As part of the preliminary evaluation of the FPC maintenance scheme given in Sec. 4, however, external coolant manifolding and support of the FPC are better resolved, and as part of that task minor changes in the PFC conduction arrangement were made. It was deemed unnecessary, however, to recompute the CRFPR(20) magnetics for this follow-on study.

The relatively tight array of PFCs depicted in Figs. 3-9 and 3-10 allows close electrical coupling to the plasma, a minimum coil mass, and minimum stored energy, but it limits access to the underlying TFCs (76.2 tonne) and FW/B/S (220.5 tonne, excluding the ~ 935 tonne of PbLi coolant) to only the outboard equatorial plane. The FW/B/S/TFC or reactor torus (304 tonne, excluding coolants but including main manifolds) underlying the 812-tonne PFC set would be

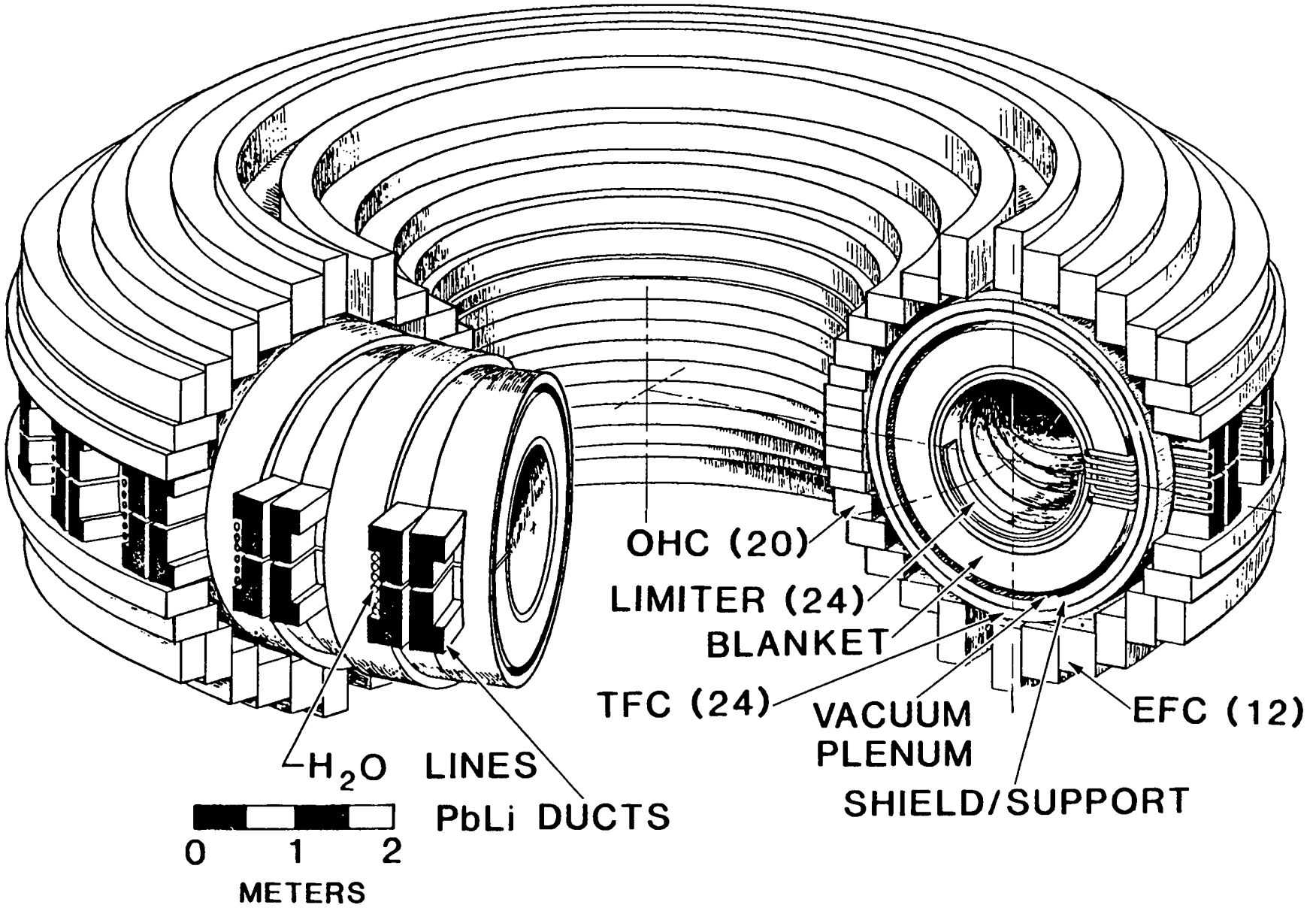

Fig. 3-10. Layout of key components of the CRFPR(20) fusion power core.

TABLE 3-VIII

FUSION-POWER-CORE MASS BREAKDOWN

Region	Thickness (m)	Volume (m^3)	Composition	Mass (tonne)
Limiter	0.008	0.32	82% Cu, 18% H_2O	2.87
• manifold	-	0.40	HT-9	3.15
• header	-	0.30	HT-9	2.33
First wall	0.005	0.20	60% Cu, 40% H_2O	1.79
Second wall	0.005	0.35	64% HT-9, 36% H_2O	2.75
• manifold	-	0.79	HT-9	6.20
• header	-	0.19	HT-9	1.51
Blanket	0.600	4.42	5% HT-9, 95% PbLi	34.45[a]
• inlet/outlet ducting	0.600	0.01	HT-9	5.80
Shield	0.10	22.25	90% PCASS, 10% H_2O	159.60
TFC	0.075	11.60		76.20 (296.65)
PFC	0.42[b]	110.33	70% Cu, 10% PCASS	
• OHC	variable	54.30	10% H_2O, 10% MgO(80%)	400.00
• EFC	variable	56.03		412.60
Main PbLi manifolds				8.
Total FPC mass				1,117.25
FPC volume (m^3)[c]				310.
FPC smear density				3.58
FPC thermal power (MWt)				3,472.6
FPC power density (MWt/m^3)				11.20
FPC mass utilization (tonne/MWt)				0.32

(a)Contains ~ 860 tonnes of PbLi in blanket and ~ 75 tonnes of PbLi in ducts to the outside of the PFC. The primary loop (including main manifolds) contains an additional ~ 4,525 tonne of PbLi.
(b)Average or smear thickness.
(c)Does not include main PbLi manifolds.

installed and removed as a single unit after removal of the top two PFC quadrants. For purposes of off-site fabrication and assembly, the reactor torus is segmented into 24 toroidal sectors, each being centered on a TFC. The ~ 1,239-tonne PbLi-filled reactor torus would be supported from below by a saddle or strongback arrangement extending through the lower gap in the PFC set. Details of the interrelationship of FPC components depicted in Figs. 1-2 and 1-3 remain as described in Ref. 10. Alterations in this approach that reflect a better resolved FPC maintenance scheme are described in Sec. 4.

3.4. Base-Case Design Summary

The flow rates, sizes, power ratings, masses, and overall engineering characteristics reflected in Tables 3-VI through 3-VIII and Fig. 3-7 give the essential elements of the CRFPR(20) at the present level of framework study. Appendix A gives major design parameters in a standard format suggested by the DOE/OFE. The Appendix A design table also makes comparisons with the Ref. 10 design, showing minor changes incurred while extending the CRFPR(20) definition. Section 3.5. describes the impact of derated (lower-wall-loading) designs on the thermal-hydraulic requirements. The design parameters listed in Appendix A are used in advancing the FPC concept to a level where approximate time estimates of the CRFPR(20) maintenance approaches can be made in Sec. 4. and the updated design can be re-costed in Sec. 6.3.3.

3.5. Derated FPC Design Options and Tradeoffs

A scoping study was conducted to predict the performance of a system having a PbLi-cooled first wall (Option D, Fig. 2-12). As discussed in Sec. 2.2.3., this option requires both a significant reduction in reactor power density and a lower PbLi outlet bulk temperature, T_{po}. Equation (1) indicates that the lower value of T_{po} will decrease the thermal-conversion efficiency. The fraction of the fusion power recovered by the lower-temperature water coolant will be less (only the limiter would require water coolant), however, and the decreased f_w would increase the thermal-cycle efficiency. The magnetic fields will also be lower for the lower power options, resulting in decreased pressure drops and pumping power in the PbLi coolant circuit. For these reasons, the thermal-hydraulic performance of the lower-power-density FPC is further examined.

In order to perform an assessment of the derated FPC without an extensive FPC redesign, particularly with respect to neutronics and magnetics aspects, the design shown in Figs. 1-2 and 1-3 is retained, and the neutron first-wall loading is systematically decreased from the I_w = 19.5 MW/m^2 base case, CRFPR(20). This approach results in a decrease in the total FPC power output, with retention of economics similar to the CRFPR(20) depicted in Table 1-I and requiring the multiplexing of an increasing number of FPCs. Since the FPC for the CRFPR(20) contributes less than 4% of the total direct cost, the increase in direct cost from the added FPCs should represent a 10-15% effect. Although the derated FPCs in principle should be identical to the CRFPR(20) designs,

maintaining the recirculating power fraction required to supply ohmic losses to the magnets will require more massive magnets and somewhat more costly FPCs if operated at the lower values of I_w. Hence, the lower-wall-loading FPC used in a multiplexed, P_E = 1000-MWe system requires a design reoptimization of the kind described in Ref. 10. (i.e., Fig. 1-5). Section 6.3.2. gives a preliminary estimate of these reoptimized, multiplexed systems. Generally, it is found that in addition to requiring better plasma confinement (e.g., increased dependence of plasma energy confinement time on current (Figs. 1-5 and 6-12)), the minimum-COE multiplexed design operates with increased power recirculated to the magnets. Hence, the COE may increase by as much as 30-40% if, for instance, four CRFPR(20) FPCs are multiplexed to generate ~ 1000-MWe(net) at a neutron first-wall loading of I_w = 5 MW/m^2. At some point, superconducting coils should become more attractive as I_w is decreased further.

For the purposes of this scoping assessment of the thermal-hydraulic aspect of the lower-wall-loading design, however, the CRFPR(20) design given in Ref. 10 and updated herein is simply derated in first-wall neutron loading without re-optimizing neutronics, magnetics, or costing (multiplexing). The blanket design, therefore, is identical to that described previously, except for the elimination of the water-cooled first wall and a modification in the blanket channel design to accommodate the decreasing magnetic fields accompanying the lower-wall-loading options. Channel-design Option A (Fig. 2-11) is preferred because a more uniform PbLi flow field results. Consistent with space limitations, the radial segment of the inside channel should be made as large as possible to minimize pumping power. Balancing of the PbLi flow in the other channels without making the radial segments of those channels unrealistically small, however, becomes difficult. A variation of channel-design Option B (Fig. 2-11), therefore, is chosen. In this variation, more practical (i.e., larger) values of $w_{Ri}(i > 1)$ are selected, and additional flow resistance is added to those channels in order to balance the system flow rates.

A blanket design was carried out for a 75% reduction in neutron first-wall loading, following the predictions of Fig. 2-14. As far as plasma performance is concerned, this design would be similar to the CRFPR(5) summary given in Table 1-II. The FPC geometry was assumed identical to that used previously, but the first-wall neutron and heat fluxes as well as the blanket neutronics response were decreased by a factor of 0.25 (I_w = 5 MW/m^2). Since $I_w \propto B^4$ and the design value of beta (β_θ = 0.2) remains unchanged, the magnetic fields were

decreased by a factor of two. The design procedure is somewhat different than that used in Sec. 3.2. because the value of PbLi outlet bulk temperature required to ensure that the PbLi/HT-9 interface temperature will not exceed a specified upper limit, T_{pM}, is not known at the outset and must be determined during the design calculation.

The most important design variables are the thickness of the poloidal and radial segments of the first channel, $w_{\theta 1}$ and w_{R1} (Fig. 2-11) and the inlet and exit PbLi bulk temperatures, T_{pi} and T_{po}, respectively. Based on space considerations, $w_{R1} = 0.4$ m is chosen. For a selected value of $w_{\theta 1}$, the temperatures T_{po} and T_{pi} can be found that yield a specified value of T_{pM} and a specified pressure drop. A trial and error procedure is used in the blanket design model. An additional result of that calculation is the interim net cycle efficiency, $\eta_{TH}(1 - \varepsilon_{pump})$.

The effect of poloidal channel size on $\eta^*_{TH} = \eta_{TH}(1 - \varepsilon_{pump})$ is shown in Fig. 3-11 for a maximum PbLi pressure, P_p, of 0.689 MPa (100 psi) and a range of maximum interface temperatures, T_{pM}. A maximum efficiency is predicted for a given value of $w_{\theta 1}$. The PbLi velocity for smaller values of $w_{\theta 1}$ must be low to limit the pressure drop below a design constraint (100 psi or $\sim$ 0.7 MPa). The pumping-power fraction, ε_{pump}, is small in this case, and $(T_{po} - T_{pi})$ must be large; a low value of T_{pi} and low thermal-conversion efficiency result. Increasing $w_{\theta 1}$ causes an increase in T_{pi} and η_{TH}, resulting in an increase in η^*_{TH}. Eventually, however, the velocity and pumping power increase to a level where ε_{pump} increases rapidly, and η^*_{TH} then decreases. The η^*_{TH} versus $w_{\theta 1}$ curve, therefore, shows a maximum value. The optimum efficiency shown on Fig. 3-11 is plotted in Fig. 3-12 for a range of P_{pM} and T_{pM} values. If a corrosion limit of $T_{pM} = 500^{o}C$ is imposed, the optimum design corresponds to a pressure drop of 0.7 MPa.

The scoping calculations described above are intended to explore design options for a lower-wall-loading CRFPR rather than to present an optimized design. Hence, when the previously described parametric study is focused onto a specific example, the FPC magnetics and plasma physics remain unaltered from the CRFPR(20) case, except for a decreased magnetic field. Generally, the CRFPR(5) option will cost more because of the increased recirculating power fraction required by the coils, increased cost related to economy of scale if $P_E < 1000$ MWe(net) is considered, and increased FPC costs related to more massive coils or multiplexing. Hence, a complete re-optimization using the

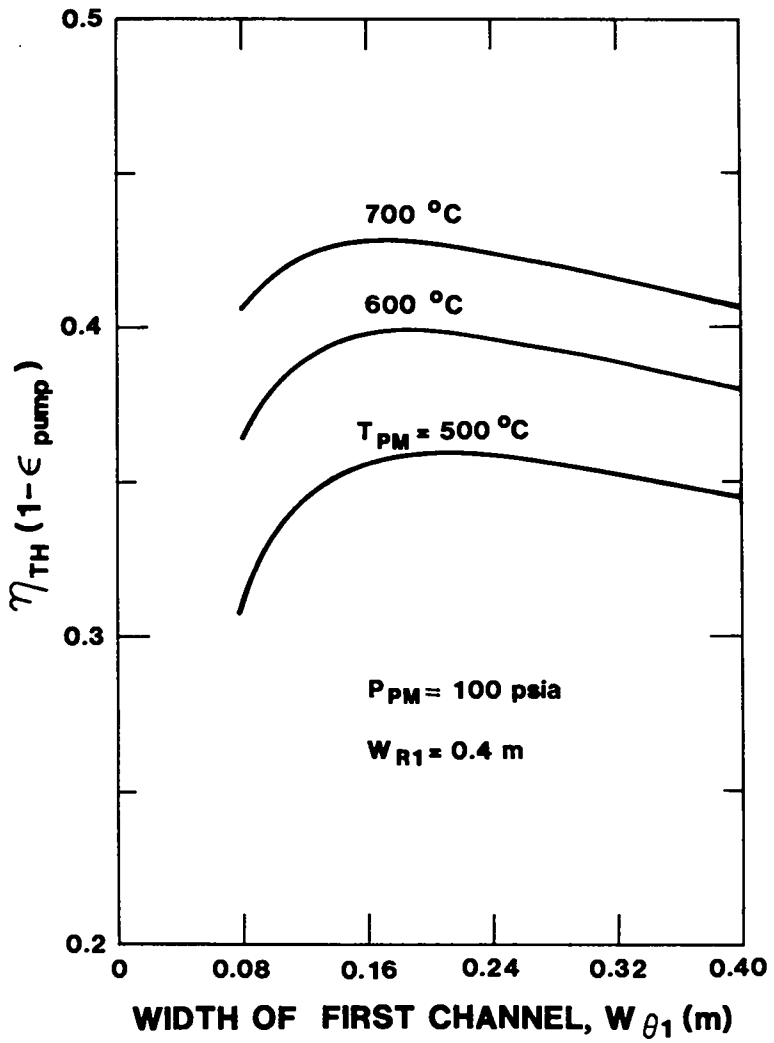

Fig. 3-11. Effect of width of first poloidal channel on $\eta^*_{TH} = \eta_{TH}(1 - \varepsilon_{pump})$ for the CRFPR(5) case with fixed radial channel width and PbLi pressure drop. The maximum structural temperatures T_{pM} are shown.

techniques described in Ref. 10 is required. The following examples serve only to give direction in the thermal-hydraulics area for a lower-wall-loading, CRFPR(5) option.

The blanket parameters for the reduced-power CRFPR(5) design are given in Table 3-IX, where the power densities and heat fluxes are 25% of the level of the CRFPR(20) base case. The total cooling rate for the blanket also includes a comparable reduction in the first-wall/second-wall cooling rate. The magnetic fields are lower for the reduced-power CRFPR(5) cases, allowing larger PbLi velocities without exceeding blanket pressure limits. Although the pumping-power fraction is larger for the CRFPR(5) design than for the CRFPR(20) case, η_{TH} is increased to an extent where η^*_{TH} shows a net increase.

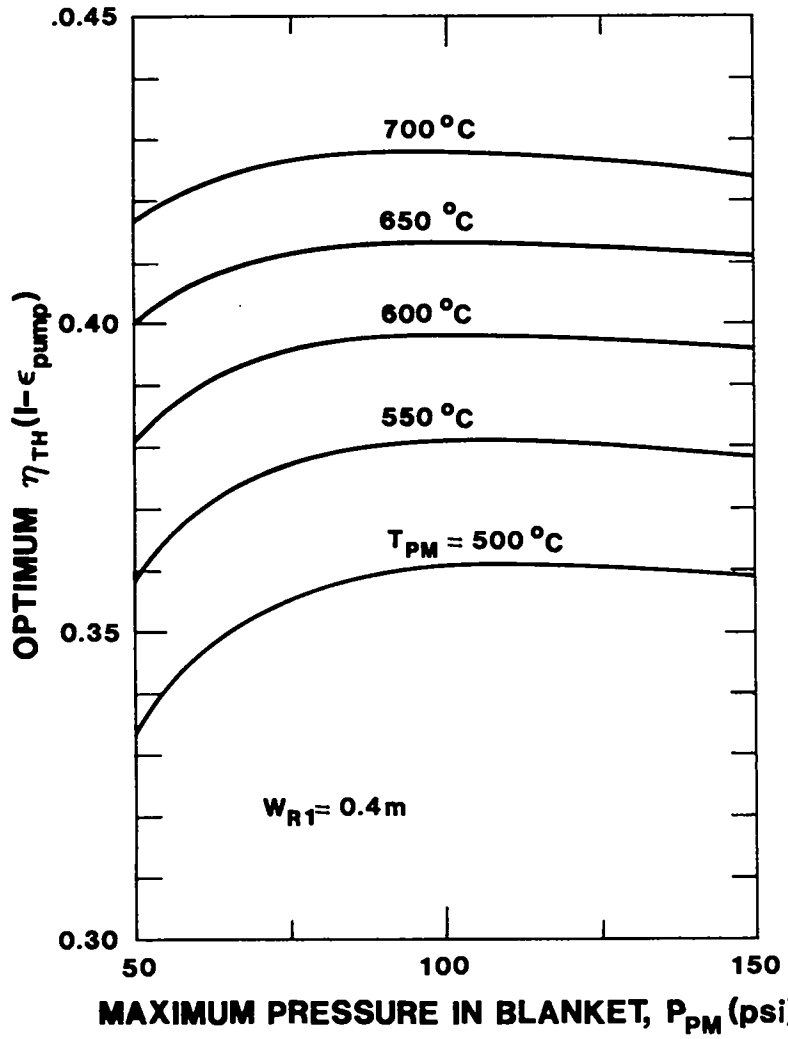

Fig. 3-12. Dependence of optimum value of $\eta_{TH}(1 - \varepsilon_{pump})$ as given on Fig. 3-11 on maximum PbLi pressure for a fixed radial channel width and a range of maximum structural temperatures.

A redesign of the limiter was also carried out for the reduced-power case. The reduction in cooling rate for the limiter by a factor of four allows higher water temperatures than were possible in the previous design; by maintaining the same maximum velocity limit ($V \simeq 10$ m/s), lower values of $T_{wo} - T_{wi}$ are allowed, and for similar film coefficients and degree of subcooling, ΔT_{SAT}, the lower heat fluxes give higher values for T_{wo}. Additional improvements to the thermal conversion efficiency result. Table 3-X summarizes key design parameters for the reduced-power limiter.

Overall design parameters for the reduced-power case are given in Table 3-XI. The thermal-conversion efficiency is higher than for the CRFPR(20) design. The net plant efficiency cannot be accurately computed because a

TABLE 3-IX

BLANKET THERMAL-MECHANICAL DESIGN PARAMETERS
FOR THE REDUCED-POWER CRFPR(5) CASE

PARAMETER	VALUE	
	CRFPR(20)	CRFPR(5)
Number of segments	48.	48.
Material	HT-9/PbLi	HT-9/PbLi
Overall dimensions		
• toroidal extent, $\ell_w/2$(m)	0.48	0.48
• radial extent, Δb(m)	0.60	0.60
• inside radius (m)	0.775	0.775
Coolant configuration (poloidal flow, Fig. 2-11)		
• channel thicknesses with increasing radius, $w_{\theta i}$(m)	0.200/0.200/0.200	0.200/0.200/0.200
• channel thicknesses entering manifold, w_{Ri}(m)	0.300/0.062/0.022	0.400/0.050/0.050
• channel wall thickness (mm)	5.0	5.0
Blanket thermal rating		
• total cooling rate, $P_{BLK} - P_{BL}$ (MW)	1865.1[a]	704.4
• peak power density (MW/m^3)	350.	87.5
• average power density (MW/m^3)	21.5	5.4
• maximum structural temperature (^{o}C)	500.	500.
Coolant properties		
• inlet temperature, T_{pi}(^{o}C)	350.	350.
• outlet temperature, T_{po}(^{o}C)	500.	378.
• nominal coolant velocity in channels, V_i(m/s)	1.25/0.35/0.14	2.5/0.70/0.28
• nominal coolant velocity in manifold, V(m/s)	1.78	1.78
• total mass flow rate, $\dot{m}$ (kg/s)	74,765.	147,765.
• pressure drop in blanket/manifold (MPa)	0.55	0.69
• pumping power (MW)[b]	5.8	21.3
Manifold/header properties		
• radial extent beyond blanket (m)	0.47	0.47
• height (m)	0.40	0.40

(a) Although P_{BLK} = 2012.1 MW is deposited in the blanket, P_{BL} = 147.0 MW leaks back to the first-wall/second-wall water coolant.
(b) Pump efficiency is η_{pump} = 0.75.

redesign of the TFCs and PFCs has not been carried out, and the ohmic power loss is unknown. The partial results obtained for the reduced-power case, however, indicate improved thermal efficiency. Overall tradeoffs and added unit costs of a smaller lower-power-density FPC, however (i.e., Sec. 6.3.2.), generally result in increased costs and a recirculating power fraction that tends to override the benefits of improved thermal conversion efficiency. As the neutron first-wall

TABLE 3-X

PUMPER-LIMITER THERMAL-MECHANICAL DESIGN PARAMETERS
FOR THE REDUCED-POWER CRFPR(5) CASE

PARAMETER	VALUE	
	CRFPR(20)	CRFPR(5)
Number of limiters, N	24.	24.
Material	MZC Copper	MZC Copper
Overall dimensions		
• toroidal extent, ℓ_L(m)	0.38	0.38
• maximum radial thickness, δ'(mm)	11.5	11.5
• stand-off distance from first wall, δ(mm)	40.	40.
Coolant configuration (toroidal flow)		
• channel height (mm)	0.8	0.8
• channel width (mm)	4.0	4.0
• wall thickness to outside surface (mm)	0.8	0.8
• number of channels per limiter	942.	942.
Limiter thermal rating		
• total cooling rate of all limiters (MW)	363.4	90.8
• manifolds, total thermal power (MW)	204.9	51.2
• shield thermal power (MW)	86.5	21.6
• total power to limiter/shield circuit (MW)	654.8	163.7
• design heat flux, q_D(MW/m^2)	6.0	1.5
• maximum limiter temperature (^{o}C)	378.	340.
Coolant properties (pressurized water)		
• inlet temperature (^{o}C)	170.	291
• outlet temperature (^{o}C)	256.	307.
• nominal coolant velocity, V(m/s)	10.0	10.0
• total mass flow rate (kg/s)	1173.	975.
• pressure drop in channel (MPa)	0.10	<0.1
Manifold/header properties		
• inlet manifold, ID/OD(mm)	83.7/84.7	83.9/84.9
• outlet manifold, ID/OD(mm)	122.7/163.8	120.6/161.1
• inlet header (single radial run), ID/OD(mm)	83.7/112.0	83.9/112.3
• outlet header (single radial run), ID/OD(mm)	89.5/119.5	86.5/115.5
• total limiter circuit pressure drop (MPa)	0.30	0.27
• limiter pumping power [(a)] (MW)	0.18	0.12
• total limiter circuit pumping power[(a)] (MW)	0.52	0.40

(a) Pump efficiency is $\eta_{pump} = 0.75$.

loading is further diminished for a fixed power output, a breakpoint in the ever increasing COE is expected where superconducting coils and thicker blanket/shields become preferable. These tradeoffs, along with the impact of changing plant reliability and plant factor require a more extensive investigation.

TABLE 3-XI

KEY THERMAL PROPERTIES FOR THE CRFPR REDUCED-POWER CRFPR(5) DESIGN

PARAMETER	VALUE	
	CRFPR(20)	CRFPR(5)
Total recoverable thermal power, P_{TH}(MW)	3472.6	868.1
Pressurized-water coolant		
• power, P_{THw}(MW)	1607.5	163.7
• flow rate (kg/s)	2693.7	975.2
• inlet temperature (^oC)	170	286
• outlet temperature (^oC)	295	340
• pressure (MPa/psi)	15.2/2200	15.2/2200
• pumping power (MW)	1.32[a]	0.40[a]
PbLi coolant		
• power (MW)	1865.1	704.4
• flow rate (kg/s)	74,765.	147,765.
• inlet temperature (^oC)	350	350
• outlet temperature (^oC)	500	378
• pressure (MPa/psi)	0.55/79.8	0.69/100.
• pumping power (MW)	5.8[a]	21.3
Steam-power-cycle efficiency, η'_{TH}	0.369	0.393
Thermal-conversion efficiency, $\eta_{TH} = \eta_{GEN}\eta'_{TH}$	0.362	0.385
Gross electric power P_{ET}(MW) = $\eta_{GEN}\eta'_{TH}P_{TH}$	1255.8[a]	334.3
Pump power fraction, ε_{pump}	0.006[b]	0.063[b]
Ohmic power to coils and plasma (MWe)	163.3[c]	(d)
Ohmic power fraction, ε_{Ω}	0.131	(d)
Auxiliary power fraction, f'_{AUX} (less pump power)	0.044	(d)
Recirculating power fraction, $\varepsilon_R = f'_{AUX} + \varepsilon_{\Omega} + \varepsilon_{pump}$	0.181	(d)
Net plant efficiency, $\eta_P = \eta_{TH}(1 - \varepsilon)$	0.296	(d)
Net electrical power, P_E(MWe)	1028.5	(d)

(a) Based on $\eta_{pump} = 0.75$.
(b) Based on $\eta_{TH} = 0.371$ and $\eta_{GEN} = 0.98$.
(c) Table 3-II, $P_{\Omega} = P^{\Omega}_{TFC} + P^{\Omega}_{PFC}$.
(d) More extensive design reoptimization must occur before these parameters can be determined (Sec. 6.3.2.).

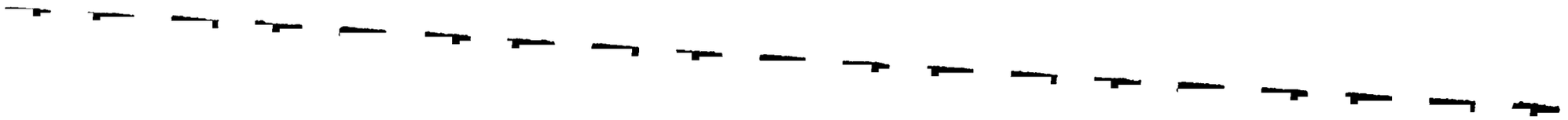

4. FPC MAINTENANCE APPROACH

The CRFPR(20) scheduled (annual) maintenance approach envisages removal/replacement of the FW/B/S/TFC or reactor torus as a single unit. A second ~ 304-tonne reactor torus (including main manifolds) would be assembled and subjected to rigorous (if not overstressed) pressure, coolant-flow, vacuum, and electrical checkout prior to the substitution for service. Access to the reactor torus is obtained by decoupling and lifting the upper inner OHC shell (149 tonne) and the upper outer EFC shell (258 tonne). Two approaches have been considered for the FPC torus removal and replacement. After being drained of coolants and remotely decoupled from all electrical leads and primary coolant lines, the reactor torus could then either be a) lifted as a unit vertically out of the saddle formed by the lower PFC shell, which remains in place, or b) removed horizontally after the upper and lower halves of the PFC set had been raised and lowered, respectively. The reactor torus in either vertical- or horizontal-replacement approaches would be transferred to a hot cell for disassembly and refurbishment. The entire FPC for both maintenance approaches is envisaged as being located in an evacuated chamber, although attaching vacuum pumps directly to the FPC and locating the vacuum boundary under the coil annulus is also possible.

Before the FPC maintenance approach can be defined quantitatively, a preliminary plant layout is required to locate and size primary pipes, coolant pumps, tritium handling, dump tanks, cold traps, superheaters, and steam generators. Once the proximity of these reactor-plant-equipment (RPE) systems is established, the access to the FPC and the maintenance approach become better defined. Preliminary estimates of maintenance operations, sequences, and times can then be made. This section begins, therefore, with an approximate definition of the CRFPR(20) balance-of-plant layout.

4.1. Plant Layout Options

The small size of the CRFPR fusion power core (1,117 tonne, 362 m^3, including the main PbLi manifold) compared to that for the STARFIRE tokamak[1] (~ 23,200 tonne, 8,100 m^3) or MARS tandem-mirror[2] (~ 23,300 tonne, 11,650 m^3, including end cells) reactors promises a reduced reactor building. Several plant layouts were considered in quantifying this promise, with a single preferred layout being adapted to both vertical- and horizontal-replacement maintenance schemes. Figures 4-1 and 4-2 show this plant layout as adapted to

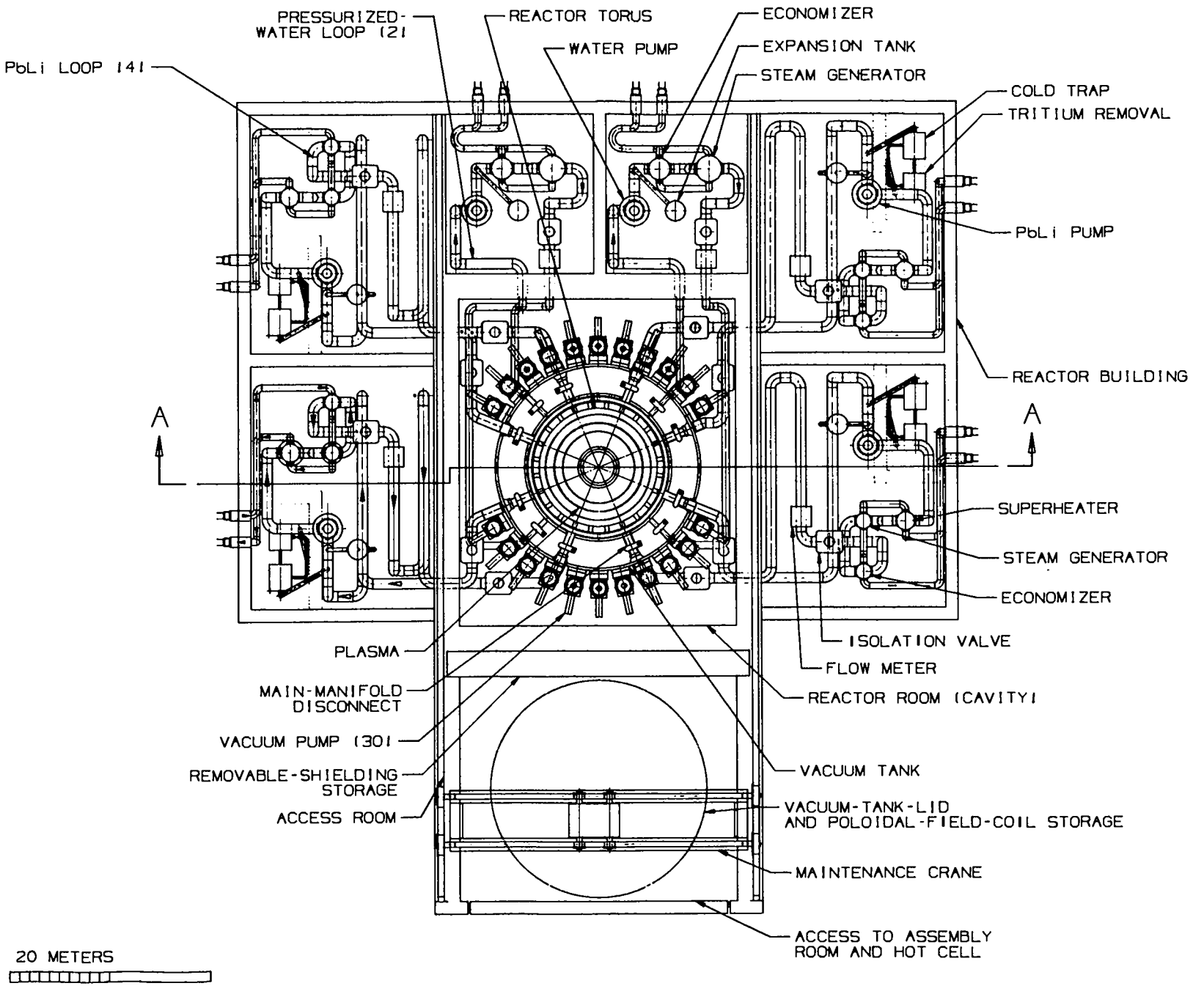
PRESSURIZED-WATER LOOP (2)
REACTOR TORUS
ECONOMIZER
WATER PUMP
EXPANSION TANK
PbLi LOOP (4)
STEAM GENERATOR
COLD TRAP
TRITIUM REMOVAL
PbLi PUMP
REACTOR BUILDING
A
A
SUPERHEATER
STEAM GENERATOR
ECONOMIZER
ISOLATION VALVE
FLOW METER
PLASMA
MAIN-MANIFOLD DISCONNECT
REACTOR ROOM (CAVITY)
VACUUM PUMP (30)
REMOVABLE-SHIELDING STORAGE
VACUUM TANK
ACCESS ROOM
VACUUM-TANK-LID AND POLOIDAL-FIELD-COIL STORAGE
MAINTENANCE CRANE
ACCESS TO ASSEMBLY ROOM AND HOT CELL
20 METERS

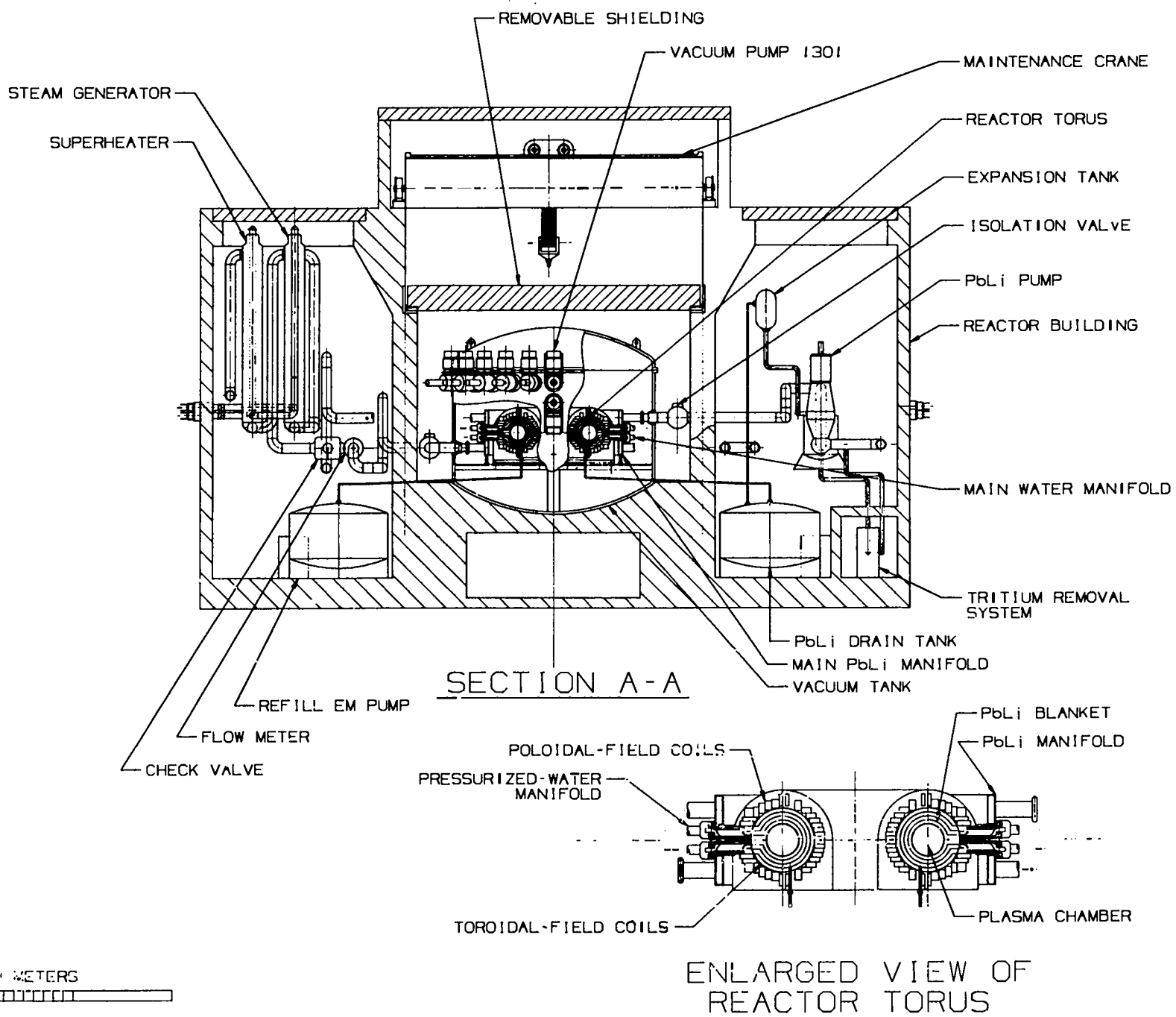

Fig. 4-1. Reactor plant layout adopted for vertical removal of the FPC.

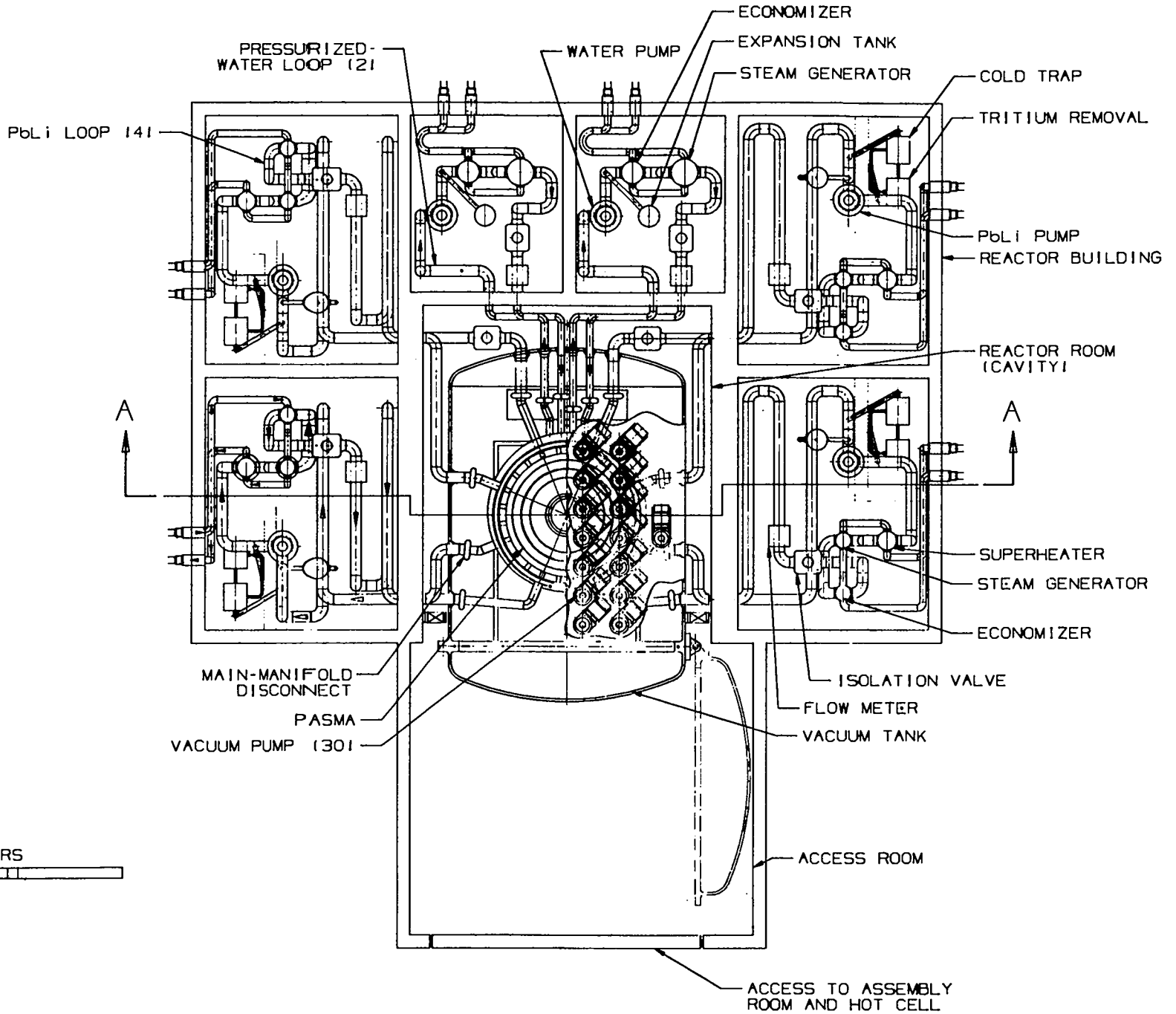
ECONOMIZER
EXPANSION TANK
PRESSURIZED-WATER LOOP (2)
WATER PUMP
STEAM GENERATOR
COLD TRAP
TRITIUM REMOVAL
PbLi LOOP (4)
PbLi PUMP
REACTOR BUILDING
REACTOR ROOM (CAVITY)
A
A
SUPERHEATER
STEAM GENERATOR
ECONOMIZER
MAIN-MANIFOLD DISCONNECT
ISOLATION VALVE
FLOW METER
PASMA
VACUUM TANK
VACUUM PUMP (30)
20 METERS
ACCESS ROOM
ACCESS TO ASSEMBLY ROOM AND HOT CELL

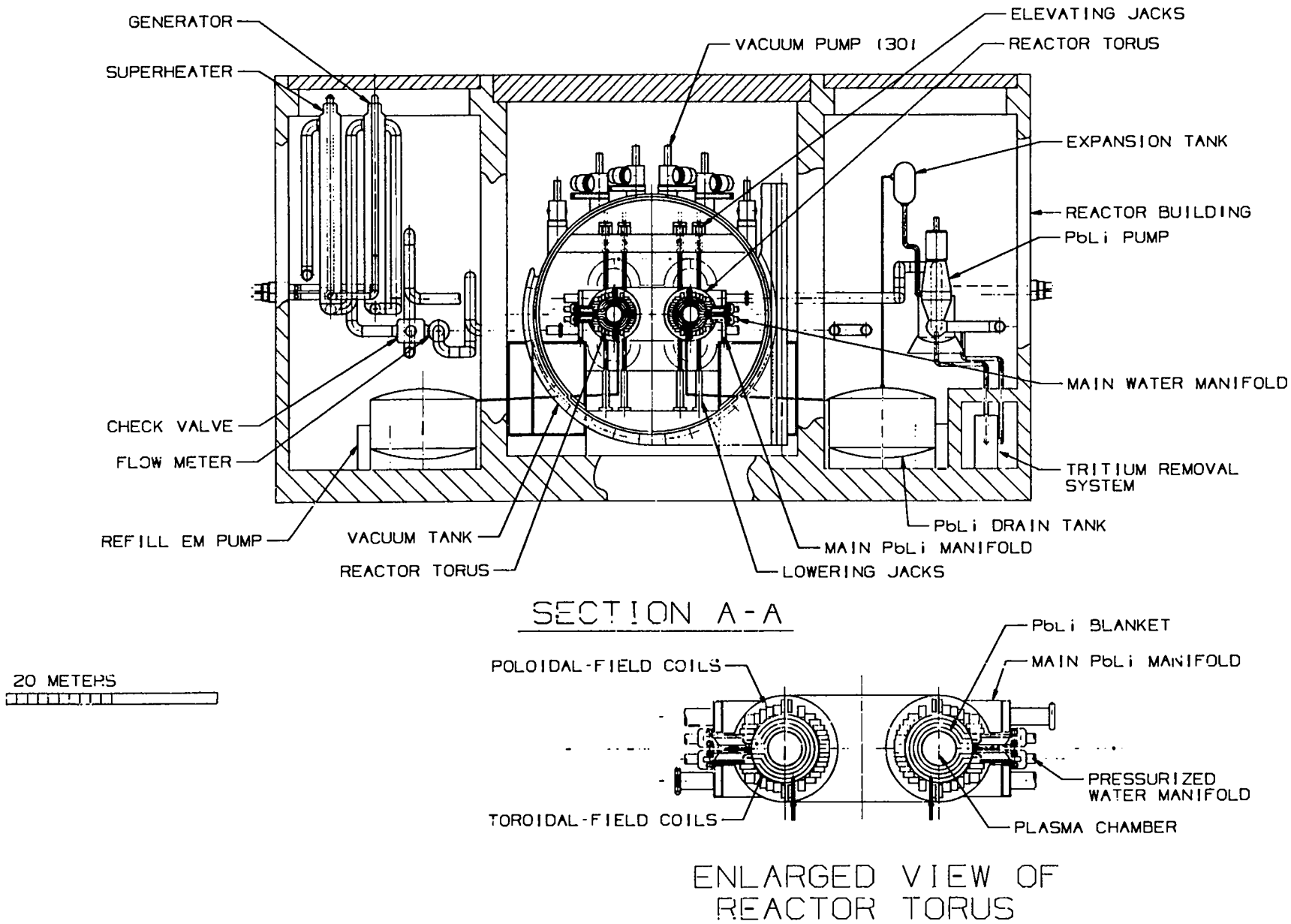

Fig. 4-2. Reactor plant layout adopted for a horizontal removal of the FPC.

each maintenance scheme. Figure 4-3 shows an isometric view of the FPC, and Figs. 4-4 and 4-5 illustrate more detail of the coolant manifolding schemes being considered.

Estimates were made of the time to replace the FPC for both the vertical- and horizontal-replacement schemes. The plant layouts depicted in Figs. 4-1 and 4-2 are basically identical, with four separate PbLi double-walled steam generators being shown along with associated pumps, pipes, and tritium clean-up facilities. Two PbLi steam-generator units are located on each side of the reactor. Steam generators for the pressurized-water coolant circuit and associated pumps are also shown in both Figs. 4-1 and 4-2. These latter two units are located at the back side of the reactor at the location opposite the reactor-building access door. The remaining front side of the reactor building is open for horizontal access to the FPC either after vertical or horizontal removal from the reactor cavity. The pressurized-water steam generators are sized for 46.2% of the total thermal power output (Table 3-I), although some of the energy carried in the pressurized-water loop may be used for feed-water heating in the other parts of the overall thermal-conversion cycle.

The turbine building [110 m × 50 m × 44 m = $2.42(10)^5$ m^3, not shown] would be located to the rear of the reactor building depicted in Figs. 4-1 or 4-2 and would house the superheated-steam turbines. The control room (30 m × 20 m) would be in the upper rear, and the tritium recovery/reprocessing building (36 m × 36 m) would be in the right rear of the reactor building. Accumulator tanks for emergency-cooling-system (ECS) afterheat control in event of a loss of coolant to the limiters (Sec. 5.) are not shown but would be located to the left and right of the reactor-room entrance. The reactor building, including the reactor torus, six steam generators and two accumulators, would be constructed from 1.25-m-thick concrete walls. The concrete walls and roof of the reactor room would be ~ 2.5-m thick and provide biological shielding. The combined volume of the steam-generator rooms for the two pressurized-water coolant circuits is 2 × 15 m × 18 m × 39 m = $2.11(10)^4$ m^3, and that for the four PbLi-circuit steam-generator rooms is 4 × 20 m × 25 m × 39 m = $7.80(10)^4$ m^3. The 30 m × 34 m × 39 m = $3.98(10)^4$ m^3 reactor room and 30 m × 30 m × 39 m = $3.51(10)^4$ m^3 access room for the horizontal-replacement scheme are less in volume than the 30 m × 32 m × 54 m = $5.18(10)^4$ m^3 reactor room and 29 m × 30 m × 54 m = $4.70(10)^4$ m^3 access room for the vertical replacement schemes, giving $1.86(10)^5$ m^3 and $2.10(10)^5$ m^3, respectively, for the total

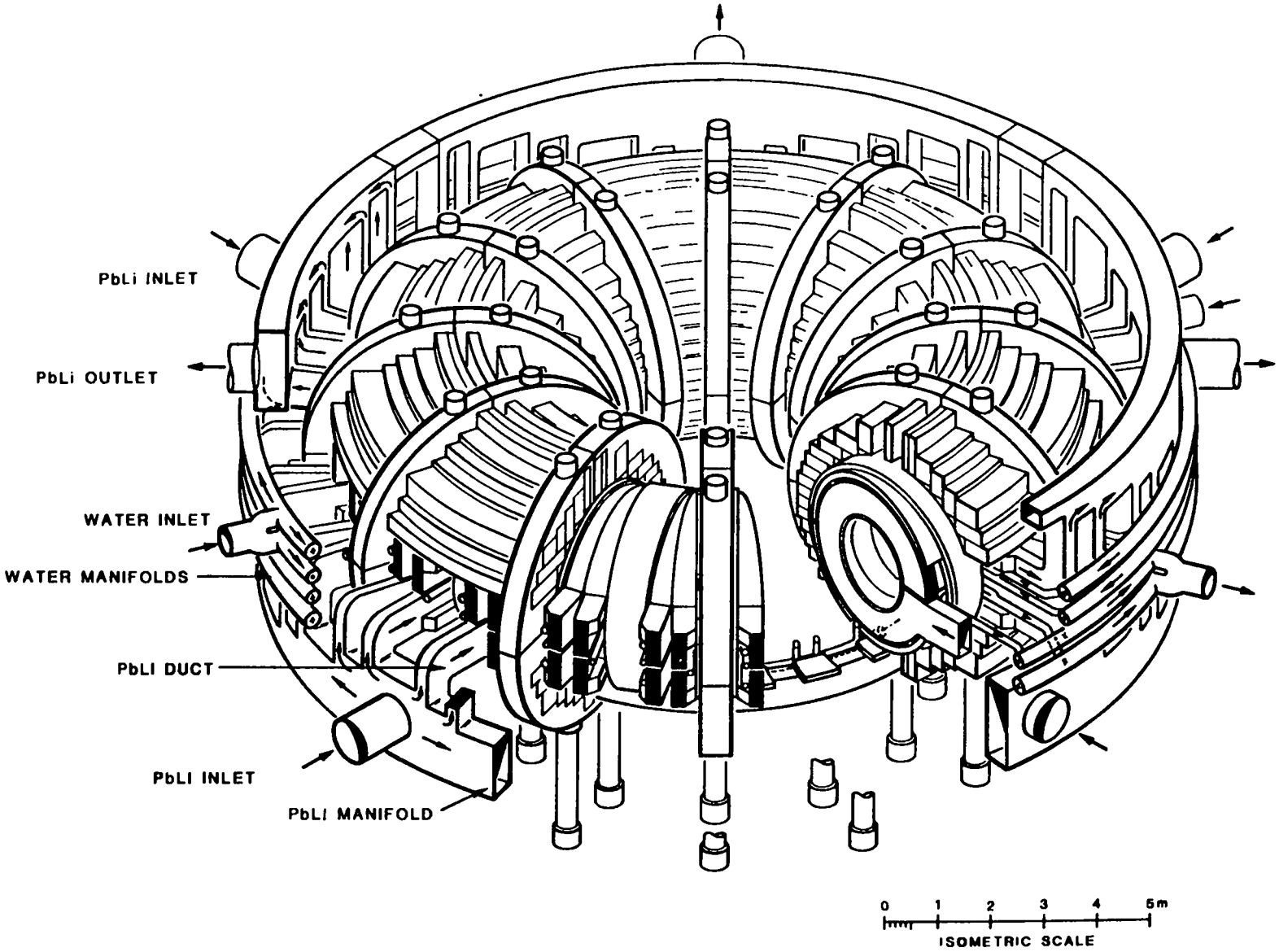

Fig. 4-3. Isometric drawing of FPC amenable for either horizontal or vertical replacement. The split PFC set (~ 813 tonne, total) can be raised/lowered by jacks to permit horizontal access to reactor torus, or the top half of PFC can be removed prior to vertical lift of reactor torus (FW/B/S/TFC).

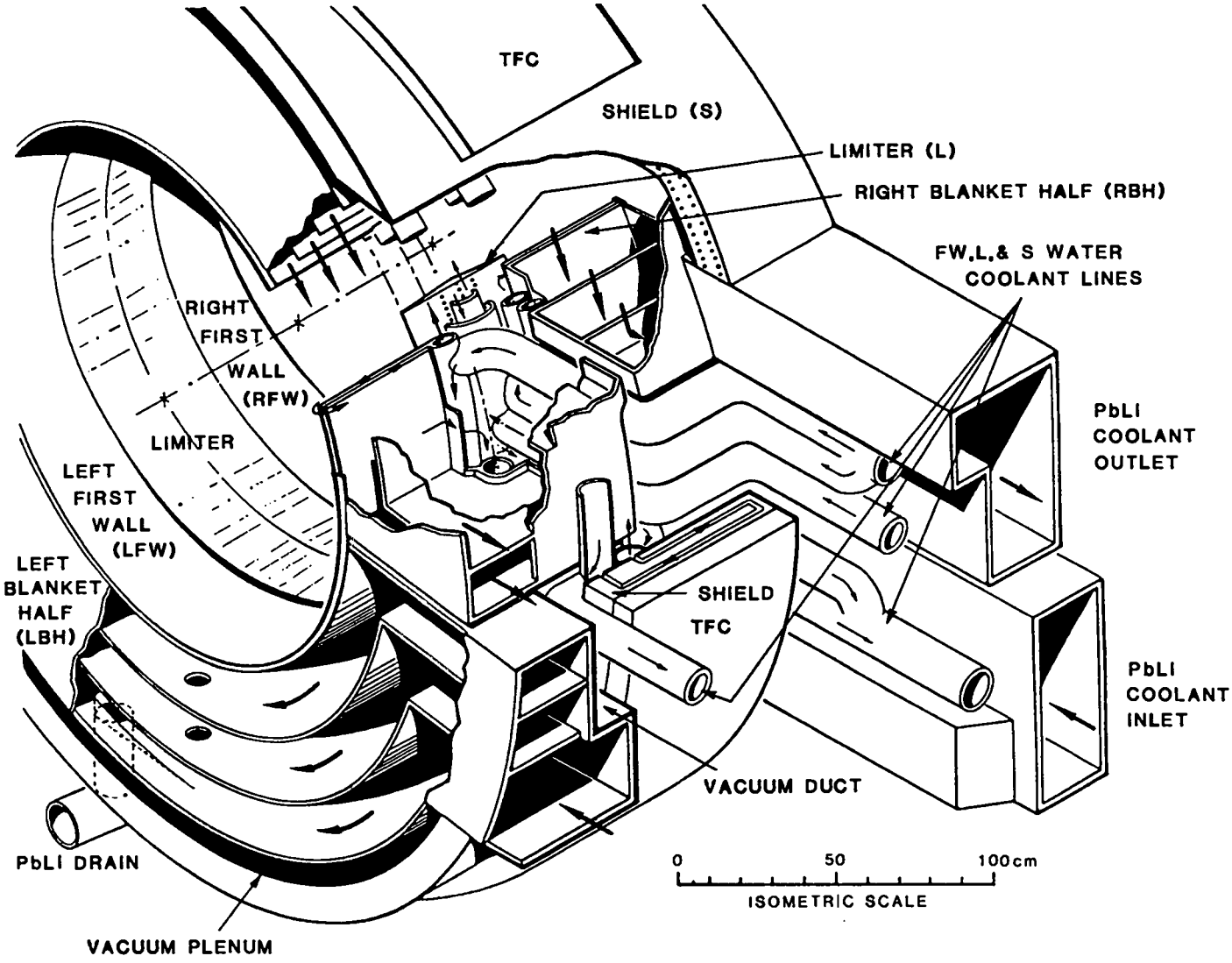

Fig. 4-4. Detailed isometric view of one of N = 24 reactor-torus sectors showing first-wall, blanket, shield, and coolant manifolding.

reactor building volumes (each total volume includes $0.12(10)^5$ m^3 for ECS accumulators). The vacuum-tank volume for the horizontal-replacement case is 9,136 m^3 (2,737 m^2) compared to 3,756 m^3 (2,217 m^2) for the vertical-replacement scheme. Hence, although the FPC volume and mass for the CRFPR(20) are much less than STARFIRE,[1] the total reactor-building volume is somewhat less than that projected for STARFIRE [$2.55(10)^5$ m^3] and significantly less than that projected for MARS[2] [$3.54(10)^5$ m^3].

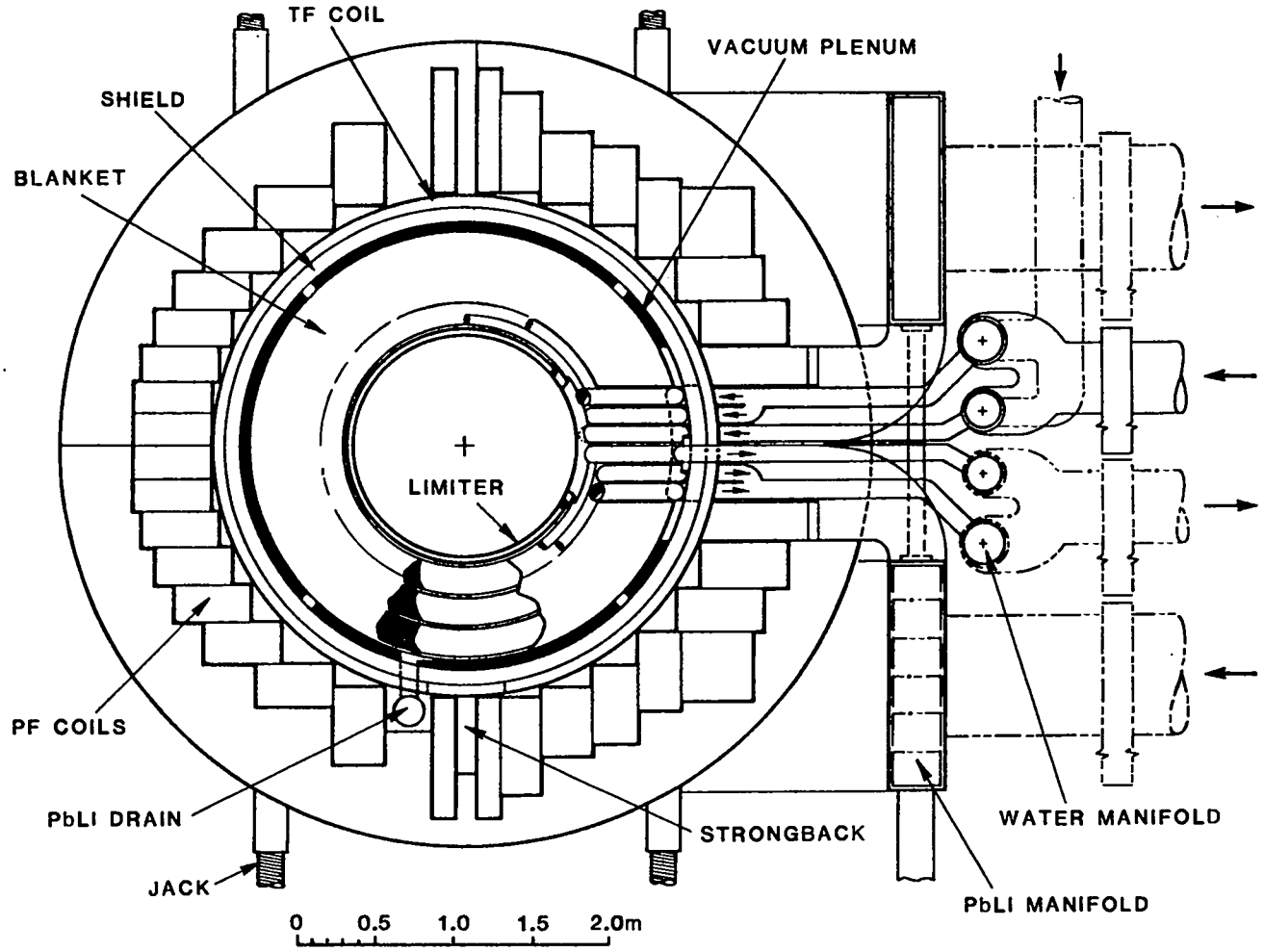

Fig. 4-5. Cross-sectional view of FPC showing coolant manifold layout.

The reactor, steam-turbine, and tritium-recovery buildings would be closely coupled to minimize piping runs (15-20 k$/m) and total building volume (300-500 $/m^3). This arrangement also minimizes the area and volumes of the plant facility that might be subjected to potential radioactivity release. The reactor, steam-turbine, and tritium-recovery buildings are maintained at negative pressure to control tritium leakage to the environment.

4.2. Plant Subsystems

Vacuum is provided to the reactor torus by enclosing the entire FPC within a vacuum tank. The primary PbLi coolant ducts join into two separate manifolds, with 12 segments of the 24 that comprise the FPC being cooled by each manifold. Each manifold then would have two separate heat-transfer loops consisting of a pump, steam-generator module, and a PbLi-cleanup and tritium-removal system. The primary water-cooling piping is also joined into two separate manifolds. Each water manifold supplies a single heat-transfer loop that is similar to the PbLi loops. Removal of the reactor torus and associated manifolds requires disconnecting 12 main cooling pipes (8 PbLi pipes and 4 water pipes) and the PbLi drain line from the drain manifold. As shown in Figs. 4-3 through 4-5, the manifolds are removed with the reactor torus as one piece, giving a total (drained) mass of 1,117 tonne or 304 tonne without the PFCs. The PbLi main manifolds would be designed to support the full weight of the reactor torus (304 tonne), with loads transmitted through the blanket to the shield structure, which in turn supports the TFCs. These manifolds are designed for normal operation to support 429-tonne of PbLi and the associated ducts. Under operating conditions, the reactor torus would be supported on a strong-back pedestal system through the lower PFC set, with loads being transmitted to the structure within the vacuum tank. Each key component located immediately outside the FPC is briefly described.

4.2.1. PbLi Pumps

One liquid-metal pump is provided in the hot leg of each PbLi loop. Each pump has a flow rate of 2 m^3/s and a developed head of 5.4 m. Because of the low-head, high-flow requirements, mixed-flow pumps are selected.[37] Each vertical, mixed-flow, 4.7-m-high × 4 m-diameter pump weighs 20 tonne and requires 1.5-MWe drive power.

4.2.2. PbLi Superheater, Steam Generator, Economizer

The PbLi superheater, steam generator, and economizer are based on a double-wall-tube design.[38] These units are counterflow systems with PbLi on the shell side and steam/water on the tube side. The PbLi superheater unit (153 MWt) is 13.3 m in height, 2.3 m in diameter, has a heat-transfer surface area of 4,240 m^2, and weighs 118 tonne. The PbLi steam-generator unit (178 MWt) is 9.8 m in height, 1.8 m in diameter, has a heat-transfer surface area of

1,820 m^2, and weighs 51 tonne. Lastly, the 8.0-m-high × 1.8-m-diameter PbLi economizer unit (90 MWt) has a heat-transfer surface area of 1,590 m^2 and weighs 44 tonnes. During manufacture of these double-wall units, the gap between the inner tube and outer tube will be exposed to helium atmosphere with 20 ppm H_2O at approximately 700°C. This moisture results in the buildup of a thin layer of oxide which provides a tritium barrier within the double wall to reduce permeation of tritium from the shell side to the tube side.

A calculation was performed to verify the sizing of the PbLi expansion loops depicted on Figs. 4-1 and 4-2 to be located between the reactor room and PbLi primary pump. This calculation was based on a method of sizing expansion loops suggested in Ref. 39. Several assumptions were required to make this calculation. The first assumption was that the pipe material would be an average steel, and average values for allowable stress and thermal expansion were taken. The second assumption was that the weight of the lead lithium coolant would not increase the stress in the plane of the expansion loops. The final assumption was that the pipe would be anchored at the reactor torus and at the pump or check valves with no intermediate anchors or guide supports being present. This calculation confirms the 1.3-m × 6-m expansion loops suggested in Figs. 4-1 and 4-2.

4.2.3. Tritium Removal

Tritium must be recovered from both the PbLi and water coolants, parameters for which are summarized in Table 3-VI. The PbLi tritium-removal system must maintain a low tritium partial pressure. Table 4-I gives an estimate of the CRFPR tritium inventory and indicates as a goal 9.5 grams of tritium for the PbLi coolant. This estimate is based on diverting 20% of the PbLi coolant and a 50% removal efficiency. The resultant tritium partial pressure would be 10^{-5} torr, which is consistent with an effective barrier in the double-walled heat exchanger that maintains a difference in tritium-partial by a factor of $\sim 10^5$. Polonium-210 is also removed from the PbLi coolant along with tritium at a rate of 9 g/yr for the first year and 40 g/yr in the 30th year. The low tritium inventory in the reactor room (209 g) is a direct consequence of high tritium partial pressure over the PbLi and the need to remove tritium from the PbLi coolant. The large portion (172 g) of this inventory is estimated to reside in the reactor vacuum-vessel compound cryopumps, which are regenerated every ~ 2 hrs. The large quantity of tritium in storage was estimated on the basis of

a one-day fuel supply and is based on the vacuum and fuel recycle model described in Ref. 10.

The tritium concentration in the primary water coolants must be kept at below 1 kCi/m^3 if single-wall steam generators are to be used. Achievement of this goal requires tritium diffusion barriers (oxides, copper triplex layers) at PbLi/H_2O interfaces both in the FPC and in steam generators.

4.2.4. Special Maintenance Tools and Disconnects

Removal of the reactor torus will require a number of remote operations involving disconnection of coolant manifold and electrical lines. Special handling tools[40] will also be required to disengage the PFCs and to move the reactor torus. Although this important area has received little attention to date, a number of approaches with specific application to the CRFPR are suggested in this section.

TABLE 4-I
ESTIMATED TRITIUM INVENTORY IN CRFPR(20)

	Subsystem Inventory (g)
Reactor room	
PbLi coolant/breeder	9.5
Water coolant (1 Ci/ℓ)	16.7
Fuel-pellet injector	14.4
Compound Vacuum cryo-pumps	172.0
Blanket structural (HT-9, copper alloy)	0.3
Reactor plasma	0.06
Total	212.96
Tritium process building	
Fuel cleanup unit	19.0
Isotope separation system	134.0
Total	153.0
Storage vault (1-day supply)	14,688.(a)
Total on-site inventory	15,054.

(a)Based on edge-plasma recycling coefficient of 0.8, and scrapeoff recycling coefficient of 0.68, and a limiter-slot reflection coefficient of 0.9 (p. 236, Ref. 10).

In order to replace the reactor torus, each coolant line must have a remotely operated disconnect. Three conceptual disconnects are suggested. The first disconnect would be used for the main manifold coolant lines in the vertical replacement scheme (Fig. 4-1) and is shown in Fig. 4-6A. This clamp uses two tapered flanges attached to the pipe and a clamp with a "V" groove to force the two flanges together onto a gasket and effect a seal. To open the clamp, a motor-driven screw separates the upper portion of the clamp. The portion of the pipe that remains with the torus can then be lifted vertically out of the clamp. The replacement reactor torus will then be lowered into position. The new flanges will each have a replacement gasket held in place by a retainer. The "V" groove in the clamp will assure the precise alignment of the new flange. Upon reversing the driver motor, the clamp tightens and seals the joint.

The second disconnect is suggested for separating the PbLi drain lines and also is based on a motorized version of a clamp with the tapered pipe flanges and "V"-groove clamp. A schematic of this clamp is shown in Fig. 4-6B. This clamp is also opened by a motor-driven screw. When the clamp is open, the drain line can be pulled straight out of the clamp. As described for the main-manifold clamp disconnect, the replacement drain line will have the appropriate flange and retained gasket.

The third disconnect is suggested for use on the main PbLi header lines in the horizontal-replacement scheme (Fig. 4-2). This design is a modification of header connections proposed for MARS.[2] The advantage of the PbLi clamps shown in Fig. 4-6C over the clamp depicted in Fig. 4-6A is the absence of "O" rings. The PbLi flanges, therefore, do not require a head-on approach, but can be slid into position at any angle, as is illustrated in Fig. 4-2. This orientation allows the PbLi headers to retain relative positions in the vertical-replacement case without significantly increasing the header length.

The flanges attached to the PbLi headers leading from the external PbLi manifold contain two rectangular grooves for placement of two PbLi rings which act as soldered joints when the flanges are joined. These rings are in place before the reactor torus is rolled through the vacuum door (Fig. 4-2). The mating flanges attached to the PbLi headers leading to the steam-generator rooms have two helium-cooling channels that align with the PbLi grooves when the flanges are brought together. Each PbLi connection has a pneumatically driven

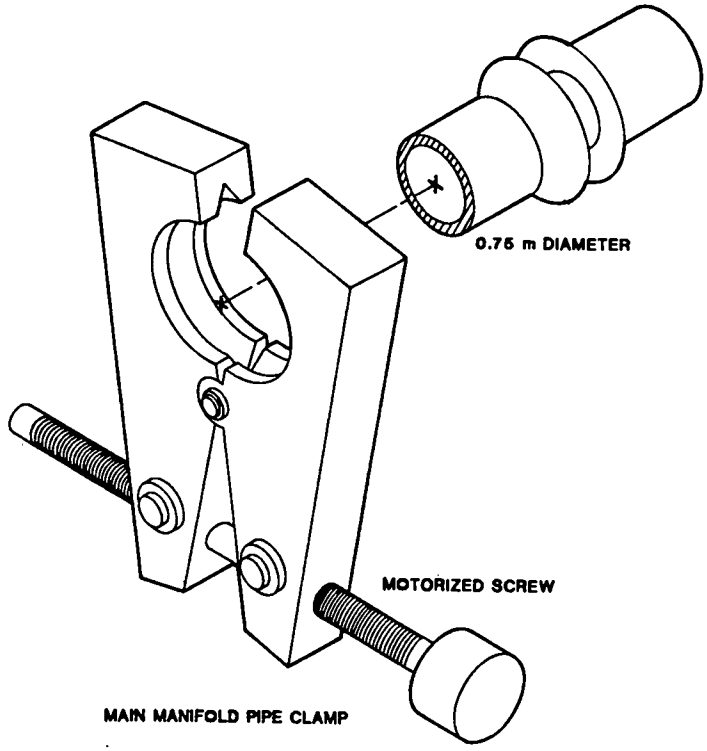

Fig. 4-6A. Clamp for remotely disconnecting main PbLi headers.

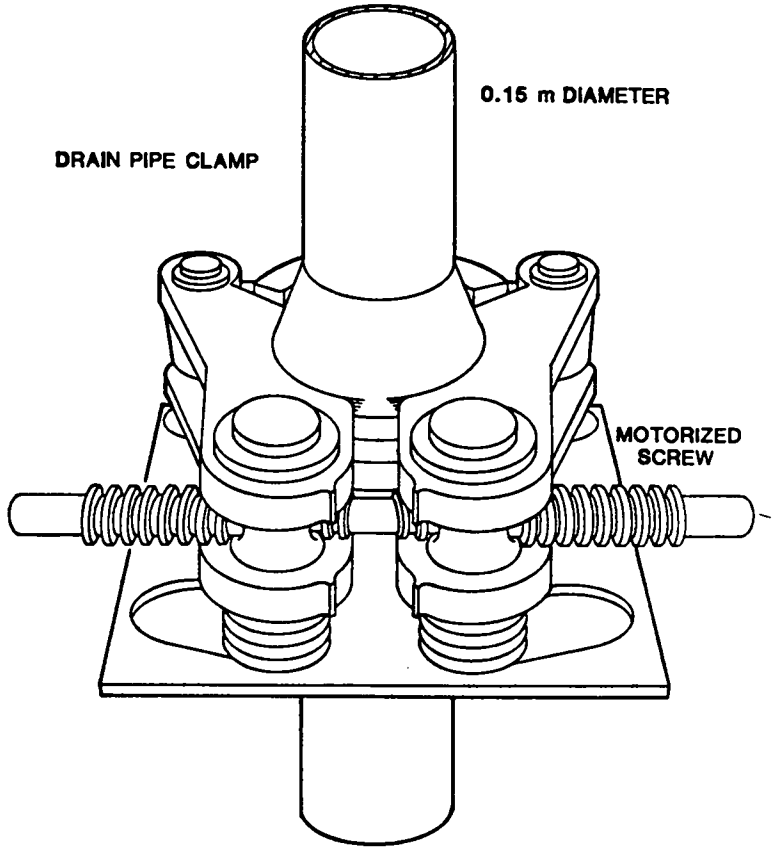

Fig. 4-6B. Clamp for remotely disconnecting PbLi drain plug.

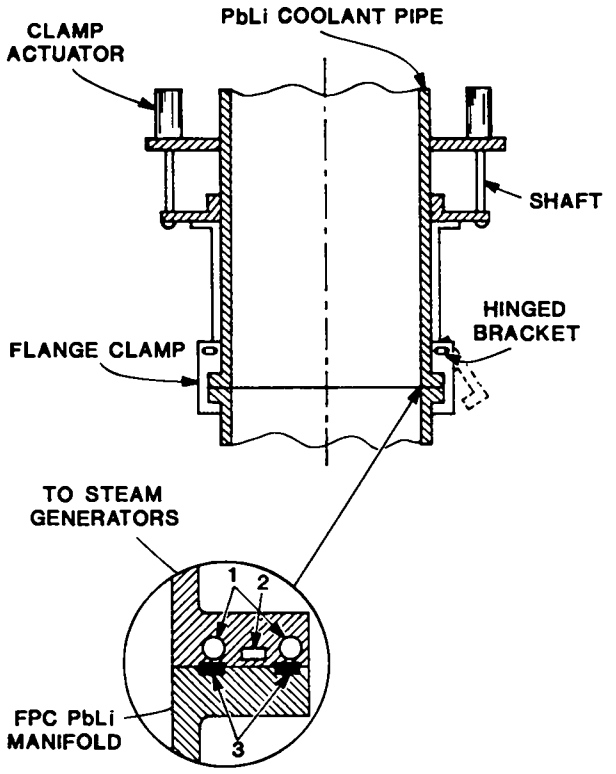

Fig. 4-6C. Schematic drawing of fusable PbLi joint for remotely disconnecting main PbLi header.

clamping mechanism that contains a floating flange with mounted levers that operate hinged brackets for clamping the seal flanges with a locking grip (Fig. 4-6C). After the flanges are clamped, the PbLi rings are melted by circulating hot helium gas through the coolant channels. After the PbLi spreads between the flange surfaces, cool helium freezes the solder, which is kept frozen by circulation of cold helium gas through the cooling channels. A groove in the header flange located between the helium coolant channels contains two concentric copper rings embedded in a ceramic insulator. In event of a PbLi coolant leak the groove will fill with PbLi, shorting the two rings, tripping an alarm, and identifying the leaky joint.

4.3. FPC Replacement Procedures

Once each year the reactor torus, together with all integral manifolding, must be replaced for the CRFPR(20) design with a nominal 15 MWyr/m^2 radiation lifetime. Several methods for accomplishing this changeout were considered. Each concept is discussed briefly. Table 4-II gives a summary of the actions required for each option, along with estimates of the time required for each action and the total changeout.

4.3.1. Vertical Replacement

The first option is based on the vertical lift of the 304-tonne reactor torus (FW/B/S/TFC and associated manifolds, Fig. 4-1). The following steps are suggested. After the system is shut down, the PbLi is transferred by gravity to the drain tanks through a manifold at the bottom of the reactor torus. This operation is accomplished by opening isolation valves to allow the drain tank and expansion tank atmospheres to communicate. Each of 21 keyblock concrete slabs (2 × 25 × 2.5 m, ~ 250 tonne each) is then removed from the top of the reactor room with the overhead crane and placed in a vertical storage against the wall between the reactor room and the access room (Fig. 4-1); the remaining four of the 25 (total) slabs remain in place. The vacuum tank is then brought to atmospheric pressure after isolation of the cryopumps, and the top of the vacuum tank (200 tonne) is removed with the overhead crane and placed in a storage pit located below the floor of the access room. Each of the upper two sections of the PFC set (149-tonne OHC, 258-tonne EFC) is then removed using the overhead crane and stored on a rack positioned above the stored vacuum-tank cover. The PbLi and pressurized-water header clamps and electrical connectors are then disengaged. The reactor torus (304 tonne) is lifted from the reactor cavity and placed in a shipping dolly located on a maintenance railroad in the front access room; this shipping dolly rides on tracks placed over the stored vacuum-tank cover and top half of the PFC set. The reactor torus is transported out of the reactor building and replaced with the pre-tested reactor torus. The replacement torus is lifted into place, the coolant-line clamps and electrical connectors are reattached, and the upper PFC set is replaced in the reverse order of disassembly. The vacuum-tank cover is then replaced, and the vacuum is re-established, with Rootes blowers being used for roughing pumps. The system is refilled with PbLi from the drain tank using a small electromagnetic pump. Table 4-IIA gives the time estimated for each of these steps. The estimated

time of 310 hours is based on substantial operational pretesting of the reactor torus prior to insertion into the reactor room to assure a high-probability, rapid restart.

4.3.2. Horizontal Replacement

A horizontal replacement option was considered (Fig. 4-2) that might further reduce the torus replacement time, requires no overhead crane, and thereby is anticipated to reduce the size of the reactor building. A larger vacuum tank is required, however. The FPC is drained of coolants, as previously described, and the vacuum tank is brought to atmospheric pressure, again, after isolation of the cryopumps. A 27-m-long cylindrical vacuum tank is oriented horizontally and has two 22.5-m-diameter end caps, one of which opens by means of a hinged door. This vacuum door uses inflatable (metal-bellows) seals during operation.

The PbLi and pressurized-water coolant-line connections are positioned to allow horizontal movement of the reactor torus. The PbLi headers use PbLi clamps (Fig. 4-6C) instead of the clamps depicted in Fig. 4-6A and are offset from each other at an appropriate angle to allow horizontal sliding into position. Once the PbLi has been drained from the blanket, the headers are disconnected by melting the frozen PbLi layer with hot helium gas and releasing the grip provided by the hinged bracket (Fig. 4-6C). To minimize flange alignment problems, bellows can be installed on the outboard side of each PbLi connection to make possible minor angular adjustments of the header flange.

The pressurized-water headers are located at rear of the vacuum tank, and the connecting flanges are aligned for direct connection and disconnection; a rectangular manhole(s) in the top of the vacuum tank permits easy access to these flanges. Although the length of the pressurized-water headers is now substantially reduced, the external pressurized-water manifolds are larger in diameter near the header outlets in order to accommodate the larger flows upon entrance to the manifolds.

Once the coolant lines are disconnected, large screw jacks that are attached to the upper and lower supporting structures within the vacuum tank are activated to spread the upper and lower segments of the PFC set. The reactor-torus mass is normally supported by a strong-back that is integral with the lower half of the PFC set. Upon lowering of the PFC the load of torus mass is transferred through the PbLi manifold to a heavy-duty roller unit. The drained

reactor torus and attached manifolding weigh 304 tonne and, through these heavy-duty roller units, are supported by angled struts under the PbLi manifolds. These two lines of rollers located on tracks positioned at each side of the reactor torus allow the torus to be rolled horizontally out of the vacuum tank. The pre-tested replacement torus would then be similarly translated into position. After the coolant header and electrical couplings are re-connected, and the screw jacks reposition the top and bottom halves of the PFC set, the reactor system is refilled with coolants, the vacuum-tank door is closed, vacuum is re-established, and the reactor restart sequence begins.

An alternative horizontal replacement option would use transhaulers, instead of heavy-duty roller units, in order to maintain the load point at the torus strong-back position instead of transferring the torus mass to the PbLi manifold. After the PFC set is separated as previously described, transhauler tracks attached to telescoping steel structures are moved into position under the torus. These track assemblies can either be initially located within the vacuum tank near the tank walls or slid into the vacuum tank from the outside and supported by jacks from the floor. Four transhaulers supporting a circular strong-back with pads identical to those normally used to support the torus during normal operation (Fig. 4-3) would move under the torus, raise the torus off the manifold supports, and move the torus out of the reactor building.

Removal of the PFC set with the reactor torus and the piping manifolding was also considered as a variation of the horizontal maintenance scheme. This option involves less initial equipment but would require an extra PFC set. The horizontal FPC replacement under these conditions proceeds exactly as before except no screw jacks are needed to separate the PFC set. After disconnecting the pipes and electrical connectors using the automatic clamps, the entire FPC (1,117 tonne, including PFCs and the main PbLi manifold) is rolled out of the vacuum building on the maintenance railroad tracks and a complete replacement FPC is rolled in and reconnected. While avoiding the automated vertical upward and downward PFC movement needed to expose the reactor torus, the replacement of the entire FPC would require a spare PFC set (~ 40 M$) and the horizontal movement of a 1,117-tonne mass. Estimates of the times required for each step required in the horizontal replacement scheme are given in Table 4-IIB. Replacement times for all maintenance schemes are relatively short (10-13 days), with the differences reported in Tables 4-IIA and 4-IIB not considered significant.

TABLE 4-IIA

TORUS REPLACEMENT TIME ESTIMATE FOR VERTICAL FPC REPLACEMENT

ACTION	TIME REQUIRED, (h)
Shut down reactor	
Circulate PbLi until the decay heat is sufficiently low for torus removal	48
Drain the system	24
Bring the vacuum chamber up to atmospheric pressure	4
Remove concrete shield from top of reactor room	20
Disconnect coolant piping, electrical leads, and controls/diagnostics	16
Lift off the vacuum chamber lid and store	4
Lift off top halves of OHC and EFC and store	6
Lift out the reactor torus and place in removal cask	4
Remove cask from the reactor building	4
Bring replacement reactor torus into the reactor building and lower into bottom half of PFCs	10
Replace top halves of OHC and EFC	10
Connect the coolant piping, electrical leads, and controls/diagnostics	16
Replace the vacuum chamber lid	6
Replace concrete shield atop reactor room	20
Evacuate the vacuum chamber and refill the FPC coolant systems	48
Restart reactor	70
TOTAL	310 (12.9 days)

TABLE 4-IIB

TORUS REPLACEMENT TIME ESTIMATE FOR HORIZONTAL FPC REPLACEMENT

ACTION	TIME REQUIRED, (h)	
	Removal of Reactor Torus (Plus Main Manifolds)	Removal of Entire FPC (Reactor Torus Plus PFCs)
Shut down the reactor		
Circulate PbLi until the decay heat is sufficiently low for torus removal	48	48
Drain the system	24	24
Bring the vacuum chamber up to atmospheric pressure	4	4
Disconnect coolant piping, electrical leads, and controls/diagnostics	16	16
Open the vacuum-chamber side door	1	1
Separate the top and bottom halves of PFCs using jacks	2	-
Remove reactor torus from the vacuum chamber and the reactor building	4	4
Move replacement reactor torus into the reactor building and vacuum chamber	4	4
Lower/raise halves of PFCs	2	-
Reconnect coolant piping, electrical leads, and controls/diagnostics	16	16
Close the vacuum-chamber door	1	1
Evacuate vacuum chamber and refill the FPC coolant systems	48	48
Restart reactor	70	70
TOTAL	240 (9.9 days)	236 (9.8 days)

5. AFTERHEAT AND RADIOACTIVITY

Radioisotopes are generated during reactor operation throughout the FPC, particularly in the limiter, first wall, second wall, and blanket. The isotopes present a long-term storage problem, a shorter-term radiological hazard to plant personnel, and a heat source that decays on a time scale long compared to the plasma run-down time (i.e., afterheat). In event of a loss-of-flow accident (LOFA) or loss-of-coolant accident (LOCA), the afterheat can melt the reactor components if adequate passive or active cooling is not provided. Since the afterheat power density is directly proportional to the operating power density, which in turn is proportional to neutron first-wall loading, passive control of afterheat becomes more difficult for high-wall-loading designs. The afterheat power density also depends on the short-term radioactivity of the alloy under irradiation, with copper being particularly active in this respect. Hence the I_w = 20 MW/m^2, copper-alloy first-wall/limiter CRFPR(20) design presented herein represents an interesting limit to examine from the viewpoint of afterheat control and consequence. This section focuses primarily on the afterheat problem and only briefly summarizes the radwaste requirements expected for the CRFPR(20) design.

As contrasted with a fission power core, where core slumpage driven by afterheat may rearrange a large fraction of the fissile fuel into an uncoolable mass with the possibility for vaporization, breaching of the primary containment, and a release of radioactive products, the parallel concern for a fusion power core (FPC) is to prevent a local slumpage or melting of the FPC structure. This issue is generally one of plant investment rather than safety to the public in that a majority of the activation products are in a less volatile form, and, depending on FPC geometry, a smaller fraction of the radioactive inventory is at risk of phase change and release to the primary containment. Furthermore, breaching of the primary containment by uncontrolled afterheat is substantially less likely for fusion.

The afterheat modeling is described in Sec. 5.1. A range of possible LOCAs is discussed in Sec. 5.2., where it is shown that the copper-alloy first wall should remain substantially below the melting temperature as long as either water coolant or natural circulation of PbLi blanket coolant is maintained. The limiter will not melt under LOCA conditions if an emergency cooling is provided for a relatively short time (1-2 hrs), but melting of the limiter is expected for the CRFPR(20) design if emergency cooling is not provided. Loss-of-flow

accidents (LOFAs) are not considered here for water-cooled components because with high water coolant pressure an LOFA would result in rapid increases in pressure that must be relieved into the containment sump; the emergency cooling would then also be used in this case for the limiter. Loss of flow is not considered for the PbLi coolant in that natural circulation would continue to provide a strong cooling mechanism for the FPC if the (resistive) magnets are de-energized and the steam generators (i.e., heat sink) are adequately elevated above the FPC. The Emergency Cooling System (ECS) design and operation for the limiter is considered in Sec. 5.3. Section 5.4. summarizes the long-term problem of radioactive waste and storage.

5.1. Afterheat Model

5.1.1. Neutronics Model

The radioactive build-up and decay in the FPC is determined by running three computer codes sequentially: a neutron transport code to produce energy and spatially resolved neutron fluxes, a cross-section collapsing code to produce flux-weighted energy activation cross sections, and an activation/decay code to solve the coupled rate equations as a function of time. The neutron flux as a function of position and energy was calculated using the two-dimensional TRIDENT-CTR code,[24] as discussed in Sec. 2.1. The source of the cross sections and kerma factors used in the calculations was a 30/12 group, coupled neutron/gamma-ray library generated from ENDF/B-V data with the NJOY[41] and TRANSX[42] codes. Region-averaged multigroup fluxes were obtained from TRIDENT-CTR for the regions of interest. The afterheat computations focused primarily on the limiter, first wall, second wall, and inner PbLi blanket channel and associated HT-9 steel structure. Region-averaged values for the prompt neutron and gamma-ray heating were also computed. Activation and depletion calculations were performed with the code FORIG[43] and the ORIGEN2[44] decay library. Cross sections for FORIG were generated using the TRIDENT-CTR region-averaged fluxes, the processing code ORLIB, and the ACTL activation cross-section library.[45]

The FORIG code is an adaption of the ORIGEN2 code for fusion reactor problems. The basic changes allow 11 rather than 6 standard reactions and up to 15 rather than 7 pathways for activation or decay of each nuclide to be read. The FORIG code produces output in the same format as ORIGEN2: composition, activity, thermal power, inhalation biological hazard potential (BHP), ingestion

BHP, chemical ingestion BHP, and gamma spectrum can be printed as a function of time for each nuclide or element. Both the total and fractional values of each quantity are also generated as a function of time.

Recently, a comparison of four standard decay codes (REAC,[46] FORIG,[43] DKR,[47] and RAC[48]) has been made for the same neutron spectrum and for 40 different parent isotopes.* The comparative agreement for the formation of the copper isotopes ^{62}Cu and ^{64}Cu and for ^{56}Mn (dominant afterheat source in HT-9) was good. The formation of these isotopes is particularly sensitive to the neutron spectrum, however, and varies substantially whether the respective metals are mixed with water or with PbLi coolants.

Afterheat calculations were performed for 15 different FPC regions that include the limiter, limiter manifold, first wall, second wall, first-wall/second-wall manifold, and PbLi coolant. The activity in these regions saturated in about 5-10 days for neutron first-wall loading of $I_w \simeq 20$ MW/m^2. The decay heat following a 10-day irradiation was computed for 100 minutes in two-minute decay intervals. Time intervals of two minutes were selected to accommodate the transient, finite-element heat-transfer calculations[49]. The afterheat deposited in the structure is taken as that from the alpha particles, beta particles, and a fraction (20-25%) of the gamma rays. The gamma-ray decay heat in the various regions was calculated using a slab attenuation model for the various regions and different energy groups. Fortunately, the dominant gamma-ray energy groups in the HT-9 and MZC copper alloy are similar. The percentages of gamma-ray energy absorbed in various regions are limiter, 25%; first wall, 23%; and second wall, 20%. The remaining gamma-ray energy is absorbed by the PbLi coolant. The afterheat absorption profile closely follows the energy-absorption profile shown in Fig. 2-4. Since the saturated afterheat values were less than 2% of the PbLi heat-generation rates given in Fig. 2-4, these afterheat values were not included in PbLi full-power analysis.

Figures 5-1A and 5-1B illustrate the decay schemes for copper and iron alloys, and Fig. 5-2 gives the afterheat expressed as a fraction of full power. The average power density in the limiter at shutdown is about 29 MW/m^3 (9% of full power) if all gamma-ray heating is included. This value decreases by a factor of two within ~ 15 minutes after shutdown and then approaches an

*Information provided by E. Cheng, "Activation Cross Section Library Comparison Study, Numerical Results," General Atomic Technology, June 1984.

asymptotic value of about 2%. The average power expressed as a percentage of full power in the first-wall copper at shutdown is about 4.2% and approaches a value of 1.2%. The decay in the first 15 minutes is dominated by ^{62}Cu (9.74-minute half life). The asymptotic value of 1.2% results primarily from ^{64}Cu (12.71-hour half-life). The short-term first-wall activity is ~ 66% lower than the limiter, this difference in average afterheat resulting from neutron shielding of a part of the first wall by the thicker limiter.

A comparison was made* of the relative formation of ^{64}Cu in three different copper/coolant configurations: Cu and PbLi; Cu and H_2O; and the Cu-H_2O-PbLi. The relative formation of ^{64}Cu from $^{63}Cu(n,\gamma)$ and $^{65}Cu(n,2n)$ increased from the PbLi-containing to the H_2O-containing configurations by a factor of 12; in changing from PbLi to the mixed H_2O/PbLi configuration characteristic of the CRFPR(20) design the relative reaction-rate increase was six. The thermalization of the neutron spectrum caused by water substantially increases the long-term afterheat generation in the copper alloy. This behavior is also true in the case of HT-9 steel. The HT-9 in the second wall at shutdown has a total afterheat equal to 2.6% of operating power. About 80% of this percentage is. generated by ^{56}Mn (2.58-hour half-life). This isotope continues to dominate the second-wall afterheat at one hour after shutdown with a value equal to 1.7% of operating power. Included in Fig. 5-2 are afterheat decay curves for the HT-9 first wall of MARS,[2] two HT-9 first-wall calculations by Cheng,** and the HT-9/PbLi blanket reported for the WITAMIR tandem-mirror reactor design.[51] Also shown is a fission-product afterheat curve.[50]

5.1.2. Thermal-Hydraulic Model

Radiation, conduction, and convection were considered as afterheat removal mechanisms. For example, the large surface area of the limiter and the relative thinness of this system lead to radiation transfer to the first wall being a dominant cooling mechanism in event of a limiter LOCA. The afterheat in PbLi averaged over the blanket was 0.01 MW/m^3 and was relatively constant for the LOCA times considered. Most of the heat deposited in the PbLi, therefore, derives from the first wall and second wall.

*Information provided by E. Cheng, "Activation Cross Section Library Comparison Study, Numerical Results," General Atomic Technology, June 1984.
**Information provided by E. Cheng, General Atomic Technology, 1985.

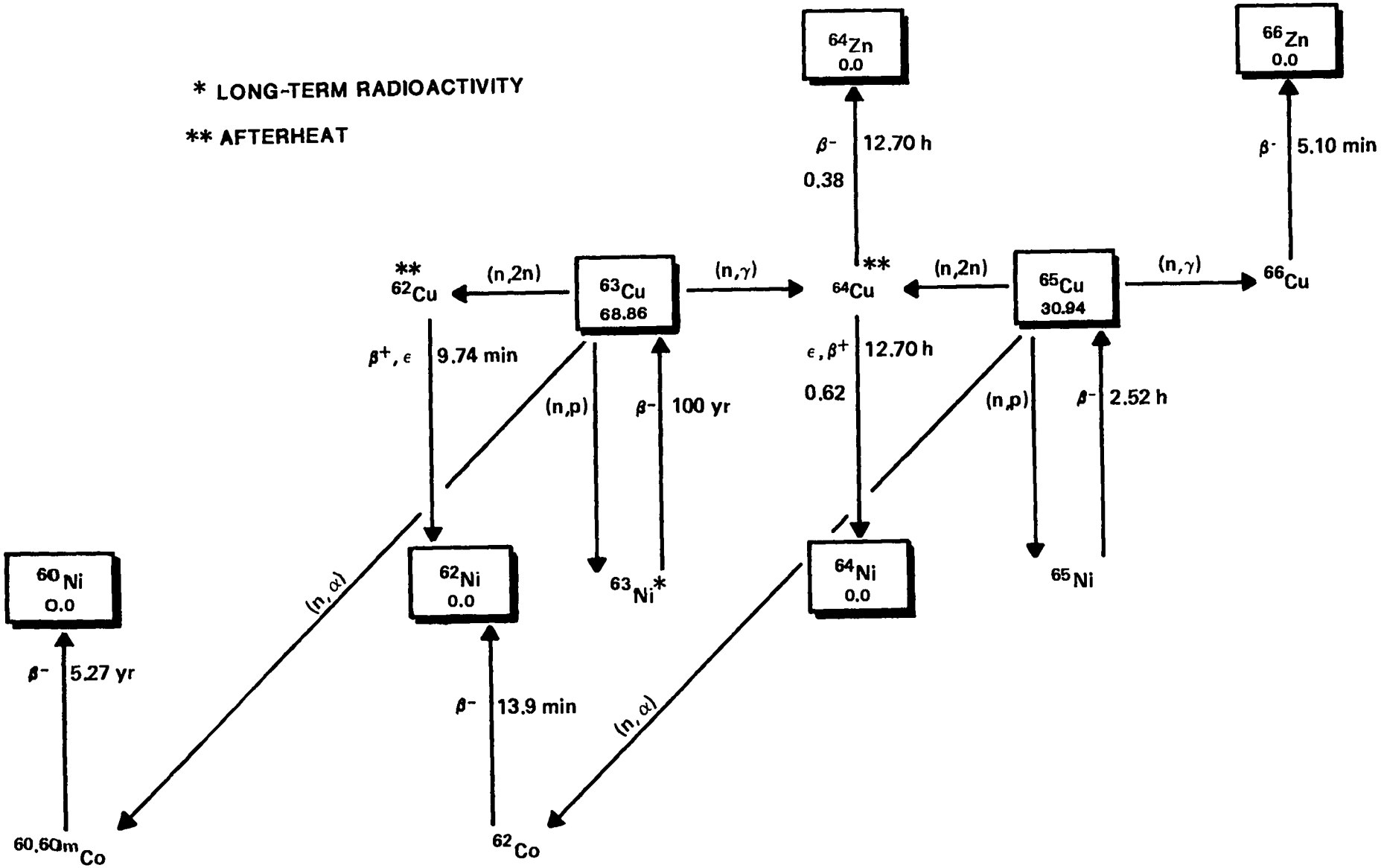

Fig. 5-1A. Activation and decay chains for copper alloy.

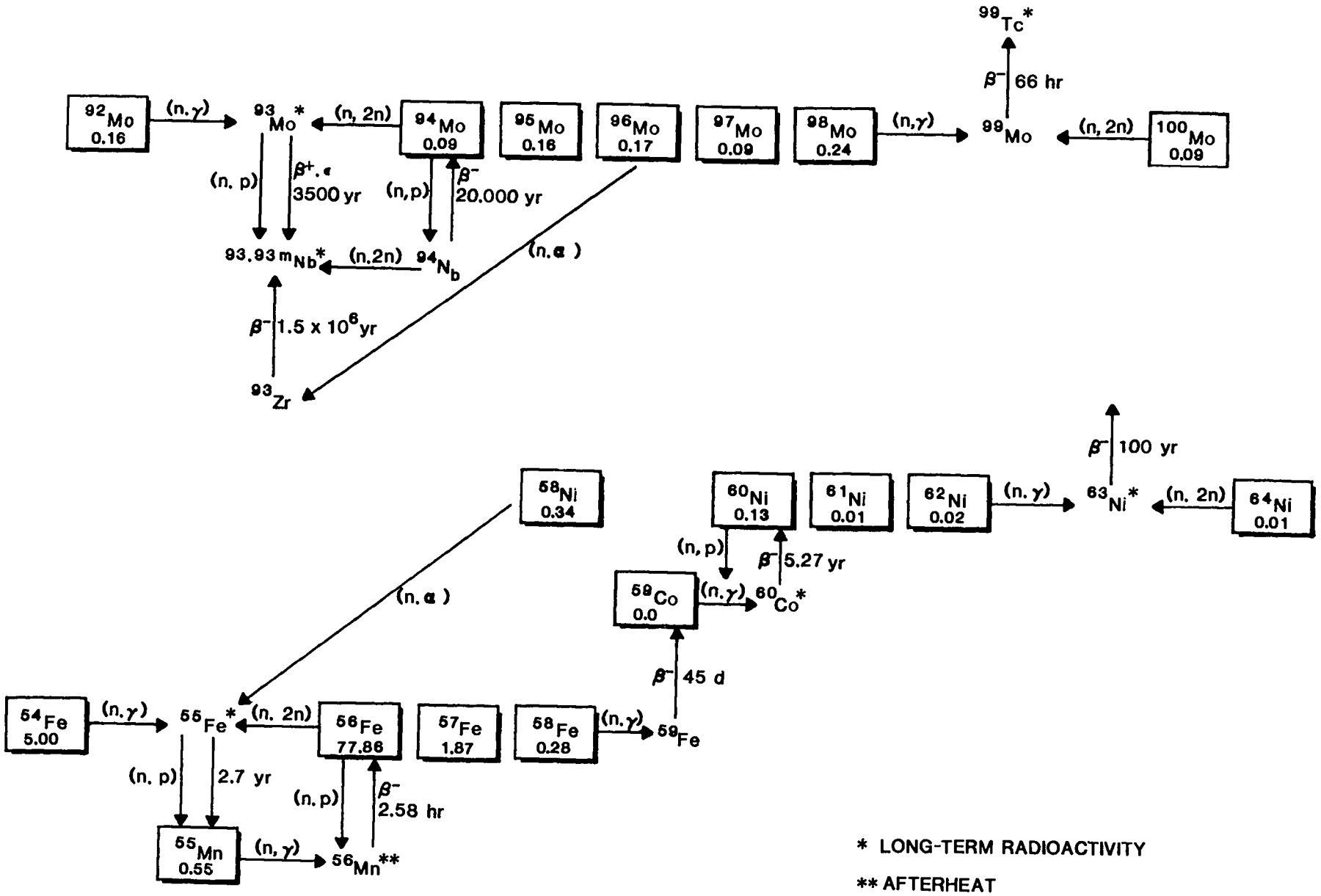

Fig. 5-1B. Activation and decay chains for iron alloy.

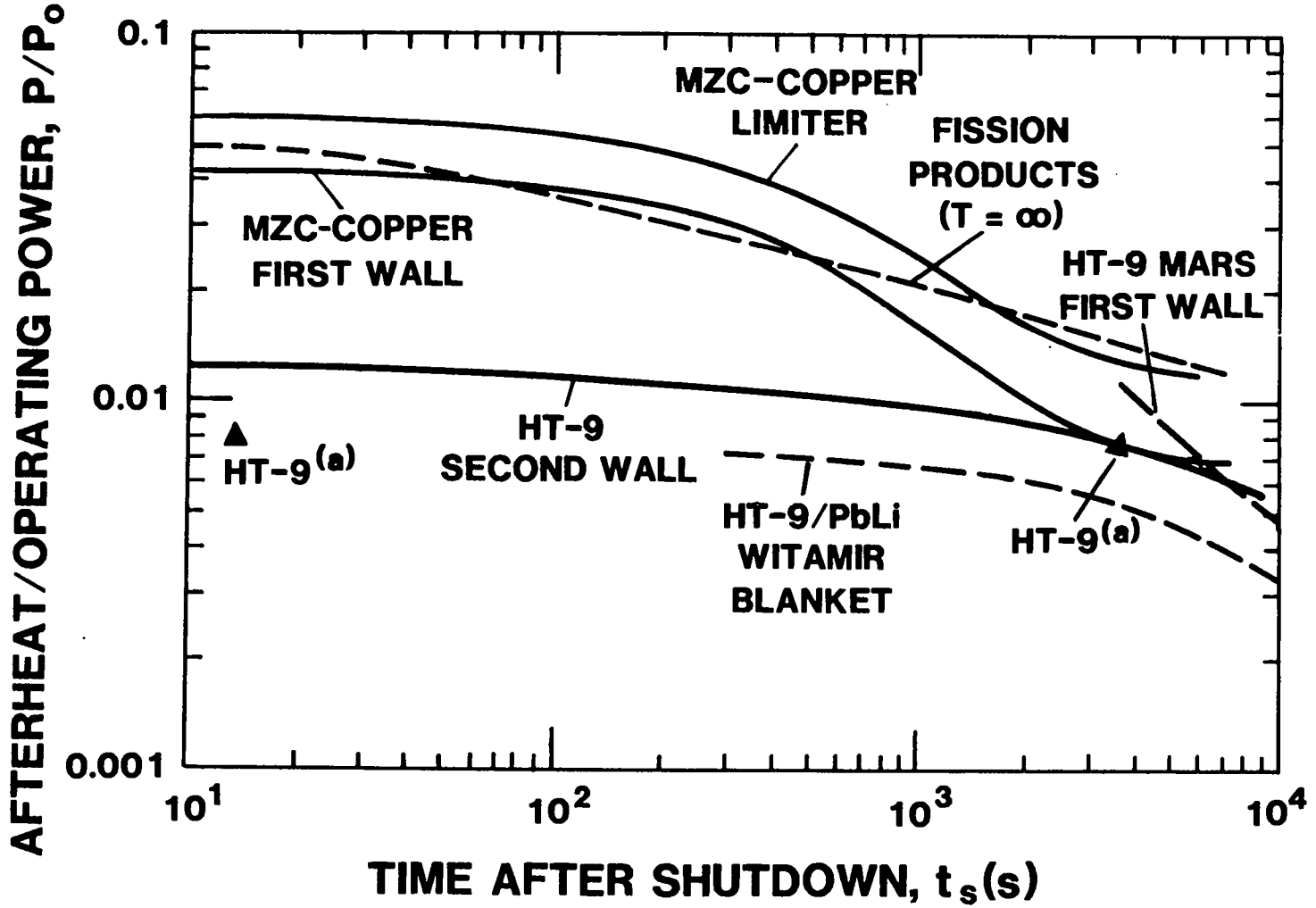

Fig. 5-2. Afterheat in MZC-copper limiter and first wall, HT-9 second wall, thermal fission reactor,[50] the HT-9 first wall in MARS,[2] the HT-9 first wall of the WITAMIR tandem-mirror reactor,[51] and some recent calibrations by E. Cheng at General Atomic [points marked (a)].

The afterheat thermal calculations used the finite-element heat-transfer code, AYER,[49] which solves the general two-dimensional heat-conduction equation and includes transients, in-plane anisotropic conductivity, three-dimensional velocity distributions, and interface thermal-contact resistance. Radiation cooling was added as a time-dependent boundary condition. This adaptation applied the following expression separately to each surface node and as a function of time.

$$q_{12} = \frac{\sigma A_1 (T_1^4 - T_2^4)}{\frac{1 - \varepsilon_1}{\varepsilon_1} + \frac{1}{F_{12}} + \frac{(1 - \varepsilon_2)A_1}{\varepsilon_2 A_2}} , \qquad (1)$$

where σ is the Stefan-Boltzmann constant [$5.67(10)^{-8}$ W/m^2 K^4], A_1 is the limiter area, A_2 is the first-wall area, ε_1 and ε_2 are the respective emissivities, and F_{12} is the view factor or fraction of energy leaving the limiter, which arrives at the first wall. Since the back of the limiter directly faces the first wall, $F_{12} \approx 1.0$, $A_1/A_2 = 1.0$, and the relationship for infinite parallel planes is obtained. For the front of the limiter, $A_1/A_2 = 0.4/0.6$ and, therefore, $F_{12} \approx 0.6$. In all cases considered, $\varepsilon_1 = \varepsilon_2 = \varepsilon$, with a nominal value of $\varepsilon = 0.4$ for copper being used[52]; with initial mechanical surface roughening and subsequent sputtering, $\varepsilon = 0.4$ is regarded as conservative. The HT-9 emissivity under comparable conditions is greater than that of copper (Table 2-II).

A time-dependent algorithm for natural circulation of PbLi was added to simulate the PbLi temperature rise through the inner channel for different PbLi natural-circulation velocities and as a function of time as the afterheat generation decays in the first and second walls. This model is described in Sec. 5.1.3.

Computations were made to determine the temperature response of different FPC regions under a range of LOCA conditions. The cases considered are identified as follows:

1) Loss of coolant to limiter, active water coolant maintained in first wall/second wall, no PbLi coolant flow.

2) Loss of coolant to limiter and first wall/second wall, forced or normal PbLi flow.

3) Loss of coolant to limiter and first wall/second wall, natural circulation of PbLi.

4) Loss of coolant to limiter, natural circulation in blanket, ECS cooling of limiter.

5) Loss of coolant in limiter and first wall/second wall, stagnant PbLi.

6) Loss of coolant in limiter and first wall/second wall, loss of PbLi coolant.

These cases are summarized in Table 5-I. The time variations of the afterheat generation in the limiter, first wall, and second wall were separately taken into account for all afterheat calculations.

5.1.3. Natural-Circulation Model

Natural circulation of the PbLi coolant presents a passive means to remove afterheat if the magnet coils can be rapidly de-energized and the FPC is located at a lower elevation than the steam generator. During normal operation, the bulk of the PbLi pressure drop results from $\vec{v}\times\vec{B}$ interaction in the outboard coolant manifolds. Following plasma shutdown, the magnets can be de-energized (the inductive time of the copper coils is about 10 s, and the stored energy is 1.7 GJ) and a substantial reduction in PbLi pressure drop occurs. Natural-circulation velocities that are comparable to the forced-circulation velocities (with fields present) result. This option is not available to fusion reactors that use superconducting magnets and require days to dissipate much larger amounts of energy in order to avoid coil damage.

Pressure balance under conditions of natural circulation equates the pressure difference resulting from buoyancy forces, ΔP_B, to the hydraulic and magnetic pressure drops, ΔP_F and ΔP_M, respectively. The expression for ΔP_B is

$$\Delta P_B = g\rho\beta H(T_{po} - T_{pi}) \ , \qquad (2)$$

where the difference in elevation of the hot and cold legs is the height of the steam generator, H = 20 m, since the inlet and outlet PbLi manifolds of the

TABLE 5-I

SUMMARY TO LOSS-OF-COOLANT CASES CONSIDERED

CASE	L	FW/SW	B	S
1	LOC	+	LOF	NA
2	LOC	LOC	+	NA
3	LOC	LOC	NC	NA
4	ECS	LOC	NC	NA
5	LOC	LOC	LOF	NA
6	LOC	LOC	LOC	NA

L = Limiter
FW/SW = First wall/second wall
B = Blanket
S = Shield
LOC = Loss of coolant
ECS = Emergency cooling system
LOF = Loss of flow
NC = Natural circulation
NA = Not analyzed
+ = Active coolant flow maintained

torus are at the same nominal elevation (Fig. 4-1). The quantity g is the acceleration of gravity, ρ is PbLi density, β is the thermal expansivity, and other parameters are listed in Table 5-II.

The heat flux through the second wall can be expressed as

$$q_w = \frac{(T_{po} - T_{pi})\rho c_p \dot{Q}_{m\gamma}}{A_{FW}} , \qquad (3)$$

so that the buoyancy pressure drop becomes

TABLE 5-II

PARAMETERS USED FOR NATURAL-CIRCULATION CALCULATION

Parameter	Value
PbLi inlet temperature, T_{pi}(°C)	350.
Blanket power density at full-power, $\dot{Q}_{m\gamma}$(MW/m^3)	200.
Gravity head from FPC to top of steam generator, H(m)	20.
PbLi density, ρ(kg/m^3)	9,400.
PbLi thermal expansivity, β(10^{-4}/K)	1.4
PbLi heat capacity, c_p(J/kg K)	168.
PbLi thermal conductivity, k(W/K m)	16.
Magnetic field causing main pressure drop, B(T)	0[a]
Electrical conductivity of HT-9 channel wall, σ_w(10^6/ohm m)	1.1
Thickness of channel wall, t_w(mm)	5.
PbLi viscosity, μ(kg/m s)	0.0029
Buoyancy coefficient, C_B(kg m^2/s^3)	52,000.
Magnetic coefficient, C_M(kg/m^4 s)	<1.0[a]
Hydraulic coefficient, C_F(kg/m^4 s)	250.
PbLi volumetric flow rate, Q(m^3/s)	7.74 (full power)
Width of first poloidal channel, $w_{\theta 1}$(m)	0.2
Combined first-wall/second-wall thickness, δ(mm)	10.
Effective PbLi flow area, A_p(m^2)	14.0

(a) Field ramped to zero from operating value of ~ 4 T in ~ 10 s. The magnetic pressure-drop parameter increases to 68,000 kg/m^4 s at full field.

$$\Delta P_B = g\rho\beta H \frac{q_w A_{FW}}{\rho c_p \dot{Q}_{m\gamma}} = \frac{C_B}{\dot{Q}_{m\gamma}} \quad , \tag{4}$$

where $C_B \equiv g\beta H q_w A_{FW}/c_p$ is defined as the buoyancy coefficient.

The hydraulic and magnetic-field pressure drops are expressed as

$$\Delta P_H = C_H Q^{1.8} \tag{5A}$$

and

$$\Delta P_M = C_M Q \quad , \tag{5B}$$

where $Q \equiv \rho V$ is the volumetric flow rate. The parameter C_H includes the pressure drop through the PbLi pipes, the blanket, and the steam generator. The parameter C_M is obtained from integrating Eq. (14) in Sec. 2.2.3.1. and is determined primarily by the pressure drop in the inlet and outlet manifolds, PbLi manifolds where the PbLi flow velocity is perpendicular to the magnet field. From Eqs. (4) and (5) and the parameters listed in Table 5-II, it follows that

$$Q(m^3/s) = (C_B/C_H)^{1/2.8} = 41.6\ \eta^{0.36} \qquad \text{(no PFC field)} \tag{6A}$$

or

$$Q(m^2/s) = (C_B/C_M)^{1/2} = 0.13\eta^{1/2} \qquad \text{(PFC at 5 T).} \tag{6B}$$

An expression for the maximum wall temperature averaged over the first-wall and second-wall thickness, δ, is obtained as follows:

$$T_w = T_p + \frac{1}{2}\frac{w_{\theta 1}\delta}{k} Q_w + \frac{w_{\theta 1}\, Q_w}{\ell V (c_p \rho)_p} \quad , \tag{7}$$

where $Q_w(W/m^3)$ is the volumetric heating rate in the composite first-wall/second-wall system, the maximum structural temperature occurs at the exit of the first-wall channel of width $w_{\theta 1}$, conduction resistance is ignored in the structure, the primary thermal resistance from the structure to the PbLi coolant is thermal conduction, and k, c_p and ρ are given in Table 5-II. Inserting

Table 5-II values into Eq. (7) and substituting $Q = VA_p$ for V, where A_p is the nominal PbLi flow area in the blanket, Eq. (7) becomes

$$T_w = T_p + 469\ I_w(P/P_o)\ (1 + 0.035/Q) \quad , \tag{8}$$

where it has been assumed $Q_w \simeq 10I_w(P/P_o)$, and P/P_o is the afterheat power fraction (Fig. 5-2).

5.2. Afterheat Results

Figure 5-3 shows the combined results for several cases of limiter temperature following shutdown with no coolant in the limiter, radiation cooling to the first wall, and conduction along the limiter manifolds/headers. The curve for Case 1 peaks at 1,210°C. The limiter response under Case 1 conditions corresponds to a first wall cooled by 230°C pressurized water. The PbLi forced-circulation case (Case 2) has a higher first-wall temperature and would lie between the two curves shown on Fig. 5-3.

The initial limiter temperature rise depicted on Fig. 5-3 reflects the time constant of the order $\dot{Q}/c_p\rho = 7.5$ K/s. For all cases, the peak in temperature occurs between 5 and 7 minutes after shutdown, and the slow decrease in temperature is associated with the afterheat decay. The limiter remains above the copper melting temperature for about 15 minutes. The lower curve in Fig. 5-3 represents Case 4 (ECS applied to limiter) and is described below. Both cases shown on Fig. 5-3 assume a copper emissivity of 0.4.

The limiter would not melt for Case 4 (ECS) under any first-wall/second-wall cooling condition. For Case 1 conditions (1,210°C peak), the ECS would be activated upon reduction of the limiter coolant pressure below a critical level or when the limiter temperature increased to 800°C, either condition occurring within a minute following shutdown. The ECS water would be provided by a series of pressurized accumulator tanks (Sec. 5.3.), which quickly would decrease the structural temperature to below 200°C, at which point the ECS would be turned off to conserve water. For the Case 4 conditions shown in Fig. 5-3, the ECS would be pulsed on for intervals of about 2 minutes, with increasingly longer intervals (average about 5 minutes) as the afterheat decays. After ~ 30 minutes, the ECS could be completely turned off, but in practice it would probably be continued until the uncooled limiter temperature dropped below 800°C

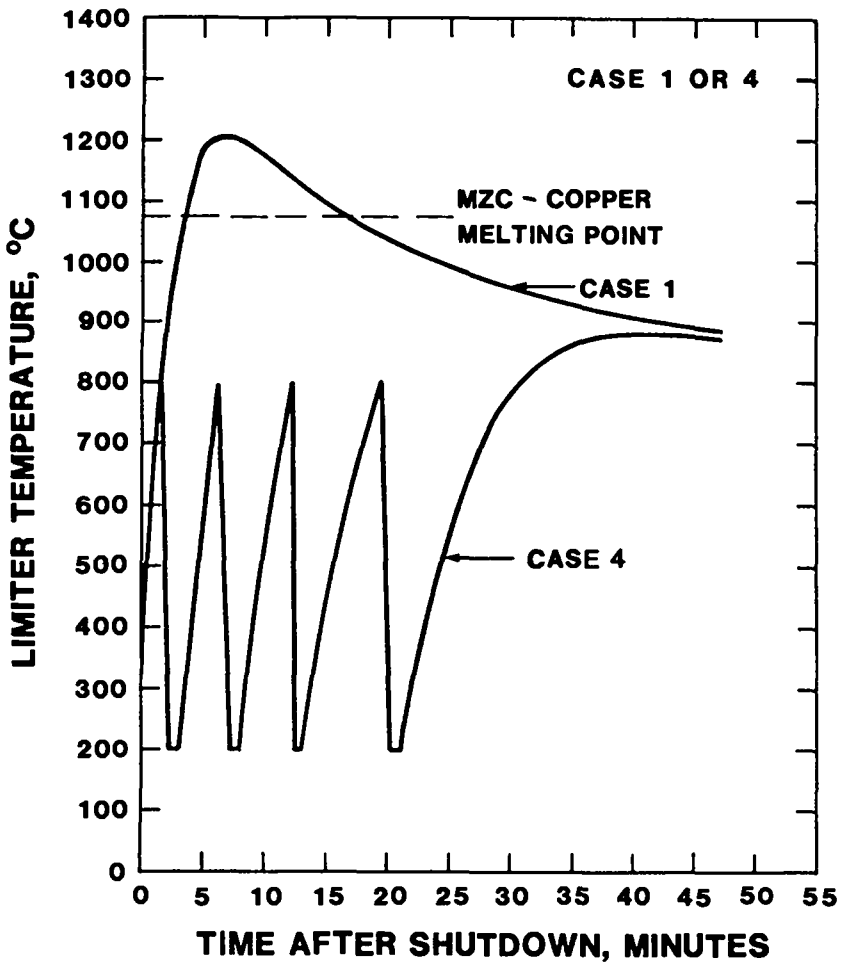

Fig. 5-3. Limiter temperature response to an LOC for Case 1 (Table 5-I, no active cooling) and Case 4 (ECS to limiter only, natural circulation of PbLi).

(within ~ 70 minutes). Reliability will decrease for this pulsed mode of operation, however, and throttling the flow may present a better solution at the cost of requiring more ECS water and larger accumulator tanks. Two 2000-m^3 pressurized accumulator tanks and an unpressurized 2000-m^3 water storage tank are required, with the latter supplying water to the limiters in event of a large loss-of-coolant accident. Pumps would transfer the water from the reactor sump (i.e., bottom of vacuum vessel) and return it to the water storage tank after passing through a residual-heat-rejection system, if necessary.

Figure 5-4 shows the maximum limiter temperature as a function of full-power neutron first-wall loading for the limiter loss of coolant with either water coolant in the first wall/second wall or PbLi natural circulation in the

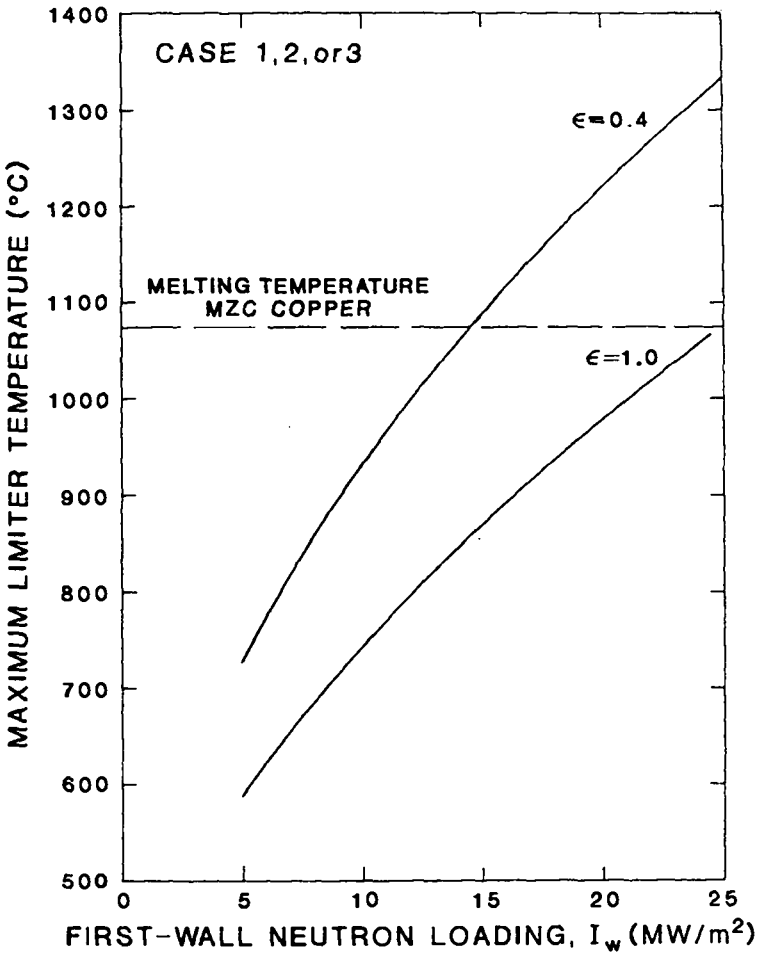

Fig. 5-4. Maximum limiter temperature (Case 1, 2, or 3) as a function of first-wall neutron loading for two values of emissivity.

blanket (Cases 1, 2, or 3, Table 5-I). For the CRFPR(20) first-wall neutron loading of 19.5 MW/m^2, the maximum limiter temperature is ~ 1,210°C. The limiter does not melt when the neutron first-wall loading falls below 15 MW/m^2 for Cases 1, 2, or 3. These cases assume copper emissivities of 0.4; for an emissivity of $\varepsilon \simeq 1.0$ (e.g., thick graphite armor on copper limiter surface), the limiter does not melt even for the full-power design case of I_w = 19.5 MW/m^2.

Figure 5-5 shows the first-wall/second-wall temperatures for a limiter LOCA described by Case 1 with active water coolant maintained to the first wall/second wall. The copper first-wall surface, the HT-9 second-wall surface, and the PbLi temperatures decrease within one minute to the first-wall coolant temperature (~ 265°C). The water temperature in this case would have to be held

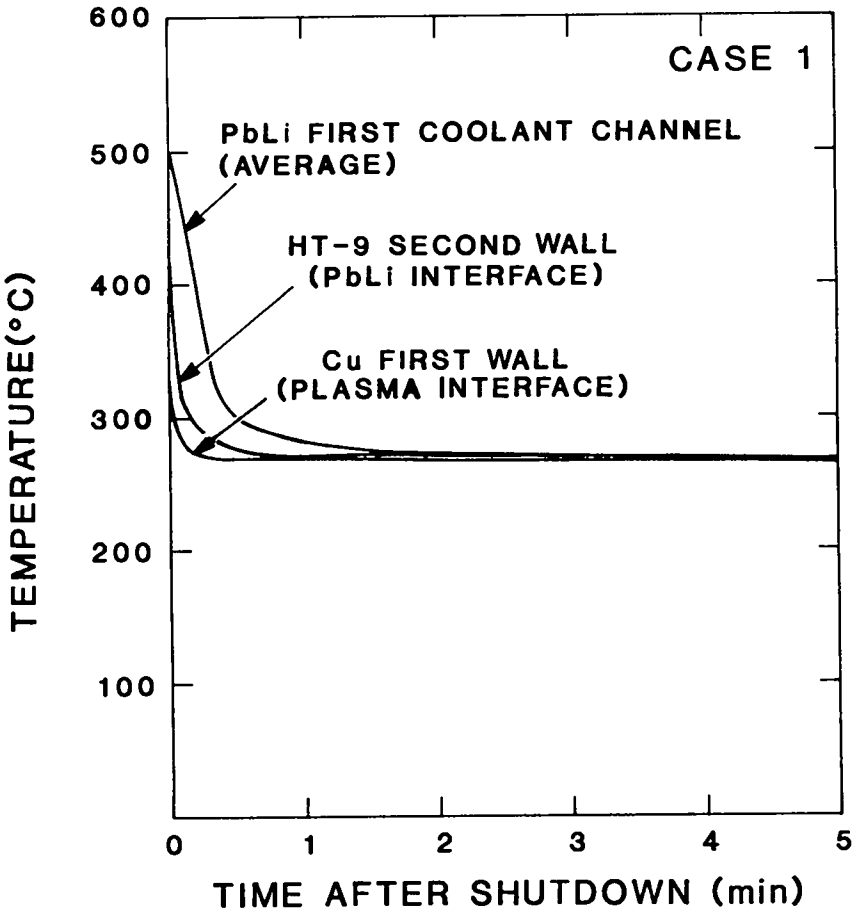

Fig. 5-5. First-wall/second-wall afterheat temperature for PbLi LOF and limiter LOCA. Active water cooling is provided to the first wall/second wall, PbLi LOF in blanket, and radiation input from limiter (Case 1).

at about the melting temperature of PbLi (235°C). Figure 5-6 shows the first-wall/second-wall temperatures for a Case 2 limiter LOCA (forced circulation of PbLi, but no first-wall/second-wall coolant). The first-wall surface temperature drops in three minutes to ~ 500°C after peaking at a temperature of 580°C.

Figure 5-7 depicts conditions for Case 3 (natural circulation of PbLi, no water coolant to the limiter or first wall/second wall). The temperatures shown are those near the exit of the inner PbLi coolant channel. The temperature of the PbLi entering the channel was taken as 350°C, and the natural circulation flow velocity is 0.1 m/s. An analysis of natural circulation, using the model described in Sec. 5.1.3., is given below.

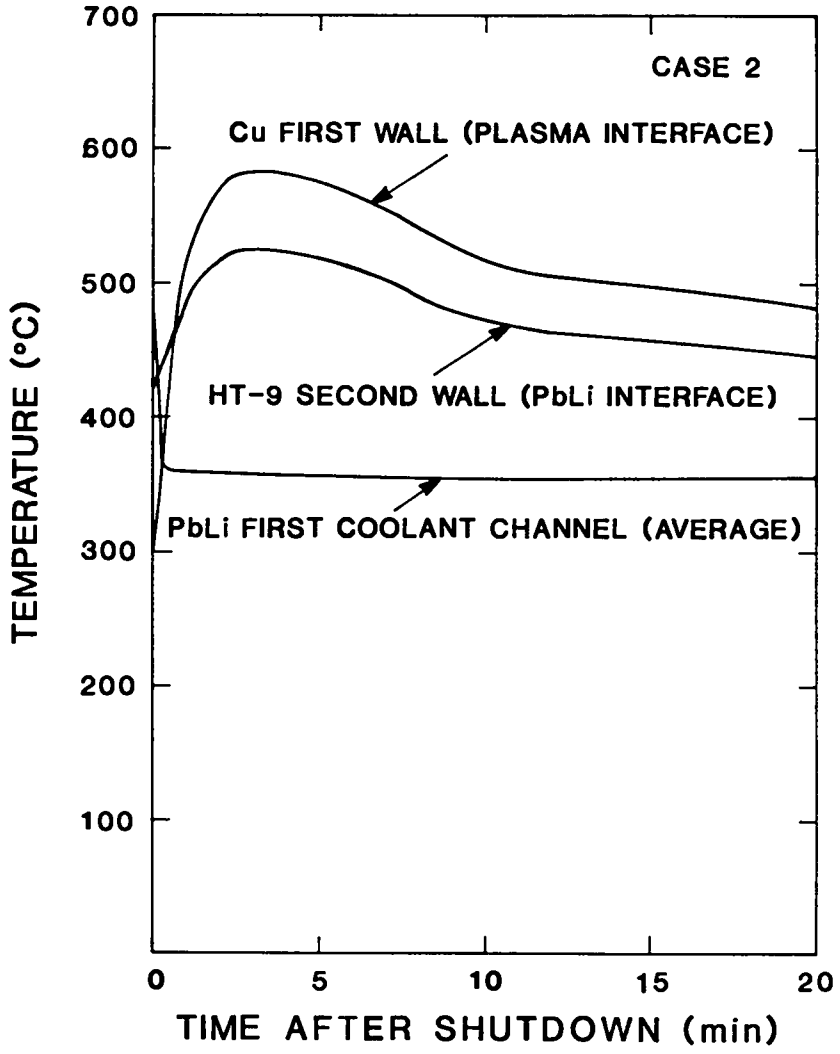

Fig. 5-6. First-wall/second-wall afterheat temperature for first-wall/second-wall and limiter LOCA with forced circulation of PbLi. No water coolant in first wall/second wall and radiation input from limiter (Case 2).

The average PbLi exit temperature in the first channel for the natural circulation case (Case 3) decreases from 500°C to 400°C in approximately one minute because of the large decrease in the PbLi heat generation. The PbLi average temperature increases shown in Fig. 5-7 after the initial decrease are caused by the increased heat load from the first and second walls. The PbLi exit temperature decreases subsequently as the afterheat continues to decrease. The copper surface of the first wall increases in about three minutes to a peak of 630°C because of a loss of water coolant in the first wall and an increase in the radiation input from the limiter. The HT-9 second-wall surface temperature in contact with the PbLi peaks at 595°C and remains above the design (corrosion) limit of 500°C for ~ 10 minutes.

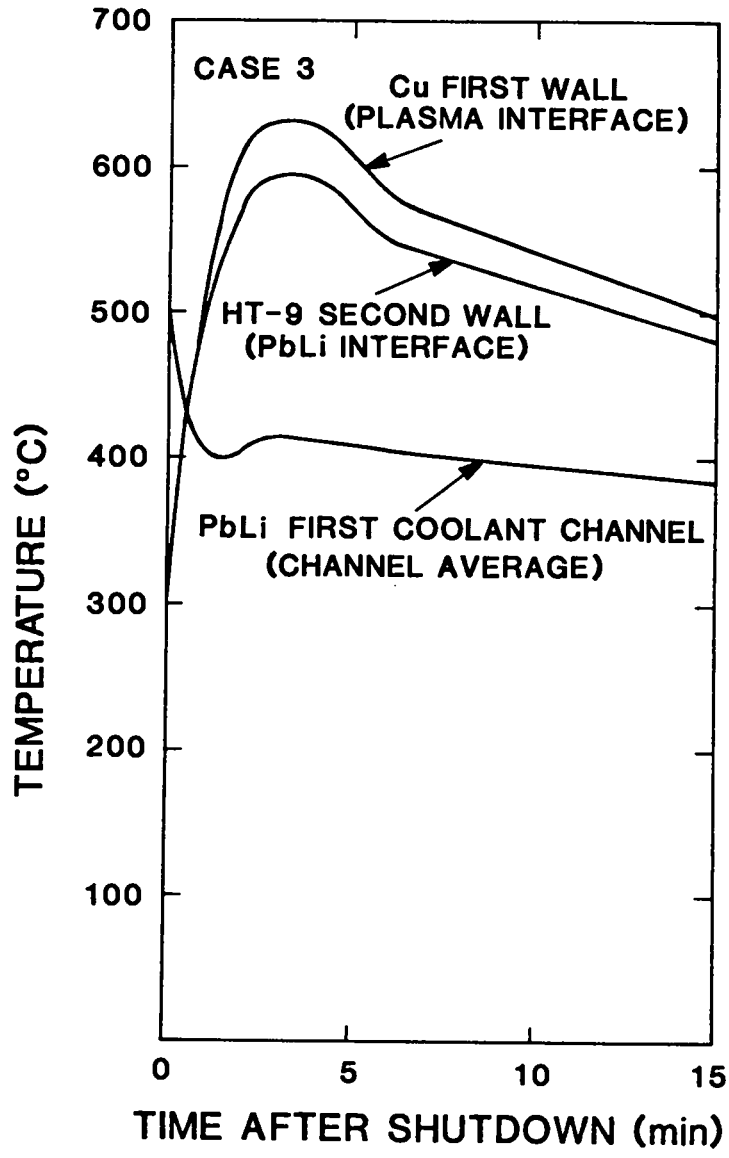

Fig. 5-7. First-wall/second-wall temperature for a first-wall/second-wall and limiter LOCA with PbLi natural circulation (Case 3).

Figure 5-8 shows the dependence of natural-circulation PbLi flow rate, $Q(m^3/s)$, and maximum first-wall/second-wall temperature on the first-wall neutron loading relative to the $I_w = 19.5\ MW/m^2$ base case. This figure indicates a maximum wall temperature of 580°C for $(P/P_o)(I_w/19.5) = 0.025$ and no magnetic field. As shown in Fig. 5-7, T_w remains at ~ 500°C for only 11 minutes, which presents no problem with respect to corrosion. With the coils fully energized, the $I_w = 19.5\ MW/m^2$ and $(P/P_o)(I_w/19.5) = 0.025$ case results in a maximum wall temperature of 970°C. In order to reduce the maximum wall

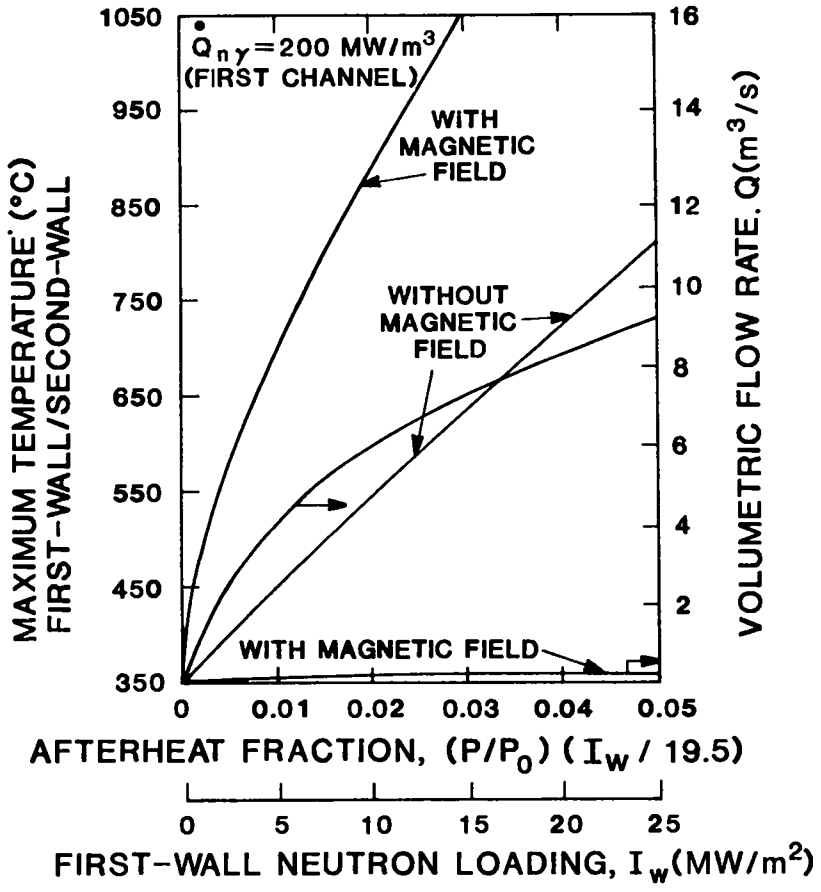

Fig. 5-8. Variation of PbLi natural circulation parameters as functions of afterheat fraction of full power ($I_w \simeq 19.5$ MW/m^2).

temperature in the presence of the magnetic field to the value reported without the magnetic field, I_w would have to be reduced to 7 MW/m^2.

The PbLi natural-circulation results are encouraging since they indicate that both the copper-alloy first wall and the HT-9 second wall will remain far below the melting point with complete loss of water coolant. The high-pressure coolant water under conditions of a first-wall/second-wall loss of coolant would undergo a rapid decompression, the blowdown occurring in ~ 10 s. Hence, the blowdown timescale is too short to reduce the peak structural temperatures, since the latter occurs in ~ 3 minutes.

The worst afterheat case would occur in the unlikely event that all the water coolant and PbLi are lost simultaneously. The temperatures of the first wall/second wall and limiter are shown in Fig. 5-9 as functions of time. The

copper-alloy first wall (1,320°C) and limiter (1,470°C) would both melt, but the HT-9 second wall (1,350°C) would not. These results were obtained by iterating between three separate AYER[49] calculations for the limiter, the first wall/second wall, and a blanket model, the latter treating the blanket structural layers as radiatively coupled to the shield and toroidal-field coils. The dominant heat-transfer mechanism is radiation, where emissivities of 0.4 and 0.5 were used, respectively, for MZC copper and HT-9. Appropriate cylindrical geometrical radiation factors were used for the first-wall/second-wall and blanket regions. The temperatures for the limiter and first wall exceed the MZC-copper melting temperature at times between three and four minutes after shutdown, as is shown in Fig. 5-9. Assuming that the molten copper flows under gravity and accumulates in the bottom of the torus formed by the second wall, the poloidal angle subtended by the molten copper is 0.8 radians (45.8°C), with a maximum thickness of 56 mm. The copper in this configuration would reach a maximum average temperature of ~ 1,650°C in approximately twelve minutes

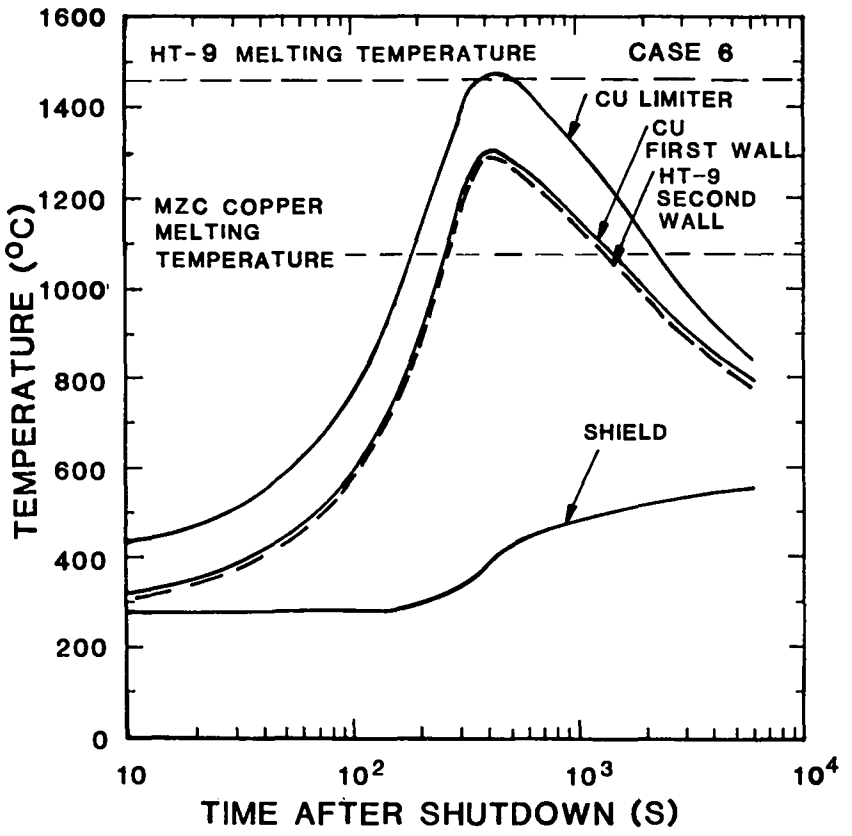

Fig. 5-9. Time dependence of first and second walls for a complete loss of all water and PbLi coolants.

TABLE 5-III

IMPACT OF A RANGE OF LOSS-OF-FLOW (LOF) AND LOSS-OF-COOLANT (LOC) SCENARIOS FOR THE CRFPR(20) DESIGN

CASE	L	FW/SW	B	S	RESPONSE
1	LOC	+	LOF	NA	Limiter temperature peaks above melting point for ~ 15 minutes, returns to ~ 0.5 homologous temperature in 90 minutes.
2	LOC	LOC	+	NA	First-wall excursion 300 → 600°C in 3 minutes, levels to slow decrease below 500°C in 10-12 minutes.
3	LOC	LOC	NC	NA	Limiter temperature peaks above melting point, returns to ~ 0.5 homologous temperature in 90 minutes.
4	ECS	LOC	NC	NA	Four cooling pulses over 20 minutes to hold limiter below 800°C, subsequent excursion limited to below melting; 70 minutes of subsequent pulsed cooling passively holds limiter temperature to below 800 °C.
5	LOC	LOC	LOF	NA	The copper alloy limiter temperature (1220°C) peaks above the melting temperature. The Cu first wall (1065°C) and the HT-9 second wall (1065°C) are both below the respective melting temperatures. Slumping of the limiters into the bottom of the second-wall torus would not propagate melting of this wall.
6	LOC	LOC	LOC	NA	The copper-alloy limiter temperature (1,470°C) and first-wall temperature (1,320°C) both peak above melting temperature. The HT-9 second wall temperature peaks (1,300°C) below the melting temperature. Slumping into the bottom of the second-wall torus could propagate melting of this wall unless copper volume is reduced by ~ 2. A propagating melt would transfer the copper to the PbLi drain system.

following shutdown. The HT-9 second wall supporting the copper-alloy melt, however, itself melts eight minutes following shutdown, and the molten mixture would flow into the PbLi drain system (Fig. 4-4). At 1,650°C the copper vapor pressure is 130 Pa. The radioactivity volatization rate under these conditions is expected to be less than the oxidation rate (steam may be present), and both

are expected to be low. The efficiency filters in the stacks would prevent any significant radioactivity escape in the form of gases or particulates.

If the limiter is designed so that only the surface exposed to the core plasma is MZC-copper, the rest being HT-9, the total volume of the molten copper would be reduced by a factor of two (0.26 m^3). The molten copper would under these conditions subtend a poloidal angle of 0.64 radians (36.6°C) with a maximum thickness of 36 mm. For this case, the HT-9 would not melt. Release of radioactivity in any event would occur also from the oxidation of the activated HT-9 structure. For instance, release of MoO_3 is expected[2] to occur for temperatures above 1000°C; the molten copper and HT-9 structure would drop below 1000°C in about 3000 seconds.

On the basis of those estimates, an ECS is required in event of the complete loss of coolant, the ECS being used after the appropriate manifold isolation check valves are closed (within one minute). This case also involves a possible PbLi-water reaction in the containment sump. However, recent experiments[35] have shown the PbLi-water reaction to be acceptably benign, and blanket concepts where PbLi and water are separated by only one wall are now being proposed for the NET blanket design.[36]

Table 5-III summarizes key results for the various loss-of-coolant scenarios applied to the CRFPR(20) design. Other than the active short-term (1-2 hr) ECS requirement of the limiter, the afterheat problem for the CRFPR(20) appears to be capable of passive control if natural circulation of the PbLi coolant can be established and maintained. The impact of active ECS for the limiter is estimated in the following section.

5.3. Emergency Cooling System

5.3.1. General Description

The ECS techniques discussed here have been proven in fission power systems and are somewhat simpler when applied to fusion power systems because the time requirements may be less stringent, the borated-water system and associated high pressure injection system are not required, and the total core radioactivity, though comparable in magnitude on a Ci/Wt basis, is less volatile in the fusion case. For a high-power-density reactor, where water is used as one of the primary coolants, an ECS is an economic and simple option to maintain high power density without substantially increasing the capital cost and COE.

The specific ECS described in the following section adds ~ 2% (~ 22.6 M$) to the total plant direct cost. The ECS costs include the accumulators (20$/kg, 12.1 M$), the residual heat exchangers (27$/kWt, 3.5 M$), pumps (0.5 M$), recirculation sump (0.9 M$), water storage tank (2.0 M$), and added building volume (300 $/m^3, 3.6 M$). The added building costs represent ~ 16% of the total ECS cost. Notwithstanding, an ECS cost of about 2.0% of total direct cost represents a small perturbation on the COE for the protection provided by a passive cooling system.

Two kinds of ECSs are used here to protect the fusion system: a) accumulator tanks are provided for low-pressure large-break (large-flow) accidents; and b) an emergency high-pressure coolant system is used for high-pressure small-break (small-flow) accidents. These ECSs are connected to the cold legs of the water-coolant systems. In any case, the ECS is designed to cool the FPC as well as to provide additional shutdown capability following initiation of the following accident conditions:

- a pipe break or spurious valve lifting in the coolant system which causes a discharge larger than that which can be made up by the normal makeup system, up to and including the instantaneous circumferential rupture of the largest pipe in the coolant system,
- a steam pipe break or spurious valve lifting in the steam system, up to and including the instantaneous circumferential rupture of the largest pipe in the steam system,
- a steam-generator tube rupture.

The ECS is designed to meet a minimum required level of functional performance by using passive accumulators for any of the above-listed occurrences, assuming a single failure. The accumulators are passive, thereby avoiding reliability problems with emergency diesel power systems.

5.3.2. ECS Description for CRFPR(20) Design

The principal mechanical components of the ECS that provide FPC cooling immediately following a loss-of-coolant accident are the accumulators, the injection pumps, the residual-heat-removal pumps, the water-storage tank, and the associated valves and piping. The ECS subsystem layout is shown in Fig. 5-10. In order to increase ECS reliability, the pressurized-water manifold

structure depicted in Figs. 4-3 and 4-4 is proposed. Both inlet and outlet manifolds are split. These sections are connected by the two main inlet and outlet water/steam-generator pipes. The first-wall/second-wall inlet and outlet manifolds are similarly split and are similarly connected to the main inlet and outlet lines. If a main coolant pipe breaks, therefore, valves can isolate the disrupted line, and the limiter and first wall/second wall can still be cooled at half the normal water-coolant flow rate. Similarly, if a half-manifold section breaks, this section can be isolated, and the other three manifold sections can provide water coolant under normal conditions. Also, if one valve remains open after a main pipe break, three half-manifolds could provide 50% of the normal coolant rate.

The principles of ECS operation apply equally to the horizontal- and vertical-replacement schemes (Figs. 4-1 and 4-2). In both cases, valves in the external water manifolds close to and on either side of the water headers isolate manifold and header sections in the event of a loss of pressure in the water-coolant system. Since the respective inlet headers and outlet headers are in close proximity for the horizontal FPC replacement case, only one manifold valve is required between headers in the short separation leg.

The water-coolant system would be depressurized and voided of coolant rapidly in event of a large pipe rupture, and a high flow rate of emergency coolant is required to provide cooling to the limiters. As shown in Fig. 5-8, the first-wall temperature does not exceed 630°C with naturally circulating PbLi. In the unlikely event that both main water coolant lines are broken, the emergency coolant would be directed around the break by valving to the limiters. The high coolant flow is provided as shown in Fig. 5-10 by passive cold-leg accumulators, the safety injection pumps, and the residual heat-removal pumps discharging into the cold legs of the FPC water-coolant manifolds.

Emergency cooling is provided in event of small ruptures primarily by the safety injection pumps (Fig. 5-10). Small ruptures have an equivalent area of $< 0.1\ m^2$ and do not immediately depressurize the water-coolant system below the accumulator discharge pressure. The safety injection pumps are also available on the longer time scale to take suction from the water-storage tank and deliver to the cold legs of the water-coolant system. The safety injection pumps begin to deliver water to the water-coolant system after the pressure has fallen below the pump-shutoff head.

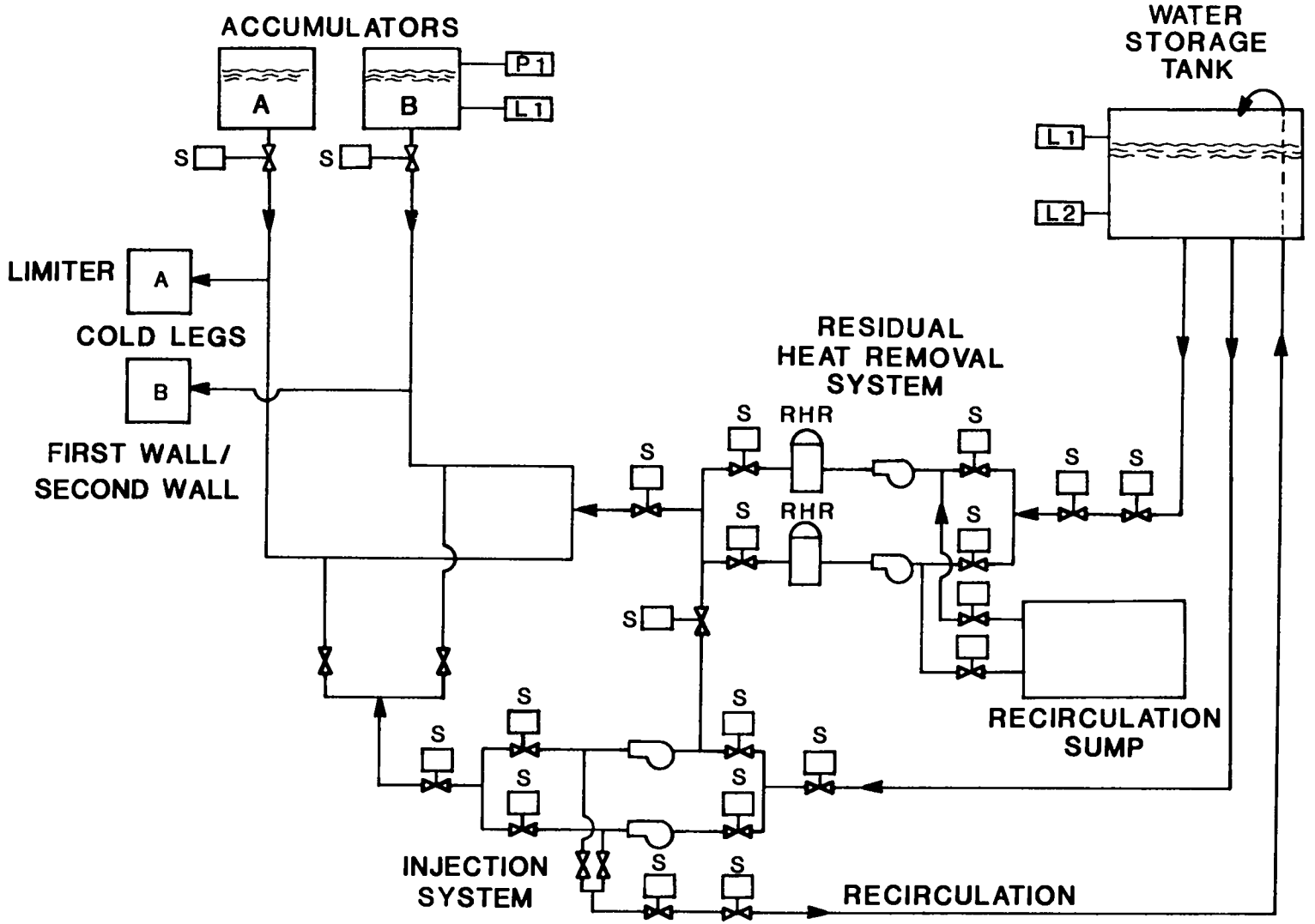

Fig. 5-10. Emergency cooling system (ECS) applied to CRFPR(20) design. The principal mechanical components of the ECS are accumulators, safety injection pumps, refueling water storage tank, and the associated valves and piping. The "S" valves indicate motor-operated values that must function on receiving a safety injection signal. The "P" and "L" designations indicate pressure and level sensors, respectively.

For large water-coolant-system ruptures, the accumulators serve to prevent melting of the limiter. An example was shown in Fig. 5-3, where accumulator coolant flow turned on for a duration of two minutes at five minute intervals within one minute following loss of limiter coolant prevents limiter melting. The water from the large rupture enters a sump for subsequent pumping to the water-storage tank to allow intermittent operation of the system.

5.3.3. ECS Component Description

This section briefly describes key ECS components identified on Fig. 5-10. Typical ECS component parameters are listed in Table 5-IV. These components must be designed to withstand appropriate seismic loadings.

5.3.3.1. Accumulators

The low pressure accumulators are 2000-m^3 pressure vessels filled with water and pressurized to 600 psi with nitrogen gas. During normal operation each accumulator is isolated from the water-coolant system by two check valves operated in series. Should the water-coolant-system pressure fall below the accumulator pressure, the check valves open, and water is forced into the water-coolant system. One accumulator is attached to each inlet coolant manifold (Figs. 4-3 and 4-4) of the water-coolant system. Mechanical operation of the swing-disc check valves is the only action required to open the injection path from the accumulators to the FPC by way of the cold leg.

Connections are provided for remotely adjusting the water level in each accumulator during normal plant operation. The accumulator water level may be adjusted either by draining to or pumping from the water-storage tank using the positive-displacement charging pump.

5.3.3.2. Pumps

The residual heat-removal pumps and injection pumps deliver water to the ECS inlet when the water coolant system pressure is reduced below the respective heads for pump shutoff. The residual heat-removal pump also delivers water from a sump when the water-coolant pressure falls below the pump shutoff head. Each residual heat-removal pump is a single-stage, vertical-position, centrifugal pump. The injection pumps are multistage, centrifugal pumps.

TABLE 5-IV

SAMPLE ECS COMPONENT PARAMETERS

Component	Parameter	Value
Low-pressure Accumulators	Number	2
	Operating temperature (°C)	50
	Operating pressure (psig)	600
	Total volume (m^3)	2,000
Safety injection pumps	Number	2
	Design temperature (°C)	100
	Design flow rate (m^3/s)	0.05
	Discharge pressure (psig)	1,500
Residual-heat-removal Pumps	Number	2
	Design temperature (°C)	100
	Design flow rate (m^3/s)	0.04
	Discharge press (psig)	600
Residual-heat-removal Exchangers	Number	2

5.3.3.3. Residual Heat Exchangers

The residual heat exchangers would only be used in the event of a complete loss of coolant to remove heat from the discharged reactor cooling water. The residual heat exchangers are conventional shell and U-tube type, and during emergency operation the reactor coolant water flows through the shell side while sump water flows through the tube side.

5.4. Long-Term Radioactivity

5.4.1. Neutronics Model Results

The neutronic procedures used to determine the radioactivity buildup and decay are essentially the same as described in Sec. 5.1.1. for afterheat. Radioactivity calculations were performed for all FPC regions, including the magnets and shield. A one-year irradiation was assumed, and the activities were computed during a 1000-yr decay period. Blanket activity inventories were computed both in curies (Ci) and as the toxicity-weighted ingestion biological hazard potential (BHP). The ingestion BHP is the ratio of actual to maximum permissible concentration in water and has units of m^3 of H_2O required for dilution to appropriate standards.

The total FPC activation after one full-power-year irradiation at I_w = 19.5 MW/m^2 is 7.62 GCi or 2.28 Ci/Wt. The total activity in Ci/Wt versus time is given in Fig. 5-11 along with the curves for MARS[2] (data included blanket and shield only) and STARFIRE.[1,53] The activation condition for MARS was two years of irradiation at I_w = 4.3 MW/m^2 and that for STARFIRE was five full-power years at 3.6 MW/m^2; the CRFPR has accumulated 19.5 MWyr/m^2, STARFIRE 21 MWyr/m^2, and MARS 8.6 MWyr/m^2 exposure. The HT-9 activation in CRFPR(20) dominates the total activation for the period one hour to 30 years after shutdown. Before one hour and in the period 30 to 1000 years the MZC copper activation in the limiter and first wall dominates.

5.4.2. Disposal Issues

The shallow burial issue has recently been addressed in federal regulation[54] 10CFR61. This regulation lists the maximum allowable concentration of each nuclide in a given class of solid waste. The actual concentrations are divided by the allowable concentrations, and the ratios are summed over all nuclides, as given below:

$$SBI = \Sigma \frac{\text{Specific Activity(i)}}{\text{Limit(i)}} . \qquad (9)$$

The resulting sum is termed the Shallow Burial Index or SBI and must be less than 1.0 before burial is allowed without dilution in that class. For an SBI between 0.1 and 1.0, the waste is termed Class C intruder waste.[54]

The potential waste disposal of various regions of the FPC is given in Tables 5-VA, 5-VB, and 5-VC. Most of the activated metallic structure is HT-9, and this can be disposed by shallow land burial. In order to meet the 10CFR61 requirements for Class C waste, however, the blanket would have to be filled with concrete and buried after 30 years. The isotopes which cause the greatest activation problems are ^{94}Nb, ^{63}Ni, ^{93}Mo, and ^{99}Tc. The isotope ^{93m}Nb is not included in Table 5-V because it is not a gamma-ray emitter. An inexplicably conservative limit for ^{94}Nb is noted in Table 1 of 10CFR61 (^{94}Nb in activated metal cannot exceed 0.2 Ci/m^3 for Class C waste). That the ^{94}Nb limit is conservative was initially pointed out by Blink,[43] who then used the procedure of calculating the amount of water required to dilute the activated (and

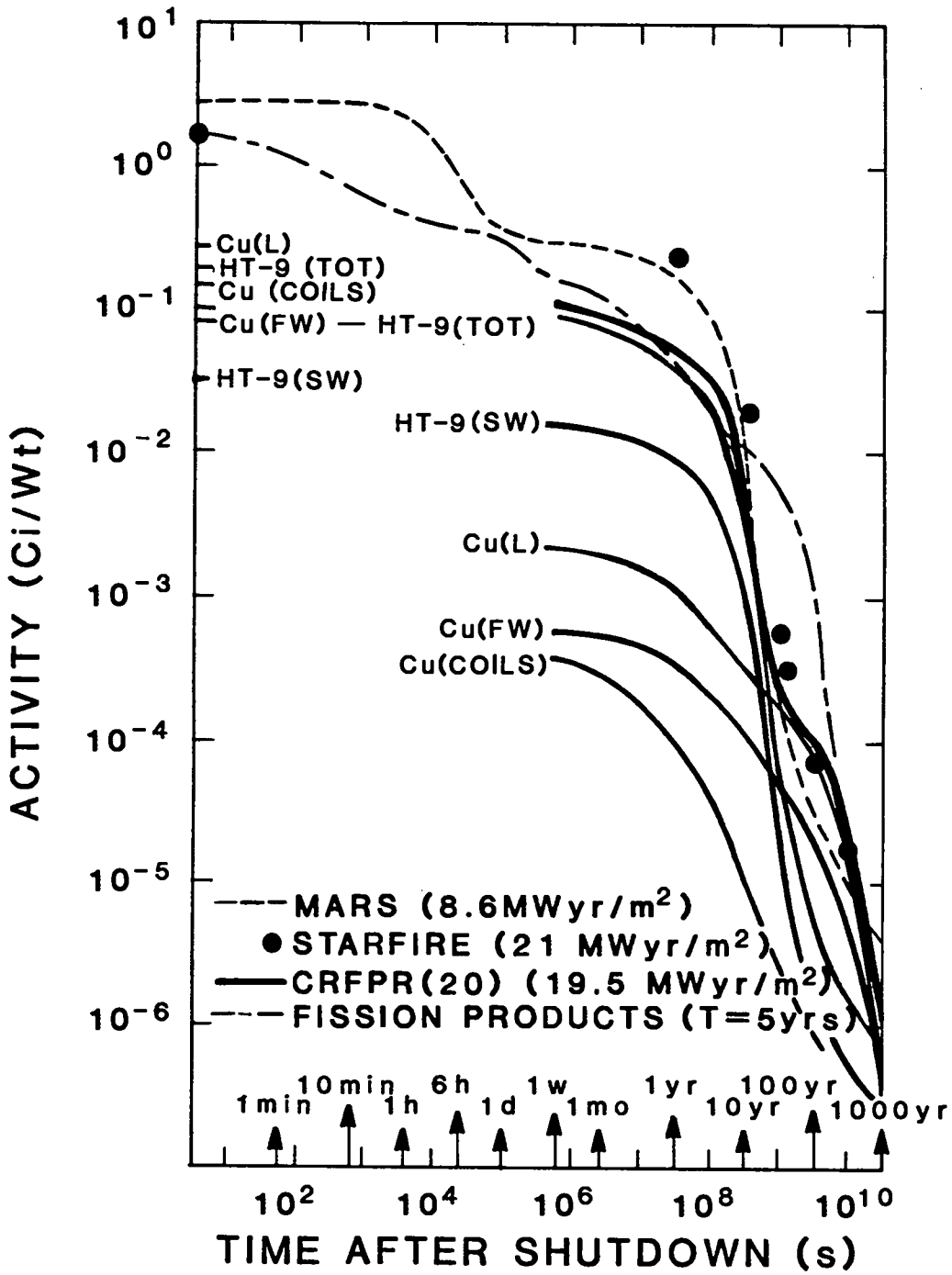

Fig. 5-11. Normalized radioactivity as a function of time after shutdown for the CRFPR(20) design. Data reported for STARFIRE[1] and MARS[2,53] are also included for comparison.

TABLE 5-VA

0 YEARS AFTER SHUTDOWN (Ci/m^3)
DISPOSAL OF VARIOUS FPC REGIONS FOLLOWING A ONE-YEAR IRRADIATION, EXCEPT FOR TFC AND PFC

	Cu Limiter	Cu First Wall	Cu/PCASS/MgO TFC(10 FPY)[a]	Cu/PCASS/MgO PFC(10 FPY)[a]	Class C Near-Surface Burial Limits
Volume(m^3)	0.32	0.20	10.6	110.3	
Fe55	24.1	7.835	$11.(10)^4$	$4.18(10)^4$	700
FE60	0.33	0.112	$5(10)^{-6}$	$7(10)^{-7}$	700
Co60	$6.18(10)^{-6}$	$2.26(10)^6$	$8.04(10)^3$	$2.44(10)^3$	700
Ni59	0.2	0.08	39.5	15.9	220
Ni63	$2.87(10)^6$	$1.0(10)^6$	$10.4(10)^3$	$3.67(10)^3$	7,000
Sr90	18.51	6.49	0.011	0.004	7,000
Zr93	0.31	0.11	0.006	0.003	700
Nb94	0.019	0.007	0.003	0.001	0.2
Mo93	0.004	0.001	41.6	15.7	220
Tc99	$2(10)^{-7}$	$5(10)^{-8}$	0.94	0.35	3.0

	HT-9 Second Wall	HT-9 First-Wall/ Second-Wall Manifold	HT-9 Second-Wall Manifold	HT-9 Total Average	Class C Near-Surface Burial Limits
Volume(m^3)	0.35	0.79	0.17	6.46	
Mn53	4.0	0.316	1.36	0.49	700
Fe55	$5.55(10)^7$	$9.55(10)^6$	$2.47(10)^6$	$7.5(10)^5$	700
Fe60	0.002	0.026	0.01	0.006	700
Co60	$5.51(10)^4$	$5.701(10)^4$	$3.057(10)^4$	$8.9(10)^3$	700
Ni59	18.9	14.4	30.5	5.54	220
Ni63	$2.679(10)^3$	$4.645(10)^3$	$6.56(10)^3$	$1.9(10)^3$	7,000
Sr90	0.264	0.011	0.004	0.011	7,000
Zr93	0.016	0.002	0.007	0.002	700
Nb94	4.2	0.45	1.66	0.58	0.2
Mo93	404.6	104.9	296.8	91.6	220
Tc99	8.0	1.5	5.2	2.2	3.0
V49	$5.04(10)^4$	$4.152(10)^3$	$1.715(10)^4$	6.9	700

(a)FPY = full power year.

TABLE 5-VB

40 YEARS AFTER SHUTDOWN (Ci/m^3)
DISPOSAL OF VARIOUS FPC REGIONS FOLLOWING A ONE-YEAR IRRADIATION, EXCEPT FOR TFC AND PFC

	Cu Limiter	Cu First Wall	Cu/PCASS/MgO TFC(10 FPY)	Cu/PCASS/MgO PFC(10 FPY)	Class C Near-Surface Burial Limits
Volume(m^3)	0.32	0.20	10.6	110.3	
Fe55	0.002	0.0005	0.747	0.284	700
Fe60	0.329	0.112	$5(10)^{-6}$	$7(10)^{-7}$	700
Co60	$5.34(10)^4$	$1.98(10)^4$	7.06	2.14	700
Ni59	0.2	0.08	3.95	1.60	220
Ni63	$21.64(10)^5$	$7.63(10)^5$	$7.90(10)^3$	$2.80(10)^3$	7,000
Sr90	7.77	2.76	0.005	0.002	7,000
Zr93	0.31	0.11	0.006	0.003	700
Nb94	0.018	0.007	0.003	0.001	0.2
Mo93	0.004	0.001	41.3	15.7	220
Tc99	$2(10)^{-7}$	$5(10)^{-8}$	0.94	0.35	3.0

	HT-9 Second Wall	HT-9 First-Wall/ Second-Wall Manifold	HT-9 Second-Wall Manifold	HT-9 Average	Class C Near-Surface Burial Limits
Volume(m^3)	0.35	0.79	0.17	6.46	
Mn53	4.0	0.316	1.36	0.46	700
Fe55	$3.77(10)^3$	$0.65(10)^3$	$1.67(10)^3$	510.0	700
Fe60	0.002	0.026	0.01	0.006	700
Co60	484.0	500.6	531.9	155.2	700
Ni59	18.9	14.4	30.5	5.54	220
Ni63	$2.043(10)^3$	$3.541(10)^3$	$5.009(10)^3$	1473	7,000
Sr90	0.112	0.005	0.002	0.005	7,000
Zr93	0.016	0.002	0.007	0.002	700
Nb94	4.2	0.45	1.66	0.58	0.2
Mo93	401.2	104.0	294.4	90.5	220
Tc99	8.0	1.5	5.2	2.2	3.0

TABLE 5-VC

100 YEARS AFTER SHUTDOWN (Ci/m^3)
DISPOSAL OF VARIOUS FPC REGIONS FOLLOWING A ONE-YEAR IRRADIATION, EXCEPT FOR TFC AND PFC

	Cu Limiter	Cu First Wall	Cu/PCASS/NgO TFC(10 FPY)	Cu/PCASS/MgO PFC(10 FPY)	Class C Near-Surface Burial Limits
Volume(m^3)	0.32	0.20	10.6	110.3	
Fe55	$3(10)^{-7}$	$2(10)^{-8}$	$8(10)^{-8}$	$4(10)^{-8}$	700
Fe60	0.33	0.112	$5(10)^{-6}$	$7(10)^{-7}$	700
Co60	20.4	7.6	0.0027	0.001	700
Ni59	0.20	0.08	3.94	0.628	220
Ni63	$13.78(10)^3$	$4.83(10)^5$	$5.03(10)^3$	$0.84(10)^3$	7,000
Sr90	1.86	0.66	0.005	0.002	7,000
Zr93	0.320	0.112	0.006	0.005	700
Nb94	0.018	0.007	0.002	0.001	0.2
Mo93	0.004	0.001	40.7	15.4	220
Tc99	$2(10)^{-7}$	$5(10)^{-8}$	0.94	0.35	3.0

	HT-9 Second Wall	HT-9 First-Wall/ Second-Wall Manifold	HT-9 Second-Wall Manifold	HT-9 Average	Class C Near-Surface Burial Limits
Volume(m^3)	0.35	0.79	0.17	6.46	
Mn53	4.0	0.316	1.36	0.46	700
Fe55	$4(10)^{-4}$	$7(10)^{-4}$	$2(10)^{-4}$	0.0003	700
Fe60	0.002	0.026	0.01	0.006	700
Co60	0.18	0.21	0.209	0.061	700
Ni59	18.9	14.4	30.5	5.54	220
Ni63	$1.3(10)^3$	$2.25(10)^3$	$3.18(10)^3$	937	7,000
Sr90	0.027	0.001	0.0045	0.001	7,000
Zr93	0.016	0.002	0.0067	0.002	700
Nb94	4.2	0.45	1.66	0.58	0.2
Mo93	398.4	102.6	290.3	89.5	220
Tc99	8.0	1.5	5.2	2.2	3.0

dissolved steel) to drinking standards (ingestion BHP) and then compared the dilution volume to the water volume required to dilute clean unactivated steel to drinking standards based on standards set by the Environmental Protection Agency. This procedure indicates that the 10CRF61 limits may be a factor of 2,500 too conservative for ^{94}Nb. Considering the average blanket ^{94}Nb, however, this isotope can be reduced to the Class C limit by the addition of concrete (HT-9 structure represents 10% of blanket volume) to the uncompacted blanket structure.

A more severe waste disposal problem is ^{63}Ni activation [^{63}Cu(n,p)^{63}Ni, 100-yr half-life, Figs. 5-1 and 5-11] in the MZC-copper limiter and first wall. Both the limiter and first wall would require dilution factors of 300 and 100, respectively. The total volume of the copper limiters and the first wall is 0.52 m^3, however, and even for deep geological burial should not present a significant annual expense for these volumes (masses).

The TFCs and PFCs are sufficiently removed and shielded by the 0.7-m-thick blanket and shield to allow shallow land burial without dilution. The coil activity reported in Table 5-V is based on 10 full-power years at I_w = 19.5 MW/m^2, although the service life may extend beyond this period.

In summary, the blanket would meet the Class C waste disposal requirement if filled with concrete and buried after 30 years. The associated burial requirement for the blanket and shield alone amounts to 19,800 Ci/yr or 263 tonnes/yr (including concrete). The TFCs and PFCs directly meet the Class C level requirement and for a 10-year life give an average burial requirement of ~ 30,000 Ci/yr or ~ 89 tonnes/yr. The small volumes of the limiter and the first wall may require deep geologic burial since a dilution factor of 100-300 is required. The cost of deep geologic burial versus Class C burial with high dilution must be carefully weighed. In any event, the combined first-wall and limiter burial requirement amounts to ~ 0.4(10)^5 Ci/yr or 4.7 tonnes/yr. The PbLi does not represent a serious waste disposal problem because of removal of Po^{210} along with the tritium at a rate of 8-30 kg/yr. Finally, isotropic tailoring of Mo would largely remove ^{93}Mo and ^{94}Nb problems from HT-9 and appears both feasible and achievable at a relatively low cost.[55]

6. COST TRADEOFFS AND UPDATES

The cost database and models used in the CRFPR study have evolved from those first used to define the compact reactor approach.[56] An improved understanding of key reactor subsystems, better resolved design detail, and developing insights evolved from more comprehensive studies have led to updates of the CRFPR costing procedure first summarized in Table III-IV of Ref. 56 and the design-basis cost estimate given in Ref. 10. This section collects all costing modifications made to date and gives a cost reassessment on the basis of this updated model. The costing model is described in Appendix B. Recent revisions of the costing model are summarized in Sec. 6.1. The parametric systems model is briefly reviewed in Sec. 6.2., and the results of tradeoff and sensitivity studies using this model are described and compared in Sec. 6.3. The analyses given in Sec. 6.3. form the basis for recommendations for future work given in Sec. 8.

6.1. Modifications to Cost Model and Database

The basic costing model follows the approach originally suggested in Ref. 57, modified by more recent detailed design studies,[1,2] adopted by Ref. 56 (Table III-IV), used in the Ref. 10 CRFPR(20) framework study, subsequently modified, and described in Appendix B. These changes reflect improved design resolution and are summarized below.

- Increase standoff between first-wall radius and TFC bore from 0.60 m to 0.775 m.
- Decrease normal-coil smear density from 8.0 tonne/m^3 to 7.3 tonne/m^3, consistent with 70% Cu, 10% PCASS, 10% H_2O, and 10% MgO(80% dense).
- Replace treatment of a smear density for the blanket, shield, and vacuum plenum with a drained PbLi enclosure of 5 v/o and 7.75 tonne/m^3 density.
- Separately account for cost of limiter and associated coolant manifolds.
- Replace smear-density treatment of the shield and vacuum plenum with a 90% stainless steel (7.8 tonne/m^3) and 10 v/o water shield.
- A scaling of the vacuum system cost calibrated with the STARFIRE plasma chamber volume[1] yields a trivial cost. Instead, a vacuum system cost is scaled from STARFIRE fusion power (DT throughout), and a separate cost for the vacuum chamber as a unit mass is included.

- A fixed volume of $1.55(10)^5$ m^3 is added to the variable FPC enclosure volume [$4\ (R_T + r_s + 9)^2(12r_s)$] to give an irreducible baseline for the reactor building volume, where R_T is the major radius and r_s is the minor radius out to and including the PFCs.

- To the variable PbLi coolant/breeder mass contained in the blanket (~ 860 tonnes for the base case) are added 9% (~ 75 tonne) for ducts and a fixed inventory (~ 4,525 tonnes) for the primary loop (including main FPC manifolds).

- The PbLi and pressurized-water main-heat transport loops are separately costed in proportion to the power handled by each.

- A number of minor changes and additions have been incorporated into the cost code.

  - Simultaneously display constant-dollar and then-current-dollar modes using updated cost escalation factors but retaining a 1980 base.

  - Include explicit (though negligible) deuterium fuel cost.

  - Report Direct (Accounts 20-26), Base (Direct plus Accounts 91-93), and Total (Base plus interest and escalation during construction) Costs.

  - Include separate architectural costs with Reactor Building cost, Turbine Building cost, and Energy-Storage Building cost accounts.

  - Include primary-loop PbLi cost under Special Materials cost (Account 26).

  - Account separately for first-wall, limiter, blanket, shield, and structural costs.

  - Add cost for ECRH plasma-breakdown system.

  - Introduce separate charges for impurity-control and magnet-cooling systems.

  - Use a Turbine Building cost of 33.5 M$(1980), which is intermediate between STARFIRE[1] and MARS[2].

  - Use a coil unit cost of 40 $/kg [$2.92(10)^5$ $/m^3$ for a smear density of 7.3 tonne/m^3].

  - Scale costs for electrical structures, wiring containers, power control, and wiring with total electrical power output.

6.2. Parametric Systems Model

The parametric model originally reported in Ref. 56 has been generalized in Ref. 10 by allowing consideration of arbitrary plasma confinement times in search of minimum-COE, resistive-coil RFP reactors. Figure 6-1 depicts this

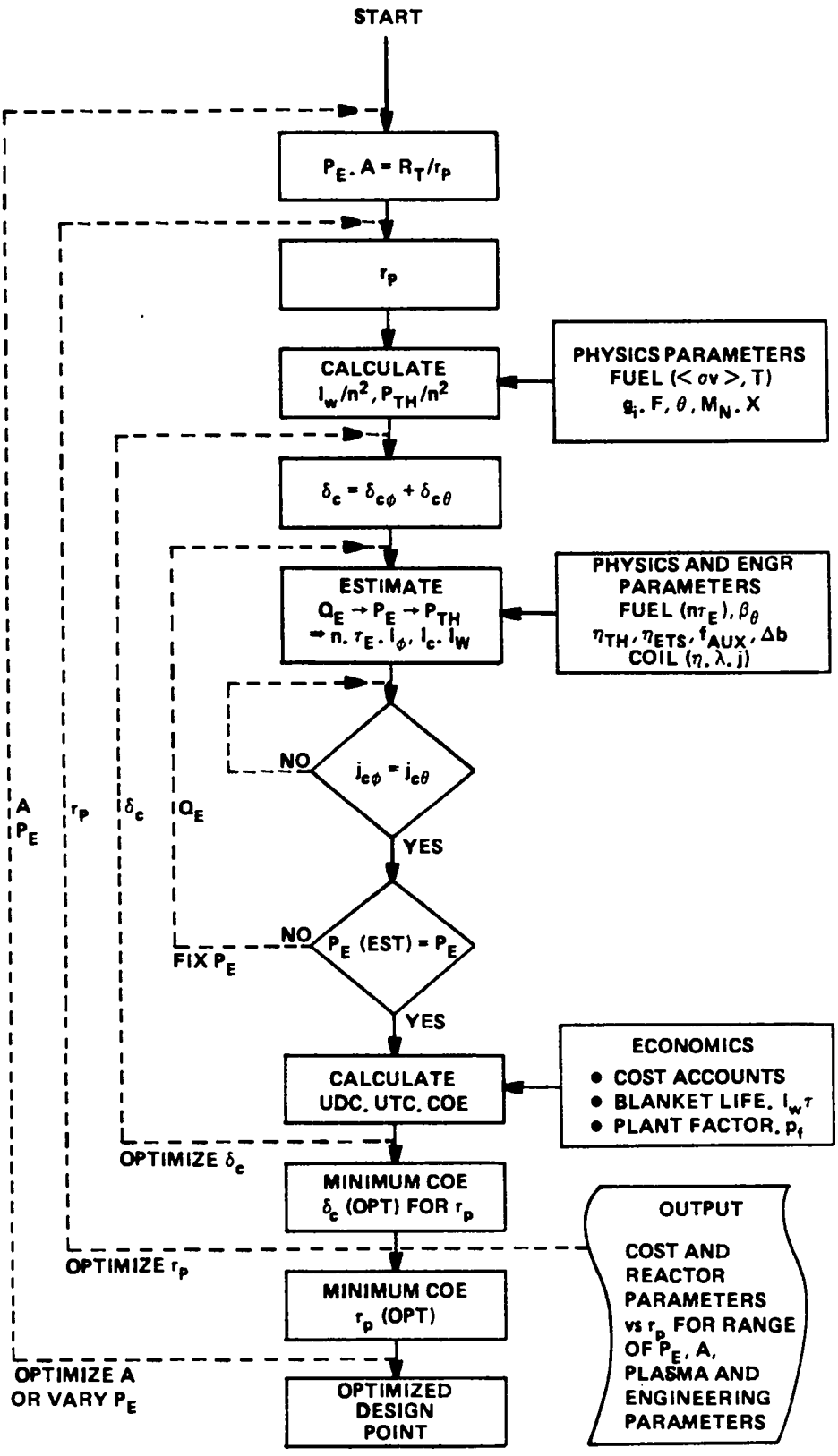

Fig. 6-1. Logic diagram for the parametric systems model used to assess economic sensitivity of the CRFPR.

model in terms of a logic diagram; a simplified geometry and engineering energy balance is depicted in Fig. 6-2. Table 6-I lists both fixed and varied parameters used to assess cost sensitivities. The parametrics systems model identifies optimal reactor parameters in a set of nested search loops centered on a convergence operation for the engineering Q-value, $Q_E = 1/\varepsilon$, and the specified net electric power, P_E, where ε is the recirculating power fraction. For a given total (TFC plus PFC) coil thickness, $\delta_c = \delta_{c\phi} + \delta_{c\theta}$, this inner iteration searches for the value of Q_E that yields the specified P_E as the split between the TFC and PFC geometry varies, subject to the constraints of equal (but unspecified) coil current densities and the matching of fixed engineering and physics parameters. The value of δ_c that produces a minimum-COE design for an otherwise fixed geometry, including plasma minor radius, r_p, is first determined after convergence of the set (Q_E, P_{TH}) for a given P_E. The outer-loop optimum is then determined as a function of r_p, which shows a higher-order (lower) COE minimum. The plasma radius is used as a display variable. The outermost loops then vary the plasma aspect ratio, $A = R_T/r_p$, in search of an even lower minimum-COE system. These fully-cost-optimized CRFPR design points are then examined as a function of P_E and the physics, engineering, and economic input variables listed both on Fig. 6-1 and Table 6-I. The results of this analysis serve as a starting point for the conceptual engineering design of a minimum-COE reactor.

6.3. CRFPR Cost Tradeoffs and Design-Point(s) Reassessment

6.3.1 Single-FPC Results

The first set of tradeoff calculations varied the plasma aspect ratio, A, for the P_E = 1000-MWe(net) design point in order to demonstrate the relative insensitivity of the minimum-COE design point to changes in aspect ratio. Figure 6-3 shows that for all intents and purposes the COE for these cost-optimized designs is independent of A. Subsequent sensitivity studies, therefore, fix A at the base-case value of 5.5, which reflects an increase from 5.35 used in Ref. 10; this increase reflects the thicker blanket used in this follow-on study. The cost tradeoff associated both with off-optimum and lower-P_E systems is displayed in Fig. 6-4. The general behavior depicted in Fig: 6-4 is described as follows:

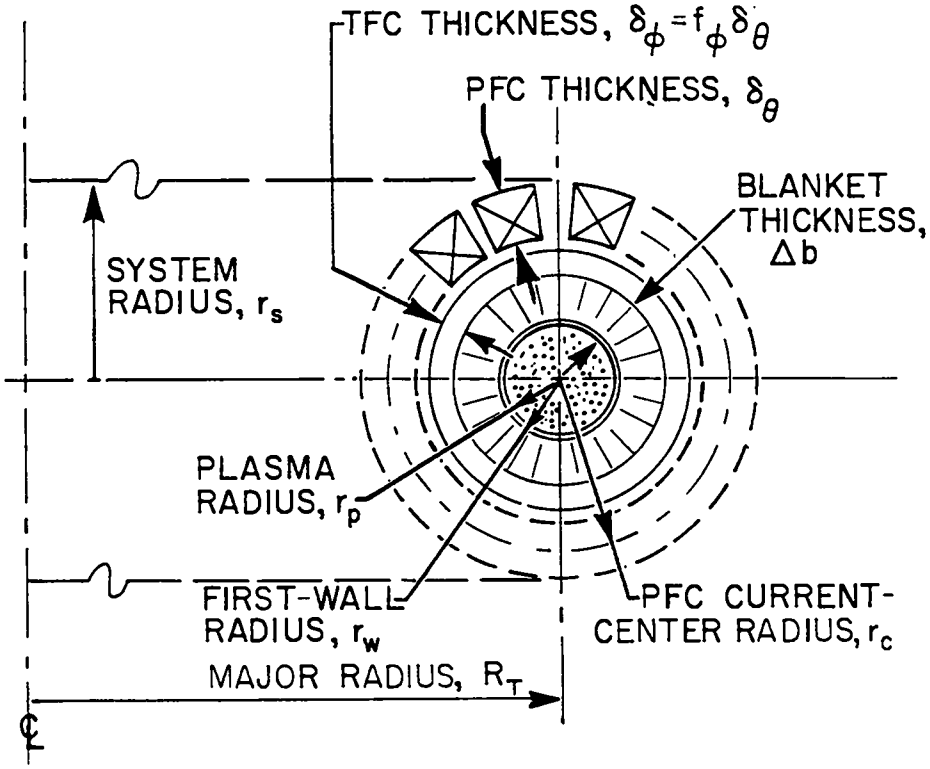

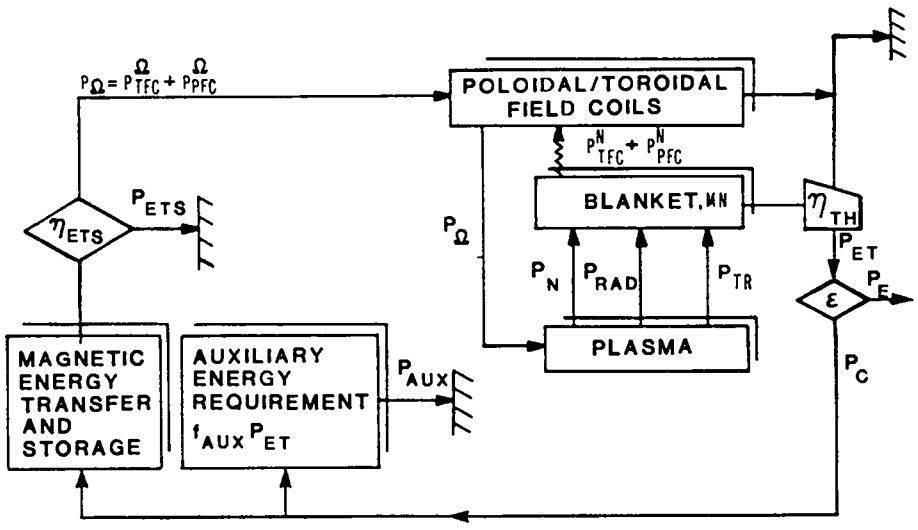

Fig. 6-2. Geometry and engineering energy balance used in the parametric systems model of CRFPR.

TABLE 6-I

LIST OF FIXED AND VARIED PARAMETERS USED IN COST SENSITIVITY STUDY

PLASMA PARAMETERS	VALUE(BASE CASE)
Minor plasma radius, r_p(m)	Varied (0.71)
Major plasma radius, R_T(m)	Varied (3.90)
Plasma aspect ratio, $A = R_T/r_p$	Varied (5.50)
Plasma density, $n(10^{20}/m^3)$	Varied (6.55)
Plasma temperature, T(keV)	$10[T(r) \propto J_o(\mu r)]$
Profile factors, g_i	BFM(MBFM)
Ignition parameter, $n\tau_E(10^{20} s/m^2)$	1.60(1.54)
Pinch parameter, Θ	1.45(1.55)
Reversal parameter, F	-0.2(-0.12)
Plasma/wall radius ratio, $x = r_p/r_w$	0.95
Poloidal beta, β_θ	0.20(0.23)
ENGINEERING PARAMETERS	
Thermal-conversion efficiency, η_{TH}	0.35
Blanket energy multiplication, M_N	1.30
Blanket/shield thickness, Δb(m)	0.775
Energy transfer and storage efficiency, η_{ETS}	1.0[a]
Auxiliary power fraction, f_{AUX}	0.07
Coil parameters	
• electrical resistivity, $\eta(10^{-8}$ ohm m)	1.8
• conductor filing fraction, λ_c	0.7
Net electrical power, P_E(MWe)	Varied (1000.)
ECONOMIC PARAMETERS[b]	
Return on investment (%/yr)	15
Operating cost (%/yr)	2
First-wall/blanket life, $I_w\tau$(MWyr/m^2)	15
Plant factor, $p_f = (365 - \tau_u - \tau_s)/365$	≥0.76
• unscheduled, τ_u(days/yr	60
• scheduled, τ_s(days/yr)	
> 1 replacement/yr	$28p_fI_w/(I_w\tau)$
< 1 replacement/yr	28
• unit costs ($/kg, $/m^3)	Appendix A

[a] Inferred long-pulsed or steady-state operation.

[b] Based primarily on the guidelines given in Ref. 57 and modified by subsequent large reactor studies.[1,2] All costs are referenced to 1980 dollars.

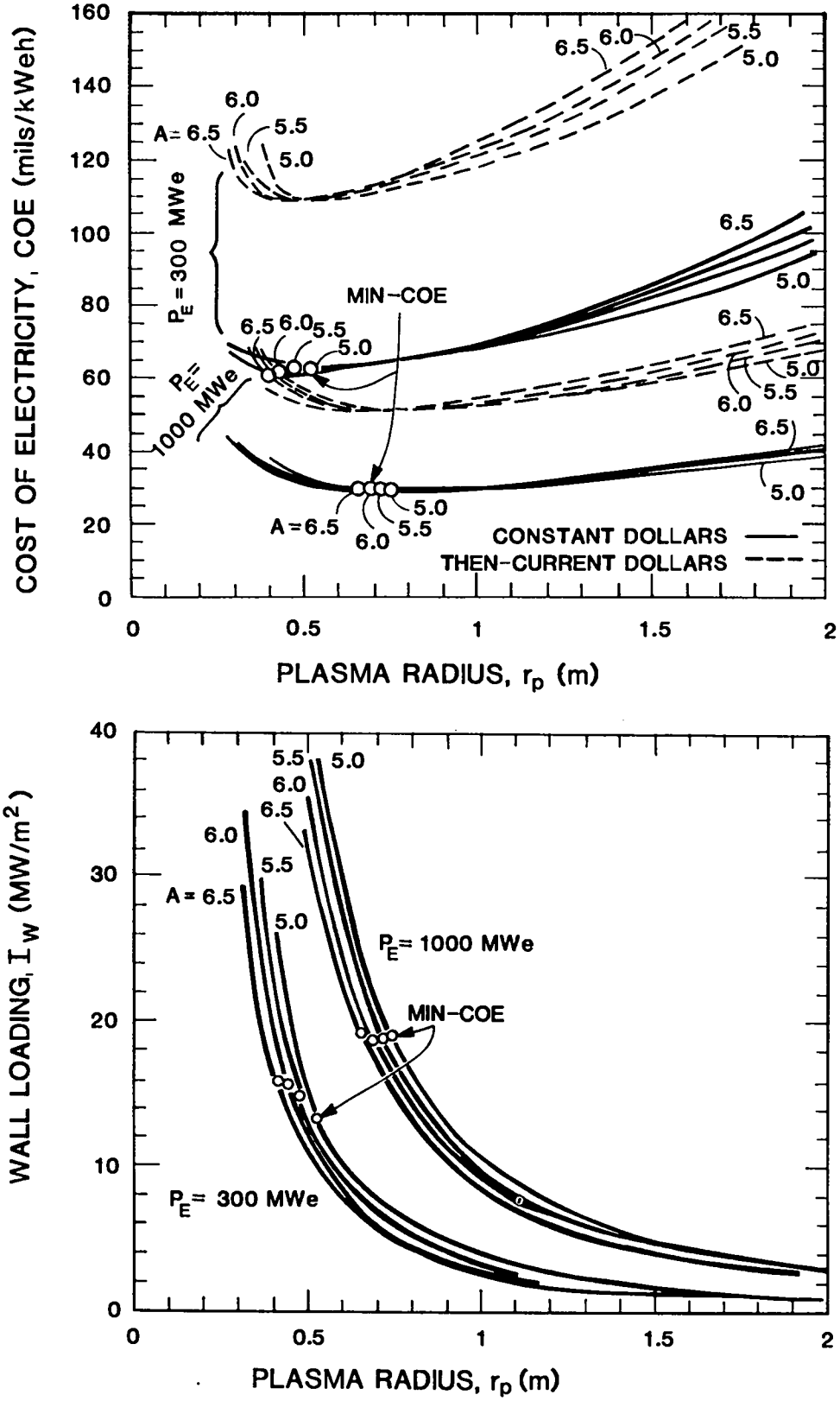

Fig. 6-3. Sensitivity of minimum-COE design points to changes in plasma aspect ratio, $A = R_T/r_p$ for P_E = 300 and 1000 MWe(net). The A = 5.5 curve is the base case.

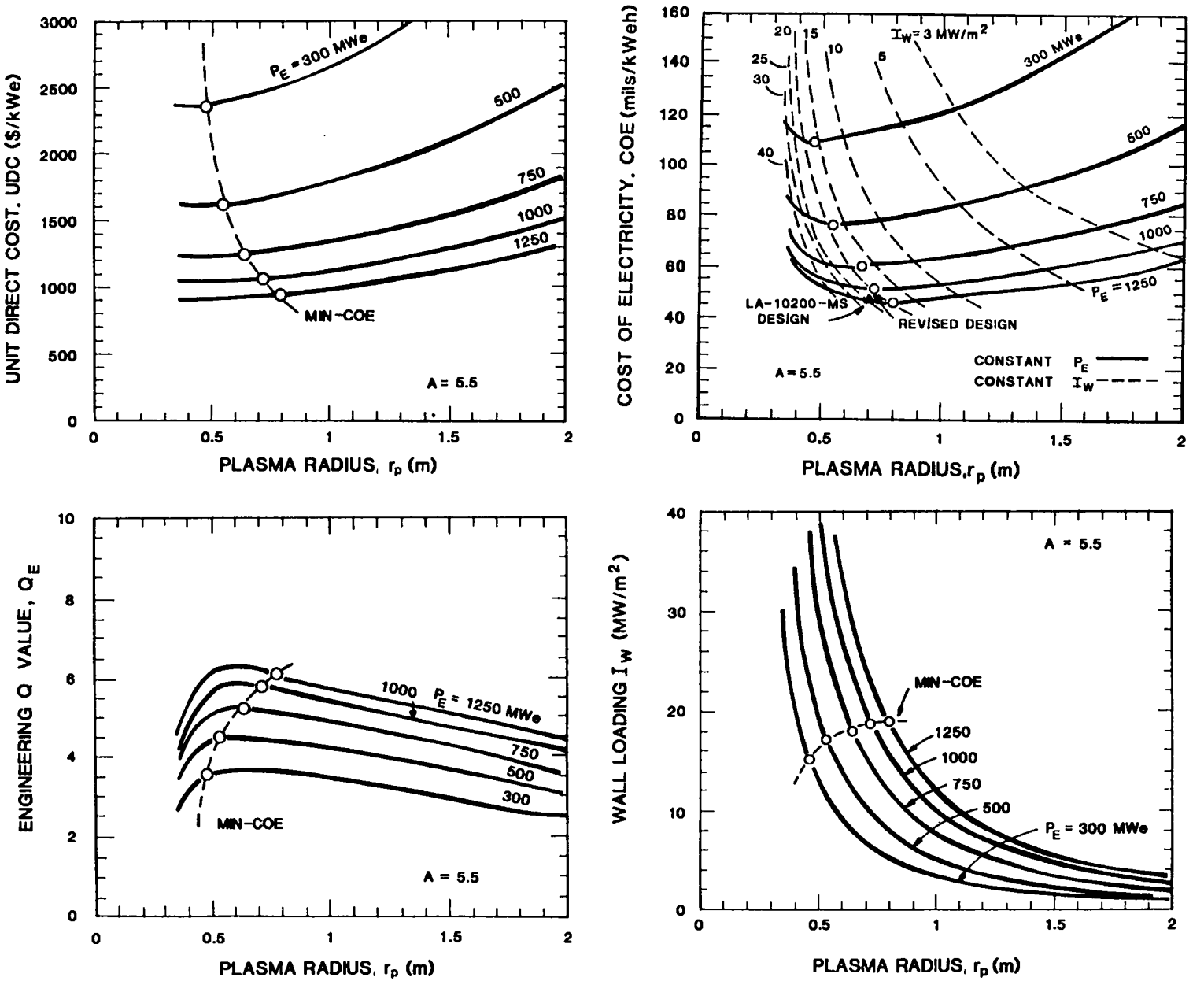

Fig. 6-4. Sensitivity of minimum-COE design points to changes in net electrical power, P_E, for the A = 5.5 base case, showing UDC, COE, I_W, and Q_E as functions of r_p.

- Increased r_p for a fixed P_E requires that I_w decrease. Since P_E is approximately proportional to $I_w r_p^2 A$, increased A decreases I_w for fixed r_p. As I_w decreases because of increased r_p, the FPC power density decreases, resulting in an increased unit direct cost [UDC($/kWe)].

- The increase in COE with increased r_p is also caused by an increase in recirculating power delivered to the resistive coils. The Q_E decreases because of increased coil resistive losses. As r_p increases, pressure balance demands slightly increased plasma currents. Since pressure balance dictates $I_w \propto I_\phi^4/r_p^3$, the total power is proportional to $I_\phi^4 A/r_p$, which for fixed P_E and A approximately required $I_\phi \propto r_p^{1/4}$. The coil currents, however, may actually decrease because of better electrical coupling, depending on the value of A when r_p is increased. Increasing r_p for a fixed A increases R_T and hence the coil resistance, which tends to override any decrease in coil current, giving a net increase in resistive coil losses and decreases in Q_E as r_p increases.

- As r_p decreases for a fixed A, the electrical coupling between plasma and coil rapidly decreases. Increased coil currents are then required to drive a given plasma current, and Q_E rapidly decreases.

- As r_p decreases for fixed A and P_E, the rapidly increasing neutron first-wall loading ($I_w \propto 1/r_p^2$) causes the plant factor, p_f, to diminish, in accordance with the algorithm given in Table 6-I. This decrease in p_f also contributes to the rapid increase in COE as r_p is decreased.

In summary, decreasing Q_E and p_f contributes to increasing COE with decreasing r_p, and decreasing (more slowly) Q_E (increasing UDC) causes the COE to increase as r_p increased. The COE optimum depicted in Fig. 6-4 results, this optimum being relatively insensitive to A (Fig. 6-3).

The values of plasma and coil currents for the parameter study described by Fig. 6-4 are shown in Fig. 6-5. Operation to the left of the minimum-COE point results in poor electrical coupling, increased coil currents and ohmic losses, decreased Q_E, and rapidly increased COE. The good coupling to the right of the minimum-cost point is not sufficient to overcome the increased coil resistance or the Q_E decreases, and COE increases again.

The changing plasma density and FPC mass utilization that occur in the parametric variations are illustrated in Figs. 6-6 and 6-7. The FPC mass utilization lies in the 0.4-0.6 tonne/MWt range for the minimum-COE design point and increases for lower neutron first-wall loadings, although only moderate increases in COE occur (Fig. 6-5) with increased r_p. These FPC mass utilizations, although increasing, remain far below those predicted for superconducting fusion approaches, a value of 5.7 tonne/MWt being predicted for

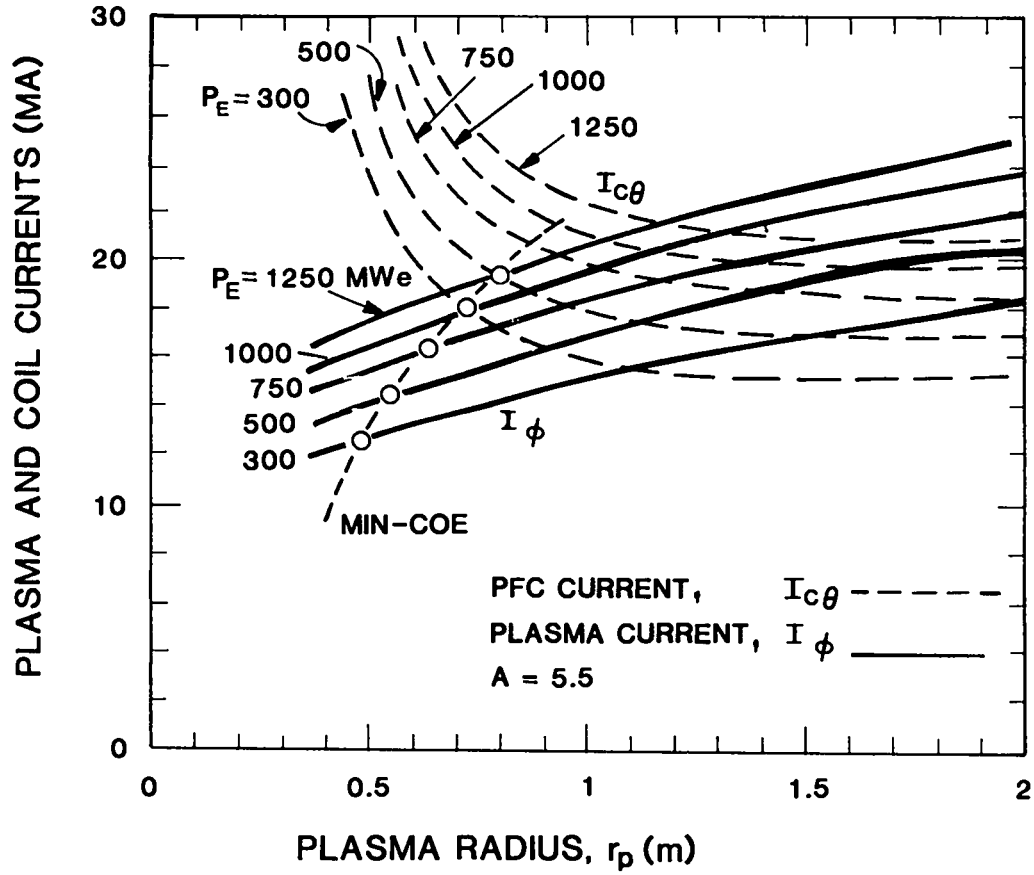

Fig. 6-5. Sensitivity of plasma (solid line) and coil (dashed line) currents as functions of r_p and P_E for the conditions depicted in Fig. 6-4.

STARFIRE[1]. The possibility for batch (single-piece) FPC maintenance is compromised, however, for the higher-COE, lower-I_w designs.

The comparison of the economic confinement time, τ_E(OPT), with RFP physics scaling, τ_E(PHYS), is shown in Fig. 6-8, which also indicates the minimum-COE design point for the range of P_E considered. As described in Sec. 1.3., the value τ_E(OPT) is the energy confinement time required to achieve the global minimum or local minimum-COE values; no physics transport scaling restricts the optimization procedure described in Fig. 6-1. Figure 6-8 illustrates a reconciliation of the minimum-COE goal with an extension of present-day physics realities (Fig. 1-4). The margins between physics and economics can be charted on Fig. 6-8, and an operating regime is indicated for $P_E \geq 750$ MWe and $\nu \geq 1$. For lower values of P_E, Fig. 6-8 indicates that the minimum-COE design is not attainable unless $\nu \geq 1$ for a scaling of the form $\tau_E \propto I^\nu r_p^2$.

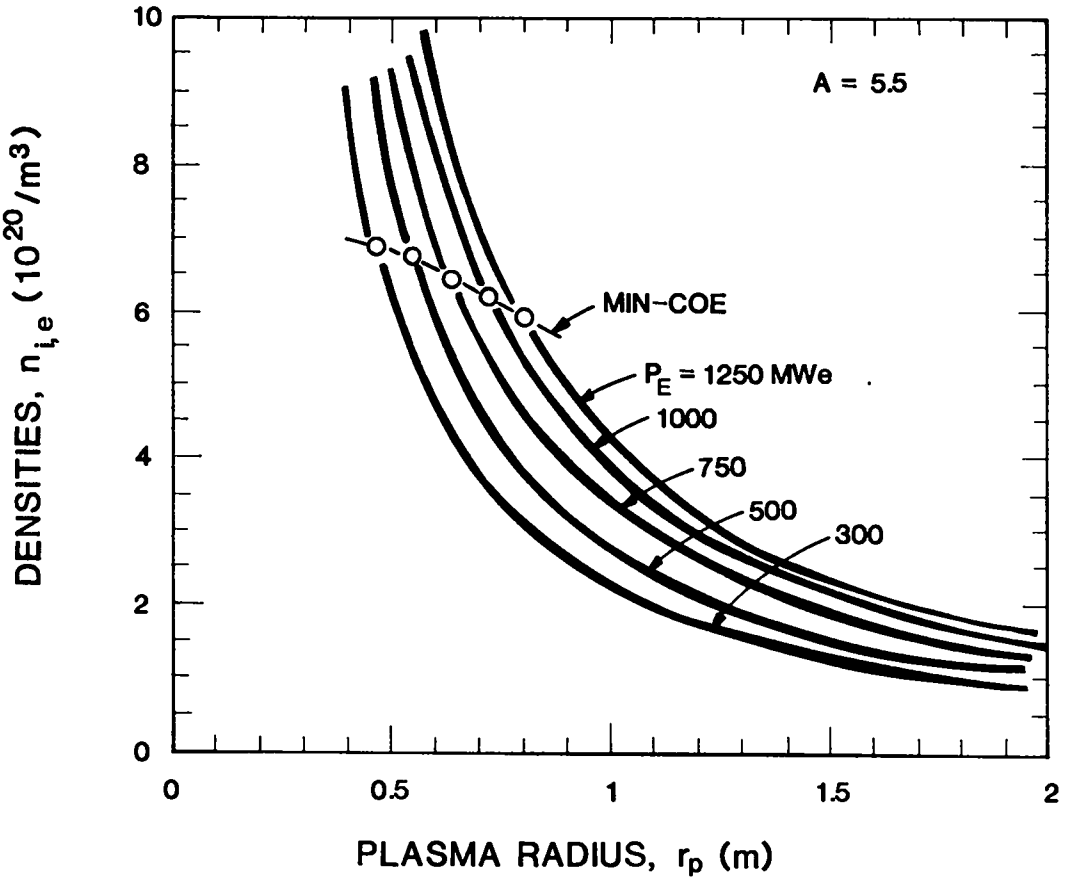

Fig. 6-6. Sensitivity of plasma density as a function of r_p and P_E for conditions depicted in Fig. 6-4.

The $I_w/P_E/COE$ tradeoff depicted on Fig. 6-4 defines the margins between technology (i.e., high heat/particle-flux surfaces, high-power-density blankets, "batch" versus "patch" maintenance, off-site versus on-site monolithic FPC construction, etc.) and economics. These margins and those expected for physics (transport) are conveniently combined on Fig. 6-9 with the $\tau_E(OPT) = \tau_E(RFP)$ constraint displayed for a range of current-scaling exponents, ν, where $\tau_E(PHYS) \propto I_\phi^\nu r_p^2 f(\beta_\theta)$. The usefulness of Fig. 6-9 rests with the comparison on a single plot of key technological (I_w), economic (COE), physics (ν, r_p), and institutional (P_E) variables.

6.3.2. Multiplexed-FPC Results

Although not a strong cost driver for $I_w > 5$ MW/m^2 within the constraints of the simplified cost model generally used to assess fusion, the first-wall neutron loading can be a strong determinant of technology. As indicated in Sec. 2.2.1., for $I_w < 5$ MW/m^2 the separately cooled first wall can be

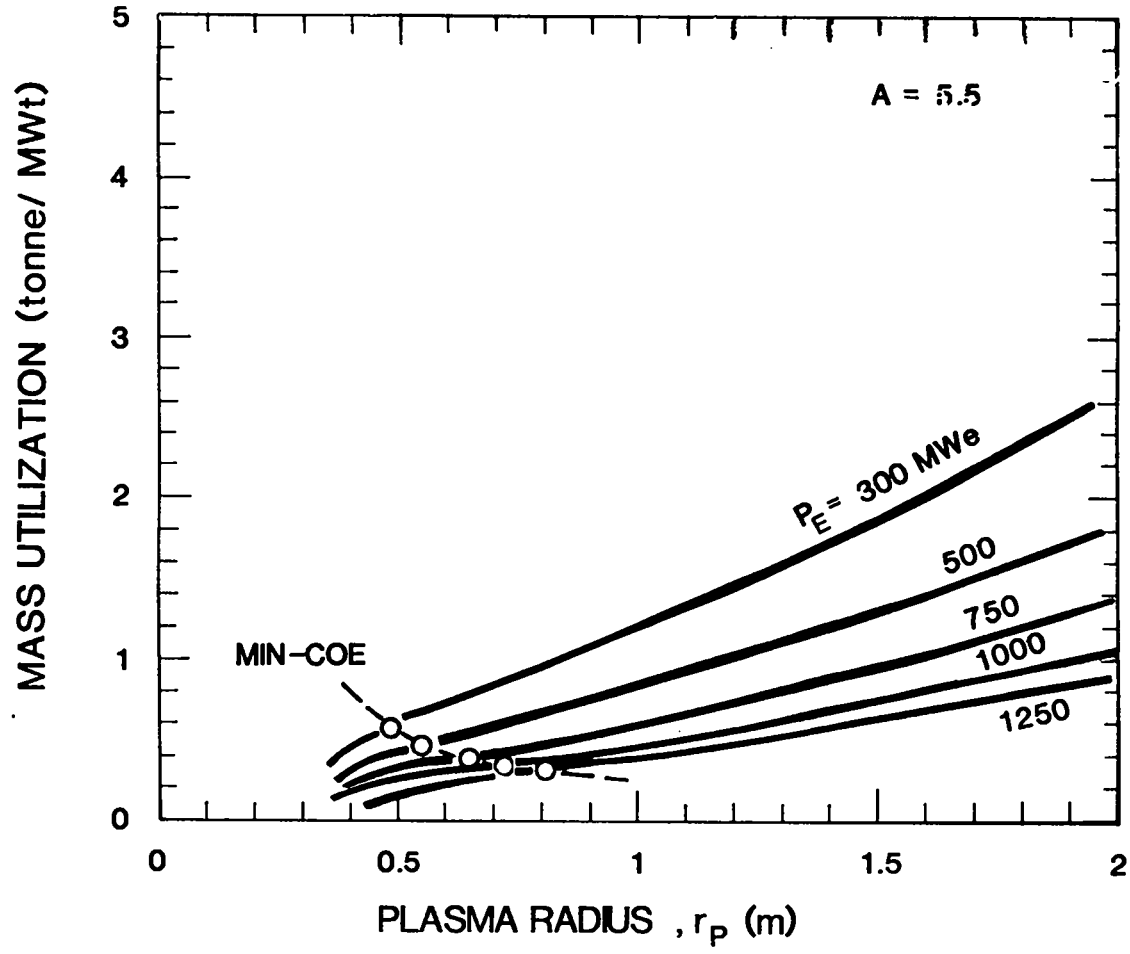

Fig. 6-7. Sensitivity of FPC mass utilization as a function of r_p and P_E for the conditions depicted in Fig. 6-4.

eliminated, resulting in a significant reduction in FPC complexity and an increase in overall plant thermal-conversion efficiency (Table 3-XI). For P_E fixed at ~ 1000 MWe, these lower-I_w systems would double in dimension and mass, as noted above and in Fig. 6-9. An increase of this magnitude for the base-case CRFPR(20) design would make single-piece maintenance more difficult (Sec. 4.3.), if not impossible. Retaining the CRFPR(20) fusion-power-core size, but decreasing I_w to ~ 5 MW/m^2 would lead to a plant with $P_E \simeq 250$ MWe. As seen from Fig. 6-9, this route to compact but low-first-wall-loading systems results in high values of COE. The increase in COE by over a factor of three results not only from the nuclear economy of scale but also from a lower optimized value of Q_E as P_E decreases; fusion power is generally proportional to I_ϕ^4, whereas coil ohmic losses are proportional to I_ϕ^2, and, hence, $Q_E \sim I_\phi^2 \sim P_E^{1/2}$. In addition, these small FPCs will require better (transport) physics, as reflected by the ν parameter on Fig. 6-9.

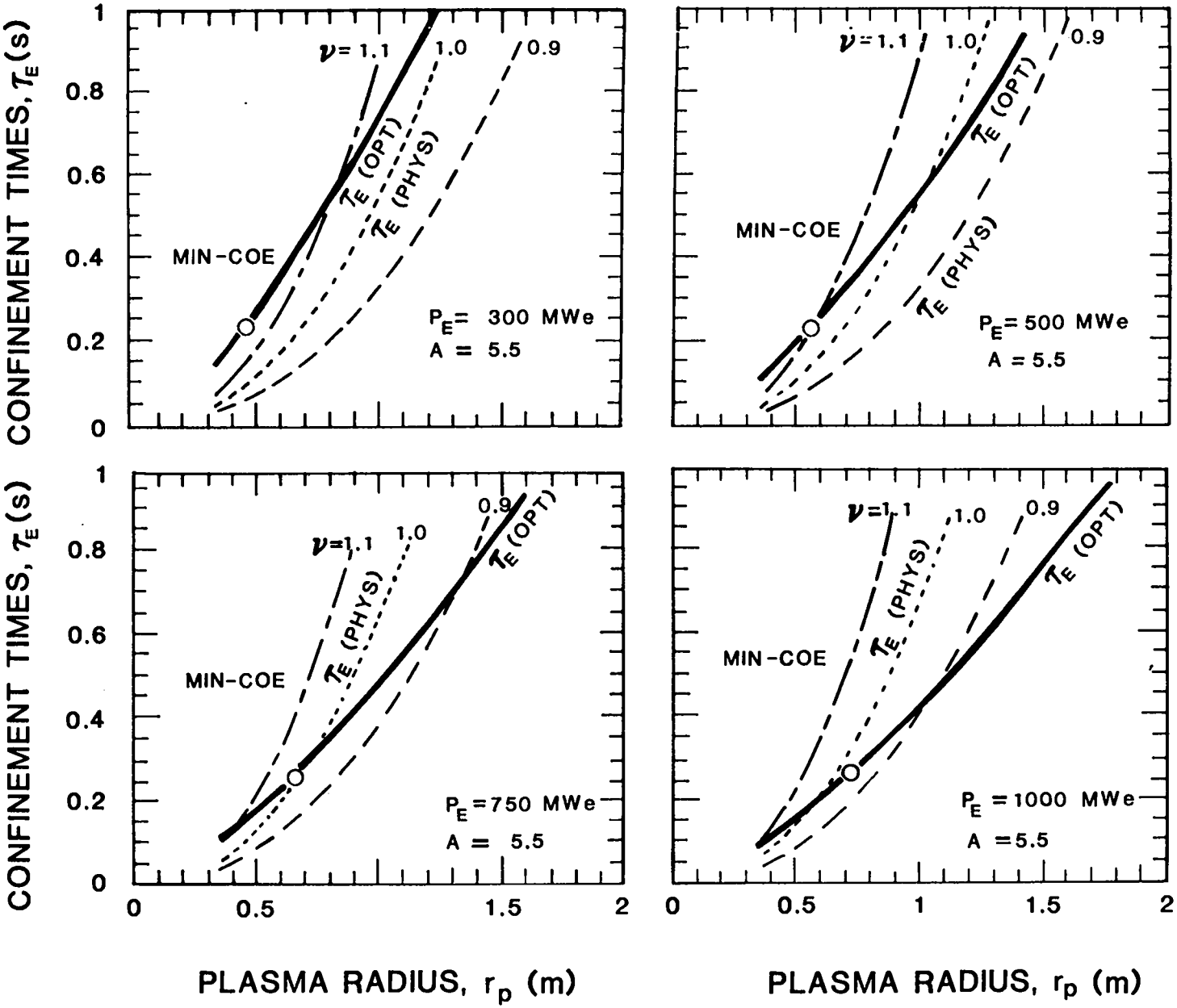

Fig. 6-8. Comparison of "economic" confinement time (solid line), τ_E(OPT), with RFP ohmic scaling (dashed curves), τ_E(PHYS), for the parametric sensitivity results depicted in Fig. 6-4.

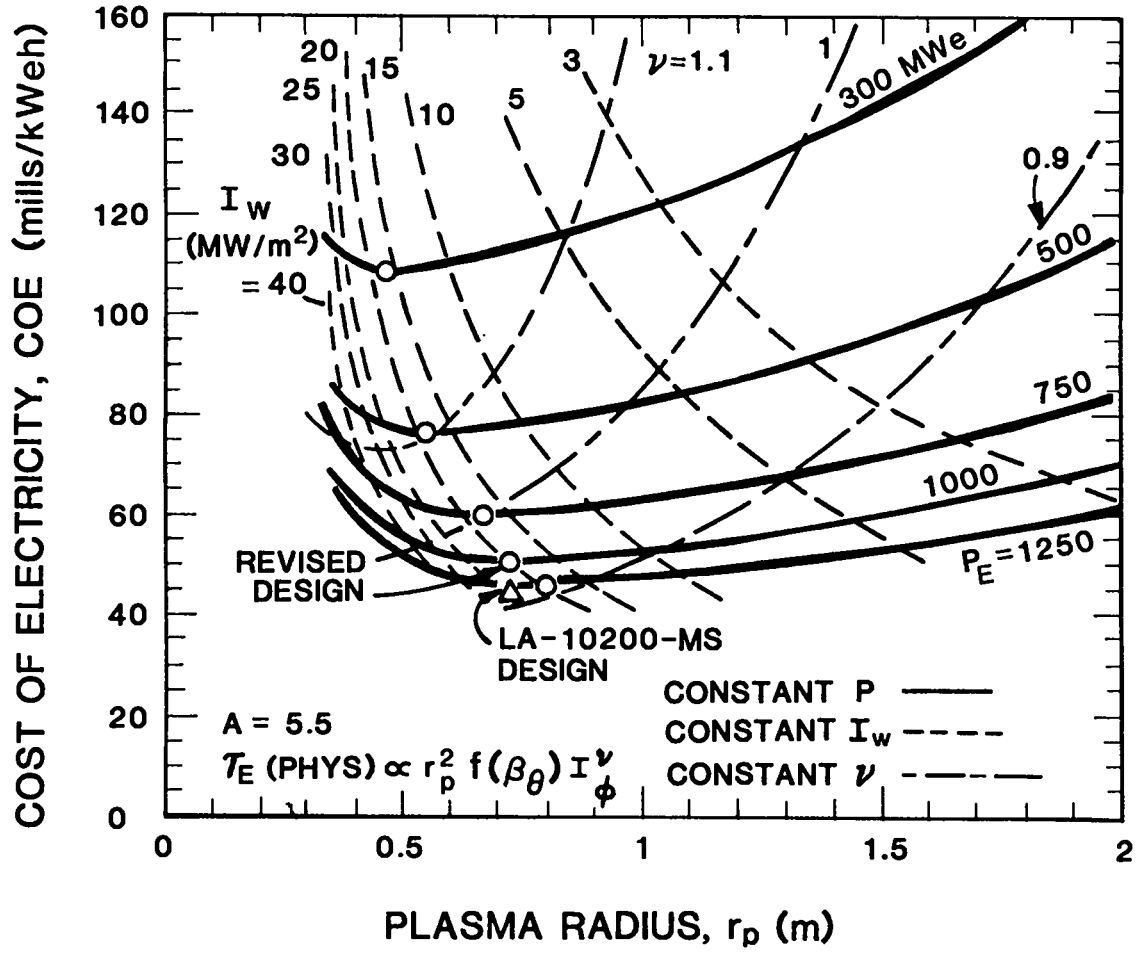

Fig. 6-9. Dependence of COE on r_p for a range of P_E values. Also shown are lines of constant I_w. The condition where $\tau_E(OPT) = \tau_E(PHYS)$ from Fig. 6-8 is also shown for $\tau_E(PHYS) \propto I_\phi^\nu r_p^2 f(\beta_\theta)$ scaling for a range of ν values.

Although the disadvantages of lower Q_E and higher ν are intrinsic to the smaller fusion-power-cores operating at lower power, the disadvantages of the nuclear economy of scale can be overcome to a great extent by using a number of derated CRFPR(20) fusion power cores operated at $I_w \simeq 5$ MW/m^2 to drive a nominal $P_E \simeq$ 1000-MWe(net) power plant. The RFP parametrics systems code (Fig. 6-1) was used to determine a minimum-COE design for a fixed-P_E power plant that is multiplexed with N fusion power cores. For the case where P_E = 1000 MWe(net), Fig. 6-10 shows the dependence of COE, UDC, Q_E, and I_w on N for the otherwise base-case values summarized in Table 6-I. Surprisingly, the minimum-COE I_w values remain above 10 MW/m^2 as the impact of the more expensive FPCs (increased

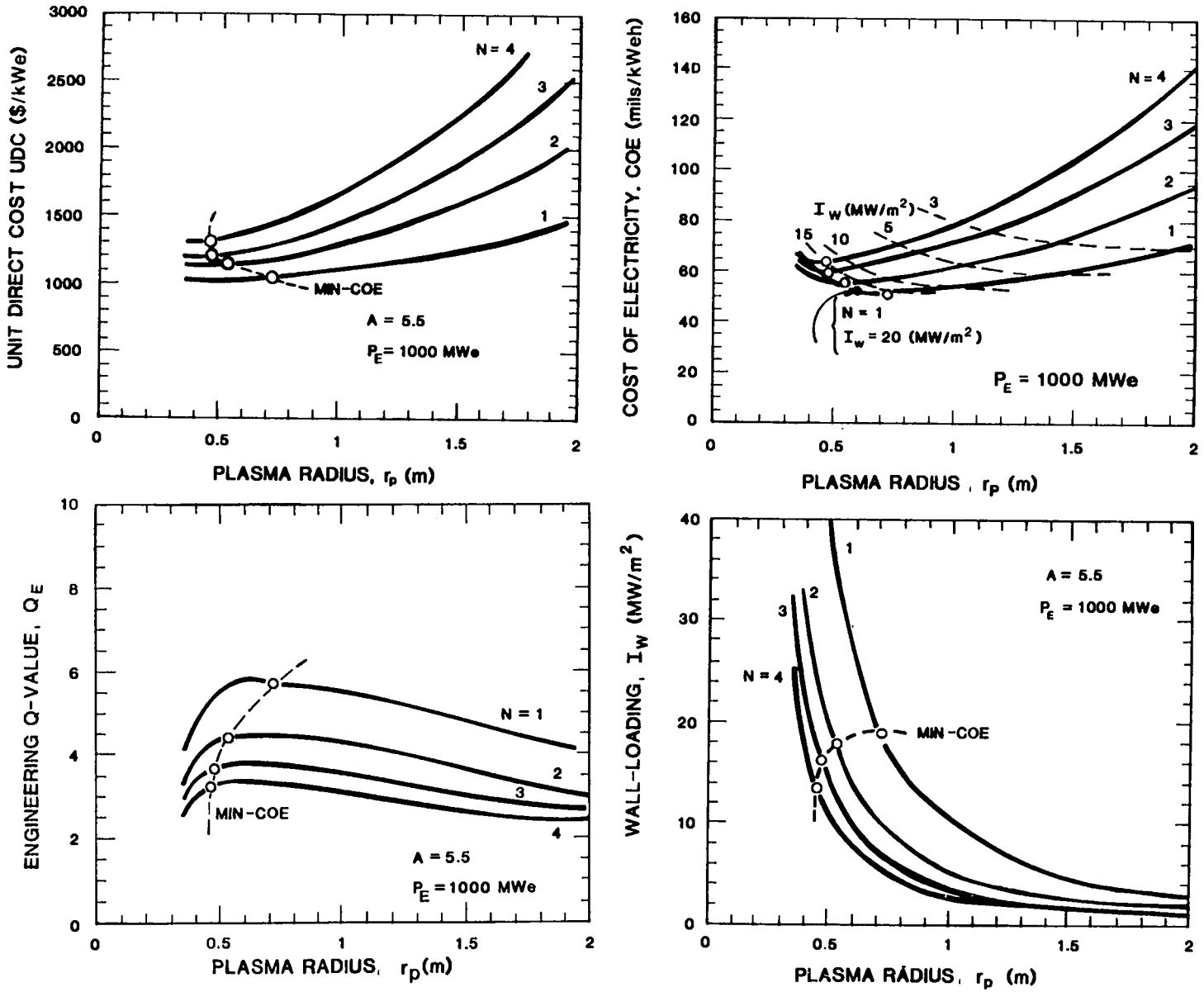

Fig. 6-10. Sensitivity of minimum-COE design points to change in degree of FPC multiplexing, N, for P_E = 1000 MWe(net), showing UDC, COE, I_w, and P_E as functions of r_p and N.

direct costs and decreased Q_E) is minimized. The Q_E plot on Fig. 6-10 illustrates the increased recirculating power fraction associated with these smaller FPCs, a penalty that expectedly increases as N increases.

A second penalty as the degree of multiplexing increases is the requirement for better confinement physics for the small (lower power, lower I_ϕ) FPCs. Figure 6-11 gives τ_E(OPT) and τ_E(PHYS) for a range of current exponents, ν, and degree of FPC multiplexing. Transport scaling with $\nu \geq 1.25$ would be required to achieve the minimum-COE, $N \simeq 4$ case, for which $I_w > 15$ MW/m^2; lower first-wall neutron loadings can be achieved only for increased COE.

The combined effects on physics and technology as the degree of multiplexing is varied are summarized in Fig. 6-12, which represents the counterpart of Fig. 6-9. For N = 4, the minimum-COE design costs 25% more than the base case, the first-wall neutron loading is $\sim$ 15 MW/m^2 and the required ν exceeds ≥ 1.25. For N = 4, but using an FPC similar to that suggested for the base case, the COE is increased by 33%, but the neutron first-wall loading is decreased to $\sim$ 6 MW/m^2. Other economic benefits, such as reduced utility financial risk and coverage ratios as well as improved plant availability, are not reflected in the cost algorithm; the ability to match better growth and to reduce capital at risk is a key argument for multiplexing these FPCs, in spite of the penalties suggested on Fig. 6-12. In any case, if lower-I_w, $P_E \simeq$ 1000-MWe(net) designs are desirable from a technological viewpoint, the route suggested by increased N in Fig. 6-12 is more desirable than increases in FPC mass or volume above the already large CRFPR(20) base-case design (albeit $\sim$ 25 times less than the STARFIRE tokamak design).

6.3.3. Design-Point Update

Since the input variables applied to the RFP parametric systems code can only approximate the design details that emerge from the two-dimensional neutronics and the FPC engineering integration that resulted therefrom, minor ambiguity in the definition of the CRFPR(20) base case inevitably results. Table 6-II gives a parameter list suggested by the parametrics systems code for the N = 1, minimum-COE, P_E = 1000-MWe(net) result depicted in Fig. 6-9. These parameters differ somewhat from those reported in Ref. 10 and updated herein because of the design and cost-code refinements and adjustments previously described and because of the basic limitations of any parametric systems code.

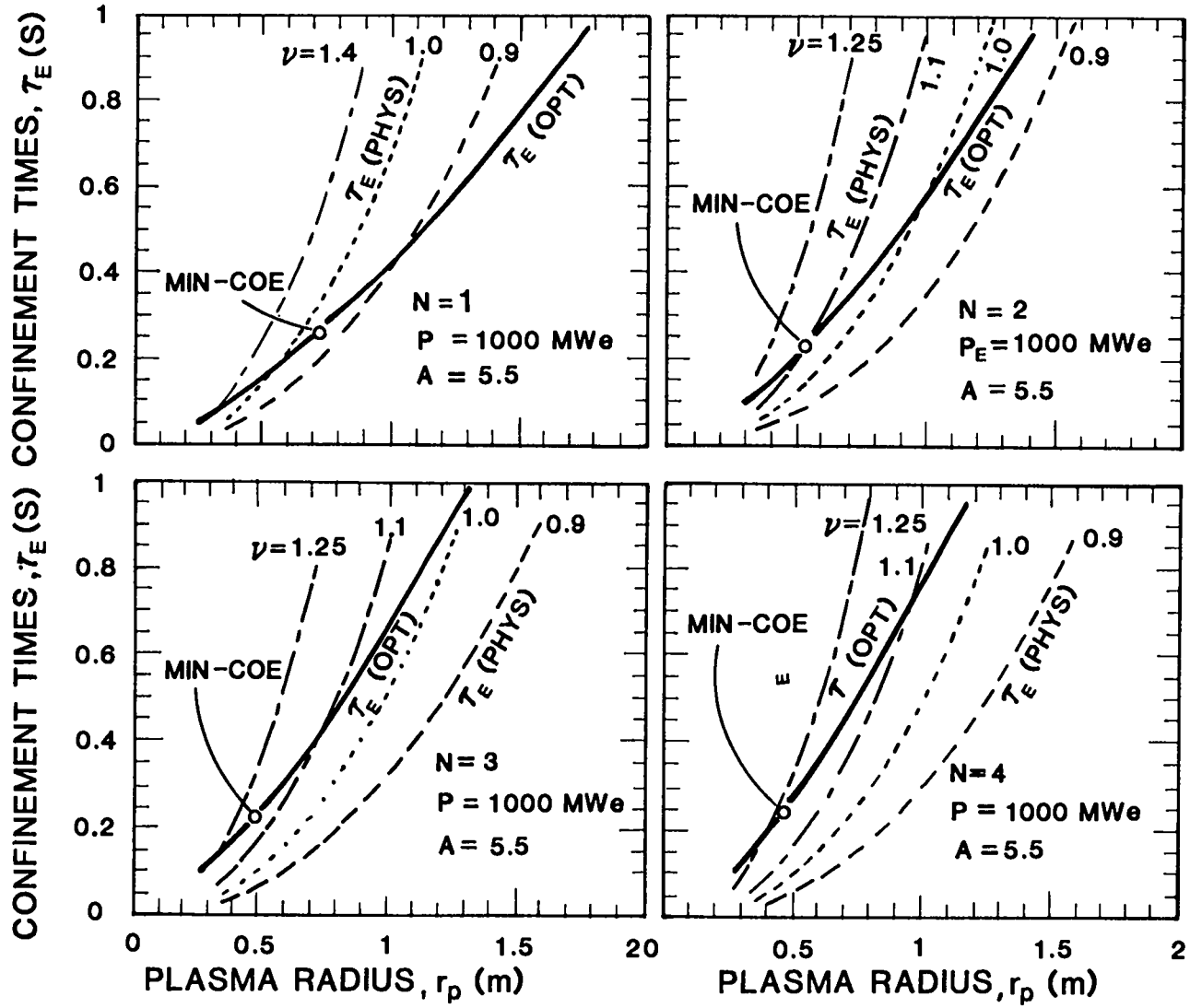

Fig. 6-11. Comparison of "economic" confinement time (solid line), τ_E(OPT), with RFP ohmic scaling (dashed curves), τ_E(PHYS), for the multiplexed-FPC parametric sensitivity results depicted in Fig. 6-10.

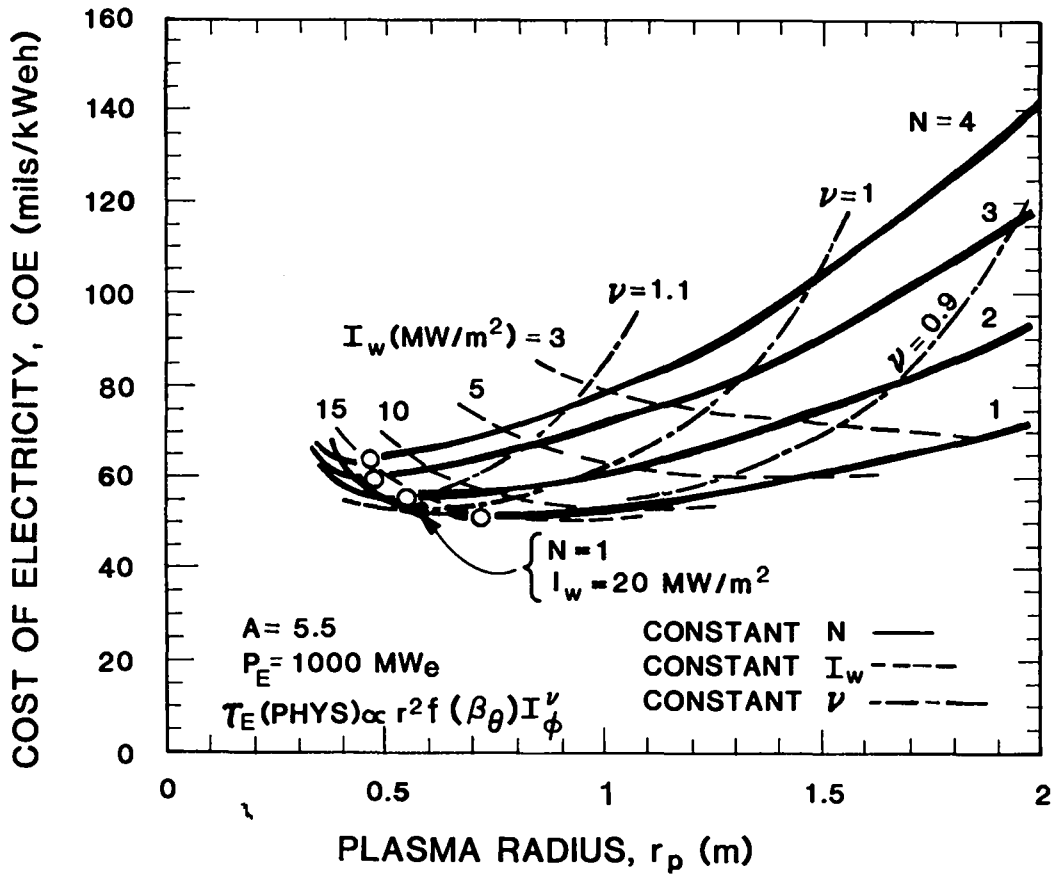

Fig. 6-12. Dependence of COE on r_p for a range of multiplexing values, N, for P_E = 1000 MWe(net). Also shown are lines of constant I_w. The condition where τ_E(OPT) = τ_E(PHYS) from Fig. 6-11 is also shown for τ_E(PHYS) $\propto I_\phi^\nu r_p^2 f(\beta_\theta)$ scaling for a range of ν values.

Differences between the minimum-COE design point suggested by the parametrics systems code and the actual design point that resulted from conceptual engineering design are listed in a second column of parameters given in Table 6-II. These differences are small, and the changes and updates serving as a basis for this report show only a few percent increase in COE relative to the Ref. 10 estimate. The CRFPR(20) design has also shifted downward from a neutron first-wall loading of 19.5 MW/m^2 to 18.7 MW/m^2 for the minimum-COE base case design, with 19.0 MW/m^2 actually being adopted.

Using the minimum-COE base-case design listed in Table 6-II, a single-point sensitivity study was performed. The results of this analysis are displayed in Fig. 6-13, which shows moderately weak dependencies of COE on β_θ, first-wall/blanket life, blanket/shield thickness, and degree of FPC multiplexity. The P_E dependence reflects the usual nuclear economy of scale that is built into

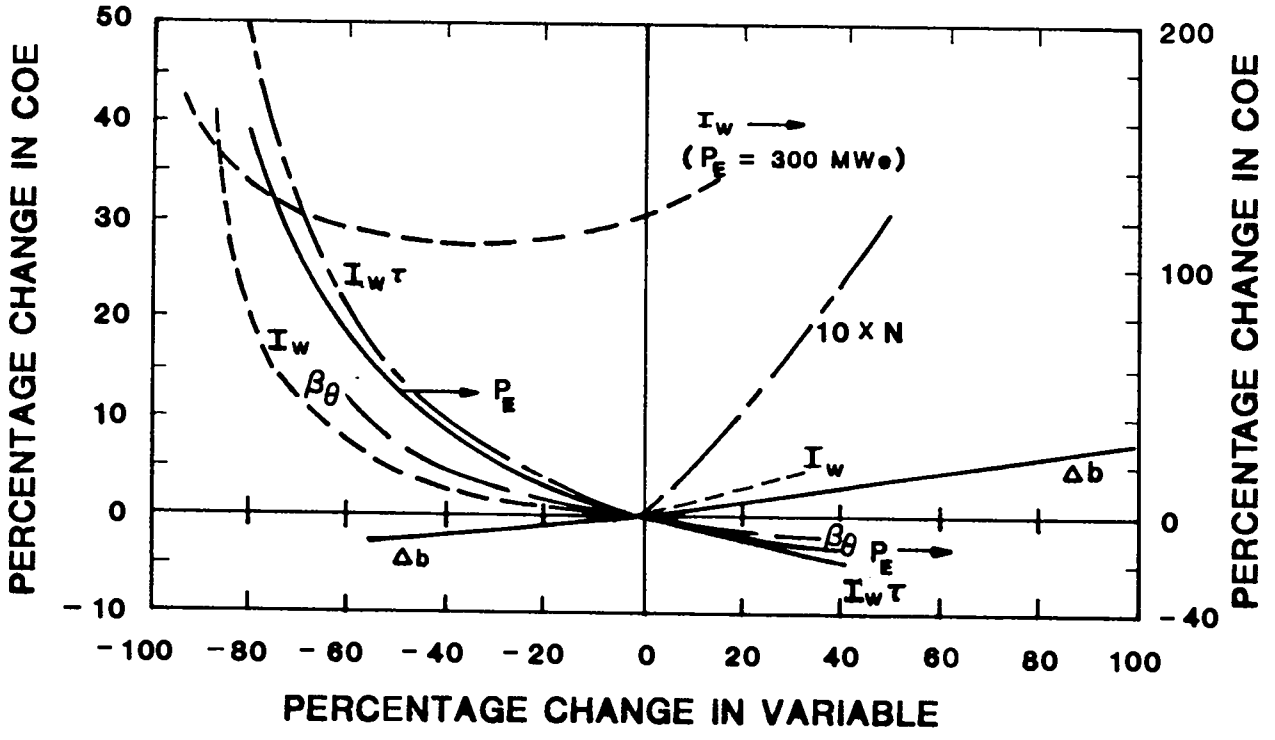

Fig. 6-13. Sensitivity of COE to changes in base-case (Table 6-II, minimum-COE) physics and engineering parameters [Δb = 0.775 m, $I_w\tau$ = 15 MWyr/m^2, β_θ = 0.20, P_E = 1000 MWe(net)].

the costing algorithm, as well as the increased recirculating power fraction. It is noted, also, that the minimum-COE value of I_w is also an optimum (minimum) value in its own right.

TABLE 6-II

COMPARISON OF MINIMUM-COE AND BASE CASE CRFPR(20) DESIGNS

	MINIMUM-COE DESIGN	BASE-CASE CONCEPTUAL DESIGN
Plasma Parameters		
Minor plasma radius, r_p(m)	0.71	0.71
Major plasma radius, R_T(m)	3.89	3.90
Plasma aspect ratio, A	5.50	5.50
Plasma current, I_ϕ(MA)	17.73	18.40
Toroidal current density, j_ϕ(MA/m^2)	11.35	11.62
Plasma density, n(10^{20}/m^3)	6.23	6.55
Plasma temperature, T(keV)	10.00	10.00
Lawson parameter, $n\tau_E$(10^{20} s/m^3)	1.60	1.51
Energy confinement time, τ_E(OPT)(s)	0.26	0.23
Poloidal beta, β_θ	0.20	0.23
Theta parameter, Θ	1.45	1.45
Reversal parameter, F	-0.20	-0.20
Plasma/first-wall radius, $x = r_p/r_w$	0.95	0.95
Streaming parameter, I_ϕ/N(10^{-14} A m)	1.81	1.78
Plasma ohmic dissipation during burn, P_Ω(MW)	22.70	25.30
Fusion power, P_F(MW)	2671.00	2733.30
Poloidal-Field Quantities		
Coil thickness, $\delta_{c\theta}$(m)	0.36	0.42
Average minor radius of coil, $r_{c\theta}$(m)	1.79	1.81
Mass of coil (tonne)	705.33	812.60
Magnetic field at the coil, $B_{c\theta}$(T)	1.98	4.50(peak)
Magnetic field at the plasma surface, B_θ(T)	5.03	5.18
Poloidal-coil current, $I_{c\theta}$(MA/m^2)	23.65	31.94
Poloidal-coil current density, $j_{c\theta}$(MA/m^2)	6.0	6.69
Maximum energy stored in coil, $W_{B\theta}$(MJ)	1167.58	1700.00
Ohmic dissipation during burn, P_Ω^{PFC}(MW)	88.43	126.5
Volumetric heating during burn (MW/m^3)	0.92	1.15

TABLE 6-II (Cont-1)

	MINIMUM-COE DESIGN	BASE-CASE CONCEPTUAL DESIGN
Toroidal-Field Quantities		
Coil thickness, $\delta_{c\phi}$(m)	0.088	0.075
Average minor radius of coil, $r_{c\phi}$(m)	1.56	1.56
Mass of coil (tonne)	153.09	76.20
Initial toroidal bias field[(a)] (T)	0.66	0.72
Reversed-toroidal field during the burn,[(a)] $B_{\phi R}$(T)	0.66	0.72
Maximum energy stored in the coil,[(a)] $W_{B\phi}$(MJ)	46.00	38.60
Toroidal-coil current density, $j_{c\phi}$(MA/m^2)	5.96	6.51
Ohmic dissipation during burn, P_{Ω}^{TFC}(MW)	19.19	12.6
Volumetric heating during burn (MW/m^3)	0.92	1.09
Engineering Summary		
Plasma Q-value, Q_P	117.10	108.00
Engineering Q-value, Q_E	5.64	4.91
Total thermal power, P_{TH}(MWt)	3376.14	3472.60
Gross electric power, P_{ET}(MWe)	1215.41	1255.80
Plant availability, p_f	0.76	0.76
Net electric power, P_E(MWe)	1000.	1000.
14.1-meV neutron loading, I_w(MW/m^2)	18.72	19.03
14.1-meV blanket multiplication, M_N	1.33	1.33
First wall radius, r_w(m)	0.75	0.75
Minor radius of system, r_s(m)	1.96	2.16
Blanket thickness, Δb(m)	0.775	0.775
First-wall/blanket mass (tonne)	42.83	220.45[(b)]
Coil mass (tonne)	858.42	888.80
FPC mass, M_{FPC}(tonne)	1063.40	1117.25
FPC power density, P_{TH}/V_{FPC}(MWt/m^3)	11.46	9.67
FPC mass utilization, P_{TH}/M_{FPC}(MWt/tonne)	3.18	3.13
Mass power density, $1000P_E/M_{FRC}$(kWe/tonne)	940.73	895.26
Blanket power density (MW/m^3)	25.11	25.59
First-wall/blanket life (MWyr/m^2)	15.0	15.0
Degree of multiplexing, N	1.0	1.0

(a) Based on supplying reversal toroidal flux by coil set rather than full toroidal flux, with RFP dynamo generating B_ϕ within plasma.
(b) Includes limiters, manifolds, headers and shields, but not PbLi coolant.

TABLE 6-II (Cont-2)

Account Number	Account Title	Million Dollars (1980)[a]	
20.	Land and land rights	3.30	[3.30]
21.	Structures and site facilities	271.32	[271.44]
22.	Reactor plant equipment	414.68	[424.41]
22.1.	Reactor equipment	128.82	[131.67]
22.1.1.	Blanket and first wall	10.55	[10.31]
22.1.2.	Shield	2.13	[2.34]
22.1.3.	Magnets	34.34	[35.60]
22.1.4.	Supplemental heating systems	0.00	[0.00]
22.1.5.	Primary structure and support	12.25	[12.25]
22.1.6.	Reactor vacuum systems	16.41	[16.41]
22.1.7.	Power supply, switching, energy storage	48.61	[50.23]
22.1.8.	Impurity control	2.52	[2.52]
22.1.9.	Direct energy conversion system	0.00	[0.00]
22.1.10.	ECRH breakdown system	2.02	[2.02]
23.	Turbine plant equipment	224.19	[229.31]
24.	Electric plant equipment	113.01	[115.04]
25.	Miscellaneous plant equipment	41.83	[41.83]
26.	Special materials	43.24	[43.24]
90.	Direct cost	1111.56	[1128.57]
91.	Construction facilities, equipment and services (10%)	111.16	[112.86]
92.	Engineering and construction management services (8%)	88.93	[90.29]
93.	Other costs (5%)	55.58	[56.43]
94.	Constant-dollar interest during construction (IDC, 5%/yr)	147.66	[149.92]
95.	Constant-dollar escalation during construction (EDC, 0%/yr)	0.00	[0.00]
99.	Total cost	1514.88	[1538.05]

	Account Number	Constant Account Dollars		Then-Current Account Dollars	
Unit direct cost, UDC($/kWe)	90	1111.54	[1128.56]	1111.54	[1128.56]
Unit base cost, UBC($/kWe)	93	1367.20	[1388.13]	1367.20	[1388.13]
Unit total cost, UTC($/kWe)	99	1514.86	[1538.05]	1922.28	[1951.72]
Capital return (mills/kWeh)		22.79	[23.14]	43.37	[44.04]
O&M (2.0%, mills/kWeh)	40-47,51	4.11	[4.18]	5.25	[5.33]
B/FW replacement (mills/kWeh)	50	1.00	[0.88]	1.28	[1.12]
Deuterium fuel (mills/kWeh)	02	0.03	[0.03]	0.03	[0.03]
COE (mills/kWeh)		27.93	[28.22]	49.93	[50.52]

[a] Values in brackets [] reflect the base-case conceptual design.

7. MAGNETIC DIVERTORS

7.1. Rationale for Divertors

Magnetic divertors are an alternative to the pumped-limiter impurity control scheme invoked by the Compact Reversed-Field Pinch Reactor (CRFPR) design.[10] Limiters have the well-known drawbacks related to erosion and the resultant plasma contamination. Impurity-control experiments in tokamaks[58,59] indicate lower impurity levels and higher edge-plasma temperatures that result in improved energy and particle confinement for plasmas operated with a magnetic divertor. This improvement stems from the placement of the divertor neutralizer plate on open field lines outside the plasma rather than on the closed field line defining the plasma surface for the pumped limiter. The neutral particles emitted from the neutralizer plate will also appear on open field lines for the divertor, whereas neutral particles can enter the plasma directly for the pumped limiter. Consequently, divertors insulate the plasma better than pumped limiters from sputtered impurities and the associated energy drain.

Unlike the tokamak case, no configurational or detailed study of divertor options existed for the RFP, until recently.[60,61] This section summarizes the work reported in Refs. 60 and 61 while extending the prognosis for magnetic divertors in RFPs to a level where future design work can proceed more directly on the most viable options.

7.2. RFP Divertor Configurations

7.2.1. Divertor Options

Figure 7-1 depicts a range of divertor approaches for confinement concepts utilizing toroidal-field coils (TFC) and poloidal-field coils (PFC) with externally induced plasma currents (i.e., tokamaks and RFPs). Either the poloidal field (B_θ, Type A in Fig. 7-1), the toroidal field (B_ϕ, Type B), or a combination (Type C) can be diverted, with each sampling the entire flux surface. The performance of each approach is determined by the connection length (i.e., the distance along a field line between divertor collector plates), which in turn is a function of the number of divertors, N. The connection length is longer for toroidal-field divertors than for poloidal-field divertors in low-q ($q \equiv B_\phi r/B_\theta R \ll 1$) RFP devices, with q^{-1} toroidal-field divertors required to yield the same connection length as one poloidal-field divertor. The toroidal-field divertor rather than the poloidal-field divertor has the shorter connection length for high-q tokamak devices, thereby enhancing divertor performance by routing particles and energy onto the divertor plate

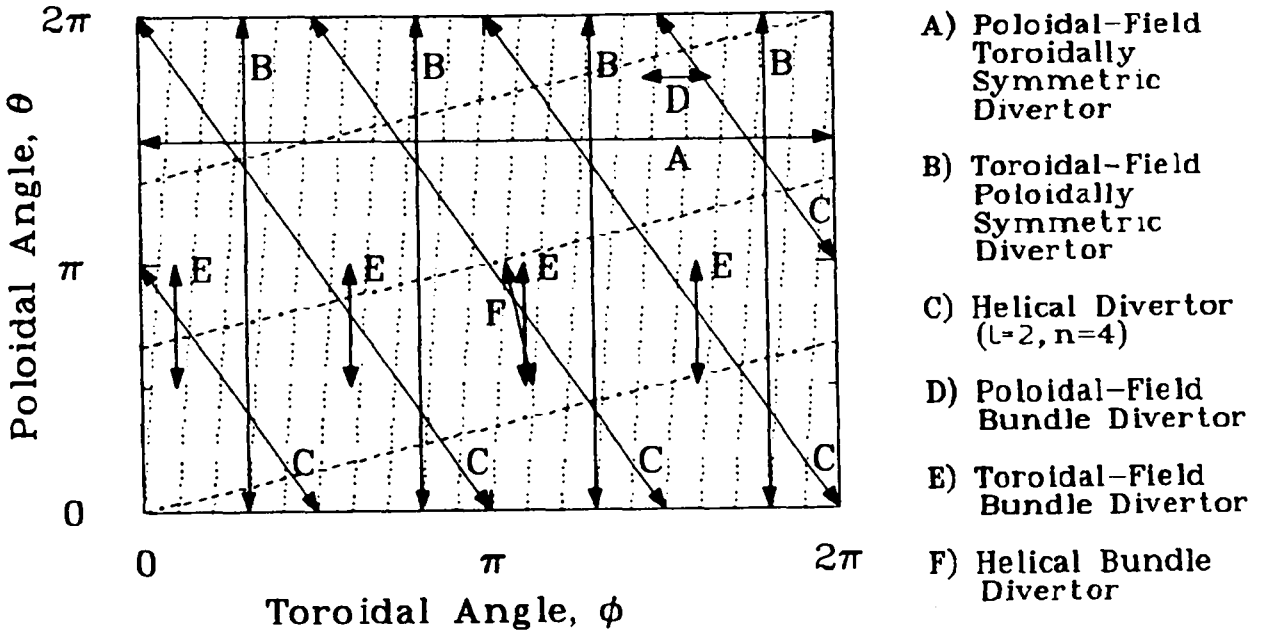

Fig. 7-1. Trajectory of a field line on the outer flux surface as a function of toroidal and poloidal angles for an RFP-like geometry (q = 0.05, dotted line) and for a tokamak-like geometry (q = 3, dashed line). Also shown are the field nulls (solid line) for a number of divertor types. Divertor connection lengths and the fraction of surface sampled by each divertor are illustrated.

before significant cross-field diffusion to and interaction with the first wall occur. The helical divertor substantially increases engineering complexity but allows a range of connection lengths depending on the poloidal-field number, ℓ, and the toroidal-field number, n. The three above-mentioned divertors (Types A-C) with field nulls encircling the plasma substantially intrude into the first-wall and blanket regions. These perturbations can be minimized with a localized divertor that extracts and diverts a small bundle of field lines from the outer flux surface. Examples of bundle divertors are also depicted in Fig. 7-1. For low-q devices, and depending on toroidal extent, only the poloidal-field and helical bundle divertors (Types D and F) have the potential of sampling the entire outer flux surface, as denoted by a field null intersecting adjacent field lines. Even if the poloidal extent of the field null is increased, the toroidal-field bundle divertor (Type E) for low-q devices

cannot sample the entire outer flux surface unless the field null encircles the plasma; this case would no longer be classified as a bundle divertor, however. As with the symmetric divertors in low-q devices, the poloidal-field divertor has a shorter connection length compared to the toroidal-field bundle divertor. The poloidal-field and toroidal-field bundle divertors for high-q tokamak devices exchange properties with respect to connection length and fraction of flux surface sampled.

7.2.2. Preferred Divertor Options for RFPs

A majority of divertor designs reported in the literature apply to tokamaks. These designs predominantly null the minority poloidal field, this choice being dictated by considerations of plasma confinement and equilibrium. Plasma equilibrium ($\vec{j}\times\vec{B} = \vec{\nabla}p$) indicates that nulling a given magnetic-field component will reduce the gradient of the plasma pressure in the vicinity of the null for comparable plasma current densities. The resulting reduction in the volume-averaged beta can be minimized only by nulling the minority field. Additionally, since particle confinement generally scales as field raised to a positive exponent,[62] a reduction of local confinement in the vicinity of a field null would reduce the volume-averaged confinement time. Lastly, large field gradients in the vicinity of the field null result in a small radius of curvature and a large particle drift velocity in a direction orthogonal to a field line, thereby reducing the efficiency with which particles enter the divertor.

To the above-mentioned plasma considerations (i.e., beta, confinement, and divertor efficiency) must be added engineering design constraints. The currents required in the divertor coils scale linearly with the magnitude of the nulled field component; the energy stored in, forces on, and power consumed by the divertor coils are minimized by nulling the minority field component. Minimum plasma effects and divertor-coil currents and maximum divertor efficiency, therefore, give preference to minority-field nulls.

Diverting the minority poloidal field in a tokamak requires that the divertor coils either be interlocked with the TFC set or reside outside the TFCs, with substantially increased currents being predicted for the latter. The minority toroidal field in an RFP, on the other hand, can be nulled without the engineering complexity of interlocking coils. Nulling the toroidal field in an RFP, however, raises concerns about plasma stability with a nonmonotonic surface-averaged q profile, relatively large toroidal gaps in the first wall,

and a general breaking of the preferred toroidal symmetry. These concerns may be unwarranted, however, because the separatrix can exert a stabilizing effect on the plasma.[63]

On the basis of the foregoing arguments, the poloidal-field divertors (Types A and D, in Fig. 7-1) and helical divertor (Type C) are not considered here for the RFP. The helical bundle divertor (Type F) is similar to the toroidal-field bundle divertor (Type E) for the low-q RFP and is also not considered here. The remaining choice between toroidal-field poloidally symmetric divertor (SD) and toroidal-field bundle divertor (BD) is the subject of this study.

A further distinction is made as to whether the divertor resides totally within the first-wall/blanket/shield (FW/B/S) system or extends beyond the TFCs. An intra-blanket BD constrained in number (i.e., $N \leq 8$) would concentrate particle and energy fluxes in a volume deemed too small to be adequately engineered for cooling and erosion control. An exoblanket SD would require that the PFC set be displaced from the plasma, resulting in a decreased field coupling efficiency measured as enhanced stored energy and ohmic losses in the coils. The choice between an exoblanket BD and an intra-blanket SD must be based upon a three-dimensional magnetics analysis of the two designs. The three-dimensional magnetics provides an accurate calculation of the divertor connection length (i.e., the distance along a field line between divertor collector plates) as well as a measure of flux surface integrity based on magnetic-island widths arising from a periodic toroidal-field ripple and the "thickening" of flux surfaces caused by non-axisymmetric toroidal-field ripple.

7.3. Model

7.3.1. Plasma Simulation

The first stage of the divertor design proceeds on the basis of a two-dimensional layout. The separatrix is located by field-line tracings that are confined to the equatorial plane and sample a region near the plasma surface. At this stage of analysis, only the divertor coils and the TFC set are simulated with the otherwise three-dimensional vacuum-magnetics code, TORSIDO.[64] The coil locations, currents, and current densities are key design variables. Coils are positioned to minimize and symmetrize the field ripple produced by the divertor; the coil currents are adjusted to locate the separatrix at the plasma surface; and the coil current densities are determined by requiring no field line to

intersect the coils. The limiter-based CRFPR(20) fusion-power-core design[10] provided a starting point for this study.

7.3.1.1. MHD Model

Determination of the divertor connection length and flux-surface integrity (i.e., magnetic islands and flux-surface broadening) can be accomplished only with a three-dimensional model that simulates both the PFCs and the plasma in addition to the TFCs and the divertor coils. The plasma simulation is based on a one-dimensional MHD model of RFP magnetic-field and current-density profiles.[10] This simulation solves the following set of simultaneous equations:

$$\vec{j}\times\vec{B} = \vec{\nabla}p \tag{1}$$

$$\vec{\nabla}\times\vec{B} = \mu_o\vec{j} \tag{2}$$

$$\mu = \mu_o \frac{(\vec{j}\cdot\vec{B})}{B^2}\ , \tag{3}$$

where $\mu_o = 4\pi(10)^{-7}$ h/m and the constancy of $\mu(r)$ defines the minimum-energy $\beta = 0$ Taylor state.[13] The pressure profile is described by $p(r) \propto J_0^2(2\Theta r/r_p)$, where $\Theta \equiv B_\theta(r_w)/\langle B_\phi\rangle$ is the pinch parameter. The normalization of the pressure profile is adjusted iteratively in order to obtain a specific poloidal beta, $\beta_\theta \equiv 2\mu_o\langle p\rangle/B_\theta^2(r_p)$. In Ref. 1, $\mu(r)/\mu(0) = 1$ for $0 \leq r < r_b$ and then ramps linearly to zero for $r_b \leq r \leq r_p$ (i.e., the Modified Bessel-function Model),[11,65,66] as shown in Fig. 7-2. This break point, r_b, is determined experimentally[65] to be at $r_b = 0.807r_p$ for $\Theta = 1.55$, is generally a function of Θ, and causes discontinuities in the radial derivatives of the current density and magnetic field profiles, as shown in Figs. 7-3 and 7-4, respectively. These discontinuities can result in large errors for numerical integration or spline fits to the profiles, a problem that can be circumvented by using a μ profile which is continuous, as is its first derivative. Two μ profiles were considered (Fig. 7-2): a parabolic profile of the form $\mu(r)/\mu(o) = 1 - (r/r_p)^\nu$ and a cosine profile of the form $\mu(r)/\mu(o) = 1$ for $0 \leq r \leq r_b'$. The cosine profile then decays to zero according to the first quarter period of a cosine function for $r_b' \leq r \leq r_p$. The exponent and the break point for these two μ profiles are determined by equating areas under the two μ profiles with the area under the

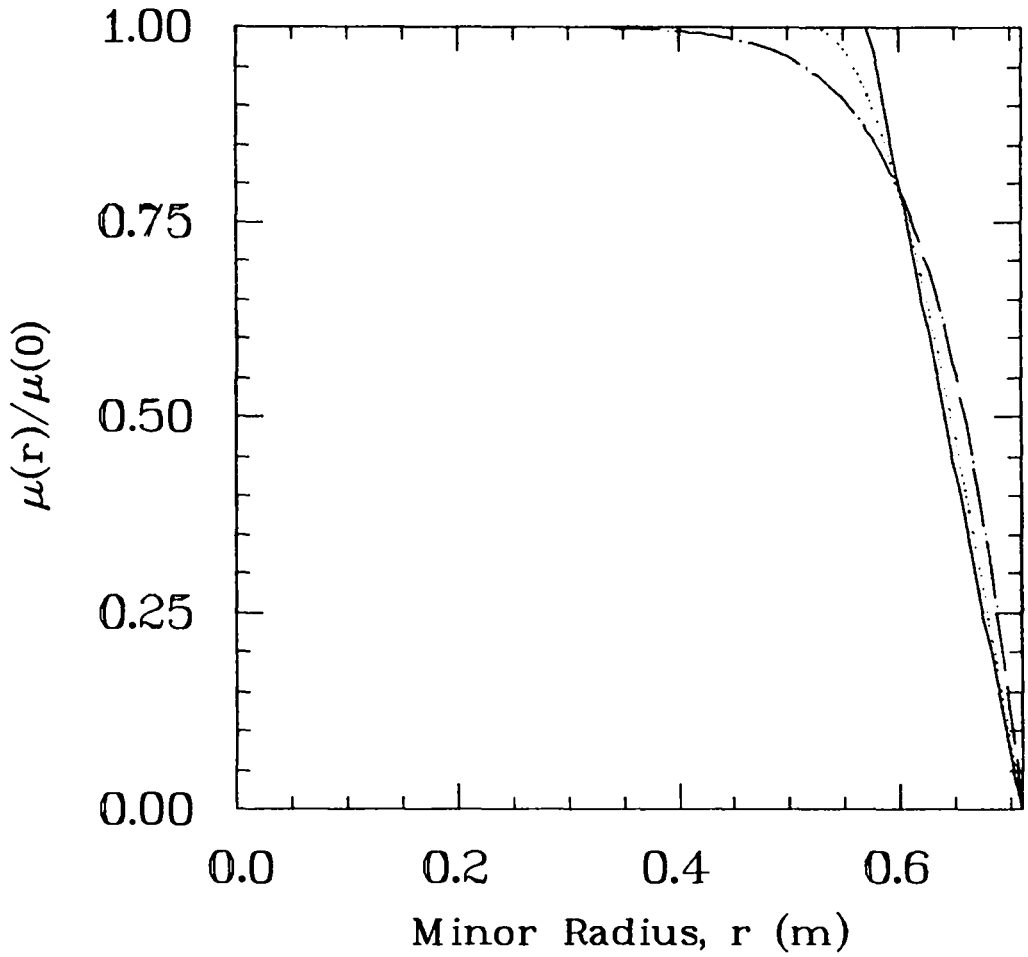

Fig. 7-2. The normalized, equal area μ profiles considered in this study are the following: the standard Modified Bessel-function Model (solid line), the cosine model (dotted line), and the parabolic profile (dashed-dotted line).

Modified-Bessel-function Model μ profile, yielding $\nu = 9.36$ and $r_b' = 0.734\ r_p$. The cosine μ profile was used in this study because the current-density (Fig. 7-3) and magnetic-field (Fig. 7-4) profiles more closely resemble the profiles from the Modified Bessel-function Model.

7.3.1.2. Magnetics

The plasma current-density and magnetic-field profiles obtained from Eqs. (1)-(3) are used by the three-dimensional magnetics model. The poloidal field is simulated by a current-carrying hoop conductor positioned in the equatorial plane at major radius R = 3.806 m. The 6-mm displacement outward from the plasma center line corresponds to the Shafranov shift as applied to an

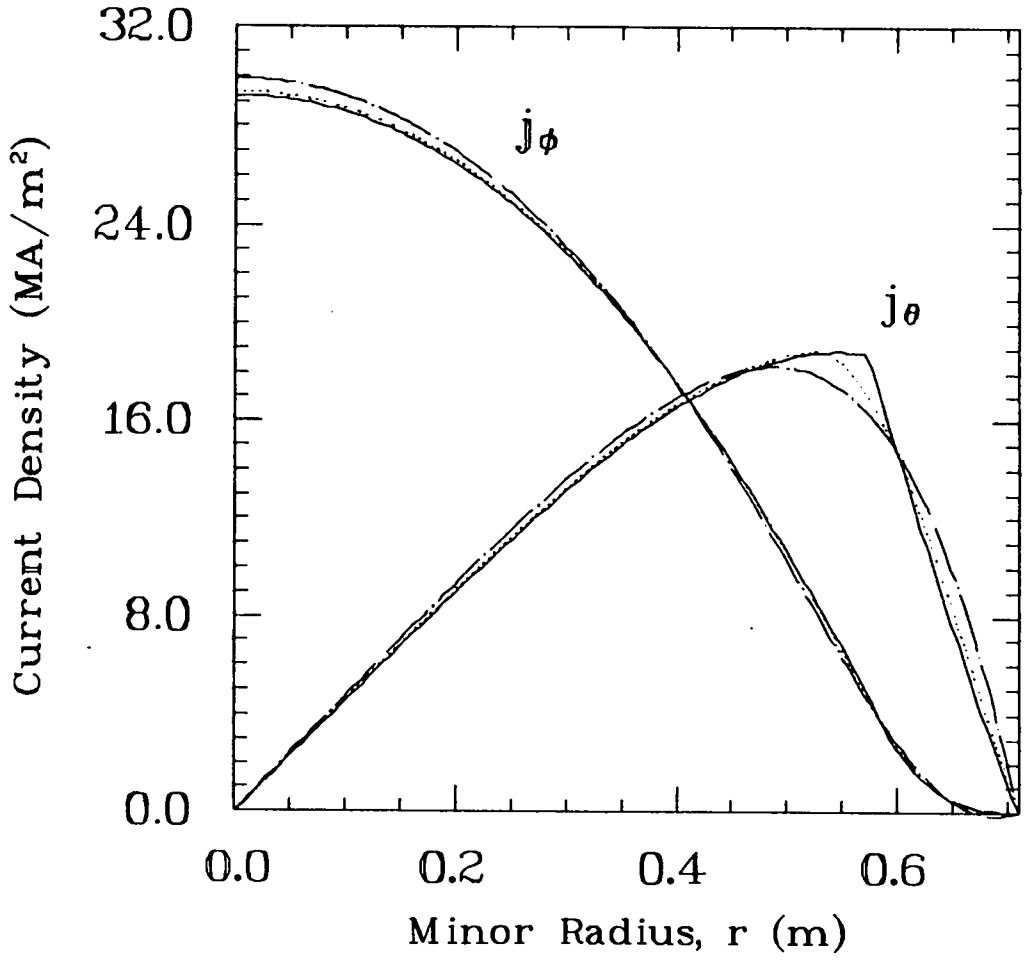

Fig. 7-3. The current density profiles corresponding to the Modified Bessel-function Model μ profile (solid lines), the cosine μ profile (dotted lines), and the parabolic μ profile (dashed-dotted lines).

RFP.[66] The toroidal current in the hoop is taken to be 18.4 MA for $r > r_p$ and varies as follows for $r \leq r_p$:

$$I(r) = 2r^{-2} \int_0^r j_\phi^{MHD}(r')r'dr' \quad , \tag{4}$$

where $j_\phi^{MHD}(r)$ is described by a cubic spline fit to the toroidal current-density profile. The toroidal field from the plasma (Fig. 7-4) is taken to be zero for $r \geq r_p$ and, for $r \leq r_p$, is determined from

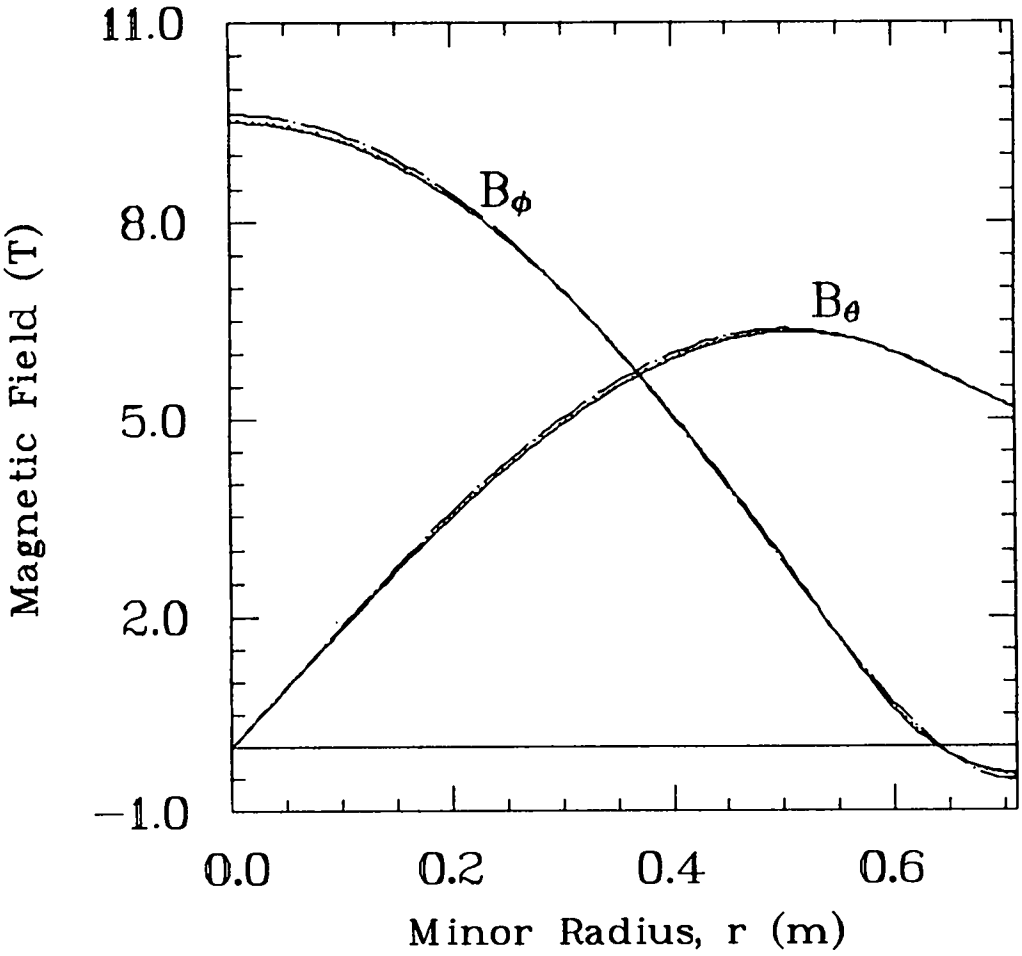

Fig. 7-4. The magnetic-field profiles corresponding to the Modified Bessel-function Model μ profile (solid lines), the cosine μ profile (dotted lines), and the parabolic μ profile (dashed-dotted lines).

$$B_\phi(r) = B_\phi^{VAC}(r)\left[1 - \frac{B_\phi^{MHD}(r)}{B_\phi^{MHD}(r_p)}\right], \tag{5}$$

where $B_\phi^{VAC}(r)$ is the toroidal vacuum field and $B_\phi^{MHD}(r)$ is the toroidal-field profile previously calculated. The effects of toroidal ripple on $j_\phi^{MHD}(r)$ and $B_\phi^{MHD}(r)$ in Eqs. (4) and (5) are simulated by scaling the minor radius according to the fluctuations observed in two-dimensional field-line tracings at the reversal-surface minor radius, r_v. These plasma poloidal and toroidal fields are added to the vacuum fields calculated by TORSIDO to complete the combined simulation of plasma and coils. The magnetic-field profiles for the combined simulation of plasma and coils are presented in Fig. 7-5, benchmarked against the infinite-cylinder MHD results. Excellent agreement is obtained between the

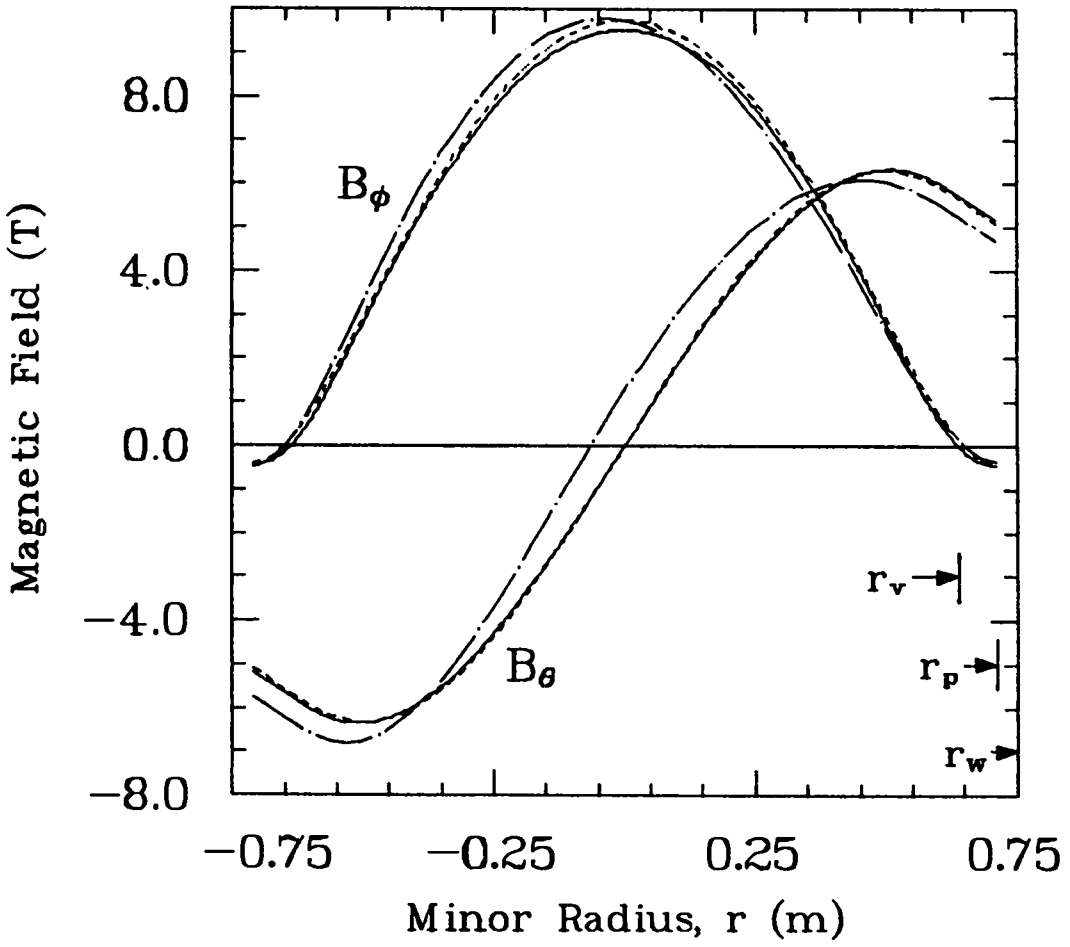

Fig. 7-5. Magnetic-field profiles from the MHD model using the cosine μ profile (solid lines) compared to the TORSIDO-calculated profiles for a vertical cut at R = 3.8 m (dashed lines) and for a horizontal cut at z = 0 m (dashed-dotted lines).

TORSIDO results and the MHD profiles along a vertical cut through the plasma. Toroidal effects produce the differences between the profiles along a horizontal cut through the plasma.

7.3.2. Scrapeoff Transport

A simple scrapeoff model used for limiters[10,29] is applied in analytic form to divertors to determine the heat-flux partition between the first-wall and divertor surfaces. This model assumes that the particle and energy transport in the scrapeoff are described by the following equations:

$$D \frac{d^2 n}{dx^2} = \frac{n}{\tau_\parallel} \tag{6}$$

$$\chi \frac{d}{dx}\left(n \frac{dT}{dx}\right) + 3D \frac{d}{dx}\left(T \frac{dn}{dx}\right) = \frac{2\gamma nT}{\tau_\parallel} , \tag{7}$$

where D is the position-independent particle diffusion coefficient, χ is the heat conduction coefficient, n is the plasma density, T is the plasma temperature, $\gamma = 2 + 1/4\ell n(m_i/m_e)$ is the enhancement of the energy flux resulting from a surface sheath potential, m_i and m_e are the masses of the ion and electron species, x is the penetration distance into the scrapeoff measured from the separatrix in this study, and $\tau_\parallel$ is the parallel confinement time. In order to simulate divertors with this model, $\tau_\parallel$ is taken to be the time of flight of an ion traveling along a field line between divertor throats:

$$\tau_\parallel = L/V_{TH} , \tag{8}$$

where V_{TH} is the ion thermal velocity and L is the field-line connection length between divertor openings. The connection length is either estimated on the basis of a two-dimensional magnetics simulation or calculated directly from a three-dimensional magnetics simulation of a divertor configuration. The solutions to Eqs. (6) and (7) are $n(x) = n_o e^{-x/\lambda n}$ and $T(x) = T_o e^{-x/\lambda T}$, respectively, where

$$\lambda_n = (D\tau_\parallel)^{1/2} \tag{9}$$

and

$$\eta \equiv \frac{\lambda_n}{\lambda_T} = \frac{[(\alpha + 3)^2 + 4\alpha(2\gamma - 3)]^{1/2} - (\alpha + 3)}{2\alpha} , \tag{10}$$

where $\alpha = \chi/D$. The density and temperature at the separatrix are given by

$$n_o = \frac{n_i \, r_p \, \tau_{\parallel}}{2 \, \tau_{pi}(1 - R^*_{Le})\lambda_n} \tag{11}$$

and

$$T_o = \frac{P_{TR} \, (1 - f_{RAD})(1 + \eta) \, \tau_{pi} \, (1 - R^*_{Le})}{4\gamma \, n_i \, \pi^2 \, r_p \, R_T} \, , \tag{12}$$

where n_i is the average plasma ion density, r_p and R_T are the plasma minor and major radii, and τ_{pi} is the particle confinement time. Since atomic processes (e.g., radiation, recombination, charge exchange) are not included in this model, a radiation fraction, f_{RAD}, and a recycle coefficient, R^*_{Le}, have been introduced into Eqs. (11) and (12). The effective plasma temperature at the first wall, which is an important factor in sputtering, is $T_w = T_o^{-x_\ell/\lambda_T}$, where x_ℓ is the distance between the separatrix and the first wall. The heat fluxes incident on the first wall and the divertor channel wall are

$$q_w = \frac{P_{TR} \, (1 - f_{RAD}) \, e^{-x_\ell(1 + \eta)/\lambda_n}}{2\pi \, r_w \, (2\pi \, R_T - Nd)} \tag{13}$$

and

$$q_{DIV} = \frac{P_{TR} \, (1 - f_{RAD}) \, [1 - e^{-x_\ell(1 + \eta)/\lambda_n}]}{N \, A_{DIV}} \, , \tag{14}$$

where r_w is the first wall radius, d is the toroidal width of the divertor throat opening, and A_{DIV} is the area within the divertor available for uniform heat absorption.

7.4. Divertor Magnetics Design

7.4.1. Design Constraints

The limiter-based CRFPR design to which divertors will be added is taken from Ref. 10, with relevant parameters being summarized in Table 7-I. The follow-on design described in Sec. 3 and Appendix A is based on 0.10 m thickness added to the blanket ($\Delta b = 0.775$). The Ref. 10 design is retained for this divertor study in anticipation of improved blanket performance (i.e., low heat loads, no limiter, eased tritium breeding) for the divertor case, although

TABLE 7-I

KEY CRFPR DESIGN PARAMETERS[10]

Parameter	Value
Fusion power, P_F(MW)	2,732.
Thermal power, P_{TH}(MW)	3,365.
Net electrical power, P_E(MWe)	1,000.
Neutron wall loading, I_w(MW/m^2)	19.5
Reversal surface radius, r_v(m)	0.64
Plasma minor radius, r_p(m)	0.71
First-wall radius, r_w(m)	0.75
Plasma major radius, R_T(m)	3.80
Blanket/shield thickness, Δb(m)	0.675
Number of TFCs, N_{TF}	24.
Toroidal field, $B_\phi(r_p)$(T)	0.403
Poloidal field, $B_\theta(r_p)$(T)	5.18
Toroidal plasma current, I_ϕ(MA)	18.4
Pinch parameter, $\Theta = B_\theta(r_p)/\langle B_\phi \rangle$	1.55
Reversal parameter, $F = B_\phi(r_p)/\langle B_\phi \rangle$	-0.12
Poloidal beta, β_θ	0.23
Plasma transport power, P_{TR}(MW)	571.8
Plasma density, $n_i(10^{20}/m^3)$	6.55
Plasma temperature, T_i(keV)	20.
Confinement time, τ_{pi}(s)	0.59
Edge safety factor, $q \simeq \lvert r_p F/\Theta R_T \rvert$	0.015
COE (mills/kWeh)	46.2

eventually a divertor-specific neutronics study will have to be performed. A minimum blanket/shield thickness of 0.1 m is specified between the plasma and the divertor coils, and an x_ℓ = 0.04-m-thick scrapeoff layer[10] is positioned between the separatrix and first wall. The current density in the divertor coils is constrained to be below 50 MA/m^2, following the MARS choke coil design.[67] Reduced self-sputtering of the first-wall material requires T_w < 50 eV. Such a relatively low temperature requires that either a large fraction, f_{RAD}, of the energy is shed from the plasma as radiation and/or significant edge-plasma recycling occurs. This requirement for high edge-plasma radiation and/or recycle is common to both divertors and limiters. The Ref. 10 limiter design invoked a radiation fraction f_{RAD} = 0.9 and an edge-plasma recycle coefficient R^*_{Le} = 0.8. With the good energy confinement reported for tokamak divertor experiments,[58,59] f_{RAD} = 0.5 seems more appropriate for the divertor cases being considered here. The tradeoff between f_{RAD}, R^*_{Le}, T_o, T_w, and n_o is depicted on Fig. 7-6, assuming a particle diffusivity D ≃ 1 m^2/s, a thermal diffusivity χ = 3D, and a connection length L = 320.87/N - 1.43 m based on a preliminary two-dimensional magnetics analysis of an SD reported in Ref. 60. A value of R^*_{Le} > 0.96 is necessary to yield T_w = 50 eV for f_{RAD} ≃ 0.5, which is consistent with experimental observations.[58] If an intrinsic plasma-edge recycle of this magnitude is not physically possible, then a low scrapeoff temperature must be maintained by gas injection (presumably from the divertor channel) to ensure the design particle flow rate. The heat fluxes to the first-wall and divertor surfaces, assuming divertor surface areas (m^2) of 12.11N and 7.02N for SD and BDs, respectively,[60] are given in Fig. 7-7 as functions of the number of divertors, N. Assuming a design limit of 6 MW/m^2 for q_{DIV} and/or q_w,[10] the minimum number of SDs is four and the minimum number of BDs is eight. Outboard maintenance of either divertor imposes an additional constraint on both divertor size and PFC and TFC locations.

7.4.2. Analysis of Basic Configuration

The three-dimensional simulation of the plasma, the PFCs, and the TFCs of the basic configuration is shown in Fig. 7-8. Magnetic islands arising from the toroidal-field ripple with ~ 0.16-m widths were expected based on an infinite-cylinder model[68] using the toroidal-field ripple on the outboard side in the equatorial plane.[10] The field-line tracings revealed, instead, flux surfaces with radial widths or volumes. The asymmetry in the toroidal-field ripple, as depicted schematically in Fig. 7-9, causes this asymmetry. The toroidally

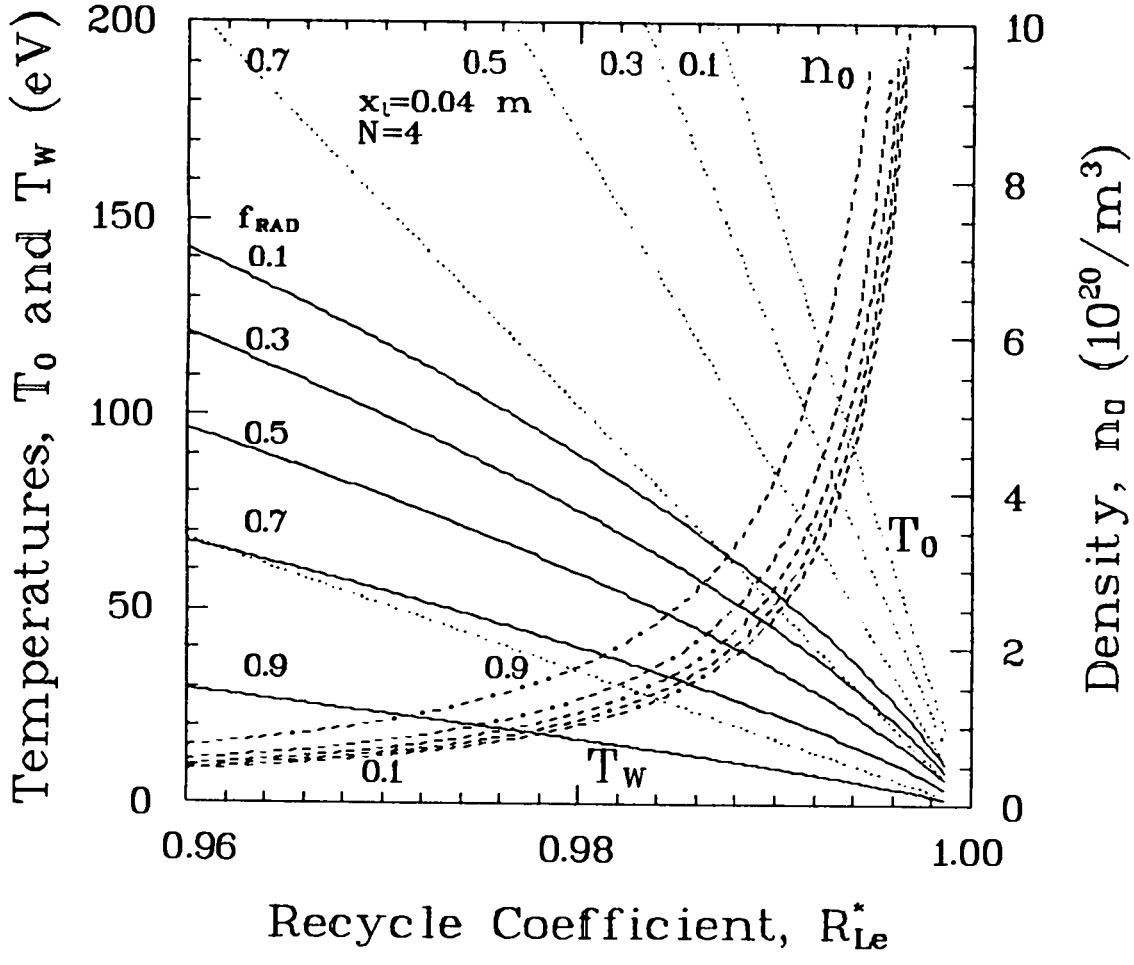

Fig. 7-6. Separatrix temperature and density and first-wall temperature as functions of edge-plasma recycle coefficient for a range of radiation fractions, f_{RAD}.

symmetric poloidal flux surfaces connect a set of outboard toroidal-field lines at some toroidal angle, which is taken as a coil plane in Fig. 7-9. When field lines progress toroidally to a midplane, the poloidal flux surfaces map the set of inboard field lines into a different set of outboard field lines and vice versa. This mapping results in blurred magnetic surfaces, shown in Fig. 7-8 with radial widths of 2-8 mm for field-line tracings of 1.8-km length. This dimension is comparable to the 8-mm difference in the amplitude of the ripple from inboard to outboard locations in the equatorial plane.

The radial width of the flux surfaces is not a concern for an RFP unless this width becomes larger than the distance $\delta' = r_p - r_v$ for a field-line tracing equal to or greater than a collisional mean-free-path (2 km for

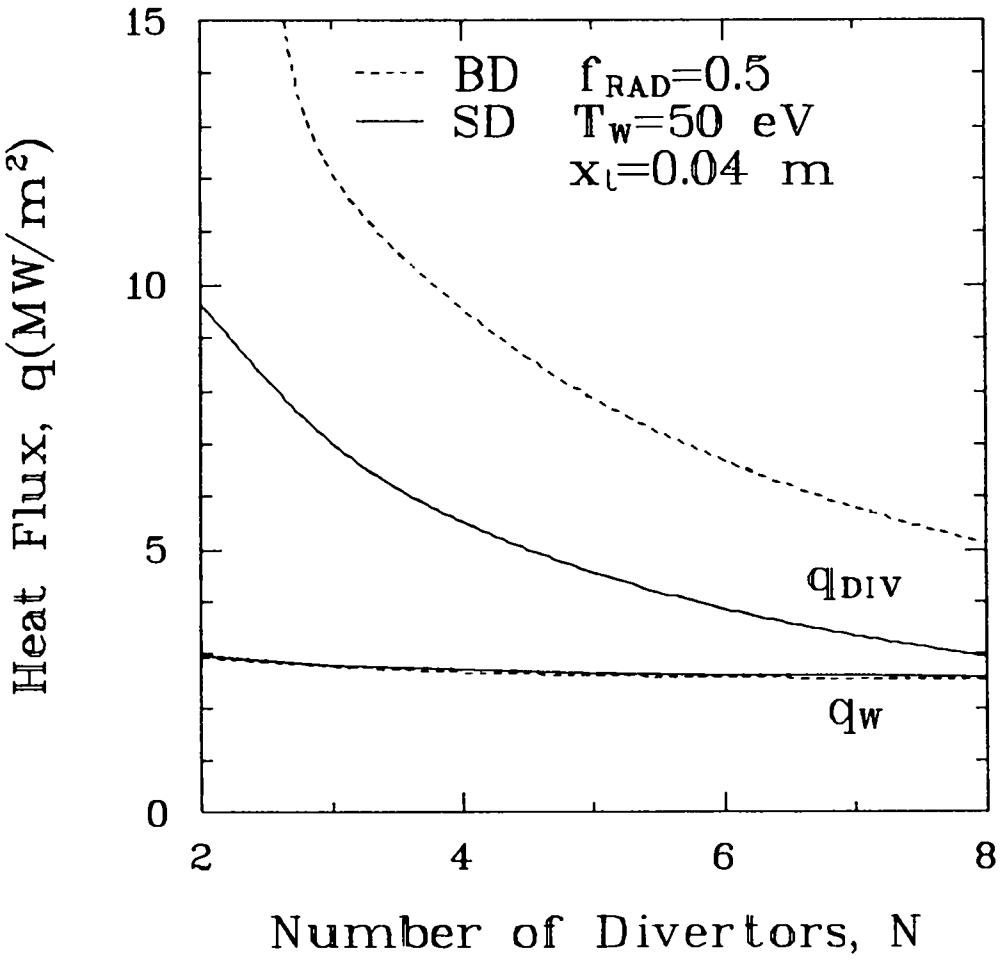

Fig. 7-7. Heat fluxes incident on the first-wall and divertor surfaces as functions of the number of divertors for both SD and BD cases.

deuterium-deuterium collisions and ~ 30 m for deuterium-electron collisions for 10-keV, $2(10)^{20}$-m^{-3} plasmas). As confinement may occur primarily in this region, field lines which connect the central plasma directly to the plasma surface would short-circuit the confinement process. The basic configuration is acceptable with respect to this constraint, since the surface width of 2-8 mm is much smaller than $\delta' \simeq 70$ mm. Flux-surface or magnetic-island widths in excess of δ' would require additional TFCs.

7.4.3. Analysis of Bundle Divertors (BD)

The BD offers strong maintenance advantages associated with a plug-in capability.[60] The parameters and physical layout for the basic configuration with 24 BDs are shown in Table 7-II and Fig. 7-10, respectively. The edge-plasma calculations reported in Sec. 7.4.1. indicate a BD connection length of

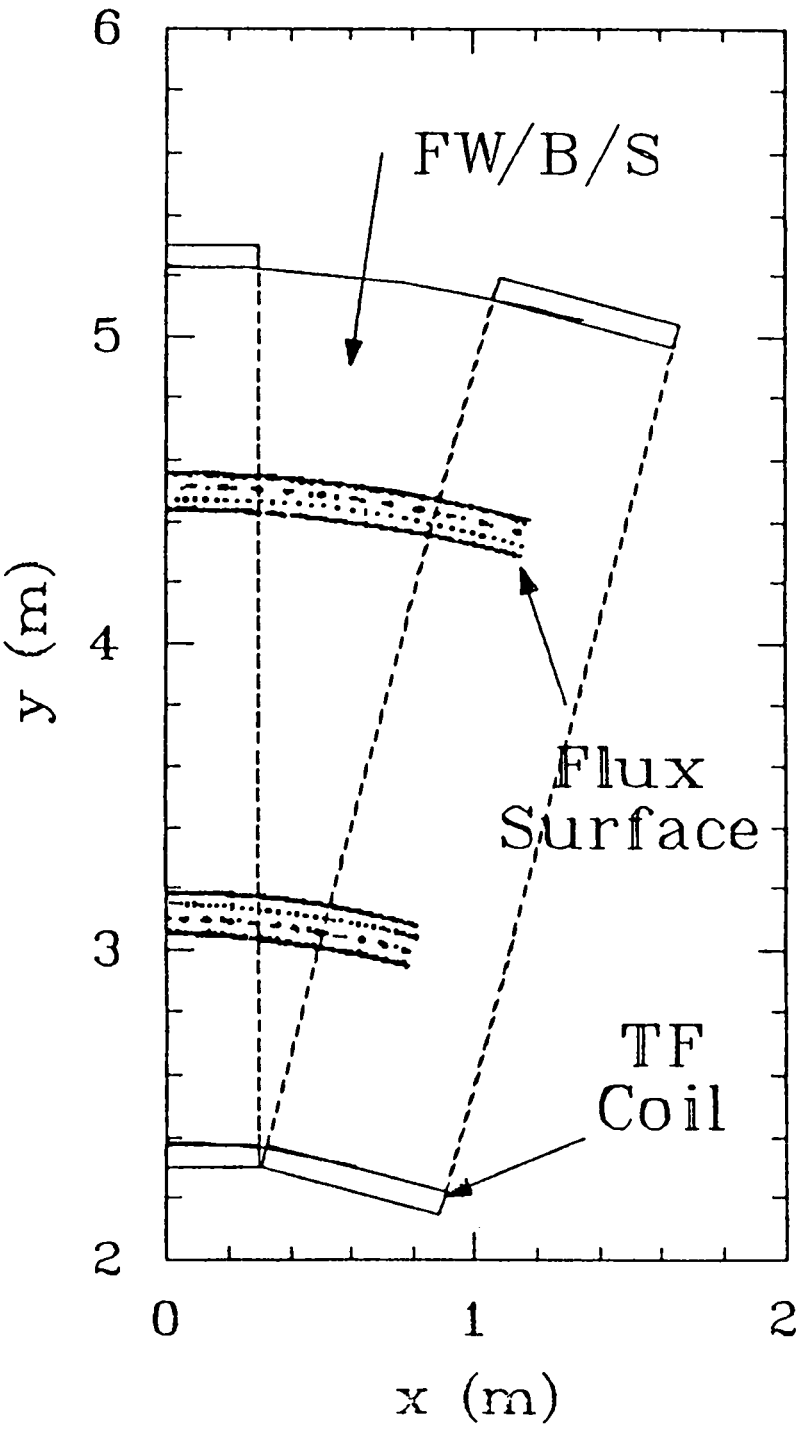

Fig. 7-8. The puncture plots (the intersection of a field line with the equatorial plane) for starting minor radii of 0.63, 0.67, 0.71, and 0.75 m and the toroidal angle of $\pi/48$ displayed in one field period. The reversal surface occurs at $r_v = 0.64$ m.

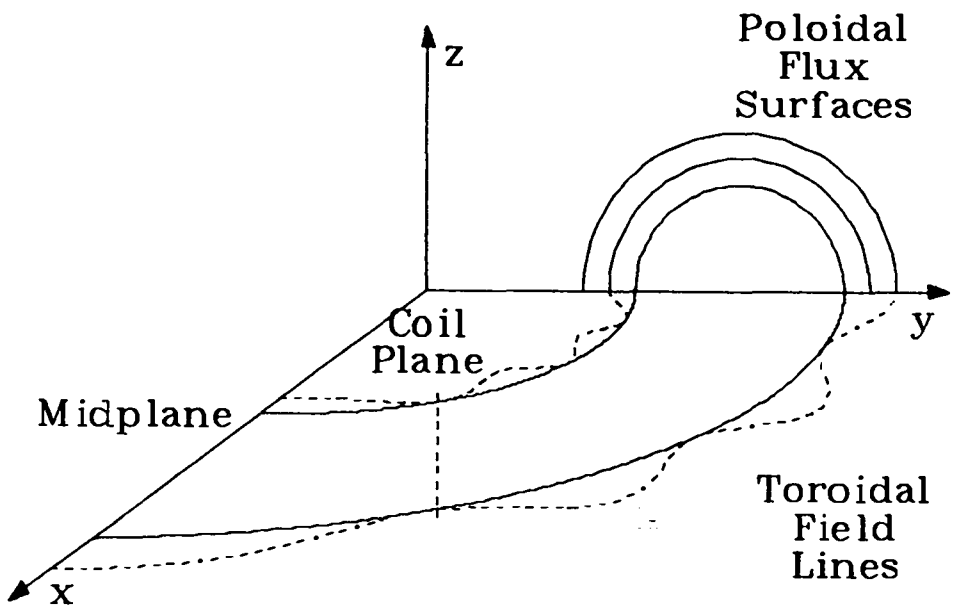

Fig. 7-9. Asymmetric toroidal-field ripple shown in the equatorial plane. Toroidally symmetric nested-poloidal-flux surfaces connect inboard toroidal-field lines to outboard field lines.

TABLE 7-II
CRFPR(20) DIVERTOR COIL DESIGN PARAMETERS

Toroidal-Field Bundle Divertor (BD)

Parameter	Value (forward/middle/rear coil)
Current (MA)	0.13/0.25/0.45
Major radius (m)	4.767/5.05/5.45
Height (m)	1.0/1.0/1.0
Width (m)	0.125/0.125/0.15
Current density (MA/m^2)	40/40/30
Angle (radians)	0.95/1.10/1.30

Toroidal-Field Poloidally Symmetric Divertor (SD)

Parameter	Value (nulling/flanking coil)
Current (MA)	-0.8/0.4
Major radius (m)	3.897/3.870
Minor radius (m)	1.088/0.970
Current density (MA/m^2)	50/40

~ 35 m (corresponding to N = 8) is needed, above which appreciable cross-field diffusion to the first-wall is expected to occur. A field line is traced for more than 300 m (more than once around the torus) without entering any of the 24 divertor channels. The puncture plots associated with the field-line tracing for the 24 BDs are also shown in Fig. 7-10. As a result of these inordinately

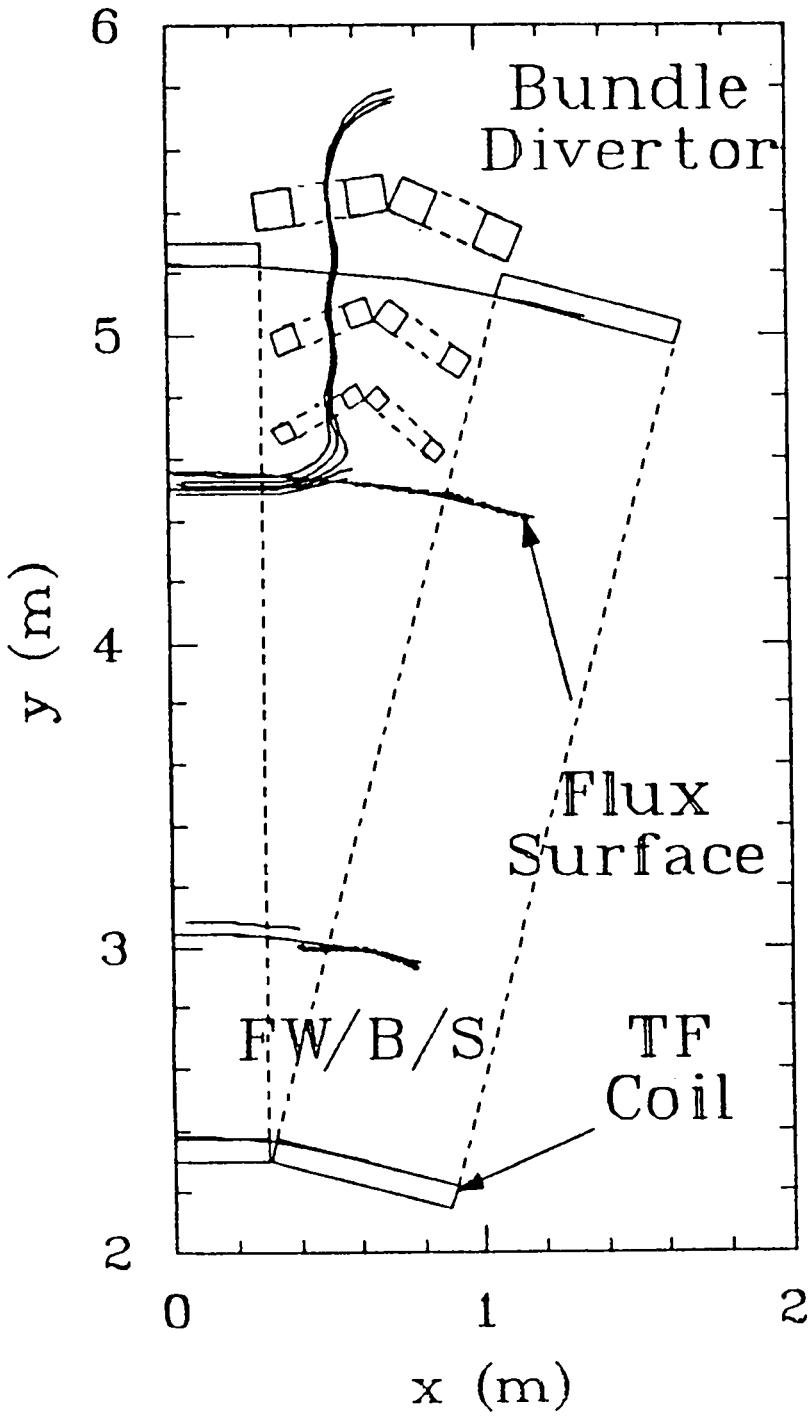

Fig. 7-10. The two-dimensional field-line tracings (solid lines) for 24 BDs for r = 0.69, 0.705, 0.715, 0.73, and 0.75 m on the outboard side and for r = 0.71 and 0.75 m on the inboard side. Also shown is the puncture plot for the three-dimensional simulation of plasma and coils for r = 0.73 m.

long connection lengths (> 1 km), most particle and associated energy loss would be transported to the first wall before entering a BD channel. Consequently, the toroidal-field bundle divertor is not considered feasible for the low-q RFP configuration.

7.4.4. Analysis of Symmetric Divertors (SD)

Interest in the SD principally rests with an inherently shorter connection length compared to the BD. The physical layout of a field period of the basic configuration with four SDs is shown in Fig. 7-11; design parameters are also given in Table 7-II. In order to permit the unobstructed extraction of the divertor coils, the TFCs have been thickened radially inward by 0.05 m, corresponding to the thickness of the defunct vacuum plenum needed for the limiter-based CRFPR(20) design.[10] The TFC cross-sectional area is preserved, however. The separatrix surface was symmetrized as well as possible to minimize the broadening of flux surfaces in the plasma at the expense of the symmetry of the divertor channel. Each divertor coil lies on a ray emanating from the major axis in order to symmetrize coil effects in a toroidal angle. The centers of the divertor coils are shifted radially outward from the plasma center line in order to equalize the magnitude of the field perturbations produced by the divertor coils about the plasma, as required by the 1/R dependence of the toroidal field. In addition, Fig. 7-11 shows the field-line tracings for the two-dimensional simulation as well as a puncture plot for a field-line tracing started at r = 0.68 m and at a toroidal angle corresponding to half way between divertors. This puncture plot demonstrates good flux surfaces with radial width less than 10 mm in the 70-mm-thick confinement region between the reversal layer, r_v and the first wall, r_w.

The existence of particle paths and their distribution into the divertor are also of interest to any eventual engineering design. Shown in Fig. 7-11 is a combination of puncture plots for eighty field lines started at a toroidal location half way between SDs, each being equally spaced on a poloidal flux surface that passes through the R = 3.07-m point and terminates in the divertor-coil plane. Such a calculation avoids the process whereby the asymmetry of the radial extent of the divertor channel in the divertor-coil plane takes a surface of small radial width upon entry into the divertor channel and greatly broadens the radial width of the surface upon exiting the divertor. This procedure nevertheless demonstrates that a path within the scrapeoff layer outside the separatrix exists for particles to enter the divertor without first intersecting

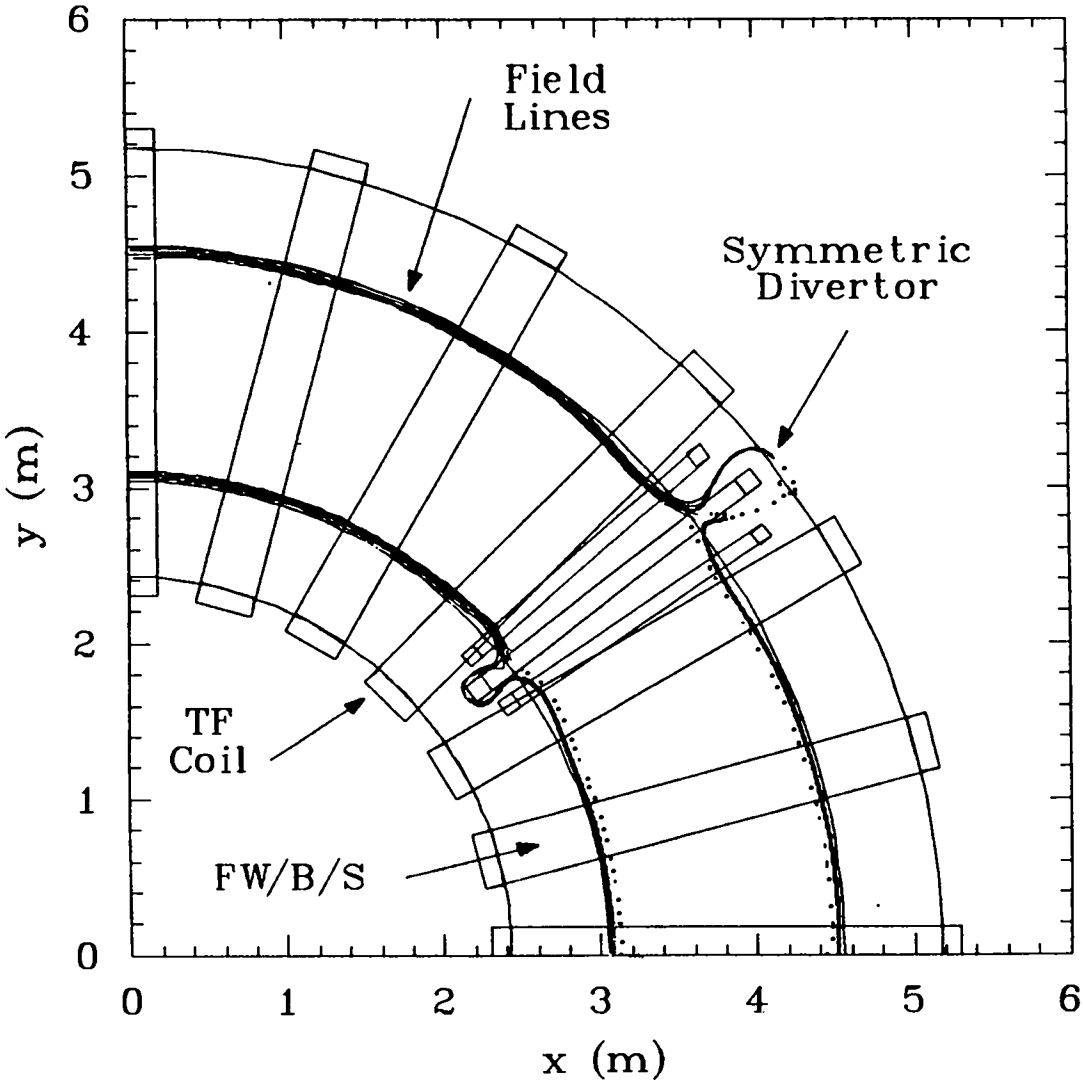

Fig. 7-11. The two-dimensional field-line tracings (solid lines) for 4 SDs for r = 0.69, 0.705, 0.715, 0.73, and 0.75 m. Also shown are the puncture plots for the three-dimensional simulation of plasma and coils for r = 0.68 and 0.73 m.

the first wall or reentering the plasma. The puncture points on Fig. 7-11 are uniformly distributed poloidally for the first 0.2 m into the blanket and, thereafter, are distributed uniformly on the inboard side only. Future efforts will complete the SD symmetrization.

The results of this calculation indicate an average divertor connection length of 73.3 m and an average connection length between divertor channel openings of 67.5 m. The two-dimensional calculations based on four SDs

indicated the latter connection length to be 72.8 m. The shorter connection length predicted by the full simulation results from the 1/R dependency of the toroidal field; the larger toroidal field on the inboard side more heavily weighs the smaller major radius at that point. The results of the three-dimensional simulations of the SD indicate a small impact on the plasma and a reasonable connection length between divertor plates.

7.4.5. Divertor Design Parameters

The connection lengths reported in the previous section and the scrapeoff model yield the design parameters of Table 7-III. Only a moderate incremental cost (5%) is associated with the addition of divertors assuming that the cost of electricity (COE) scales inversely with net electrical power. The blanket volume loss of only 10.4% pessimistically assumes no breeding can occur between the outermost divertor coils and, therefore, requires a total tritium breeding ratio greater than 1.12.

TABLE 7-III

PRELIMINARY ESTIMATE OF IMPACT ON REF. 10 CRFPR(20) FUSION-POWER-CORE DESIGN USING SD IMPURITY CONTROL

Parameter	Value	
Dimension of model	2D	3D
Number of divertors	4	
Blanket loss (%)	10.4	
Ohmic power (MW)	47.7	
COE increase (%)	5.0	
First-wall area decrease (%)	5.36	
Divertor/first-wall area (m^2)	0.65	
Divertor efficiency	0.93	0.94
Power to first wall (MW)	305.7	304.3
Power to divertor (MW)	266.1	267.5
First wall heat flux (MW/m^2)	2.87	2.86
Divertor heat flux (MW/m^2)	3.82	3.84
Typical edge plasma conditions		
• Edge-plasma temperature (eV)	143.4	147.7
• Wall-plasma temperature (eV)	50.	
• Edge-plasma density ($10^{20}/m^3$)	1.46	1.38

The divertor maintenance can be accomplished by one of two approaches. The outboard quadrants of the PFC set can be simultaneously raised and lowered to permit horizontal extraction. An ~ 0.7-m vertical lift is required for the PFC set, as shown in the upper half of Fig. 7-12. A second, less-complicated maintenance scheme allows a permanent PFC clearance at the outboard side that is sufficient to permit horizontal extraction. This latter design is shown in the lower half of Fig. 7-12 and would dissipate an additional 19.1 MW of ohmic power in the PFC (mainly EFC) set. Both PFC designs provide access to the high-performance coils and divertor channel surfaces, where frequent maintenance is expected.

7.5. Conclusions

The three-dimensional simulation of both plasma and coils indicates that the broadening of flux surfaces because of toroidal-field ripple asymmetries is more important than the magnetic islands expected from the toroidal-field ripple. Flux-surface broadening should be present in any toroidal device with TFCs and another toroidally symmetric field coil set (e.g., tokamaks).

The SD is clearly preferable to the BD on the basis of reduced connection length. The presence of an SD does not significantly perturb the flux surfaces in the outer region of the RFP plasma and, therefore, should not significantly affect confinement. The SD preserves the FPC compactness in a maintainable geometry. Preliminary analysis indicates manageable heat fluxes (~ 3 MW/m^2) on all surfaces for a ~ 5% cost penalty. The results of this study indicate that a more detailed design of both the divertor channel and FPC integration (i.e., coolant manifolding/headering, heat flux distributions, etc.) is warranted.

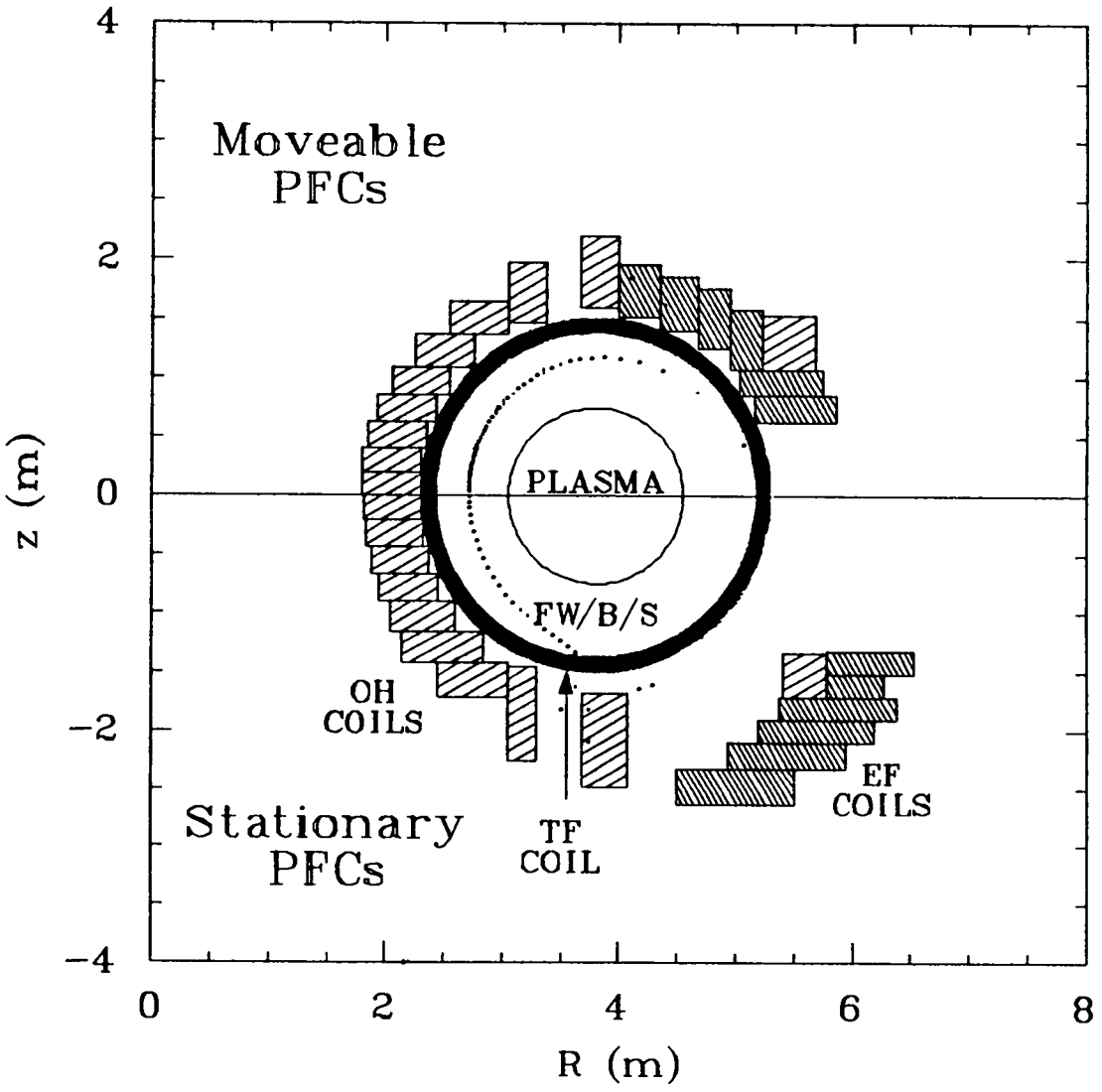

Fig. 7-12. The top half of the PFC set for the basic configuration and the bottom half of the PFC set for the easier divertor maintenance scheme. Also shown is the puncture plot (the field line intersections with the divertor-coil plane) for the three-dimensional simulation of plasma and coils, using the lower PFC set.

8. CONCLUSIONS AND RECOMMENDATIONS

This study indicates that substantial reductions are possible in the mass and cost of the FPC. These reductions allow the FPC to become a relatively insignificant part (< 5%) of the total direct capital cost of the power plant. The mass power density for the compact RFP reactor exceeds the threshold target of 100 kWe(net)/tonne suggested on the basis of generic arguments[4] and adopted recently[6] as a definition of "high power density." Furthermore, this threshold target is exceeded by factors of 5-10 for a range of neutron first-wall loadings. These high mass-power-density systems inject an important resiliency into the overall cost of fusion power that can accommodate unexpected shortfalls in physics goals (e.g., β, χ_E, etc.) and underestimates of both required needs and associated unit costs (e.g., \$/kg, \$/m^3, \$/Wt, etc.) attributed to key FPC subsystems. Furthermore, both the risk and cost (time and dollars) of the development of fusion may be significantly reduced, although this perceived benefit of high mass power density or low mass utilization, particularly when accompanied by low unit power, remains to be quantified.

The conclusions stemming from this follow-on study, as well as from the Ref. 10 framework study, are present at three levels. First, Sec. 8.1. summarizes general findings, after which more design-specific conclusions and findings are given in Sec. 8.2. Although this follow-on study did not focus on physics issues it seems appropriate to list these issues very briefly in Sec. 8.3. A short list of recommendations for future, more-detailed study of the RFP reactor concept is given in Sec. 8.4.

8.1. General Conclusions

The unique character of the poloidal-field-dominated RFP allows both of the following elements in the general prescription for increased mass power density to be invoked:

- increased plasma power density and higher neutron first-wall loading in a plasma of reduced volume, and
- shrinkage of the engineering structure (first wall, blanket, shield, coils) surrounding this higher performance plasma.

Both means to increase mass power density and reduce capital cost are relatively independent of each other, but the efficacy of both is strongly dependent on the

confinement approach. The CRFPR(20) design used both approaches to achieve mass power densities as high as 900-1000 kWe/tonne, which in value is comparable to light-water fission reactors. Although this resistive-coil, high-I_w design was optimized within reasonable design margins and constraints, the combination of $I_w \simeq 20$ MW/m^2 and high coverage (poloidal) pumped-limiter impurity control requires the following advanced, high-performance systems:

- copper-alloy first walls and limiter surfaces to deal with the high surface heat loads (5-6 MW/m^2),
- a separate cooling system with high velocity pressurized water for the first-wall and limiters to deal with the high heat fluxes, and
- a self-cooled, liquid-metal breeder blanket (PbLi) to deal with high local power density and the need to enhance tritium breeding.

In addition to limiting material choices, these design necessities lead to the following uncertainties and/or penalties:

- uncertainty of the radiation-damage database for copper alloy and the development needed to achieve the radiation lifetimes upon which the CRFPR(20) design is based (15 MWyr/m^2 or $\sim$ 210 dpa);
- the required development of a materials database pertaining to alloy stability, corrosion/erosion, fabricability, radwaste, and afterheat control when copper alloy is used as a semi-structural element in a separately cooled first wall; and
- reduced thermal-conversion efficiency, diminished operational safety (i.e., active short-term cooling of afterheat in limiters), and increased complexity related to dual-media coolant and power-conversion systems.

These key uncertainities can be reduced, if not eliminated, by invoking one of the following design changes:

- Maintain the minimum-COE $I_w \simeq 20$ MW/m^2 design, but invoke an impurity-control scheme based on efficient magnetic divertors to reduce the heat load on the first wall and to remove the high-heat-flux surface to regions outside the main plasma chamber and to regions of lower neutron flux, also allowing better maintenance access to these critical components.
- Decrease I_w to $\sim$ 5 MW/m^2, where the first wall can receive the full plasma power loss, but cooling as an integral part of the blanket is possible. Blanket options other than self-cooled liquid metals also become available.

A strong impetus for FPCs at or below the mass and volumes suggested by the CRFPR(20) design, nevertheless, exists for the following reasons:

- reduced development cost and enhanced probability for success because of a flexible and affordable development path;
- rapid extension of learning curves to assess availability on the basis of an affordable experience of failure (availability cannot be improved without actual operating experience);
- factory fabrication of FPCs and reduced nuclear envelope for the power station, allowing less-expensive conventional items to be used more extensively throughout the plant;
- extensive non-nuclear pre-testing and FPC overstressing prior to commitment to service in the reactor room, thereby providing a strong, effective quality assurance and rapid FPC restarts; and
- single-piece maintenance of a fully pretested FPC to reduce down time.

Although not directly reflected in the COE models generally used to assess the prospects for fusion, these attributes are expected to exert a strong positive impact on plant availability and COE. Maintaining the FPC at or below the CRFPR mass and volume while decreasing I_w, however, will a) result in lower unit power and higher COE because of lost economies of scale or b) require multiplexing a number of "derated" FPCs of the CRFPR(20) size into a ~ 1000-MWe(net) power station. The latter approach allows utility expansion with reduced capital at risk and an improved capability to match capacity and demand while promising increased plant availability. The resistive-coil FPCs of the kind examined herein, however, become inherently inefficient as the FPC power output is lowered; for sufficiently low power output, superconducting coils may offer an economic edge for these higher-COE units.

8.2. Design-Specific Conclusions

The reactor framework and FPC integration study reported herein and in Ref. 10 has quantified a number of issues related to high-power-density FPC operation. Key design-specific conclusions and/or findings are summarized below:

- Design Resiliency: High-mass-power-density or low-mass-utilization, low-COE FPC designs are possible for neutron first-wall loadings over the range 5-20 MW/m^2. These designs are properly constrained by adequate engineering safety margins, but the 20-MW/m^2 designs based on pumped-limiter impurity

control require water-cooled copper alloys for the high-coverage limiter surfaces, as well as for the first wall.

- Neutron First-Wall Loading Limits: For closed-field plasmas requiring edge-plasma definition and active impurity control by limiters, steady-state fusion-neutron first-wall loadings much above ~ 20 MW/m^2 seem technologically improbable.

  - Alloy/coolant systems capable of handling steady-state heat fluxes much above ~ 5 MW/m^2 in an engineering system delivering power at a thermodynamically interesting temperature could not be identified. The copper-alloy/water-coolant system operates at this limit (~ 5 MW/m^2) with little erosion margin allowed at either side of the coolant tube. Rejection of the energy shed by the plasma at $\leq 100^{\circ}C$ will allow heat fluxes in excess of ~ 10 MW/m^2 for the Cu/H_2O system, however.

  - Local blanket power densities, particularly near regions that strongly moderate the fusion neutrons (i.e., H_2O coolant headers and manifolds), will be high (350-400 MW/m^3) at neutron first-wall loadings of ~ 20 MW/m^3. Self-cooled liquid-metal blankets will be required for these conditions. Even for the moderate magnetic fields in the CRFPR(20) blanket, the PbLi coolant pressure can approach 0.7 MPa (100 psi) in attempting to hold corrosion-related structural temperatures.

- Limits for Integrally Cooled First Wall: The CRFPR(20) design leads to a separately cooled first wall, which leads to a complicated dual-media heat-transport system of reduced efficiency, as well as adding problems of coolant-coolant interaction. Elimination of a separately cooled first wall will require the neutron first-wall loadings to be below ~ 5 MW/m^2. This CRFPR(5) design for the same 1000-MWe(net) power output requires an FPC with twice the volume and mass, halving the mass power density to 400-500 kWe(net)/tonne. Although the COE increases by only 10-15% for this CRFPR(5) design, the single-piece maintenance option becomes less likely.

- Impact of Low Neutron First-Wall Loadings: Compared to the 5-MW/m^2 CRFPR(5) design ($\eta_{TH} = 0.385$), the CRFPR(20) must operate with a reduced thermal-conversion efficiency ($\eta_{TH} = 0.351$). The more costly dual-media coolant system required for the CRFPR(20) delivers ~ 46% of the total thermal power through the pressurized-water coolant circuit. This percentage is higher than the $(1 + 5/Q_p)/(4M_N + 1) \simeq 0.16$ theoretical minimum because of a) the thickness of the first wall/second wall, b) nuclear heating in water-coolant manifolds and headers, and c) back leakage of heat from the PbLi blanket to the first wall/second wall. Recovery of all thermal power at the higher PbLi temperature, except for the ~ 16% delivered to the water-cooled limiter, amounts to a factor of 1.086 increase in thermal-conversion efficiency or a ~ 9% decrease in COE for the CRFPR(5) design. The total impact on COE depends on the route to lower neutron first-wall loadings.

  - If the CRFPR(5) design is achieved by lowering the total output power while maintaining the CRFPR(20) fusion-power-core size, the increased recirculating power fraction and the unfavorable nuclear economy of scale more than cancel the advantage of high thermal-conversion efficiency.

- Multiplexing about four derated CRFPR(20) FPCs to give 5-MW/m^2 neutron first-wall loading in a ~ 1000-MWe(net) plant will also show an increased COE (30-40%) compared to the base-case CRFPR(20) design, again canceling any advantage of increased thermal-cycle efficiency.

- Achieving the CRFPR(5) design and higher thermal-conversion efficiency in a thermal hydraulically simplified FPC by simply increasing size and mass by a factor of approximately two is expected to give a COE that is close to the base-case value. The option for single-piece maintenance, however, most likely will be lost.

- Impact of Divertors: In addition to providing better isolation of the plasma, magnetic divertors can significantly reduce first-wall heat fluxes, remove the plasma-interactive high-heat-flux surfaces to regions of less intense neutron flux, and possibly allow neutron first-wall loadings above ~ 5 MW/m^2 with integrally cooled first walls and blankets.

  - Considerations of plasma beta, plasma confinement, stored energy, forces, and ohmic losses lead to magnetic divertors based on the minority toroidal field for the RFP. Further consideration of field-line connection length leads to the choice of a poloidally symmetric toroidal-field divertor (SD) for the CRFPR(20).

  - Four SDs will be required for the CRFPR(20) with ~ 5% loss in first-wall area, ~ 10% loss in blanket volume, ~ 50 MW of added power consumption, and a ~ 5% increase in COE.

  - A simplified edge-plasma model predicts first-wall heat flux that remains significant (2-3 MW/m^2), and better isolation of the plasma from the first wall will be required if separately cooled first walls are to be eliminated.

  - Divertor maintenance without FPC removal is possible, representing a distinct advantage over the permanently fixed poloidal pumped limiters envisaged for the CRFPR(20) design.

- Reactor Building Size: The feasibility assessment of single-piece FPC installation and maintenance required preliminary estimates of sizes and locations of key components and major equipment housed in the reactor building (vacuum systems, pipe runs, pumps, steam generators, superheaters, tritium cleanup systems, dump tanks, access rooms, etc.). Although the FPC volume for the CRFPR(20) is 4.5% that of STARFIRE[1] and only 3.1% that of MARS,[2] the reactor building is 73-82% that reported for STARFIRE and 52-59% that suggested for MARS. The ranges indicate the vertical (low) and horizontal (high) FPC replacement schemes. The reactor room is 21-24% of the reactor-building volume for the CRFPR(20). The majority of this ~ 300-$/m^3 building volume is occupied by the aforementioned heat-transport equipment.

- Single-Piece FPC Replacement: Two single-piece FPC replacement schemes were considered: a) vertical removal by a crane and b) horizontal removal by transhaulers. In both cases the FPC is located in a vacuum tank to which is affixed compound cryogenic vacuum pumps. Although the horizontal

maintenance scheme requires less overhead (no crane), a larger vacuum tank is required, and to within ~ 12% both approaches require comparable reactor building volumes. The estimated maintenance times for both vertical and horizontal maintenance schemes were within 10-15%, both being on the order of 10-13 days (for costing purposes, 28 days was assumed), and the required remote disconnect and motion technologies appear equally difficult. Both approaches also share an important but difficult-to-quantify attribute: the ability to install an FPC that has experienced the highest level of pre-operational testing and non-nuclear service simulation.

- Afterheat Control: The afterheat power density of copper expressed as a fraction of full power density is 2-3 times greater than for HT-9 ferritic steel (blanket structure) for approximately the first hour after shutdown. This situation coupled with the higher power density for the CRFPR(20) design requires an active emergency cooling system (ECS) for the limiters to guard against damage (melting) in event of a loss of water coolant. Natural circulation of a properly designed PbLi coolant circuit should protect the copper-alloy first wall against damage in event of a loss of active pressurized-water or PbLi cooling. The ECS required to protect the limiters is not demanding in terms of duty time (1-2 hours of pulsed, intermittent cooling), reactor building volume (~ 6%), cost (~ 2% of total direct cost), or technology (pressurized accumulator tanks, valves, sumps, coolers, and pumps). Generally the melting of an FPC component represents an issue for plant investment (i.e., downtime) rather than one of public safety. The limiter is the highest risk component from the afterheat viewpoint, but the probability of damage from causes other than a loss of coolant is judged to be much higher. Elimination of this component in favor of magnetic divertors offers a number of operational and safety advantages. The afterheat control provided by naturally circulating PbLi can be very effective for resistive-coil systems (rapid coil de-energization).

- Long-Term Radioactive Waste: In addition to aggravating the afterheat-control problem, the use of copper alloy at the high-heat-flux first wall and limiter adds somewhat to the long-term radwaste problem. The more severe waste disposal problem stems from the 100-year half-life ^{63}Ni [$^{63}Cu(n,p)^{63}Ni$]. The annual generation rate of disposable radioactive copper alloy for the CRFPR(20) design, however, amounts only to ~ 0.52 m^3/yr (~ 400 kCi/yr after ~ 30 yrs). This material would require dilution by a factor of 300 to qualify for Class C shallow land burial after 30 years. The cost tradeoff between deep-geologic and shallow-land burial remains to be fully appreciated. Long-term activity in the HT-9 blanket structure results primarily from ^{93}Mo and ^{94}Nb, but Class-C shallow-land burial should be possible if the blanket is filled with concrete; an annual disposal rate of 19.8 kCi/yr or 263 tonne/yr (including concrete) results. Averaged over a ~ 30-yr life, the TFC and PFC disposal rates amount to ~ 10 kCi/yr and 30 tonne/yr. Polonium-210 formed in the PbLi coolant is removed along with the tritium and is produced at a rate 8-30 kg/yr, depending on the time into the plant life.

8.3. Physics Issues

The present follow-on study and the Ref. 10 framework study have identified a number of physics goals, operating limits, and uncertainties/unknowns. These physics issues can be categorized according to transport scaling, plasma heating, stability/equilibrium, current drive, and impurity/ash control. A brief recapitulation of these physics issues is given for the benefit of both the RFP experimental program and future RFP reactor studies.

- Transport
  - scaling of the form: $\tau_{ce} \propto I_\phi^\nu r_p^2 f(\beta_\theta)$, $\tau_{pi} \simeq 4\tau_{ce}$ has been assumed to relate desirable reactor performance to the evolving RFP physics database
    - sufficiently strong I_ϕ dependence desirable
    - ohmic startup (flux requirement) and device size are impacted if $\nu < 0.8$
    - scaling of beta limits is not known, but reactor study assumes $f(\beta_\theta) = (\beta_{\theta c}/\beta_\theta)^2$ if $\beta_\theta > \beta_{\theta c} \simeq 0.13$, which serves as a convenient means to stabilize the burn
  - impact of field ripple and field error on confinement, $\Delta B_R/B_\theta < 0.003$
    - dependence on coil placement, number, gaps/holes
    - uniformity of first-wall thermal load
    - degree of flux-surface broadening and "bounded ergodicity" caused by asymmetric toroidal ripple
  - streaming parameter limits, $\xi \equiv v_{TH}/v_D \propto I_\phi/NT_e^{1/2}$, are not a concern at ignition but must be monitored during startup approach to ignition from low-density, low-temperature RFP
- Heating
  - ohmic heating is not an intrinsic issue; powerful compared to other methods; critical issues related more to transport scaling
  - current [$\mu(r) \equiv \mu_o \vec{j}/\vec{B}$] and (electron) temperature profiles important; effects may be opposed for startup (i.e., high ohmic-heating rates) versus steady-state (current-drive) conditions
    - strong heating desired at startup; $\mu \simeq$ constant is preferred

- - for current drive, $\mu \to 0$ at edge is preferred to minimize power, but the ideal $\mu(r)$ and $T(r)$ for helicity injection are uncertain

- important to FPC design is the ability to use RFP dynamo during slow startup to generate B_ϕ from a low bias-field RFP formation in order to minimize TFC requirements

- impact of changing heating profiles during startup and ignition on q-profiles and MHD stability

  - - at startup, strong edge-plasma heating during ohmic heating phase (25.3 MW)

  - - during ignition/burn, more uniform alpha-particle heating (546.5 MW)

- anomalous ion heating as observed in experiment would ease startup

- Stability/Equilibrium

  - plasma-current terminations observed in present experiments and must be understood and controlled for the reactor

    - - plasma kinetic energy during burn is ~ 120 MJ (1.1 MJ/m^2) and poloidal-field energy is ~ 1,700 MJ

    - - reactor design assumes density and refueling control of current termination

  - role of conducting shell is not well understood, but has large impact on reactor: thickness (TBR), uniformity (gaps, penetrations), composition (first-wall versus liquid-metal blanket), FPC assembly, penetrations (vacuum, divertor or limiter channel), and current paths in first-wall, blanket, and limiter segments for both inductive startup and F-Θ pumping current-drive phases

  - active (long-term) feedback assumed for global plasma positioning, but assumed not required to control local modes

  - potential for alpha-particle-driven plasma oscillations and impact on

    - - transport (both fuel and ash)

    - - stability and beta limits

    - - RFP dynamo

- Current Drive

  - inductive pulse length more limited in RFPs than in tokamaks

- - higher plasma resistance dominates L/R, but

- - better plasma/coil coupling (higher aspect ratio) compensates

- electromagnetic or electrostatic current-drive (helicity injection) possibilities remain to be explored

  - - required (desired) current [$\mu(r) = \mu_o \vec{j}/\vec{B}$] and temperature profiles not known

  - - impact on dynamo, transport, impurity control not known

- electromagnetic current drive (F-Θ pumping)

  - - drive coil location, access, TBR, radiation lifetime (MWyr/m^2, dpa), number, and ripple constraint

  - - minimum frequency dictates whether main coils can be used versus separate, more-closely coupled coils

  - - only small current and magnetic-flux fluctuations ($\lesssim$ 1%) are required, reducing concern about fusion-power fluctuations, MHD effects, compressions/decompressions, oscillating beta, etc.

  - - degree to which F-Θ pumping can be used to drive the startup phase and minimize the inductive startup and OHC requirement represents an important unresolved tradeoff

- electrostatic (dc) drive

  - - divertor/electrode and auxiliary-coil configuration for efficient helicity injection

  - - fraction of flux diverted to electrode/divertor remains to be determined

  - - key uncertainties/unknowns are current density uniformity at electrodes, helicity injection efficiency, ohmic dissipation in edge plasma, edge temperature, electrode arc drops, etc. (similar uncertainties and problems for spheromak)

- other ways to use the RFP dynamo to drive current non-inductively

  - - EM waves

  - - density modulations with pellets or beams (profile and plasma inductance tailoring)

- Impurity Control
  - poloidal pumped limiter
    - - poloidal orientation, high first-wall coverage possible (~ 50%)
    - - partition of plasma energy loss between radiation ($f_{RAD} \simeq 0.9$) and conduction/convection requires more extensive (two-dimensional) edge-plasma modeling
    - - edge-plasma and scrapeoff density profiles, need for cold/dense edge for wall protection
    - - impact stability/equilibrium (shell uniformity, gaps, bulges, etc.)
    - - eddy-current paths and design for startup/rundown transients
  - magnetic divertors
    - - toroidal-field divertors of the bundle or poloidally symmetric type are preferred, with consideration of connection lengths giving strong preference for the latter
    - - open versus closed divertor-channel/plate configurations remain to be quantified
    - - formation and size of magnetic islands may not be as crucial as flux-surface broadening; the impact on transport and RFP dynamo remains to be assessed, particularly if reversal-surface is overlapped
    - - impact on q-profile (pitch minimum) at plasma edge and impact on stability not understood
    - - effectiveness in reducing charge exchange and wall sputtering by energetic neutrals again requires detailed edge-plasma and divertor-channel model
  - fueling
    - - edge-plasma fueling helps protect wall; usable primarily with pumped limiter
    - - effective divertor requires pellet refueling to some extent
      - - - as for most fusion concepts, deep-penetration, low-inventory pellets require advanced accelerators for electron-ablated pellets (> 50-100 km/s, rail-gun or laser-ablation drives would be required)

- - - pellet ablation by energetic alpha particles may require even higher velocities

- - - low-penetration pellets combined with subsequent near-edge refueling may be possible

8.4. Recommendations

The following recommendations are made for future, more detailed studies of the RFP fusion reactor:

- Single-piece FPC maintenance should be retained, stressed, quantified, and further developed as a major goal and constraint.

- Impurity control using magnetic divertors should receive a strong focus as a means to reduce significantly physical heat fluxes that must be accommodated in the first-wall neutron environment while permitting operation with high-power-density (high-neutron-wall-loading) blankets.

- Lower power units [~ 500 MWe(net)] should be examined, in spite of higher COE compared to large units. Both design and operational means should be developed to "break" the nuclear economy of scale that leads to higher COE for these lower-unit-power plants.

- Tradeoffs between resistive and superconducting coils should be quantified, particularly for more-thinly-shielded, advanced superconducting designs, as applied to systems generating low net-power output.

- Current drive using oscillating fields (i.e., F-Θ pumping) and the impact on FPC design should be emphasized. The role, if any, of F-Θ pumping during startup in reducing the resistive volt-second requirement imposed on the (bipolar) OHC set should also be examined. Lastly, the optimal long-pulsed, high-mass-power-density FPC should also be better defined.

- The catalyzed-DD fuel cycle using water-cooled steel blankets should be examined if a strong case can be made for magnetic-divertor impurity control and reduced first-wall heat fluxes. The resistive-coil versus superconducting-coil options should be thoroughly compared for this fuel cycle.

- The FPC burn and energy-balance dynamics should be examined in terms of load-following capability, particularly in view of varying recirculating power fraction (and overall plant efficiency) as total power output is varied. Other reactor transients related both to startup, load-following, and run-down for plasma, thermal-hydraulic, and auxiliary-power responses should be examined for the lead RFP reactor embodiment.

- For a given reactor design, the development path and associated risks and costs should be quantitatively resolved in conjunction with relevant experimental groups.

- A number of engineering issues remain for the specific FPC design adopted for the CRFPR(20). While future, more-detailed designs may not elect the CRFPR(20) route described herein, key issues related to that approach are nevertheless summarized below.

  - Placing the first-wall/second-wall water-coolant manifold further back into the blanket will improve the tritium breeding ratio, reduce power peaking in the PbLi coolant, increase thermal efficiency by reducing the power deposited into the pressurized-water coolant, and possibly reduce both the copper-alloy afterheat and radioactivity (by maintaining a harder neutron spectrum).

  - Multi-dimensional analyses of MHD flow in entrance and bend regions of the PbLi blanket coolant circuit is needed to better assess flow constriction and increased MHD pressure drop.

  - A detailed blanket structural analysis should be performed to define better the maximum allowable PbLi pressure; higher pressure limits will give more margin in meeting corrosion-related structural temperature limits, in that pumping power per se does not appear to be limiting. The implication of cold trapping, gettering, and reduced PbLi/structural interface area also needs better quantification.

  - Tritium and polonium-210 control in the PbLi coolant require understanding. The cost and feasibility of double-walled heat exchangers require more study, as does the means by which barriers can be applied to the FPC water-coolant circuits.

  - The entire issue of afterheat, inherent or passive safety, and level of neutron first-wall loadings requires better understanding from the viewpoint of site-boundary dose limits required for evacuation. The cost advantage of ECS in allowing higher-power-density FPCs at low capital cost needs better quantification. Even for CRFPR(20) copper-alloy limiter/first-wall melting caused by a total loss of all coolants, the source available for contribution to the site-boundary dose seems negligible in terms of time and quantity at risk and the level of risk per se. If fusion can be shown to be a "sourceless" radiation risk to the public, even for systems with the CRFPR power density, a key advantage for fusion would emerge. The ECS then would be a protector only of plant investment, rather than a mitigator of a publicly hazardless accident. The role of natural circulation of coolants in mitigating FPC damage under LOFA conditions also requires better understanding.

REFERENCES

1. C. C. Baker and M. A. Abdou (Principal Investigators), "STARFIRE - A Commercial Tokamak Fusion Power Plant Study," Argonne National Laboratory report ANL/FPP-80-1 (September 1980).

2. B. G. Logan, C. D. Henning, G. A. Carlson, R. W. Werner, D. E. Baldwin, W. L. Barr, et al., "MARS Mirror Advanced Reactor Study Final Report," Lawrence Livermore National Laboratory report UCRL 53480 (July 1984).

3. R. F. Allen (Prog. Manager), "Energy Economic Data Base (EEDB) Program," Argonne National Laboratory/United Engineers and Constructors report UEC-ANL-821115 (November 1982).

4. J. Sheffield, R. A. Dory, S. M. Cohn, F. G. Delene, L. Parsly, D. E. T. F. Ashby, and W. T. Reiersen, "Cost Assessment of a Generic Magnetic Fusion Reactor," Oak Ridge National Laboratory report ORNL/TM-9311 (1985).

5. B. G. Logan, "A Rationale for Fusion Economics Based on Inherent Safety," Lawrence Livermore National Laboratory report UCRL-91761 (November 13, 1984).

6. R. W. Conn (Chairman and editor), "Panel X Report to the Magnetic Fusion Advisory Committee" (May 8, 1985).

7. R. A. Jacobsen, C. E. Wagner, R. E. Covert, "Systems Studies of High-Field Tokamak Ignition Experiment," J. Nucl. Fus. 3 (4), 217 (1983).

8. L. Bromberg, D. R. Cohn, and D. L. Jassby, "Commercial Tokamak Reactor with Resistive Toroidal Field Coils," Nucl. Technol. 6, 597 (1984).

9. R. F. Bourque, "OHTE Reactor Concepts," Proc. 9th Symp. on Eng. Problems of Fus. Research II, p.1851, Chicago, IL (October 26-29, 1981).

10. R. L. Hagenson, C. G. Bathke, R. L. Miller, M. J. Embrechts, N. M. Schnurr, M. E. Battat, R. J. LaBauve, and J. W. Davidson, "Compact Reversed-Field Pinch Reactors (CRFPR): Preliminary Engineering Considerations," Los Alamos National Laboratory report LA-10200-MS (August 1984).

11. R. S. Massey, R. G. Watt, P. G. Weber, G. A. Wurden, D. A. Baker, C. G. Buchenauer, et al., "Status of the ZT-40M RFP Experimental Program," 6th ANS Top. Mtg. on the Technol. of Fus. En., San Francisco, CA (March 3-7, 1985).

12. R. A. Krakowski, "Alternative Fusion Concepts and the Prospects for Improved Reactors," Proc. 20th Intersoc. Energy Conv. Eng. Conf., Miami Beach, Florida (August 18-23, 1985).

13. J. B. Taylor, "Relaxation of Toroidal Plasma and Generation of Reversed Magnetic Fields," Phys. Rev. Lett. 33, 1139-1141 (1979).

14. H. A. B. Bodin and A. A. Newton, "Review Paper: Reversed-Field Pinch Research," Nucl. Fus. 20, 1255-1324 (1980).

15. K. F. Schoenberg, C. J. Buchenauer, R. S. Massey, J. G. Melton, R. W. Moses, Jr., R. A. Nebel, and J. A. Phillips, "F-Θ Pumping and Field Modulation Experiments on a Reversed Field Pinch Discharge," Phys. Fluids 27 (3), 548 (1984).

16. R. L. Hagenson and R. A. Krakowski, "Steady-State Spheromak Reactor Studies," 6th ANS Top. Mtg. on the Technol. of Fus. En., San Francisco, CA (March 3-7, 1984).

17. J. W. Conner and J. B. Taylor, "Resistive Fluid Turbulence and Energy Confinement," Phys. Fluids 27 (11), 2076 (1984).

18. K. F. Schoenberg, R. W. Moses, Jr., R. L. Hagenson, "Plasma Resistivity in the Presence of a Reversed-field Dynamo," Phys. Fluids 27 (7), 1671 (1984).

19. K. Ogawa, Y. Maejima, T. Shimada, Y. Hirano, P. G. Carolan, C. W. Gowers, A. Nagata, H. Ashida, T. Amano, and Y. Kondoh, "Experimental and Computational Studies of Reversed-Field Pinch on TPE-1R(M)," 1, 575-585, Proc. 9th Int. Conf. on Plasma Physics and Controlled Nuclear Fusion Research, Baltimore, MD (September 1-8, 1982) IAEA Vienna.

20. D. A. Baker, C. J. Buchenauer, L. C. Burkhardt, E. J. Caramana, J. N. DiMarco, J. N. Downing, et al., "Experimental and Theoretical Studies of the ZT-40M Reversed-Field Pinch," 10th Inter. Conf. on Plasma Physics and Controlled Nuclear Fusion Research, London, UK (September 12-19, 1984).

21. M. K. Bevir, H. A. B. Bodin, C. A. Bunting, D. Brotherton-Ratcliffe, H. Ahmed, P. Carolan, et al., "New Results from HBTX1A Reversed Field Pinch," Paper D-II-3 10th Intern. Conf. on Plasma Physics and Controlled Nucl. Fusion Research, London, UK (September 12-19, 1984).

22. T. Tamano, W. D. Bard, T. N. Carlstrom, C. Chu, B. Curwe, R. K. Fisher, et al., "High Current, High Beta Toroidal Pinch Experiment in OHTE," paper D-II-1, 10th Intern. Conf. on Plasma Physics and Controlled Nucl. Fusion Research, London, UK (September 12-19, 1984).

23. R. D. O'Dell, F. W. Brinkley, Jr., and D. R. Marr, "User's Manual for ONEDANT: A Code Package for One-Dimensional Diffusion-Accelerated Neutral-Particle Transport," Los Alamos National Laboratory report LA-9184-M (February 1982).

24. T. J. Seed, "TRIDENT-CTR User's Manual," Los Alamos Scientific Laboratory report LA-7835-M (May 1979).

25. R. E. Alcouffe, F. W. Brinkley, D. R. Marr, and R. D. O'Dell, "User's Guide for TWODANT: A Code Package for Two-Dimensional, Diffusion-Accelerated, Neutral Particle Transport," Los Alamos National Laboratory report LA-10049-M (March 1984).

26. Los Alamos Monte Carlo Group, "MCNP - a General Monte Carlo Code for Neutron and Photon Transport," Los Alamos National Laboratory report LA-7396-M, Revised (April 1981).

27. J. W. Davidson, M. E. Battat, and D. J. Duziak, "Two-Dimensional TBR Calculations for Conceptual Compact Reversed-Field Pinch Reactor Blanket Designs," 6th ANS Top. Mtg. on the Technol. of Fus. En., San Francisco, CA (March 3-7, 1985).

28. D. L. Smith (Prog. Manager), "Blanket Comparison and Selection Study, Final Report," Argonne National Laboratory report ANL/FPP-84-1 (September 1984).

29. H. C. Howe, "Physics Considerations FED Limiter," Oak Ridge National Laboratory report ORNL/TM-703 (1982).

30. W. H. Rohsenow, "Boiling," Handbook of Heat Transfer, W. H. Rohsenow and J. P. Hartnett, eds, McGraw-Hill Book Company, NY (1973).

31. A. K. Lee and N. J. Grant, "Properties of Two High Strength, High Temperature, High Conductivity Copper Base Alloys," Mater. Sci. Eng. 60, 213-223 (1983).

32. M. A. Hoffman and G. A. Carlson, "Calculation Techniques for Estimating the Pressure Losses for Conducting Fluid Flows in Magnetic Fields," Lawrence Livermore National Laboratory report UCRL-51010 (1971).

33. P. A. Roth and H. Chow, "Analysis of a Liquid-Metal Cooled Blanket Transient Using ATHENA," 6th ANS Top. Mtg. on the Technol. of Fus. En., San Francisco, CA (March 3-7, 1985).

34. S. V. Patankar and D. B. Spalding, Heat and Mass Transfer in Boundary Layers, Intertext Books, London, 1970.

35. H. M. Kottowski and G. Grossi, "Interaction of Eutectic LiPb and Water with Respect to Safety Aspects in the Fusion Reactor Blanket," 13th Sym. on Fus. Tech., Varese, Italy (September 24-28, 1984).

36. G. Casini, M. Biggio, F. Farfaletti-Casali, C. Ponti, M. Rieger, G. Vieider, et al., "First Wall and Blanket Concepts for Experimental Fusion Reactors," 6th ANS Top. Mtg. on the Technol. of Fus. En., San Francisco, CA (March 3-7, 1985).

37. M. W. McDowell, K. A. Murray, "Pulse*Star.ICF.Reactor-Heat Transfer Loop and Balance of Plant Considerations," Lawrence Livermore National Laboratory report UCRL-15598 (May 1984).

38. "Equipment Specification-Intermediate A Prototype Steam Generator," Westinghouse Electric Corporation Breeder Reactor Component Project (June 1980).

39. M. W. Kellogg Company, Designs of Piping Systems, John Wiley and Sons, Inc., New York (1956).

40. L. Waganer, "Designer's Guidebook for First Wall/Blanket/Shield Assembly, Maintenance, and Repair," Argonne National Laboratory report DOE/NBM 1053 (December 30, 1983).

41. R. E. MacFarlane, D. W. Muir, and R. M. Boicourt, "The NJOY Nuclear Data Processing System, Volumes I and II," Los Alamos National Laboratory report LA-9303-M, Vols. I and II (ENDF-324) (May 1982).

42. R. J. Barrett and R. E. MacFarlane, "The MATXS-TRANSX System and the CLAW-IV Nuclear Data Library," National Bureau of Standards Special Publication 495 (September 1980).

43. J. A. Blink, "FORIG: A Modification of the ORIGEN2 Isotope Generation and Depletion Code for Fusion Problems," Lawrence Livermore National Laboratory report UCRL-53263 (December 1981).

44. A. G. Croff, "A User's Manual for the ORIGEN2 Computer Code," Oak Ridge National Laboratory report ORNL/TM-7175 (1980).

45. M. A. Gardner and R. J. Howerton, "ACTL: Evaluated Neutron Activation Cross Section Library-Evaluation Techniques and Reaction Index," Lawrence Livermore National Laboratory report UCRL-50400, Vol. 18 (October 17, 1978).

46. F. W. Mann, "Reduced Activations Calculations for the STARFIRE First Wall," Hanford Eng. Dev. Lab. report HEDL-TME 83-27 (October 1983).

47. G. Y. Tung and W. F. Vogelsang, "DKR Radioactivity Calculation Code for Fusion Reactors," University of Wisconsin report UWFDM-170 (1976).

48. J. Jung, "Theory and the Use of Radioactivity Code RACC," Argonne National Laboratory report ANL/FPP/TM-122 (1979).

49. R. G. Lawton, "The AYER Heat Conduction Computer Program," Los Alamos Scientific Laboratory report LA-5613-MS (May 1974).

50. K. Shure and D. J. Dudziak, "Calculating Energy Release by Fission Products," Trans. Am. Nucl. Soc. 4, 30 (1961).

51. B. Badger, K. Audenaerde, J. B. Beyer, B. Braun, J. D. Callen, G. A. Emmert, et al., "Witamir-I: A University of Wisconsin Tandem Mirror Reactor Design," University of Wisconsin report UWFDM-400 (September 1980).

52. R. Siegel and J. R. Howell, Thermal Radiation Heat Transfer, McGraw-Hill Book Company, NY (1981).

53. R. W. Conn, N. M. Ghoniem, F. Najmabadi, J. P. Blanchard, M. Firestone, D. M. Goebel, et al., "Lower Activation Materials and Magnetic Fusion Reactors," Nuclear Technology/Fusion 5, 291-310 (May 1984).

54. Code of Federal Regulation, Chapter 10, Part 61, "Licensing Requirements for Land Disposal of Radioactive Wastes," Vol. 47, No. 248 (1982).

55. J. D. Gordon, J. J. Thomson, and S. N. Suehard, "Isotopically Tailored HT-9 Steel for Radioactive Waste Management," Proc. of 10th Symposium on Fusion Engineering, IEEE, Philadelphia, PA (December 1983).

56. R. L. Hagenson and R. A. Krakowski, "Compact Reversed-Field Pinch Reactors," Los Alamos National Laboratory report LA-9389-MS (July 1982).

57. S. C. Schulte, W. E. Bickford, C. E. Willingham, S. K. Ghose, and M. G. Walker, "Fusion Reactor Design Studies--Standard Unit Costs and Cost Scaling Rules," Pacific Northwest Laboratory report PNL-2987 (September 1979).

58. F. Wagner, M. Keilhacker, and the ASDEX and NI Teams, "Importance of the Divertor Configuration for Attaining the H-Regime in ASDEX," J. Nucl. Mater. 121, 103 (1984).

59. S. M. Kaye, M. G. Bell, K. Bol, D. Boyd, K. Bran, D. Buchenauer, et al., "Attainment of High Confinement in Neutral Beam Heated Divertor Discharges in the PDX Tokamak," ibid, p. 115.

60. C. G. Bathke, R. L. Miller, and R. A. Krakowski, "Magnetic Divertor Design for the Compact Reversed Field Pinch Reactor," Proc. 13th Sym. on Fus. Tech., Varese, Italy, 2, 1259 (September 24-28, 1984).

61. C. G. Bathke, R. A. Krakowski, and R. L. Miller, "A Comparison of Toroidal-Field Divertors for a Compact Reversed-Field Pinch Reactor," 6th Top. Mtg. on the Technol. of Fus. En., San Francisco, CA (March 4-7, 1985).

62. W. Pfeiffer and R. E. Waltz, "Empirical Scaling Laws and Energy Confinement in Ohmically-Heated Tokamaks," Nucl. Fusion 19, 51 (1979).

63. T. H. Osborne, R. N. Dexter, and S. C. Prager, "Discharges With Safety Factor, q, < 1 in a Noncircular Tokamak," Phys. Rev. Lett. 49, 734 (1982).

64. R. L. Miller, C. G. Bathke, R. A. Krakowski, F. M. Heck, L. Green, J. S. Karbowski, et al., "The Modular Stellarator Reactor: A Fusion Power Plant," Los Alamos National Laboratory report LA-9737-MS (July 1983).

65. K. F. Schoenberg, R. F. Gribble, and J. A. Phillips, "Zero-Dimensional Simulations of Reversed-Field Pinch Experiments," Nucl. Fus. 22, 1433 (1982).

66. P. Thullen and K. F. Schoenberg (eds), "ZT-H Reversed-Field Pinch Experiment Technical Proposal," Los Alamos National Laboratory document LA-UR-84-2602 (June 1984).

67. J. F. Parmer, R. A. Sutton, K. L. Agarwal, and M. W. Liggett, "Design of the MARS Magnet Set," Proc. 13th Sym. on Fus. Tech., Varese, Italy (September 24-28, 1984).

68. R. L. Spencer, "Magnetic Islands and Stochastic Field Lines in the RFP," Proc. RFP Theory Workshop, Los Alamos, NM (April 29 - May 2, 1980), Los Alamos National Laboratory report LA-8944-C, p. 129 (January 1982).

LIST OF NOMENCLATURE

a_i	PbLi coolant-channel half-width (m)
A	Area (m^2) or aspect ratio (R_T/r_p)
A^+	Empirical constant in Eq. (20) of Sec. 2.
A_{DIV}	Area of divertor wall surfaces (m^2)
A_p	Area for PbLi flow or plasma cross-sectional area (m^2)
A_{FW}	First-wall area (m^2)
AFDC	Allowance for Funds During Construction
B	Magnetic-field strength (T) or "blanket"
B_R	Radial component of magnetic field (T)
B_ϕ	Toroidal magnetic field (T)
$\langle B_\phi \rangle$	Average toroidal magnetic field in plasma chamber (T)
$B_{\phi R}$	Reversed toroidal field at plasma edge (T)
B_θ	Poloidal magnetic field (T)
$B_{\theta c}$	Maximum poloidal field at coil (T)
BD	Bundle (toroidal-field) divertor
BFM	Bessel Function Model
BHP	Biological Hazard Potential
BOP	Balance of Plant
C	Coil
C_1	Constant in τ_E(PHYS) physics scaling
C_{AC}	Annual Capital-Cost Charge ($/yr)
C_B	Buoyancy coefficient, Eq. (4) of Sec. 5. (kg m^2/s^3)
C_F	Annual fuel charge ($/yr)
C_H	Hydraulic coefficient, Eq. (5B) of Sec. 5. (kg/m^4 s)
C_{IJ}	Account IJ Cost
C_M	Magnetic coefficient, Eq. (5A) of Sec. 5. (kg/m^4 s)
$C_{O\&M}$	Annual Operation-Cost Charge ($/yr)
c_p	Specific heat (J/kg K)
C_{SCR}	Annual scheduled component replacement charge ($/yr)
COE	Cost of Electricity (mills/kWeh)
CRFPR(20)	Compact Reversed-Field Pinch Reactor of nominal neutron first-wall loading, I_w = 20 MW/m^2
d	Toroidal width of divertor throat (m)
d_H	Hydraulic diameter (m)

d_i	Inside tube diameter (m)
D	Scrapeoff particle diffusivity (m^2/s)
E	Young's modulus (Pa), or escalation rate (yr^{-1})
ECRH	Electron cyclotron reservance heating
ECS	Emergency Cooling System
EDC	Escalation During Construction
EFC	Equilibrium-Field Coil
f_{AUX}	Auxiliary power fraction, P_{AUX}/P_{ET}
f_F	Fanning friction factor
f_L	Fraction of plasma transport power delivered to limiter
f_p	Fraction of scrapeoff particles entering limiter
f_{RAD}	Fraction of plasma energy lost by radiation
f_w	Fraction of thermal power deposited in water coolant
$f(\beta_\theta)$	Beta function for τ_E(PHYS) physics scaling, $\sim (\beta_{c\theta}/\beta_\theta)^2$
f_ϕ	Ratio of TFC to PFC thicknesses
F	Reversal parameter, $B_{\phi R}/\langle B_\phi \rangle$
F_{ij}	Radiation view factor between surfaces i and j
FPC	Fusion Power Core
FPY	Full Power Year
FW	First wall
G&A	General and Administrative Costs
g	Gravitational constant (9.8 m^2/s)
g_i	Plasma profile factor (i = DT, OHM, BR)
h	Convective conductance (W/m^2 K)
H	Hartmann number, $aB(\sigma_p/\eta)^{1/2}$, or FPC/SG elevation difference
H_T	Hartmann number at laminar/turbulent transition
i	Specific enthalpy (J/kg)
I_c	Coil current (MA)
I_ϕ	Plasma toroidal current (MA)
I_w	Neutron first-wall loading (MW/m^2)
$I_w\tau$	First-wall/blanket radiation lifetime ($MWyr/m^2$)
I&C	Instrumentation and Control
ID	Inside diameter (m)
IDC	Interest During Construction
j_ϕ	Plasma current density (MA/m^2)
j_c	Coil current density (MA/m^2)

$j_{c\phi}$	Toroidal-field coil current density (MA/m^2)
$j_{c\theta}$	Poloidal-field coil current density (MA/m^2)
k	Thermal conductivity (W/m K)
k_{eff}	Effective thermal conductivity of fluid including turbulent contribution (W/m K)
$k_{w,p}$	Thermal conductivity of water, PbLi (W/m K)
ℓ	Poloidal mode number or coolant-tube length (m)
ℓ_L	Length of a limiter segment (m)
ℓ_w	Length of first-wall segment (m)
L	Tube connection length (m) or "limiter"
LOFA	Loss-of-Flow Accident
LOCA	Loss-of-Coolant Accident
LWR	Light-Water Reactor
$\dot{m}$	Mass flow rate of water, PbLi for the i^{th} channel (kg/s)
$\dot{m}_w/N_T$	Mass flow rate of water for a single tube (kg/s)
$\dot{m}_{w,p}$	Total mass flow rate of water, PbLi (coolant kg/s)
M_N	FW/B/S energy multiplication
$M_N P_N$	Recoverable nuclear heating (MW)
M_{FPC}	FPC mass (tonne)
M_{PbLi}	Mass of PbLi (tonne)
M_{VAC}	Mass of FPC vacuum tank (tonne)
M_{BFM}	Modified Bessel Function Model
n	Toroidal mode number, scrapeoff or average plasma density (m^{-3})
n_i	Average plasma ion density (m^{-3})
n_o	Separatrix density (m^{-3})
N	Number of divertors or toroidal sectors, or plasma line density (m^{-1})
N_T	Number of coolant tubes in first wall or second wall
N_{TF}	Number of toroidal field coils
NA	Not applicable
NC	Natural Circulation
OHC	Ohmic-Heating Coil
OD	Outside diameter (m)
p	Plasma pressure (Pa)
p_f	Plant availability factor
P_B	Buoyancy pressure (Pa)
P	Power (MW), or pressure (MPa), or plant construction period (yr)

P/P_o	Afterheat power as a fraction of full power
P_α	Alpha-particle power (MW)
P_Ω	Plasma ohmic power (MW)
P_{AUX}	Auxiliary plant power (MW)
P_{BLB}	Blanket nuclear bulk heating (MW)
P_{BLK}	Total blanket nuclear heating (MW)
P_{BLS}	Blanket structure nuclear heating (MW)
P_{BL}	Power back-leakage from blanket to SW (MW)
P_E	Net electrical power (MWe)
P_{ET}	Gross electrical power (MWe)
P_c	Recirculating power (MW)
P_c^Ω	Ohmic power recirculated to FPC (MW)
P_{ETS}	Energy transfer/storage power loss (MW)
P_F	Fusion power (MW)
P_{FW}	Total power to first wall (MW)
$P_{FW/SW}$	Total power to first-wall/second-wall system (MW)
P_{FW}^N	Total first-wall nuclear heating (MW)
P_{FWM}	First-wall manifold nuclear heating (MW)
P_{FWW}	First-wall nuclear heating (MW)
P_L	Total power to limiter (MW)
P_L^N	Total limiter nuclear heating (MW)
P_{LL}	Limiter nuclear heating (MW)
P_{LM}	Limiter manifold nuclear heating (MW)
P_N	Fusion-neutron power (MW)
P_p	PbLi coolant pressure (MPa)
P_{pump}	Power requirements of PbLi or water coolant pumps (MW)
P_{PFC}	Total poloidal-field-coil heating (MW)
P_{PFC}^N	PFC nuclear heating (MW)
P_{PFC}^Ω	PFC Ohmic heating (MW)
Pr	Prandtl number
Pr_{eff}	Effective Prandtl number
P_{RAD}	Plasma radiated power (MW)
P_{SLD}	Shield nuclear heating (MW)
P_{SW}	Total second-wall nuclear heating (MW)
P_{SWM}	Second-wall manifold nuclear heating (MW)
P_{SWW}	Second-wall nuclear heating (MW)

P_{TFC}	Total toroidal-field-coil heating (MW)
P_{TFC}^{N}	Toroidal-field-coil nuclear heating (MW)
P_{TFC}^{Ω}	Toroidal-field-coil ohmic heating (MW)
P_{TH}	Total recoverable thermal power (MWt)
P_{THp}	Total thermal power to PbLi coolant, excluding pump power (MW)
P_{THw}	Total power to water-cooled first-wall/second-wall/limiter systems (MW)
P_{TR}	Plasma transport power (MW)
P_w	Water coolant pressure (MPa)
PbLi	Eutectic mixture of lead and lithium corresponding to $Pb_{83}Li_{17}$
PCASS	Primary Candidate Alloy, Stainless Steel(316)
PFC	Poloidal-Field Coil
PWR	Pressurized-Water Reactor
q	Plasma safety factor, $(B_\phi/B_\theta)/(R_T/r_p)$
q_D	Design heat flux (MW/m^2)
q_{DIV}	Divertor channel heat flux (MW/m^2)
q_w	First wall heat flux (MW/m^2)
q_z	Particle energy flux for limiter (MW/m^2)
Q	PbLi volumetric flow rate (m^3/s)
Q_E	Engineering Q-value, $P_{ET}/P_c = 1/\varepsilon$
Q_p	Plasma Q-value, P_F/P_Ω
$Q_{m\gamma}$	Energy generation per unit volume (MW/m^3)
r	Minor radius (m)
r_b, r_b'	Plasma minor radius of break point for μ profiles (m)
r_p	Plasma minor radius (m)
r_s	FPC system minor radius, $r_w + \Delta b + \delta_{c\phi} + \delta_{c\theta}$ (m)
r_v	Plasma reversal-surface minor radius (m)
r_w	First-wall minor radius (m)
R	Major radius
Re	Reynolds number
Re_T	Transition Reynolds number
RFP	Reversed-Field Pinch
R_{Le}^*	Edge-plasma particle recycle coefficient
R_p	Plasma resistance (ohm)
R_T	Major toroidal radius of plasma (m)
R&D	Research and Development
RPE	Reactor Plant Equipment

S	Shield
SBI	Shallow Burial Index
SD	Symmetric (toroidal-field) divertor
SG	Steam Generator
SW	Second Wall
t	Time (s)
t_w	Thickness of channel walls in the blanket (m)
T	Temperature of coolant or average plasma (^oC, K, keV)
T_E	Environment or heat-rejection temperature for thermal cycle (K)
T_o	Separatrix temperature (keV)
T_{pi}	Inlet PbLi bulk temperature (K)
T_{pM}	Maximum local PbLi temperature (K)
T_{po}	Outlet PbLi bulk temperature (K)
T_s	Surface temperature (K)
T_{si}	Inside tube-wall temperature or maximum local water temperature (K)
T_w	Plasma temperature at first wall (keV)
T_{wi}	Inlet water bulk temperature (K)
T_{wo}	Outlet water bulk temperature (K)
TBD	To be determined
TBR	Tritium Breeding Ratio
TDC	Total Direct Cost
TFC	Toroidal-Field Coil
UBC	Unit Base Cost ($/kWe)
UDC	Unit Direct Cost ($/kWe)
UTC	Unit Total Cost ($/kWe)
v_{TH}	Ion thermal velocity (m/s)
$v_{w,p}$	Local water or PbLi coolant velocity (m/s)
$V_{w,p}$	Bulk water or PbLi coolant velocity (m/s)
V	Bulk fluid velocity (m/s)
V_c	Volume of coils (m^3)
V_p	Plasma volume (m^3)
V_{BL}	Volume of blanket (m^3)
V_{FPC}	FPC volume (m^3)
V_{RB}	Volume of reactor building (m^3)
V_{SHD}	Volume of shield (m^3)
V_{STR}	Volume of FPC structure (m^3)

V_{VAC}	Volume of vacuum system (m^3)
V_ϕ	Toroidal plasma voltage (V)
w	Channel width = 2a (m)
$w_{\theta i}$	Width of i^{th} poloidal PbLi-coolant channel (m)
w_{Ri}	Width of i^{th} radial PbLi-coolant channel (m)
x	Radial scrapeoff distance, axial distance along tube or channel (m), ratio of plasma to first-wall radius
x_ℓ	Scrapeoff radial thickness (m)
y	Distance from blanket coolant-channel wall (m)
z	Toroidal distance for limiter (m)
α	Thermal expansion coefficient (1/K) or ratio of heat and particle diffusivities in edge-plasma scrapeoff, χ/D
β	Volumetric thermal expansion coefficient (1/K) or normalized plasma pressure
$\beta_{\theta c}$	Critical plasma beta above which confinement is degraded
β_θ	Poloidal plasma beta
δ	Coolant-tube wall thickness (m)
δ'	Distance between reversal surface and plasma surface (m)
$\delta_{c\phi}$	Toroidal-field-coil thickness (m)
$\delta_{c\theta}$	Poloidal-field-coil thickness (m)
δ_c	$= \delta_{c\phi} + \delta_{c\theta}$ nominal coil thickness (m)
Δb	First wall/blanket/shield thickness (m)
Δi	Change in bulk specific enthalpy (J/kg)
ΔP	Coolant pressure drop (Pa)
ΔP_B	Buoyancy pressure drop (Pa)
ΔP_F	Friction pressure drop (Pa)
ΔP_M	Magnetic pressure drop (Pa)
ΔT_{SAT}	Saturation temperature of water coolant
ε	Emissivity of first wall or limiter, or total recirculating power fraction (P_c/P_{ET})
ε_{pump}	Pump power fraction
ε_Ω	Ohmic power fraction
η	Viscosity (kg/m s), efficiency, ratio of density and temperature e-folding lengths in scrapeoff (λ_n/λ_T), coil resistivity
η_{eff}	Effective visiosity including turbulence contribution (kg/m s)
η_{ETS}	Energy transfer/storage efficiency

η_{GEN}	Electrical generator efficiency
η_I	Ideal thermal-cycle efficiency
η_p	Plant efficiency, $\eta_{TH}(1 - \varepsilon) = P_E/P_{TH}$
η_{pump}	Efficiency of pumps
η'_{TH}	Actual cycle efficiency = .75 η_I
η_{TH}	Thermal-conversion efficiency (P_{ET}/P_{TH}) = $\eta_{GEN}\eta'_{TH}$
η^*_{TH}	η_{TH} $(1 - \varepsilon_{pump})$
θ	Poloidal direction
Θ	Pinch parameter, $B_\theta/\langle B_\phi \rangle$
ϕ	Toroidal direction
Φ	Toroidal flux
κ	Constant in Eq. (20), Sec. 2.
λ_c	Coil conductor filling fraction
λ_T,λ_n	Temperature or density e-folding distances in scrapeoff (m)
μ	Ratio of parallel current density to magnetic field (m^{-1}) or viscosity (kg/m s)
μ_o	$4\pi(10)^{-7}$ H/m
ν	Poisson's ratio or exponent on current dependence of τ_E(PHYS)
ρ	Density (kg/m^3)
σ	Stress (Pa) or Stefan-Boltzmann constant ($W/m^2\ K^4$)
σ_D	Design stress (Pa)
σ_p	Electrical conductivity of PbLi (1/ohm m)
σ_Y	Yield stress (MPa)
σ	Stefan-Boltzmann constant ($W/m^2\ K^4$)
σ_w	Electrical conductivity of wall (1/ohm m)
τ	Shear stress (Pa)
τ_{pi}	Plasma particle confinement time (s)
$\tau_\parallel$	Parallel confinement time in scrapeoff (s)
τ_{ce}	Electron conduction/convection confinement time (s)
τ_E	Global energy confinement time (s)
τ_E(OPT)	Minimum-COE confinement time (s)
τ_E(PHYS)	Physics-based confinement-time scaling (s)
τ_u	Unscheduled down time (d)
τ_s	Scheduled down time (d)
χ_E	Heat conduction coefficient (m^2/s) or thermal diffusivity

ACKNOWLEDGMENTS

The authors wish to acknowledge useful discussions with J. D. Gordon of TRW, J. R. Bilton of EBASCO, E. T. Cheng of GA Technologies, and K. A. Murray of Rockwell International. The mechanical-design and neutronic contributions of R. E. Lujan and M. E. Battat, respectively, are greatly acknowledged. Several discussions with B. Boyack, D. Liles, and J. Mahaffy of the Los Alamos Safety Code Development Group proved particularly useful. Lastly, the unflagging accurate and rapid typing and editing skills of Marion Clark throughout the evolution of this report are especially acknowledged.

APPENDIX A. TABLE OF CRFPR(20) DESIGN PARAMETERS

This table contains the comprehensive and uniform design data for the CRFPR(20). The format of this table follows the DOE/OFE guidelines.[1] Superscripted numbers in parenthesis refer to notes found at the end of this table.

TABLE OF REACTOR DESIGN PARAMETERS

Parameter	Unit	Ref. 2 Value	Modified Value
1. Characteristic Machine Dimensions			
1.1. Reactor envelope(1a)			
1.1.1. Height (coil outside diameter)	m	3.90	4.25
1.1.2. Width (coil outside diameter)	m	3.90	4.25
1.1.3. Length (major circumference)	m	23.9	24.5
1.1.4. Volume of reactor envelope(1b)	m^3	285	359.2
1.2. Plasma chamber			
1.2.1. Major toroidal radius, R_T	m	3.80	3.90
1.2.2. Minor radius	m	0.75	0.75
1.2.3. Plasma volume, V_p	m^3	37.7	38.8
1.2.4. Plasma chamber volume	m^3	42.2	43.3
1.2.5. Wall surface area	m^2	112	115.5
1.2.6. Number of sectors, N(1c)	-	24	24
2. Plasma Parameters (Steady State)			
2.1. Plasma dimensions			
2.1.1. Major toroidal radius, R_T	m	3.80	3.90
2.1.2. Average minor radius, r_p	m	0.71	0.71
2.2. Average ion density, n_i	$10^{20}/m^3$	6.55	6.55
2.3. Average alpha-particle density, n_α	$10^{20}/m^3$	0.19	0.19
2.4. Energy confinement time, τ_E	s	0.23	0.23
2.5. Electron confinement time, τ_{pe}	s	0.15	0.15
2.6. Ion confinement time, τ_{pi}	s	0.59	0.59
2.7. Average Lawson parameter, $n_i\tau_E$	10^{20} s/m^3	1.51	1.51
2.8. Average poloidal beta,(2a) $\langle\beta_\theta\rangle$	-	0.23	0.23
2.9. Average plasma toroidal current	MA	18.4	18.4
2.10. Average ion temperature, $\langle T_i\rangle$(2b)	keV	10.	10.
2.11. Average electron temperature, $\langle T_e\rangle$(2b),	keV	10.	10.
2.12. Average alpha-particle energy, $\langle T_\alpha\rangle$(2c)	keV	805.	805.

2.13. Effective plasma ion charge[2d], Z_{eff}	-	1.06	1.06
2.14. Reactor cycle			
2.14.1. Burn pulse length	s	Steady state	
2.14.2. Total pulse length	s	Steady state	
2.15. Fuel cycle	-	DT/Li	DT/Li
2.16. Plasma-heating method	-	Ohmic (to ignition)	
2.16.1. Plasma-heating power[2e]	MW	25.3	25.3
2.16.2. Plasma-heating frequency	GHz	NA	NA
2.17. Plasma energy gain[2f], Q_p	-	108.	108.
3. Power-Output			
3.1. Plasma fusion power, $P_F = P_N + P_\alpha$	MWt	2732.5	2733.3
3.1.1. 14.1-MeV neutron power, P_N	MWt	2186.0	2186.8
3.1.2. 3.5-MeV alpha-particle power, P_α	MWt	546.5	546.5
3.2. Reactor thermal power	MWt	3364.9	3472.6
3.2.1. Power to first wall	MWt	626.0	952.7
3.2.2. Power to limiter	MWt	440.8	568.3
3.2.3. Power from blanket ($M_N \simeq 1.33$)	MWt	2057.6	2012.1
3.2.4. Power to shield	MWt	143.3	86.5
3.3. Blanket power amplification factor, M_N	-	1.28	1.33
3.4. Plasma chamber power density (total cycle time average)[3a]	MWt/m^3	64.8	63.1
3.5. Plasma power density[3b]	MWt/m^3	72.5	70.4
3.6. Engineering power density[3c]	MWt/m^3	11.8	9.66
3.7. Blanket power density[3d]	MWt/m^3	30.6	25.6
3.8. Total thermal power to conversion cycle[3e], P_{TH}	MWt	3364.9	3472.6
3.9. Plant gross electrical output, P_{ET}	MWe	1226.7	1255.8
3.10. Plant net electrical output, P_E	MWe	1000.	1000.
3.11. Thermal cycle efficiency, η_{TH}	-	0.365	0.362
3.12. Net plant efficiency, $\eta_p = \eta_{TH}(1 - \varepsilon)$	-	0.297	0.288
3.13. Recirculating power fraction, ε[3f]	-	0.185	0.204
4. Reactor Coolant System			
4.1. Blanket coolant	-	$Pb_{83}Li_{17}$	$Pb_{83}Li_{17}$
4.2. Blanket outlet temperature (hot leg)	K	773	773

4.3. Blanket inlet temperature (cold leg)	K	623	623
4.4. Blanket outlet pressure	MPa	~0.0	0.10
4.5. Blanket inlet pressure	MPa	1.1	0.65
4.6. Blanket coolant flow rate (total)	kg/s	72,840	74,765
4.7. Blanket structural material[4a]	-	HT-9	HT-9
4.8. First-wall coolant type	-	H_2O	H_2O
4.9. First-wall outlet temperature	K	536.6	551.3
4.10. First-wall inlet temperature	K	463.	443.
4.11. First-wall outlet pressure	MPa	15.2	14.8
4.12. First-wall inlet pressure	MPa	15.6	15.2
4.13. First-wall coolant flow rate (total) (first wall + limiter)	kg/s	4,898.8	2,694.
4.14. Total number of blanket coolant loops	-	TBD	4
4.15. Type of blanket coolant circulator	-	TBD	PbLi Pump
4.16. Power input to each circulator[4b]	MWe	TBD	1.5
4.17. Peak temperature in case of loss-of-coolant-flow accident			
4.17.1. First wall (limiter)[4c]	K	TBD	750(1100)
4.17.2. Blanket multiplier	K	TBD	NA
4.17.3. Breeder	K	TBD	NA
4.18. Thermal-energy storage[4b]	J	not required	
5. Intermediate Coolant System	-	TBD	NA
6. Steam Generation (SG) System (PbLi/H_2O circuits)[6a,b]		TBD	
6.1. Steam outlet temperature	K	TBD	758./543.
6.2. Steam outlet pressure	MPa	TBD	17.1/5.6
6.3. Steam flow rate (total)	kg/s	TBD	771./302.
6.4. Feedwater temperature	K	TBD	547./418.
6.5. Number of steam generators (SG) per loop	-	TBD	1/1[6b]
6.6. Number of reactor sectors per SG	-	TBD	6/12
6.7. SG materials, shell/tube[6c]	-	TBD	6
7. Shield Coolant System[7a]			
7.1. Total power deposited in the shield	MWt	143.3	86.5
7.2. Shield coolant type	-	H_2O	H_2O
7.3. Shield outlet temperature	K	463	561.2
7.4. Shield inlet temperature	K	597	546.9
7.5. Coolant outlet pressure	MPa	15.2	14.8

7.6. Coolant inlet pressure	MPa	15.2	14.9
7.7. Coolant flow rate (total)	kg/s	272.2	1,173.
8. Reactor Auxiliary System			
8.1. Vacuum pumping system			
8.1.1. Vacuum and plasma chamber pressure			
8.1.1.1. Plasma chamber pressure	Pa	2.0	2.0
8.1.1.2. Vacuum chamber pressure	Pa	TBD	0.005
8.1.2. Plasma chamber volume(8a)	m^3	42.2	60.3
8.1.3. Vacuum chamber volume(8b)	m^3	TBD	3,746.
8.1.4. Number of vacuum pumps	-	TBD	30
8.1.5. Regeneration interval(8c)	h	TBD	2
8.1.6. Helium-pumping speed (per pump)	m^3/s	TBD	120.0
8.2. Magnet cooling system (chilled H_2O)			
8.2.1. TFC cooling load(8d)	MWt	42.6	48.3
8.2.2. PFC cooling load(8e)	MWt	141.0	163.7
8.3. Plasma-heating-system cooling load(3f,8e)	MWt	73.0	73.0
8.4. Plasma-fueling system			
8.4.1. Type(8f)	-	DT pellet	
8.4.2. Fuel composition	-	50% D, 50% T	
8.4.3. Fueling rates	g/s(D)	0.11	0.11
	g/s(T)	0.17	0.17
8.4.4. Pellet diameter	mm	4.22	4.22
8.4.5. Pellet injection frequency	s^{-1}	~ 28	28
8.5. Tritium-processing and recovery system(8g)			
8.5.1. Total tritium inventory	kg	TBD	15.1
8.5.2. Vulnerable tritium inventory	kg	TBD	0.2
8.6. Impurity control system		Pumped limiter	
8.6.1. Limiter coolant type	-	H_2O	H_2O
8.6.2. Limiter outlet temperature	K	545	546.9
8.6.3. Limiter inlet temperature	K	463	443
8.6.4. Limiter outlet pressure	MPa	15.2	14.9
8.6.5. Limiter inlet pressure	MPa	15.4	15.2
8.6.6. Limiter coolant flow rate	kg/s	1,311	1,521

9. Reactor Components

9.1. First wall/blanket

9.1.1.	Structural material (first-wall/blanket)	-	MZC-Copper/HT-9	
9.1.2.	Breeding material	-	$Pb_{83}Li_{17}$ (60% Li)	$Pb_{83}Li_{17}$ (90% Li)
9.1.3.	Neutron multiplier material	-	Pb	Pb
9.1.4.	Breeding ratio[9a]	-	1.11	1.06
9.1.5.	Number of modules[9b]	-	1	1
9.1.6.	Weight of modules[9b]	tonnes	307	304
9.1.7.	Weight of largest single component	tonnes	307	304
9.1.8.	Dimensions of largest component[9c]	m	3.8×1.5	3.9×1.6
9.1.9.	First-wall power loading			
9.1.9.1.	14.1-MeV neutron current	MW/m^2	19.5	19.0
9.1.9.2.	Alpha-particle flux	MW/m^2	0.0	0.0
9.1.9.3.	Radiation, charge-exchange, and conduction power to first wall	MW/m^2	5.0	5.0
9.1.9.4.	Radiation, charge-exchange, and conduction/convection power to limiter	MW/m^2	6.0	6.0
9.1.9.5.	First-wall life	$MWyr/m^2$	15	15

9.2. Shielding

9.2.1.	Material	-	H_2O/W/B_4C/Fe (10%/40%/40%/10%)	H_2O/PCASS (10%/90%)
9.2.2.	Number of modules		1	1
9.2.3.	Weight of each module	tonnes	188.9 (included in 9.1.6.)	159.6 (included in 9.1.6.)
9.2.4.	Weight of largest single component	tonnes	188.9 (included in 9.1.6.)	159.6 (included in 9.1.6.)
9.2.5.	Dimensions of largest component	m	torus, 3.9×1.4	3.9×1.5

9.3. Magnets

9.3.1.	Superconducting	-	none	
9.3.2.	Conductor material (insulator)	-	Cu-alloy/none 70%/10%	MgO

9.3.3. Structural material	-	PCASS(10%)	
9.3.4. Operating temperature	K	300-350	
9.3.5. Coolant	-	H_2O	H_2O
9.3.6. Mean stress in coil[9d]	MPa	7-90	7-90
9.3.7. Maximum force transmitted to building[9e]	MN	2.7	2.7
9.3.8. Maximum field[9f]	T	4.5	4.5
9.3.9. Field on plasma axis[9g]	T	9.5(toroidal)	
9.3.10. Field at plasma surface	T	5.2(poloidal)	
9.3.11. Number of magnets			
9.3.11.1. Toroidal-field coils	-	24	24
9.3.11.2. Equilibrium-field coils	-	12	12
9.3.11.3. Ohmic-heating coils	-	20	20
9.3.12. Mean coil radius	m	3.31	3.41
9.3.12.1. Toroidal-field coil	m	1.46	1.56
9.3.12.2. Poloidal-field coil	m	3.80	3.90
9.3.13. Total stored energy (full torus)	GJ	1.72	1.72
9.3.13.1. Toroidal-field coil	GJ	0.02	0.02
9.3.13.2. Poloidal-field coil	GJ	1.7	1.7
9.3.14. Weight of largest single component[9h]	tonnes	200	258
9.3.15. Dimension of largest single component	m	torus, 4.8×1.0	4.9×1.0
9.4. Energy transfer and storage[9i]		Not required	
9.5. Plasma heating			
9.5.1. Type	-	ohmic dissipation	
9.5.2. Frequency	GHz	NA	NA
9.5.3. Power to the plasma	MW	25.3	25.3
9.5.4. Transmission method	-	Induction	
9.5.5. Power reflected from plasma	MW	0.0	0.0
9.5.6. Power loss in transmission[9j]	MW	73.0	73.0
9.5.7. Power loss in amplifiers	MW	NA	NA
9.5.8. Power loss in power supplies	MW	TBD	0.0
9.5.9. System input power	MW	~100.	~100.
9.5.10. Heating time	s	8-10	8-10

9.5.11. Number of waveguide grills	-	NA	NA
9.5.12. Number of amplifiers	-	NA	NA
10. Electrical Power Requirements			
10.1. Cold-plasma start-up power from grid	MWe/s	300/8	(300-400)/8
10.2. Auxiliary power requirements[10a] (normal operation)	MWe	62.6	91.3
10.2.1. Electrical energy storage	MWe	none required	
10.2.2. Magnet power supply (other than ohmic losses)	MWe	0.0	0.0
10.2.3. First-wall circulators[10b]	MWe	1.85	0.80
10.2.4. Limiter-coolant circulators[10b]	MWe	0.94	0.52
10.2.5. Blanket circulators[10b]	MWe	13.2	5.8
10.2.6. Shield-coolant circulators[10b]	MWe	0.0	0.01
10.2.7. Refrigeration system	MWe	NA	NA
10.2.8. Vacuum system (roughing)	MWe	TBD	0.1[8c]
10.2.9. Miscellaneous reactor plant auxiliaries	MWe	TBD	TBD
10.2.10. Feedwater pump system	MWe	TBD	23.[8c]
10.2.11. Condensing system	MWe	TBD	12.[8c]
10.2.12. Heat rejection system	MWe	TBD	TBD
10.2.13. Miscellaneous BOP auxiliaries	MWe	TBD	15.[8c]
11. Buildings			
11.1. Reactor Building			
11.1.1. Characteristic dimensions[11a] (includes steam-generators and accumulators)	m	TBD	72×81×54
11.1.2. Enclosed volume			
11.1.2.1. Free volume[11b]	m^3	TBD	$2.8(10)^5$
11.1.2.2. Total volume	m^3	TBD	$3.1(10)^5$
11.1.3. Minimum wall thickness for shielding	m	TBD	2.5
11.1.4. Internal pressure normal/accident[11c]	MPa	TBD	145
11.1.5. Containment atmosphere	-	TBD	CO_2
11.2. Turbine Building			
11.2.1. Characteristic dimensions	m	TBD	110×50×44
11.2.2. Enclosed volume	m^3	TBD	$2.42(10)^5$

11.3. Reactor Service Building			
11.3.1. Characteristic dimensions	m	TBD	TBD
11.3.2. Special functions (i.e., tritium handling, radwaste, maintenance and storage, hot cells, blanket processing equipment, etc.	m	TBD	TBD
12. Reactor Maintenance			
12.1. First-wall/blanket			
12.1.1. Annual percentage	% area/yr	100	100
12.1.2. Area	m^2/yr	112	115
12.1.3. Weight[12a]	tonnes/yr	45.2	60.9
12.2. Radioactive material storage for life of plant (30 yr)			
12.2.1. Total long-term storage[12b]	m^3/tonnes	TBD	15.6/138.
12.2.2. Remaining recycled blanket storage	m^3/tonnes	TBD	2,783/1,688[12c]
12.2.3. Total recycled reactor equipment[12d] (after plant decommissioning)	m^3/tonnes	TBD	355/1,348
12.3. Reactor availability	-	TBD	TBD
12.4. Overall plant availability[12e]	-	0.75	0.76

Footnotes for Reactor Design Table

1. Characteristic Machine Dimensions
   (a) The reactor envelope encloses the poloidal-field coils and has the dimensions given with a circumference (length) of 23.9 m (at the major toroidal radius of 3.9 m).
   (b) Based on an effective systems radius of r_s = 2.16 (Fig. 2-3) and a major radius of R_T = 3.9 m.
   (c) Sectors are used only for off-site assembly of reactor torus with full torus being installed as a single unit into reactor room.
2. Plasma Parameters
   (a) Includes average alpha-particle pressure; total beta is 0.12.
   (b) Based on $T(r) \propto J_o(\mu r)$ profiles and BFM pressure profiles.
   (c) Thermalized Maxwellian component has been subtracted.

(d) Based only on steady-state alpha-particle density, $Z_{eff} = (1 + 4f_\alpha)/(1 + 2\ f_\alpha)$ $f_\alpha = n_\alpha/n_i = 0.029$.

(e) At steady state, 200-300-MWe grid power required during bipolar startup.

(f) Based on ratio of fusion power to ohmic dissipation in plasma; inclusion of ohmic power dissipated in TFCs and PFCs gives a Q-value of 16.62.

3. Power Output

(a) Based on fusion power (2733.3 MWt) divided by plasma chamber volume (43.3 m^3).

(b) Based on fusion power (2733.3 MWt) divided by plasma volume (38.8 m^3).

(c) Based on total thermal power (3472.6 MWt) and net volume (359.2 m^3) enclosed by and including magnets.

(d) Based on first-wall, blanket, and shield volume (137.3 m^3) and on thermal power actually delivered to primary coolant (3472.6 MWt). Peak value of blanket power density is ~ 360 MWt/m^3 and actual average for the blanket is 25.4 MWt/m^3.

(e) Does not include primary-coolant pumping power.

(f) Includes 73 MW delivered to OHCs, which under steady-state operation could be reduced to zero.

4. Reactor Coolant System

(a) HT-9 is a ferritic steel (85.0 Fe/11.5 Cr/1.0 Mo/0.55 Mn/0.5 Ni/ 0.5 W/0.4 Si/0.3 V/0.2 C).

(b) Energy stored in the ~ 943-tonne PbLi coolant contained within the FPC amounts to 77 GJ over the temperature range from room temperature to 773 K, when ratio to the total thermal output gives ~ 20 s.

(c) Based on application of ECS for ~ 90 minutes to the limiter only and on natural circulation of PbLi in the blanket. Without ECS but with natural circulation of PbLi coolant, the first wall reaches a temperature of 900 K, but the limiter melts.

6. Steam Generation (SG) System

(a) Scaled from STARFIRE[3] and MARS results.[4]

(b) Each of four PbLi loops contains a superheater, steam generator, and an economizer. Each of two pressurized-water loops contains a steam generator and an economizer.

(c) HT-9 double-tube heat exchangers, PbLi/water on shell side and water/ system on tube side, with stagnant helium gas separating double tubes.

7. Shield Coolant System

(a) Thin (0.10-m) second-wall coolant operates at first-wall/second-wall coolant conditions and contributes to overall reactor power cycle through the pressurized-water coolant circuit.

8. Reactor Auxiliary System

(a) Vacuum volumes within the FPC include 4.5 m^3 for the 24 radial slots, 10.7 m^3 for the vacuum plenum, 1.7 m^3 for 24 ducts to outer edge of PFCs, plus 43.3 for the plasma chamber, giving a total of 60.2 m^3.

(b) Vacuum chamber volumes for the vertical and horizontal replacement cases are respectively 3,746 m^3 and 9,136 m^3.

(c) Adopted from the STARFIRE design.[3]

(d) Of this total, 35.7 MW is nuclear heating and 12.6 is ohmic heating.

(e) Of this total, 37.2 MW is nuclear heating; 126.5 is ohmic heating, of which 73.0 MW appears in the OHCs and 53.5 MW appears in the EFCs.

(f) Pellet speed ~ 100-200 km/s for deep penetration with ratio of pellet inventory to plasma inventory equal to 0.05. Significant edge-plasma fueling would be highly desirable to reduce required pellet velocity and/or injection frequency.

(g) Refer to Table 4-I for breakdown of tritium inventory.

9. Reactor Components

(a) Theoretical two-dimensional breeding ratio for updated value; does not include losses, decay, first-wall area reduction. The value given in Ref. 5 corresponds to a one-dimensional estimate made at the time of that study.

(b) The first-wall/blanket/shield/TFC forms a single, integral unit; weight does not include the ~ 943 tonne of PbLi coolant.

(c) Dimensions indicate effective major and and minor radii, respectively, of reactor torus.

(d) Lower value at PFC #12 (upper, inboard) and higher value at PFC #6 (equatorial plane, inboard); compares to 550 MPa (TFC) and 14 MPa (PFC) for STARFIRE and 127 MPa (TFC/ARE) for EBTR.

(e) Centering force for TFC.

(f) Maximum field at inboard side of PFC.

(g) Toroidal field at plasma edge is -0.40 T and increases to -0.72 T at the TFC.

(h) Total mass of PFC is 813 tonne, with EFC being 413 tonne and the OHC being 400 tonne. Each EFC and OHC set would in turn be divided into two segments for maintenance purposes (Sec. 4.).

(i) If a grid-assisted startup proves unfeasible, a transferred energy store of ~ 2 GJ will be required.

(j) Ohmic losses in OHC, which would be driven to zero once current drive initiated.

10. Electrical Power Requirements

(a) Taken nominally as $f_{AUX} = 0.05$ of the gross electrical power, $P_{ET} = 1255.8$ MWe, but increased to 0.07 to maintain $P_E = 1000$-MWe(net) (Table 3-VII).

(b) Based on 75% pump efficiency.

11. Buildings

(a) The reactor building heights for the vertical and horizontal replacement cases are respectively 54 m and 39 m.

(b) Includes volume of reactor hall and primary-coolant component room; value used to calculate overpressure in event of coolant line rupture.

(c) Normal operating pressure is slightly less than atmospheric, as in the present-day nuclear power plants. The accident condition is assumed to be the loss of primary coolant into the containment building.

12. Reactor Maintenance

(a) Based on replacing entire first wall and blanket each year of operation, and recycling the shield (159.6 tonne) and TFCs (76.2 tonne).

(b) Includes copper-alloy first-wall and limiter components, possible for deep geologic burial or dilution by a factor in excess of ~ 300 for Class C burial.

(c) Includes all blanket structure, headers, and manifolds inboard of coils (Table 3-VIII), which amounts to 56.8 tonnes or 1,688 tonnes per 30 years. Volume quoted corresponds to uncompressed state, which when loaded with concrete gives a total mass of 7,900 tonnes.

(d) Includes all shielding, coils, primary structure and support, and vacuum cryopumps but excludes long-term storage in Item 12.2.1. and blanket articles in Item 12.2.2.

(e) Based on 60 day/year unscheduled maintenance and 28 day/FPC replacement, this algorithm being sensitive to fusion neutron first-wall loading and giving an optimal wall loading based on COE.

REFERENCES FOR APPENDIX A

1. C. R. Head, "Standard Fusion Reactor Design Study Contents," Department of Energy, Office of Fusion Energy letter RS&A:CRH:#478 (March 7, 1979).

2. R. L. Hagenson, C. G. Bathke, R. L. Miller, M. J. Embrechts, N. M. Schnurr, M. E. Battat, R. J. LaBauve, and J. W. Davidson, "Compact Reversed-Field Pinch Reactors (CRFPR): Preliminary Engineering Considerations," Los Alamos National Laboratory report LA-10200-MS (August 1984).

3. C. C. Baker and M. A. Abdou (Principal Investigators), et al., "STARFIRE - A Commercial Tokamak Fusion Power Plant Study," Argonne National Laboratory report ANL/FPP-80-1 (September 1980).

4. B. G. Logan, C. D. Henning, G. A. Carlson, R. W. Werner, D. E. Baldwin, W. L. Barr, et al., "MARS Mirror Advanced Reactor Study Final Report," Lawrence Livermore National Laboratory report UCRL-53480 (July 1984).

5. R. L. Hagenson, C. G. Bathke, R. L. Miller, M. J. Embrechts, N. M. Schnurr, N. E. Battat, R. J. LaBauve, and J. W. Davidson, "Compact Reversed-Field Pinch Reactors (CRFPR): Preliminary Engineering Considerations," Los Alamos National Laboratory report LA-10200-MS (August 1984).

APPENDIX B. COST DATABASE

B.1. Cost Basis

Capital and operating costs leading to an estimate of the cost of electricity (COE) for the Compact Reversed-Field Pinch Reactor (CRFPR) are calculated using a costing code based on widely used DOE guidelines[1,2] and a unit-cost database (or a set of scaling rules) developed over a number of years and implementing information from a number of studies.[3-20] A new system of accounts,[4] presently under community review, will eventually supersede the system used here.

The CRFPR cost estimate is specific to this system and reflects the ground rules applied to this study. It is expected, however, that many of the results can be used to assess economic trends for many other magnetic fusion concepts, particularly since the database has been calibrated by other recent studies. When comparing results with an estimated cost of an existing power plant, it should be emphasized that the CRFPR design is preconceptual, with most subsystems not fully defined or developed. Cost estimates for poorly defined subsystems were determined with implicit design allowances to account for uncertainties. Fortunately, many of the balance-of-plant (BOP) and heat-transport systems are similar to existing Pressurized-Water Reactor (PWR) fission systems, and this similarity should enhance the credibility of the capital-cost estimates. The direct-capital cost estimates associated with the reactor plant equipment (RPE), the BOP equipment, land, and all the related structures and site facilities, are based upon supplier quotes, historical data, and costs of analogous systems, as compiled, assimilated, and modified by the Ref. 3-20 studies. The indirect-cost estimates related to construction are based upon DOE recommendations,[1,2] as modified by recent studies. Time-related costs account for both interest and escalation during construction. The annual costs include annualized capital cost, operations and maintenance costs, fuel costs, and any scheduled component replacement costs. Given these costs along with the plant capacity (i.e., net power) and the plant availability, the bus-bar energy cost estimate is determined. These costs are presented in both constant (1980) dollars and then-current (1985) dollars, reflecting the assumed 5-yr construction time.

This Appendix defines the economic guidelines and assumptions used in the study and analyses. The key design, performance, and operational features and their impact on the economics of the overall system are discussed. The capital cost accounts summarized in Table B-I generally follow the DOE guidelines[1,2] and provide a uniform evaluation/accounting tool by which possible comparisons can be made with other studies. The estimated costs for CRFPR(20) are discussed, and any significant influencing factors or components are highlighted. Table B-II shows the total bus-bar energy cost components for fusion-generated energy.

B.1.1. Economic Guidelines and Assumptions

To assure a consistent economic evaluation of the CRFPR, the DOE guidelines[1,2] for costing fusion systems were adopted to the maximum extent for this study. This procedure assists in an evaluation of the CRFPR that is consistent with procedures used for alternate energy systems. These guidelines apply both to design and economic analyses. All costs quoted in this report are referenced to 1980 dollars in order to facilitate comparison with past studies. It is assumed that the user of the power plant will be an investor-owned utility.

B.1.2. Level of Technology

The CRFPR design philosophy adopts the state-of-the-art technology for all BOP systems except where incorporation of specific advances in technology will enhance the performance, schedule, and/or cost. The CRFPR turbine cycle efficiency is determined by calculation (Sec. 2.2.) or by default is assumed to be $\eta_{TH} = 0.35$. With the exception of the PbLi steam generator, most of the BOP systems selected for the CRFPR represent current PWR technology (i.e., the pressurized-water circuit steam generators, superheaters, turbine and electric plant equipment, Condensing and Heat Rejection Equipment, and most of the Miscellaneous Plant Equipment). All buildings are also considered to be of conventional design.

Three levels of technology compose the RPE. The first level represents technologies that have been demonstrated for a commercial power plant. Typical of this level are the Primary and Closed Coolant Systems, power supplies, portions of the Radioactive Waste Treatment and Disposal System, and most of the Other Reactor Plant Equipment. The second level represents technologies that have been demonstrated in existing power plants but that have new or unique

TABLE B-I

SUMMARY OF STANDARD CAPITAL COST ACCOUNTS[1]

Cost Account Title

Direct Costs:

20. Land and Land Rights
21. Structures and Site Facilities
22. Reactor Plant Equipment (RPE)
23. Turbine Plant Equipment
24. Electric Plant Equipment
25. Miscellaneous Plant Equipment
26. Special Materials

    Total Direct Cost (TDC)

    Unit Direct Cost (UDC/$kWe)

Indirect Costs:

91. Construction Facilities, Equipment, and Services
92. Engineering and Construction Management Services
93. Other Costs

    Total Base Cost

    Unit Base Cost ($/kWe)

94. Interest During Construction (IDC)
95. Escalation During Construction (EDC)
99. Total Cost

    Unit Total Cost ($/kWe)

Annual Costs:

40. Salaries of Facility Personnel
41. Miscellaneous Supplies and Equipment
42. Outside Support Services
43. General and Administrative Costs
44. Coolant Makeup
45. Process Materials
46. Fuel Handling Costs
47. Miscellaneous Costs
50. First Wall/Blanket/Limiter Replacement
51. Replacement of Other Reactor Components
02. Fuel Cost
03. Fuel Cycle Materials Cost

TABLE B-II

TOTAL BUS-BAR ENERGY COST COMPONENTS

- Annualized Capital Cost (Account 99)
- Operations and Maintenance (Accounts 40-47)
- Scheduled Component Replacement (Accounts 50-51)
- Fuel (Accounts 02-03)

Total Annual Cost

Cost of Electricity (COE, mills/kWeh)

application, design, and/or configuration. Systems at this level represent only a modest extrapolation of the existing state of the art; examples are elements of the shielding, the Atmospheric Tritium Cleanup System, elements of the Maintenance Equipment, Special Heating Systems, Inert Atmosphere System, and Reactor I&C System. The third level of technology remains to be demonstrated in a commercial power plant, but the technology may have been commercially demonstrated by other industries. Typical of this third level are the FPC, PbLi steam generator, PbLi pumps, and associated heat-transport equipment. All these systems and related technologies are assumed to have been commercially demonstrated in power plants by the time the CRFPR is constructed (i.e., first-wall/blanket/limiter systems, the radiation-hardened copper-alloy coils, large vacuum cryopumps, tritium processing and storage, and special remote maintenance equipment).

Another aspect of the level of technology involves the design and operational philosophy of remote maintenance. This philosophy will require a re-evaluation of present power-plant design criteria, procurement procedures, and operational practices. Designs will have to be modified or redesigned for modular or single-piece replacement, and firmer control will have to be enforced on specifications and interchangeability of parts. Present trends in the nuclear industry indicate advantages to more off-site, factory construction. This philosophy represents an evolutionary change in the power industry, may be necessary in the future, but is not reflected directly in the costing procedure.

It is implied in all of the foregoing discussions that the CRFPR, like STARFIRE[13] and EBTR,[14] is not the first-of-a-kind fusion power plant. These systems are assumed to be based on a specific design technology wherein all systems have been proved thoroughly. Equipment R&D costs, therefore, are not

included, and the equipment is costed with appropriate learning curves applied. Engineering and Construction Management Services (Account 92) are reduced to a degree that reflects the design standardization of the reactor and BOP. No tooling costs are included in the cost estimate as all initial tooling costs are amortized over previously constructed CRFPR fusion power plants. Learning-curve design allowances and site assumptions are consistent with those assumed for STARFIRE.[13]

A contingency allowance is added to account for the difference between the sum of individual estimated costs and the total amount that is reasonably expected to be spent, considering the degrees of uncertainty in the estimated quantities, prices, and labor productivity. This contingency allowance is intended to reduce the risk of an overrun. The CRFPR estimate uses the recommended value[2] of 15% for Accounts 21, 22, 23, 24, and 25.

Spare parts required by the power plant must be held in inventory in order that the plant can quickly recover operation in event of a breakdown. Spare parts do not include equipment that is permanently connected in the systems to assure a desired level of redundancy. The spare-parts allowance is assumed to be a percentage of direct equipment cost, with the following spare-parts allowances being adopted:[1,13]

Cost Account	Spare-Parts Allowance
21, 22, 23	2%
24	4%
25	3%
Others	0%

The cost of the CRFPR(20) reactor torus (FW/B/S/TFC) is incurred every year and is included as an operating expenditure, although the relatively low cost of this ~ 304-tonne item (~ 10-15 M$) would allow inclusion of extras under the spare-part allowance. It is expected that certain reactor-torus components (e.g., shield and TFCs) could be reused and reassembled into refurbished tori, although the tradeoff associated with component reuse remains to be understood.

B.1.3. Indirect-Cost Allowances

The indirect-cost allowances are expenses resulting from the support activities required to design, fabricate, assemble, and check out the entire power plant. The three major accounts are Construction Facilities, Equipment and Services (Account 91), Engineering and Construction Management Services (Account 92), and Other Costs (Account 93). Appendix G of Ref. 14 gives additional detail for specific items included in each account.

Construction Facilities, Equipment and Services (Account 91) for the CRFPR(20) are not unlike those for fission plants, although some assembly and checkout of the reactor torus may be conducted offsite. This preassembled FPC (less PFCs) will be similar in size to most fission reactor components, including the PWR pressure vessel. The cost estimate of the Construction Facilities, Equipment and Services adopts an allowance of 10% of the total direct cost. This procedure is based on that adopted for STARFIRE,[13] which, because of a higher total direct cost for the latter, may be underestimated for the CRFPR(20). Present fission nuclear experience sets this percentage more in the range 15-20%. The FPC will require very little on-site handling and no field construction, with the possible exception of minor assembly of the PFCs.

Engineering and Construction Management Services (Account 92) consists of the expenses for reactor and plant engineering and construction management services. The design philosophy of applying the present and envisaged power-plant technology will certainly reduce the required engineering for the BOP and the Heat Transfer and Transport systems. The only engineering services being considered are those which are necessary for site development, utility requirements, new or updated regulatory guides, and design improvements. Services required of the construction management will be eased somewhat because of familiarity with the PWR systems. Based upon these considerations and the capital-intensive cost base, Account 92 costs are taken to be 8% of the TDC.

Associated with other costs (Account 93) are taxes, insurance, staff training, plant startup, and owner's General and Administrative (G&A) costs. Most of these items scale directly with the direct capital expense, and the CRFPR(20) estimate, therefore, adopted the recommended 5% of TDC for Other Costs.[1] A proposal[4] for an update and re-standardization of the indirect cost accounts is presently under review by the fusion community and has not been implemented into the CRFPR cost package. The new methodology would increase

implemented into the CRFPR cost package. The new methodology would increase indirect costs from the 23% value, used in this study and for STARFIRE[13] to 35%.

B.1.4. Time-Related Costs

Time-related costs are incurred because the fabrication, installation, construction, checkout, and startup occur over a finite period of time. These expenses are related to the opportunity cost of money and the changes in the purchasing power of the dollar with respect to time. Account 94 represents the allowance for funds used during construction (AFDC) or interest during construction (IDC). The IDC is the expense of the interest charges of financing the debt, the charges on the equity (common stock) portion of the financing, and any administrative charges on the financing. The interest during construction is determined by three elements: the total direct and indirect capital cost of the facility, the time distribution of the capital expenditures, and the aggregate interest rate on all financing charges. The time distribution of the capital expenditures is dependent upon the construction schedule, the construction techniques, the material and equipment purchases and progress payments, and the checkout and startup schedule. The expenditure pattern[1,13] shown in Fig. B-1 is adopted by this study. At a point 60% through the construction period, one-half of the direct costs have been incurred.

The aggregate interest rate is representative of a privately owned utility. The following assumptions[1] are used as a basis for determining the cost of capital:

- Utility is investor owned.
- Capital structure is 53% debt financing and 47% equity (common stock) financing.
- Nominal cost of debt financing is 8% per year.
- Nominal cost of equity financing is 14% per year.
- Power plant economic lifetime is 30 yr with no salvage value.
- Cost escalation and general inflation is 5% per year.

Given these assumptions, the nominal cost of capital is 10% per year, and the real (deflated) cost of capital is 5% per year.

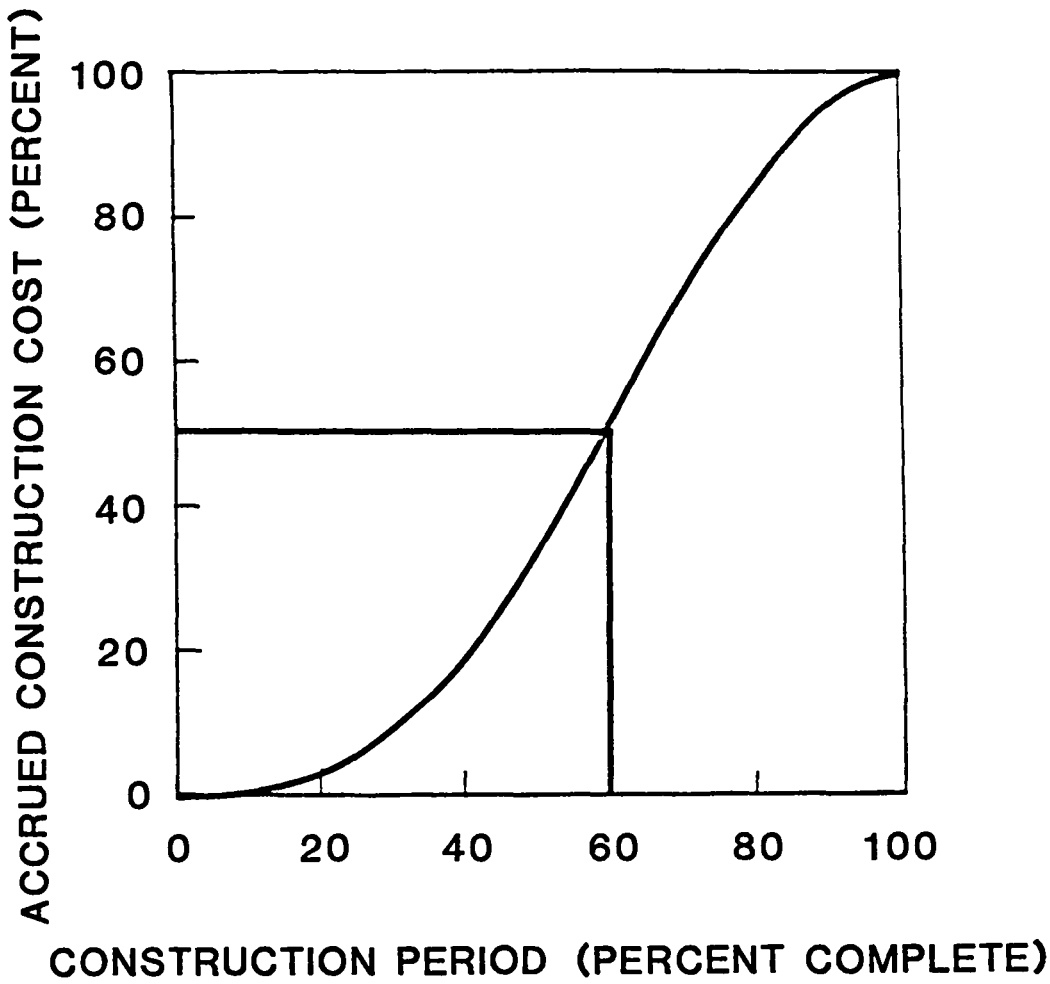

Fig. B-1. Fusion-power-plant expenditure pattern.[1,13]

Two modes of economic analysis are utilized in this study. The first mode is a "constant-dollar" mode, which assumes the purchasing value of the dollar remains constant over time. This constant-dollar analysis expresses the cost in 1980 dollars. The inflation is assumed to be zero and the cost of capital is 5% per year. The second mode of analysis uses the "then-current-dollar" mode which assumes that purchasing value changes over time (inflation rate is not zero). The cost of capital for this mode is 10% per year, and the escalation is 5% per year. Figure B-2 illustrates the means by which interest and escalation are additive to the direct and indirect cost of capital. The specific values assumed for interest and escalation have been standardized[1-3] for comparison

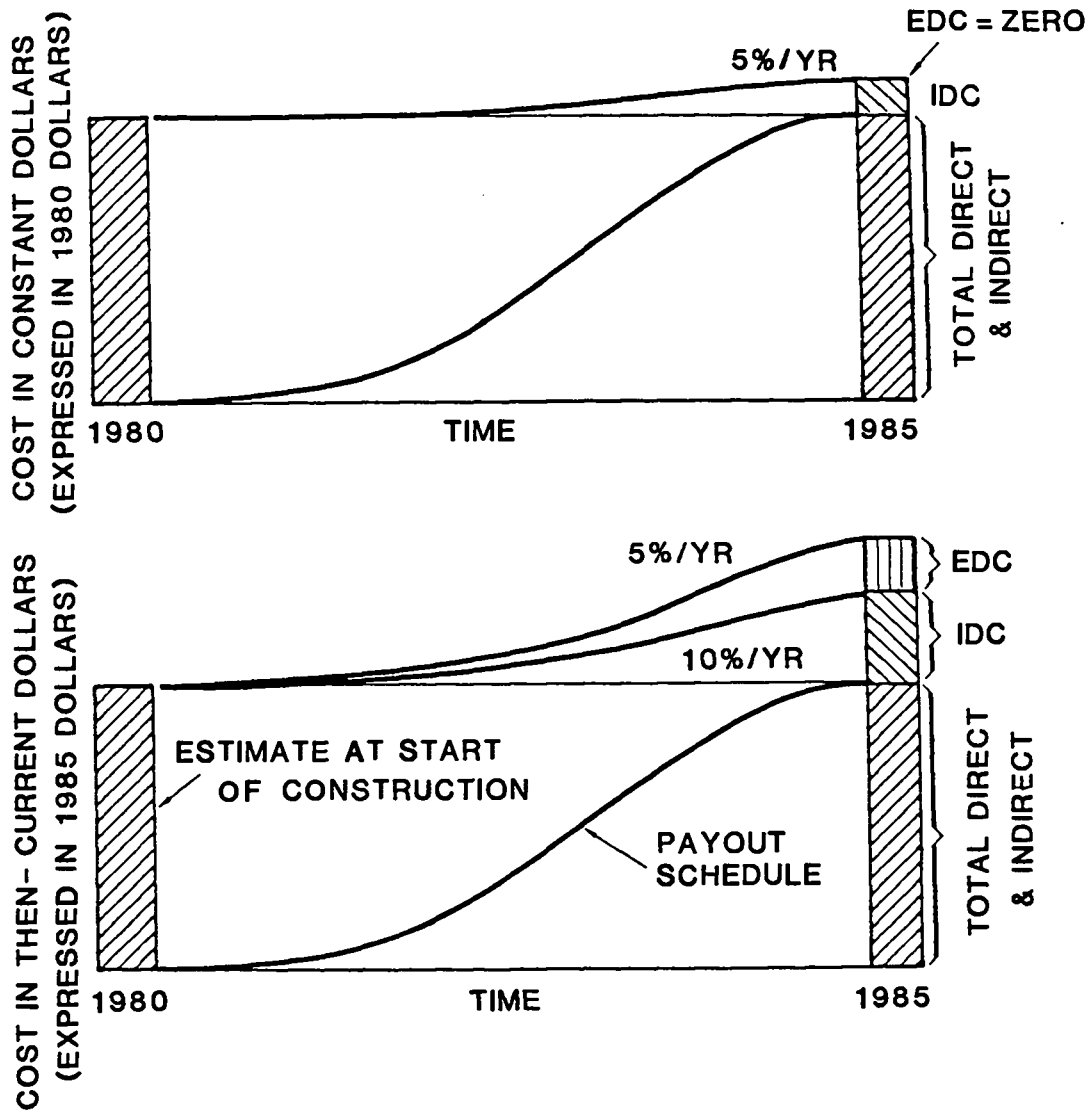

Fig. B-2. Comparison of constant and then-current dollar analyses for a 5-yr construction period.[1,13]

purposes with other fusion studies and are not intended to reflect actual interest and inflation fluctuations. The multipliers of the direct cost as a function of construction time are illustrated in Fig. B-3. All costs reported in Accounts 20-26 and 91-93 are presented in 1980 dollars, and all effects of cost of capital and escalation during construction are reported, respectively, in Accounts 94 and 95 as factors of total direct and indirect costs.[1] The then-current-dollar analysis gives essentially a nominal first-year facility cost, with escalation only computed during construction.

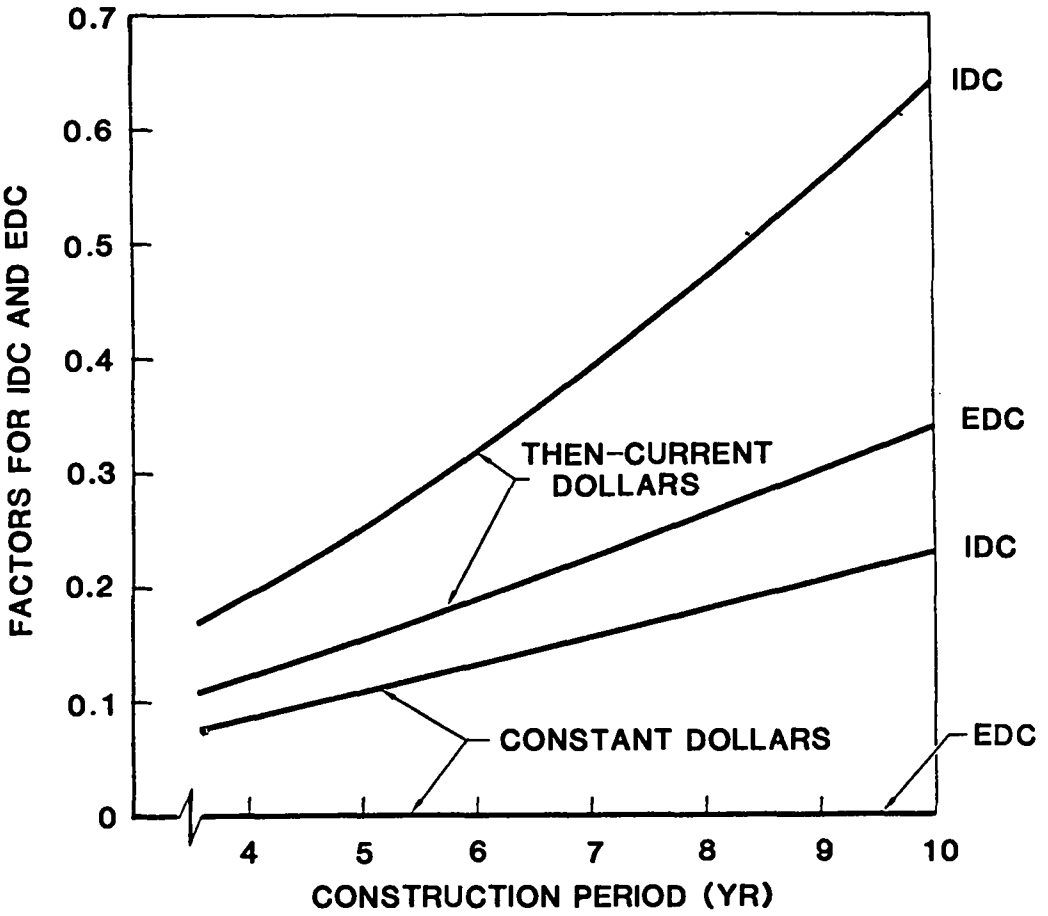

Fig. B-3. Factors used for Interest During Construction (IDC) and Escalation During Construction (EDC) as a function of construction duration.[1,3,13]

Care should be exercised when comparing the cost of CRFPR to that of other energy sources. Key factors involve the cost basis of the estimate (usually the start of construction), the length of construction, the basis for the cost of capital and escalation, and the presentation mode of the facility economics (e.g., constant, then-current, or levelized). Any new energy source presently starting construction will certainly cost more than an existing energy source as a result of inflation. Any comparison, therefore, should only consider new starts on alternative energy sources. Also, the preliminary nature of the present CRFPR cost estimates, based on incomplete engineering designs, is again emphasized, this uncertainty being reflected both in uncertain physics performance (i.e., UDC) and plant availability (i.e., COE).

B.1.5. Key Design, Performance, and Operational Features

Several key features of a power plant directly influence the capital and operational cost. Table B-III lists the major design, performance, and operational features that can significantly affect the power plant economics. The CRFPR design philosophy assumes a developed fusion-energy industry, as reflected by several design features: steady-state operation, enhanced maintenance access, and limiter/vacuum impurity-control system. These features remain to be thoroughly demonstrated but would be qualitatively typical of the design features needed for a fusion power plant.

Steady-state operation of the CRFPR reactor relieves thermal-fatigue problems and increases the system reliability. Steady-state operation also eliminates the need for thermal and electrical energy storage. These features are particularly necessary for the high-power-density CRFPR(20). Commercial operation also requires adequate maintenance access. The decision to incorporate fully remote, single-piece maintenance in the reactor building and hot cell exerts another strong influence on system economics, particularly from the viewpoint of plant availability. Remote handling is presently undergoing

TABLE B-III

KEY CRFPR DESIGN, PERFORMANCE, AND OPERATIONAL FEATURES

- A specific design technology dictated by past construction and operating experience
- Moderate aspect ratio device
- Batch (single-piece) maintenance of FPC reactor torus (FW/B/S/TFC)
- Steady-state operation
- Ohmic heating to ignition
- Limiter/vacuum impurity-control system
- Copper-alloy high-heat flux surfaces
- High neutron first-wall loading ($I_w \sim 20$ MW/m^2)
- Reactor thermal power output ~ 3500 MWt
- Dual-media PbLi/H_2O primary coolant loop
- No intermediate coolant loop
- Plant availability ~ 0.76
- Low fuel cost, typically expected of fusion

rapid development, and it is assumed that the necessary equipment has been developed and is being utilized.

System redundancy, steady-state operation, ease of reactor torus replacement, and development of reliable components should permit the assumed overall plant availability of 76% for the CRFPR designs. This plant availability also includes a major 120-day shutdown every ten years. Steady-state operation should considerably improve reliability for the application of economically optimum engineering safety factors. The plant availability is reduced from 100% because of outage time for scheduled, t_s, and unscheduled, t_u, maintenance periods. The plant availability equals $(365 - t_u - t_s)/365$, where t_u and t_s are expressed in days. The scheduled outage time has been estimated as 28 days per reactor-torus changeout, including 120 days every 10 yrs for turbine-generator overhaul. To achieve the target availability of 76%, the unscheduled outage is set at 60 days per year.

The periodic first-wall and blanket replacement is an important operational feature. An integral neutron first-wall loading or lifetime of $I_w\tau = 15$ MWyr/m^2, an average neutron wall load of ~ 20 MW/m^2, and an overall plant availability of 76% yield a first-wall life of approximately one calendar year. The remote maintenance scenario is designed to accomplish the required single-piece replacement within the annual maintenance period. Estimates given in Table 4-II of Sec. 4. indicate a wide margin exists in achieving these goals.

An attractive feature of a DT fusion power plant is the low cost of fuel. Deuterium is estimated to cost 2200 \$/kg. Adequate tritium would be bred by the reactor and, therefore, is not considered as a cost item. The future tritium cost will be dependent upon the then-current supply and demand for tritium but will unlikely ever decrease below the cost of processing and handling. The startup cost for tritium has not been taken into account.

B.1.6. Cost of Electricity

All prior analyses are utilized to calculate the bus-bar cost of energy available from the CRFPR(20) fusion power plant. The COE is the most important evaluation tool to optimize (Sec. 6.2.) and to compare with alternative energy sources. Both constant-1980 and then-current-1985 dollar analyses are used to evaluate the CRFPR economic parameters. The general equation for bus-bar energy cost is given by

$$COE = \frac{C_{AC} + (C_{O\&M} + C_{SCR} + C_F)(1 + E)^P}{8760\ P_E P_f} \quad , \tag{1}$$

where

COE = Cost of electricity in constant or then-current dollars (mills/kWeh),

C_{AC} = Annual capital cost charge, equals total capital cost multiplied by fixed charge rate (0.10 for constant-dollar analysis or 0.15 for then-current-dollar analysis),

$C_{O\&M}$ = Annual operations and maintenance cost, $C_{40} + C_{41} + \ldots + C_{47}$,

C_{SCR} = Annual scheduled component replacement cost, $C_{50} + C_{51}$,

C_F = Annual fuel costs, C_{02} and C_{03},

E = Escalation rate equals 0.0 for constant-dollar analysis and 0.05 for then-current-dollar analysis,

P = Construction period (yr),

P_E = Net plant capacity (MWe), and

P_f = Plant availability factor.

The essential elements of the CRFPR cost database are summarized in Table B-IV, updating the database summarized in Table III-IV of Ref. 12. A number of minor changes and several offsetting major changes have been introduced, with the former being summarized in Sec. 6.1. and the latter being summarized below. Most of the latter changes reflect attempts to adopt procedures from or rectify differences between the STARFIRE[13] and MARS[18] designs, as well as to include better estimates emerging from this follow-on study (i.e., reactor vacuum vessel and pumps, reactor room, pipe runs, reactor building, etc.).

For purposes of costing in the parametric systems model, the reactor building is divided into a variable-volume reactor cell, housing the FPC and vacuum tank, and a fixed-volume region, housing the dual-media primary heat-transfer/transport loops. The volume of the latter portion, consistent with the

TABLE B-IV

SUMMARY FUSION REACTOR COST DATABASE[a]

ACC. NO	ACCOUNT TITLE	(M$, 1980)
20.	Land and land rights	3.3
21.	Structures and site facilities	
21.1	Site improvements and facilities	11.15
21.2	Reactor building	$3(10)^{-4}V_{RB}$ + 39.5
21.3	Turbine building	33.5
21.4	Cooling structures	$7.13(P_{ET}/1000)^{0.3}$
21.5	Power supply and energy storage	9.16
21.6	Miscellaneous buildings	76.5
21.7	Ventilation stack	1.81
21.98	Spare parts (2%)	
21.99	Contingency (15%)	
22.	Reactor Plant Equipment	
22.1	Reactor Equipment	
22.1.1	Blanket and first wall	$0.31\ V_{BL}$
22.1.2	Shield	$0.105\ V_{SHD}$
22.1.3	Magnets	$0.292\ V_{C}$
22.1.4	Supplemental heating systems	0.0
22.1.5	Primary structure and support	$0.1125\ V_{STR}$
22.1.6	Reactor vacuum system	$0.015\ M_{VAC}$ + $0.83\ (P_F/250)$
22.1.7	Power supply (switching & energy storage)	$0.04\ P_{ET}$
22.1.8	Impurity control system	$0.0026\ V_{VAC}$
22.1.9	Direct energy conversion	0.0
22.1.10	ECRH Breakdown system	2.82
22.2	Main heat transfer system	
22.2.1	Primary coolant (PbLi)	$0.035\ P_{TH}\ (1 - f_w)$
22.2.2.	Intermediate coolant system	0.0
22.2.3.	FW/Limiter/Shield coolant system (H_2O)	$0.035\ P_{TH}\ f_w$
22.3	Auxiliary cooling systems	$6.7(10)^{-4}\ P_{TH}$
22.4	Radioactive waste treatment	$1.2(10)^{-3}\ P_{TH}$
22.5	Fuel handling and storage	$9.65(10)^{-3}\ P_{TH}$
22.6	Other reactor plant equipment	$1.09(10)^{-2}\ P_{TH}$
22.7	Instrumentation and control	23.41
22.98	Spare parts allowance (2%)	
22.99	Contingency allowance (15%)	
23.	Turbine plant equipment	
23.1	Turbine-generators	$59.9\ (P_{ET}/1000)^{0.7}$
23.2	Main steam system	$4.80\ (P_{TH}/2860)$
23.3	Heat rejection systems	$33.0\ (P_{TH}/2860)^{0.8}$
23.4	Condensing system	$13.8\ (P_{ET}/1000)^{0.9}$
23.5	Feed heating system	$7.55\ (P_{TH}/2860)$
23.6	Other turbine plant equipment	$40.9\ (P_{ET}/1000)^{0.6}$
23.7	Instrumentation and control	$7.80\ (P_{ET}/1000)^{0.3}$
23.98	Spare parts allowance (2%)	
23.99	Contingency allowance (15%)	

TABLE B-IV (cont)

ACC. NO	ACCOUNT TITLE	(M$, 1980)
24.	Electric plant equipment	
24.1	Switchgear	8.6 (P_{ET}/1000)
24.2	Station service equipment	14.2.(P_{ET}/1000)
24.3	Switchboards	5.4 (P_{ET}/1000)
24.4	Protective equipment	2.11
24.5	Electrical structures and wiring containers	16.4
24.6	Power and control wiring	33.9
24.7	Electrical lighting	8.2
24.98	Spare parts allowance (4%)	
24.99	Contingency allowance (15%)	
25.	Miscellaneous plant equipment	
25.1	Transportation and lifting equipment	15.68
25.2	Air and water service systems	12.35
25.3	Communications equipment	6.22
25.4	Furnishings and fixtures	1.20
25.98	Spare parts allowance (3%)	
25.99	Contingency allowance (15%)	
26.	Special Materials	$0.25 + 9.5(10)^{-3}M_{PbLi}$
90.	Total direct cost (TDC)	
91.	Construction facilities, equipment, and services (10%)	
92.	Engineering and construction management services (8%)	
93.	Other costs (5%)	
94.	Interest during construction, (IDC, 10%/yr)	
95.	Escalation during construction, (EDC, 5%/yr)	
99.	Total cost	

(a) Gross electric, P_{ET}, net electric, P_E, and total thermal, P_{TH}, powers given in MW. Volumetric V(m^3) abbreviations or corresponding mass M(tonne) costs for the fusion power core (FPC) and related items are given as follows:

Reactor building, $V_{RB} = 4(R_T + r_s)^2(12r_s) + 1.55(10)^5$ (m^3)
Blanket structure (5%), $V_{BL}(m^3)$
Shield, $V_{SHD}(m^3)$
Magnet, $V_C(m^3)$
Structure, $V_{STR}(m^3)$
Vacuum tank, $M_{VAC} = (0.07)(7.8)2\pi[(R_T + r_s + 3)^2 + (R + r_s + 3)(4r_s)]$ (tonne)
PbLi coolant, $M_{PbLi} = (0.95)(1.09)V_{BL}(9.4) + 4{,}525$ (tonne)

layout depicted in Fig. 4-1, is estimated to be $1.55(10)^5$ m^3 and is similar to that of the STARFIRE design.[13] The reactor room is modeled by a rectilinear enclosure extending horizontally 9 m beyond the FPC with a height approximately 6 times that of the FPC, such that $V_{RB} = [2(R_T + r_s + 9)]^2[12r_s]$ m^3. The basic building structure (Account 21.2.1.) is costed at 300 $/m^3, a value intermediate between that of STARFIRE[13] and MARS,[18] to which is added 2 M$ for building services (Account 21.2.2.), 30 M$ for containment structures (Account 21.2.3.), and 7.5 M$ for architectural costs (Account 21.2.4.). Previous CRFPR studies[12,19] used STARFIRE-like unit costs (~ 500 $/$m^3$) applied to a smaller building volume estimate.

A treatment of the CRFPR blanket in terms of a drained PbLi tank (HT-9 structure, 5 v/o at 7.75 tonnes/m^3) replaces a treatment of a smeared blanket/shield/vacuum plenum with a density 5.5 tonnes/m^3. A separate limiter and manifolding mass has been added. The unit cost is 40 $/kg for these items. As for most of the costing adjustments reported herein, these changes reflect a better-resolved FPC design.

The CRFPR vacuum system cost includes the cost of the vacuum cryopump system,[9,13] which scales with He exhaust gas throughout and is, therefore, proportional to fusion power [i.e., 0.83 M$ (P_F/250 MWt)], and the cost of the vacuum tank enclosure, which is taken to be a 0.07-m-thick steel cylinder with an estimated radius of $R_T + r_s + 3$ m, a height of $4r_s$, and a unit cost of 15 $/kg, where $r_s = r_w + \Delta b + \delta_c$ is the system radius and R_T is the major radius of the reactor torus. This model supersedes the vacuum model used to perform the parametric calculation for Sec. 6. and adds ~ 10 M$ to the cost of this item.

The CRFPR Main Heat Transfer System includes a PbLi loop serving the blanket and a pressurized-water loop serving the first wall/limiter/shield. The fraction of thermal power delivered to the pressurized-water loop is denoted by $f_w \simeq 0.47$ (Fig. 3-1, Table 3-I). The cost of the PbLi loop (Account 22.2.1.) is estimated to be $3.40(10)^4$ $P_{TH}(1 - f_w)$ M$ and that of the pressurized-water loop (Account 22.2.3.) is estimated to be $3.5(10)^4$ P_{TH} f_w M$, these estimates being calibrated by the dual-media MARS design[18] with a reduction of 80% of the dominant piping costs of that design to reflect the shorter pipe runs in the CRFPR(20) case. This model results in a ~ 50 M$ increase in cost over the pressurized-water Main Heat Transfer System in STARFIRE.[13,16] The PbLi inventory

in the system consists of 95% of the blanket volume, corrected by a factor of 1.09 to account for the FPC ducts connecting the blanket through the TFC/PFC sets to the main PbLi manifolds. To this variable volume is added a fixed inventory of 4,525 tonnes for the primary-loop inventory, a value estimated from Fig. 4-1 and assumed to be relatively constant over the parameter range of interest. The PbLi density is 9.4 tonnes/m^3 and its unit cost (90% enriched) is taken to be 9.5 \$/m^3, a value intermediate to those of UWTOR-M[15] and MARS[18] estimates, both being close to each other. The cost of the primary-loop PbLi is reported under Special Materials (Account 26), insofar as it is salvageable and reuseable (once cleaned of Po^{210}).

The first-wall/blanket/limiter replacement cost estimate applies a factor of two to the direct cost of these components to allow for the handling/replacement of the spent reactor torus. For an assumed first-wall/limiter/blanket life of $I_w\tau$ = 15 MWyr/m^2 at a cost-optimized first-wall loading $I_w \simeq 20$ MW/m^2 and a plant factor ≃ 0.76, routine replacement occurs on an annual schedule. Account 50. represents ~ 3% of the base-case CRFPR COE and is distinct from the nominal annual O&M charge (Accounts 40-47, 51) conservatively estimated[2] to be 2% of the direct cost. This scheme costs the first reactor torus twice, and credit for any reactor-torus component reuse (i.e., TFCs or shield) is not taken.

B.2. Sample Cost-Code Output

Output from the cost code includes a cost-database summary. Table B-V is a typical example for the CRFPR(20) with cited reference numbers corresponding to the list at the end of this Appendix. In addition, a detailed cost summary, as shown in Table B-VI, is given. A global recapitulation of the major cost accounts and CRFPR major parameters is included at the end of Table B-VII along with the COE estimate based on constant (1980) and then-current (1985) dollars.

TABLE B-V

COMPUTER LISTING OF CRFPR(20) COST DATABASE

cost data base CRFPR 4/18/85

acc. no.	account title	1980 unit cost		no. of units	reference
20. 1. 0. 0	land & privilege acquisition	3.000e+03	$/acre	1.000e+03	13,14,16
20. 2. 0. 0	relocation of buildings, utilities, highways, etc.	3.000e+02	$/acre	1.000e+03	13,14,16
20. 0. 0. 0	land & land rights	0.		1.000e+00	
21. 1. 1. 0	general yard improvements	0.		1.000e+00	
21. 1. 2. 0	waterfront improvements	0.		1.000e+00	
21. 1. 3. 0	transportation access (off site)	0.		1.000e+00	
21. 1. 0. 0	site improvements & facilities	1.115e+07	$	1.000e+00	13,14
21. 2. 1. 0	basic building structures	3.000e+02	$/m3	1.757e+05	13,18
21. 2. 2. 0	building services	2.000e+06	$	1.000e+00	13,14,+
21. 2. 3. 0	containment structures	3.000e+07	$	1.000e+00	13,14,+
21. 2. 4. 0	architectural	7.500e+06	$	1.000e+00	13,14,+
21. 2. 0. 0	reactor building	0.		1.000e+00	
21. 3. 1. 0	basic building structures	3.000e+07	$	1.000e+00	13,14,18
21. 3. 2. 0	building services	2.000e+06	$	1.000e+00	13,14,+
21. 3. 3. 0	architectural	1.500e+06	$	1.000e+00	13
21. 3. 0. 0	turbine building	0.		1.000e+00	
21. 4. 1. 0	intake structures	0.		1.000e+00	
21. 4. 2. 0	discharge structures	0.		1.000e+00	
21. 4. 3. 0	unpressurized intake & discharge conduits	0.		1.000e+00	
21. 4. 4. 0	recirculating structures	0.		1.000e+00	
21. 4. 5. 0	cooling tower systems	0.		1.000e+00	
21. 4. 0. 0	cooling system structures	8.982e+05	$/unit	8.422e+00	2,13,14
21. 5. 1. 0	basic building structures	8.030e+06	$	1.000e+00	13,14
21. 5. 2. 0	building services	5.300e+05	$	1.000e+00	13,14
21. 5. 3. 0	architectural	6.000e+05	$	1.000e+00	13
21. 5. 0. 0	power supply & energy storage building	0.		1.000e+00	
21. 6. 1. 0	reactor auxiliaries building(incl. switchgear bay)	3.260e+06	$	1.000e+00	13,14
21. 6. 2. 0	hot cell building	5.396e+07	$	1.000e+00	13,14
21. 6. 3. 0	fuel storage building	8.630e+06	$	1.000e+00	13,14
21. 6. 4. 0	control room building	3.100e+06	$	1.000e+00	13,14
21. 6. 5. 0	diesel generator building	2.050e+06	$	1.000e+00	13,14
21. 6. 6. 0	administration building	8.700e+05	$	1.000e+00	13,14
21. 6. 7. 0	service building	1.880e+06	$	1.000e+00	13,14
21. 6. 8. 0	cryogenics building	9.100e+05	$	1.000e+00	13,14
21. 6. 9. 0	miscellaneous structures & building work	1.840e+06	$	1.000e+00	13,14
21. 6. 0. 0	miscellaneous buildings	0.		1.000e+00	
21. 7. 0. 0	ventilation stack	1.810e+06	$	1.000e+00	13,14
21.98. 0. 0	spare parts allowance	2.000e-02	fraction	-1.000e+00	2,13,14
21.99. 0. 0	contingency allowance	1.500e-01	fraction	-1.000e+00	2,13,14
21. 0. 0. 0	structures & site facilities	0.		1.000e+00	
22. 1. 1. 1	breeding material(incl. tritium breeding)	9.500e+00	$/kg	9.353e+05	15,18
22. 1. 1. 2	first wall & structural material	3.100e+05	$/m3	5.354e+00	19
22. 1. 1. 3	attenuators, reflectors, & multipliers	0.		1.000e+00	
22. 1. 1. 4	wall modifiers(coatings, liners, limiters, etc.)	0.		1.000e+00	
22. 1. 1. 5	others	0.		1.000e+00	
22. 1. 1. 0	blanket & first wall	0.		1.000e+00	
22. 1. 2. 1	primary	0.		1.000e+00	
22. 1. 2. 2	secondary	0.		1.000e+00	
22. 1. 2. 0	shield	1.050e+05	$/m3	2.026e+01	12,19
22. 1. 3. 1	principal field magnet	2.920e+05	$/m3	2.097e+01	9,12,19
22. 1. 3. 2	secondary field magnet	2.920e+05	$/m3	9.662e+01	9,12,19
22. 1. 3. 0	magnets	0.		1.000e+00	

22. 1. 4. 1	beam heating(neutral, ion or electron)	0.		1.000e+00		
22. 1. 4. 2	rf heating	1.654e+00	$/W	0.		16,17
22. 1. 4. 3	laser heating	0.		1.000e+00		
22. 1. 4. 4	other heating systems	0.		1.000e+00		
22. 1. 4. 0	supplemental heating systems	0.		1.000e+00		
22. 1. 5. 1	reactor structure	0.		1.000e+00		
22. 1. 5. 2	equipment support structure	0.		1.000e+00		
22. 1. 5. 0	primary structure & support	1.125e+05	$/m3	1.089e+02	13,14	
22. 1. 6. 1	plasma chamber vacuum(incl. pumps/comp./pipe)	1.500e+01	$/kg	5.061e+05	9	
22. 1. 6. 2	magnet dewar vacuum(incl. pumps/comp./pipe)	0.		1.000e+00		
22. 1. 6. 3	suppl. heating vacuum(incl. pumps/comp./pipe)	0.		1.000e+00		
22. 1. 6. 4	direct convertor vacuum(incl. pumps/comp./pipe)	0.		1.000e+00		
22. 1. 6. 5	reactor vacuum system(low grade)	0.		1.000e+00		
22. 1. 6. 6	reactor vacuum wall	2.500e+06	$/unit	3.527e+00	9	
22. 1. 6. 0	reactor vacuum systems(unless integral elsewhere)	0.		1.000e+00		
22. 1. 7. 1	heating	0.		1.000e+00		
22. 1. 7. 2	confinement	0.		1.000e+00		
22. 1. 7. 3	control system	0.		1.000e+00		
22. 1. 7. 4	central energy storage	0.		1.000e+00		
22. 1. 7. 5	other	0.		1.000e+00		
22. 1. 7. 0	power supply, switching & energy storage	8.000e+04	$/MWeg	6.077e+02	13,14	
22. 1. 8. 0	impurity control	2.519e+06	$	1.000e+00	13,14	
22. 1. 9. 1	vacuum tank	0.		1.000e+00		
22. 1. 9. 2	direct convertor modules	0.		1.000e+00		
22. 1. 9. 3	thermal panels	0.		1.000e+00		
22. 1. 9. 4	power conditioning equipment	0.		1.000e+00		
22. 1. 9. 0	direct energy conversion system	0.		1.000e+00		
22. 1.10. 0	ecrh breakdown system	2.015e+06	$	1.000e+00	13	
22. 1. 0. 0	reactor equipment	0.		1.000e+00		
22. 2. 1. 1	pumps & motor drives(modular & nonmodular)	0.		1.000e+00		
22. 2. 1. 2	piping	0.		1.000e+00		
22. 2. 1. 3	heat exchangers	0.		1.000e+00		
22. 2. 1. 4	tanks(dump,make-up,clean-up,trit..hot storage)	0.		1.000e+00		
22. 2. 1. 5	clean-up system	0.		1.000e+00		
22. 2. 1. 6	thermal insulation, piping & equipment	0.		1.000e+00		
22. 2. 1. 7	tritium extraction	0.		1.000e+00		
22. 2. 1. 8	pressurizer	0.		1.000e+00		
22. 2. 1. 9	other	0.		1.000e+00		
22. 2. 1. 0	primary coolant system	3.400e+04	$/MWth	1.789e+03	13,18	
22. 2. 2. 1	pumps & motor drives(modular & nonmodular)	0.		1.000e+00		
22. 2. 2. 2	piping	0.		1.000e+00		
22. 2. 2. 3	heat exchangers	0.		1.000e+00		
22. 2. 2. 4	tanks(dump,make-up,clean-up,trit.,hot storage)	0.		1.000e+00		
22. 2. 2. 5	clean-up system	0.		1.000e+00		
22. 2. 2. 6	thermal insulation, piping & equipment	0.		1.000e+00		
22. 2. 2. 7	tritium extraction	0.		1.000e+00		
22. 2. 2. 8	pressurizer	0.		1.000e+00		
22. 2. 2. 9	other	0.		1.000e+00		
22. 2. 2. 0	intermediate coolant system	0.		1.000e+00		
22. 2. 3. 1	pumps & motor drives(modular & nonmodular)	0.		1.000e+00		
22. 2. 3. 2	piping	0.		1.000e+00		
22. 2. 3. 3	heat exchangers	0.		1.000e+00		
22. 2. 3. 4	tanks(dump,make-up,clean-up,trit.,hot storage)	0.		1.000e+00		
22. 2. 3. 5	clean-up system	0.		1.000e+00		
22. 2. 3. 6	thermal insulation, piping & equipment	0.		1.000e+00		
22. 2. 3. 7	tritium extraction	0.		1.000e+00		
22. 2. 3. 8	pressurizer	0.		1.000e+00		
22. 2. 3. 9	other	0.		1.000e+00		

22. 2. 3. 0	secondary coolant system	3.500e+04	$/MWth	1.587e+03	13,18
22. 2. 0. 0	main heat transfer & transport systems	0.		1.000e+00	
22. 3. 1. 1	refrigeration	1.000e+07		1.000e+00	13,16
22. 3. 1. 2	piping	0.		1.000e+00	
22. 3. 1. 3	fluid circulation driving system	0.		1.000e+00	
22. 3. 1. 4	tanks	0.		1.000e+00	
22. 3. 1. 5	purification	0.		1.000e+00	
22. 3. 1. 0	magnet cooling system	0.		1.000e+00	
22. 3. 2. 1	refrigeration	0.		1.000e+00	
22. 3. 2. 2	piping	0.		1.000e+00	
22. 3. 2. 3	fluid circulation driving system	0.		1.000e+00	
22. 3. 2. 4	tanks	0.		1.000e+00	
22. 3. 2. 5	purification	0.		1.000e+00	
22. 3. 2. 0	shield & structure cooling system	6.700e+02	$/MWth	3.376e+03	13
22. 3. 3. 1	refrigeration	0.		1.000e+00	
22. 3. 3. 2	piping	0.		1.000e+00	
22. 3. 3. 3	fluid circulation driving system	0.		1.000e+00	
22. 3. 3. 4	tanks	0.		1.000e+00	
22. 3. 3. 5	purification	0.		1.000e+00	
22. 3. 3. 0	supplemental heating system cooling system	0.		1.000e+00	
22. 3. 4. 1	refrigeration	0.		1.000e+00	
22. 3. 4. 2	piping	0.		1.000e+00	
22. 3. 4. 3	fluid circulation driving system	0.		1.000e+00	
22. 3. 4. 4	tanks	0.		1.000e+00	
22. 3. 4. 5	purification	0.		1.000e+00	
22. 3. 4. 0	power supply cooling system	0.		1.000e+00	
22. 3. 5. 0	other cooling systems	0.		1.000e+00	
22. 3. 0. 0	auxiliary cooling systems	0.		1.000e+00	
22. 4. 1. 0	liquid waste processing & equipment	0.		1.000e+00	
22. 4. 2. 0	gaseous wastes & off-gas processing system	0.		1.000e+00	
22. 4. 3. 0	solid waste processing equipment	0.		1.000e+00	
22. 4. 0. 0	radioactive waste treatment & disposal	1.200e+03	$/MWth	3.376e+03	13,14
22. 5. 1. 0	fuel purification systems	0.		1.000e+00	
22. 5. 2. 0	liquefaction	0.		1.000e+00	
22. 5. 3. 0	fuel preparation	0.		1.000e+00	
22. 5. 4. 0	fuel injection	0.		1.000e+00	
22. 5. 5. 0	fuel storage	0.		1.000e+00	
22. 5. 6. 0	tritium recovery	0.		1.000e+00	
22. 5. 7. 0	emergency air detritiation	0.		1.000e+00	
22. 5. 0. 0	fuel handling & storage systems(fuel injection)	9.650e+03	$/MWth	3.376e+03	13,14
22. 6. 1. 1	blanket & coil maintenance equipment	0.		1.000e+00	
22. 6. 1. 2	components rotated into service to allow maint.	0.		1.000e+00	
22. 6. 1. 3	other maintenance equipment	0.		1.000e+00	
22. 6. 1. 0	maintenance equipment	0.		1.000e+00	
22. 6. 2. 0	special heating systems(start-up,trace, etc.)	0.		1.000e+00	
22. 6. 3. 0	coolant receiving, storage & make-up systems	0.		1.000e+00	
22. 6. 4. 0	gas systems	0.		1.000e+00	
22. 6. 5. 0	building vacuum systems	0.		1.000e+00	
22. 6. 0. 0	other reactor plant equipment	1.094e+04	$/MWth	3.376e+03	13,14
22. 7. 1. 0	reactor i&c equip.(burn control, diagnostics, etc.	0.		1.000e+00	
22. 7. 2. 0	radiation monitoring systems	0.		1.000e+00	
22. 7. 3. 0	isolated indicating & recording gauges, etc.	0.		1.000e+00	
22. 7. 0. 0	instrumentation & control(i&c)	2.341e+07	$	1.000e+00	13,14
22.98. 0. 0	spare parts allowance	2.000e-02	fraction	-1.000e+00	2,13,14
22.99. 0. 0	contingency allowance	1.500e-01	fraction	-1.000e+00	2,13,14
22. 0. 0. 0	reactor plant equipment	0.		1.000e+00	
23. 1. 1. 0	turbine-generators & accessories	0.		1.000e+00	
23. 1. 2. 0	foundations	0.		1.000e+00	

23. 1. 3. 0	standby exciters	0.		1.000e+00			
23. 1. 4. 0	lubricating system	0.		1.000e+00			
23. 1. 5. 0	gas systems	0.		1.000e+00			
23. 1. 6. 0	reheaters	0.		1.000e+00			
23. 1. 7. 0	shielding	0.		1.000e+00			
23. 1. 8. 0	weather-proof housing	0.		1.000e+00			
23. 1. 0. 0	turbine-generators	4.758e+05	$/unit	1.443e+02	2,13,14		
23. 2. 0. 0	main steam (or other fluid) system	1.678e+03	$/MWth	3.376e+03	12		
23. 3. 1. 0	water intake common facilities	0.		1.000e+00			
23. 3. 2. 0	circulating water systems	0.		1.000e+00			
23. 3. 3. 0	cooling towers	0.		1.000e+00			
23. 3. 4. 0	other systems which reject heat to the atmosphere	0.		1.000e+00			
23. 3. 0. 0	heat rejection systems	5.668e+04	$/unit	6.649e+02	2,13,14		
23. 4. 1. 0	condensers	0.		1.000e+00			
23. 4. 2. 0	condensate system	0.		1.000e+00			
23. 4. 3. 0	gas removal system	0.		1.000e+00			
23. 4. 4. 0	turbine by-pass systems(excl. piping)	0.		1.000e+00			
23. 4. 0. 0	condensing systems	2.753e+04	$/unit	5.974e+02	2,13,14		
23. 5. 1. 0	regenerators & recuporators	0.		1.000e+00			
23. 5. 2. 0	pumps	0.		1.000e+00			
23. 5. 3. 0	tanks	0.		1.000e+00			
23. 5. 0. 0	feed heating system	2.640e+03	$/unit	3.376e+03	2,13,14		
23. 6. 1. 0	turbine auxiliaries	0.		1.000e+00			
23. 6. 2. 0	auxiliaries cooling system(excl. piping)	0.		1.000e+00			
23. 6. 3. 0	make-up treat. system(excl. piping)	0.		1.000e+00			
23. 6. 4. 0	chemical treat. & condensate purification systems	0.		1.000e+00			
23. 6. 5. 0	central lubrication service system(excl. piping)	0.		1.000e+00			
23. 6. 0. 0	other turbine plant equipment	6.482e+05	$/unit	7.093e+01	2,13,14		
23. 7. 0. 0	instrumentation & control(i&c) equipment	9.820e+05	$/unit	8.422e+00	2,13,14		
23.98. 0. 0	spare parts allowance	2.000e-02	fraction	-1.000e+00	2,13,14		
23.99. 0. 0	contingency allowance	1.500e-01	fraction	-1.000e+00	2,13,14		
23. 0. 0. 0	turbine plant equipment	0.		1.000e+00			
24. 1. 1. 0	generator circuits	0.		1.000e+00			
24. 1. 2. 0	station service	0.		1.000e+00			
24. 1. 0. 0	switchgear	8.600e+03	$/unit	1.215e+03	2,13,14		
24. 2. 1. 0	station service & startup transformers	0.		1.000e+00			
24. 2. 2. 0	low voltage unit substation & lighting transformer	0.		1.000e+00			
24. 2. 3. 0	battery system	0.		1.000e+00			
24. 2. 4. 0	diesel engine generators	0.		1.000e+00			
24. 2. 5. 0	gas turbine generators	0.		1.000e+00			
24. 2. 6. 0	motor generator sets	0.		1.000e+00			
24. 2. 0. 0	station service equipment	1.420e+04	$/unit	1.215e+03	13,16		
24. 3. 1. 0	main control board for electric system	0.		1.000e+00			
24. 3. 2. 0	auxiliary power & signal boards	0.		1.000e+00			
24. 3. 0. 0	switchboards (incl. heat tracing)	5.400e+03	$/unit	1.215e+03	2,13,14		
24. 4. 1. 0	gen. station grounding sys. & cathodic protection	0.		1.000e+00			
24. 4. 0. 0	protective equipment	2.110e+06	$	1.000e+00	13,14		
24. 5. 1. 0	concrete cable tunnels, trenches & envelopes	0.		1.000e+00			
24. 5. 2. 0	cable trays & support	0.		1.000e+00			
24. 5. 3. 0	conduit	0.		1.000e+00			
24. 5. 4. 0	other structures	0.		1.000e+00			
24. 5. 0. 0	electrical structures & wiring containers	1.642e+07	$	1.000e+00	13,14,+		
24. 6. 1. 0	generator circuits wiring	0.		1.000e+00			
24. 6. 2. 0	station service power wiring	0.		1.000e+00			
24. 6. 3. 0	control wiring	0.		1.000e+00			
24. 6. 4. 0	instrument wiring	0.		1.000e+00			
24. 6. 5. 0	containment penetrations	0.		1.000e+00			
24. 6. 0. 0	power & control wiring	3.397e+07	$	1.000e+00	13,14,+		

24.	7.	1.	0	reactor building lighting	0.		1.000e+00	
24.	7.	2.	0	turbine building lighting	0.		1.000e+00	
24.	7.	3.	0	reactor auxiliaries building lighting	0.		1.000e+00	
24.	7.	4.	0	radioactive waste building lighting	0.		1.000e+00	
24.	7.	5.	0	fuel storage building lighting	0.		1.000e+00	
24.	7.	6.	0	miscellaneous buildings lighting	0.		1.000e+00	
24.	7.	7.	0	yard lighting	0.		1.000e+00	
24.	7.	0.	0	electrical lighting	8.200e+06	$	1.000e+00	13,14,+
24.98.	0.	0		spare parts allowance	4.000e-02	fraction	-1.000e+00	2,13,14
24.99.	0.	0		contingency allowance	1.500e-01	fraction	-1.000e+00	2,13,14
24.	0.	0.	0	electric plant equipment	0.		1.000e+00	
25.	1.	1.	0	cranes, hoists, monorails, & conveyors	0.		1.000e+00	
25.	1.	2.	0	railway	0.		1.000e+00	
25.	1.	3.	0	roadway equipment	0.		1.000e+00	
25.	1.	4.	0	watercraft	0.		1.000e+00	
25.	1.	5.	0	vehicle maintenance equipment	0.		1.000e+00	
25.	1.	0.	0	transportation & lifting equipment	1.568e+07	$	1.000e+00	13,14
25.	2.	1.	0	air systems(excl. piping)	0.		1.000e+00	
25.	2.	2.	0	water systems(excl. piping)	0.		1.000e+00	
25.	2.	3.	0	auxiliary heating boilers(excl. piping)	0.		1.000e+00	
25.	2.	0.	0	air & water service systems	1.235e+07	$	1.000e+00	13,14
25.	3.	1.	0	local communications systems	0.		1.000e+00	
25.	3.	2.	0	signal systems	0.		1.000e+00	
25.	3.	0.	0	communications equipment	6.220e+06	$	1.000e+00	13,14
25.	4.	1.	0	safety equipment	0.		1.000e+00	
25.	4.	2.	0	shop, laboratory, & test equipment	0.		1.000e+00	
25.	4.	3.	0	office equipment & furnishings	0.		1.000e+00	
25.	4.	4.	0	change room equipment	0.		1.000e+00	
25.	4.	5.	0	environmental monitoring equipment	0.		1.000e+00	
25.	4.	6.	0	dining facilities	0.		1.000e+00	
25.	4.	0.	0	furnishings & fixtures	1.200e+06	$	1.000e+00	2
25.98.	0.	0		spare parts allowance	3.000e-02	fraction	-1.000e+00	2,13,14
25.99.	0.	0		contingency allowance	1.500e-01	fraction	-1.000e+00	2,13,14
25.	0.	0.	0	miscellaneous plant equipment	0.		1.000e+00	
26.	1.	0.	0	reactor coolant	9.500e+00	$/kg	4.525e+06	15,18
26.	2.	0.	0	intermediate coolant	0.		1.000e+00	
26.	3.	0.	0	turbine cycle working fluids	0.		1.000e+00	
26.	4.	0.	0	other materials	2.500e+05	$	1.000e+00	13,14
26.98.	0.	0		spare parts allowance	0.	fraction	-1.000e+00	
26.99.	0.	0		contingency allowance	0.	fraction	-1.000e+00	
26.	0.	0.	0	special materials	0.		1.000e+00	
90.	0.	0.	0	direct cost	0.		1.000e+00	
91.	1.	0.	0	temporary facilities	0.	fraction	-1.000e+00	
91.	2.	0.	0	construction equipment	0.	fraction	-1.000e+00	
91.	3.	0.	0	construction services	0.	fraction	-1.000e+00	
91.	0.	0.	0	construction facilities, equipment & services (10%)	1.000e-01	fraction	-1.000e+00	13,14
92.	0.	0.	0	engineering & construction management services (8%)	8.000e-02	fraction	-1.000e+00	13,14
93.	1.	0.	0	taxes & insurance	0.	fraction	-1.000e+00	
93.	2.	0.	0	staff training & plant startup	0.	fraction	-1.000e+00	
93.	3.	0.	0	owner's g&a	0.	fraction	-1.000e+00	
93.	0.	0.	0	other costs (5%)	5.000e-02	fraction	-1.000e+00	2,13,14
94.	0.	0.	0	interest during construction (IDC)	1.080e-01	fraction	-1.000e+00	3
95.	0.	0.	0	escalation during construction (EDC)	1.000e-08	fraction	-1.000e+00	3
99.	0.	0.	0	total cost	0.		1.000e+03	

TABLE B-VI

SAMPLE COST ACCOUNT LISTING FOR THE CRFPR(20) DESIGN

fusion reactor economic evaluation (ver. 1.9) CRFPR 4/18/85

acc. no.	account title	million dollars (1980)		
20. 1.	land & privilege acquisition		3.000	
20. 2.	relocation of buildings, utilities, highways, etc.		0.300	
20.	land & land rights			3.300
21. 1. 1.	general yard improvements			
21. 1. 2.	waterfront improvements			
21. 1. 3.	transportation access (off site)			
21. 1.	site improvements & facilities		11.150	
21. 2. 1.	basic building structures	52.710		
21. 2. 2.	building services	2.000		
21. 2. 3.	containment structures	30.000		
21. 2. 4.	architectural	7.500		
21. 2.	reactor building		92.210	
21. 3. 1.	basic building structures	30.000		
21. 3. 2.	building services	2.000		
21. 3. 3.	architectural	1.500		
21. 3.	turbine building		33.500	
21. 4. 1.	intake structures			
21. 4. 2.	discharge structures			
21. 4. 3.	unpressurized intake & discharge conduits			
21. 4. 4.	recirculating structures			
21. 4. 5.	cooling tower systems			
21. 4.	cooling system structures		7.565	
21. 5. 1.	basic building structures	8.030		
21. 5. 2.	building services	0.530		
21. 5. 3.	architectural	0.600		
21. 5.	power supply & energy storage building		9.160	
21. 6. 1.	reactor auxiliaries building(incl. switchgear bay)	3.260		
21. 6. 2.	hot cell building	53.960		
21. 6. 3.	fuel storage building	8.630		
21. 6. 4.	control room building	3.100		
21. 6. 5.	diesel generator building	2.050		
21. 6. 6.	administration building	0.870		
21. 6. 7.	service building	1.880		
21. 6. 8.	cryogenics building	0.910		
21. 6. 9.	miscellaneous structures & building work	1.840		
21. 6.	miscellaneous buildings		76.500	
21. 7.	ventilation stack		1.810	
21.98.	spare parts allowance		4.638	
21.99.	contingency allowance		34.784	
21.	structures & site facilities			271.317

22. 1. 1. 1.	breeding material(incl. tritium breeding)	8.885	
22. 1. 1. 2.	first wall & structural material	1.660	
22. 1. 1. 3.	attenuators, reflectors, & multipliers		
22. 1. 1. 4.	wall modifiers(coatings, liners, limiters, etc.)		
22. 1. 1. 5.	others		
22. 1. 1.	blanket & first wall		10.545
22. 1. 2. 1.	primary		
22. 1. 2. 2.	secondary		
22. 1. 2.	shield		2.127
22. 1. 3. 1.	principal field magnet	6.123	
22. 1. 3. 2.	secondary field magnet	28.213	
22. 1. 3.	magnets		34.336
22. 1. 4. 1.	beam heating(neutral, ion or electron)		
22. 1. 4. 2.	rf heating	0.000	
22. 1. 4. 3.	laser heating		
22. 1. 4. 4.	other heating systems		
22. 1. 4.	supplemental heating systems		
22. 1. 5. 1.	reactor structure		
22. 1. 5. 2.	equipment support structure		
22. 1. 5.	primary structure & support		12.251
22. 1. 6. 1.	plasma chamber vacuum(incl. pumps/comp./pipe)	7.591	
22. 1. 6. 2.	magnet dewar vacuum(incl. pumps/comp./pipe)		
22. 1. 6. 3.	suppl. heating vacuum(incl. pumps/comp./pipe)		
22. 1. 6. 4.	direct convertor vacuum(incl. pumps/comp./pipe)		
22. 1. 6. 5.	reactor vacuum system(low grade)		
22. 1. 6. 6.	reactor vacuum wall	8.817	
22. 1. 6.	reactor vacuum systems(unless integral elsewhere)		16.409
22. 1. 7. 1.	heating		
22. 1. 7. 2.	confinement		
22. 1. 7. 3.	control system		
22. 1. 7. 4.	central energy storage		
22. 1. 7. 5.	other		
22. 1. 7.	power supply, switching & energy storage		48.616
22. 1. 8.	impurity control		2.519
22. 1. 9. 1.	vacuum tank		
22. 1. 9. 2.	direct convertor modules		
22. 1. 9. 3.	thermal panels		
22. 1. 9. 4.	power conditioning equipment		
22. 1. 9.	direct energy conversion system		
22. 1.10.	ecrh breakdown system		2.015
22. 1.	reactor equipment		128.819
22. 2. 1. 1.	pumps & motor drives(modular & nonmodular)		
22. 2. 1. 2.	piping		
22. 2. 1. 3.	heat exchangers		
22. 2. 1. 4.	tanks(dump,make-up,clean-up,trit.,hot storage)		
22. 2. 1. 5.	clean-up system		
22. 2. 1. 6.	thermal insulation, piping & equipment		
22. 2. 1. 7.	tritium extraction		
22. 2. 1. 8.	pressurizer		
22. 2. 1. 9.	other		
22. 2. 1.	primary coolant system		60.826
22. 2. 2. 1.	pumps & motor drives(modular & nonmodular)		
22. 2. 2. 2.	piping		
22. 2. 2. 3.	heat exchangers		

22. 2. 2. 4.	tanks(dump,make-up,clean-up,trit.,hot storage)				
22. 2. 2. 5.	clean-up system				
22. 2. 2. 6.	thermal insulation, piping & equipment				
22. 2. 2. 7.	tritium extraction				
22. 2. 2. 8.	pressurizer				
22. 2. 2. 9.	other				
22. 2. 2.	intermediate coolant system				
22. 2. 3. 1.	pumps & motor drives(modular & nonmodular)				
22. 2. 3. 2.	piping				
22. 2. 3. 3.	heat exchangers				
22. 2. 3. 4.	tanks(dump,make-up,clean-up,trit.,hot storage)				
22. 2. 3. 5.	clean-up system				
22. 2. 3. 6.	thermal insulation, piping & equipment				
22. 2. 3. 7.	tritium extraction				
22. 2. 3. 8.	pressurizer				
22. 2. 3. 9.	other				
22. 2. 3.	secondary coolant system			55.545	
22. 2.	main heat transfer & transport systems				116.371
22. 3. 1. 1.	refrigeration		10.000		
22. 3. 1. 2.	piping				
22. 3. 1. 3.	fluid circulation driving system				
22. 3. 1. 4.	tanks				
22. 3. 1. 5.	purification				
22. 3. 1.	magnet cooling system			10.000	
22. 3. 2. 1.	refrigeration				
22. 3. 2. 2.	piping				
22. 3. 2. 3.	fluid circulation driving system				
22. 3. 2. 4.	tanks				
22. 3. 2. 5.	purification				
22. 3. 2.	shield & structure cooling system			2.262	
22. 3. 3. 1.	refrigeration				
22. 3. 3. 2.	piping				
22. 3. 3. 3.	fluid circulation driving system				
22. 3. 3. 4.	tanks				
22. 3. 3. 5.	purification				
22. 3. 3.	supplemental heating system cooling system				
22. 3. 4. 1.	refrigeration				
22. 3. 4. 2.	piping				
22. 3. 4. 3.	fluid circulation driving system				
22. 3. 4. 4.	tanks				
22. 3. 4. 5.	purification				
22. 3. 4.	power supply cooling system				
22. 3. 5.	other cooling systems				
22. 3.	auxiliary cooling systems				12.262
22. 4. 1.	liquid waste processing & equipment				
22. 4. 2.	gaseous wastes & off-gas processing system				
22. 4. 3.	solid waste processing equipment				
22. 4.	radioactive waste treatment & disposal				4.051
22. 5. 1.	fuel purification systems				
22. 5. 2.	liquefaction				
22. 5. 3.	fuel preparation				
22. 5. 4.	fuel injection				
22. 5. 5.	fuel storage				
22. 5. 6.	tritium recovery				

22. 5. 7.	emergency air detritiation		
22. 5.	fuel handling & storage systems(fuel injection)	32.578	
22. 6. 1. 1.	blanket & coil maintenance equipment		
22. 6. 1. 2.	components rotated into service to allow maint.		
22. 6. 1. 3.	other maintenance equipment		
22. 6. 1.	maintenance equipment		
22. 6. 2.	special heating systems(start-up,trace, etc.)		
22. 6. 3.	coolant receiving, storage & make-up systems		
22. 6. 4.	gas systems		
22. 6. 5.	building vacuum systems		
22. 6.	other reactor plant equipment	36.933	
22. 7. 1.	reactor i&c equip.(burn control, diagnostics, etc.		
22. 7. 2.	radiation monitoring systems		
22. 7. 3.	isolated indicating & recording gauges, etc.		
22. 7.	instrumentation & control(i&c)	23.410	
22.98.	spare parts allowance	7.088	
22.99.	contingency allowance	53.164	
22.	reactor plant equipment		414.677
23. 1. 1.	turbine-generators & accessories		
23. 1. 2.	foundations		
23. 1. 3.	standby exciters		
23. 1. 4.	lubricating system		
23. 1. 5.	gas systems		
23. 1. 6.	reheaters		
23. 1. 7.	shielding		
23. 1. 8.	weather-proof housing		
23. 1.	turbine-generators	68.658	
23. 2.	main steam (or other fluid) system	5.665	
23. 3. 1.	water intake common facilities		
23. 3. 2.	circulating water systems		
23. 3. 3.	cooling towers		
23. 3. 4.	other systems which reject heat to the atmosphere		
23. 3.	heat rejection systems	37.687	
23. 4. 1.	condensers		
23. 4. 2.	condensate system		
23. 4. 3.	gas removal system		
23. 4. 4.	turbine by-pass systems(excl. piping)		
23. 4.	condensing systems	16.446	
23. 5. 1.	regenerators & recuporators		
23. 5. 2.	pumps		
23. 5. 3.	tanks		
23. 5.	feed heating system	8.913	
23. 6. 1.	turbine auxiliaries		
23. 6. 2.	auxiliaries cooling system(excl. piping)		
23. 6. 3.	make-up treat. system(excl. piping)		

23. 6. 4.	chemical treat. & condensate purification systems		
23. 6. 5.	central lubrication service system(excl. piping)		
23. 6.	other turbine plant equipment	45.977	
23. 7.	instrumentation & control(i&c) equipment	8.270	
23.98.	spare parts allowance	3.832	
23.99.	contingency allowance	28.742	
23.	turbine plant equipment		224.190
1			
24. 1. 1.	generator circuits		
24. 1. 2.	station service		
24. 1.	switchgear	10.449	
24. 2. 1.	station service & startup transformers		
24. 2. 2.	low voltage unit substation & lighting transformer		
24. 2. 3.	battery system		
24. 2. 4.	diesel engine generators		
24. 2. 5.	gas turbine generators		
24. 2. 6.	motor generator sets		
24. 2.	station service equipment	17.253	
24. 3. 1.	main control board for electric system		
24. 3. 2.	auxiliary power & signal boards		
24. 3.	switchboards (incl. heat tracing)	6.561	
24. 4. 1.	gen. station grounding sys. & cathodic protection		
24. 4.	protective equipment	2.110	
24. 5. 1.	concrete cable tunnels, trenches & envelopes		
24. 5. 2.	cable trays & support		
24. 5. 3.	conduit		
24. 5. 4.	other structures		
24. 5.	electrical structures & wiring containers	16.420	
24. 6. 1.	generator circuits wiring		
24. 6. 2.	station service power wiring		
24. 6. 3.	control wiring		
24. 6. 4.	instrument wiring		
24. 6. 5.	containment penetrations		
24. 6.	power & control wiring	33.970	
24. 7. 1.	reactor building lighting		
24. 7. 2.	turbine building lighting		
24. 7. 3.	reactor auxiliaries building lighting		
24. 7. 4.	radioactive waste building lighting		
24. 7. 5.	fuel storage building lighting		
24. 7. 6.	miscellaneous buildings lighting		
24. 7. 7.	yard lighting		
24. 7.	electrical lighting	8.200	
24.98.	spare parts allowance	3.799	
24.99.	contingency allowance	14.244	

24.	electric plant equipment		113.006
25. 1. 1.	cranes, hoists, monorails, & conveyors		
25. 1. 2.	railway		
25. 1. 3.	roadway equipment		
25. 1. 4.	watercraft		
25. 1. 5.	vehicle maintenance equipment		
25. 1.	transportation & lifting equipment	15.680	
25. 2. 1.	air systems(excl. piping)		
25. 2. 2.	water systems(excl. piping)		
25. 2. 3.	auxiliary heating boilers(excl. piping)		
25. 2.	air & water service systems	12.350	
25. 3. 1.	local communications systems		
25. 3. 2.	signal systems		
25. 3.	communications equipment	6.220	
25. 4. 1.	safety equipment		
25. 4. 2.	shop, laboratory, & test equipment		
25. 4. 3.	office equipment & furnishings		
25. 4. 4.	change room equipment		
25. 4. 5.	environmental monitoring equipment		
25. 4. 6.	dining facilities		
25. 4.	furnishings & fixtures	1.200	
25.98.	spare parts allowance	1.063	
25.99.	contingency allowance	5.317	
25.	miscellaneous plant equipment		41.831
26. 1.	reactor coolant	42.987	
26. 2.	intermediate coolant		
26. 3.	turbine cycle working fluids		
26. 4.	other materials	0.250	
26.98.	spare parts allowance		
26.99.	contingency allowance		
26.	special materials		43.237

TABLE B-VII

SAMPLE FUSION REACTOR COST AND PARAMETER SUMMARY FOR THE CRFPR(20) DESIGN

Los Alamos fusion reactor economic evaluation (ver. 1.9) CRFPR 4/18/85

acc. no.	account title	million dollars (1980)		
20.	land & land rights	3.300		
21.	structures & site facilities	271.317		
22.	reactor plant equipment	414.677		
22. 1. 1.	blanket & first wall	10.545		
22. 1. 2.	shield	2.127		
22. 1. 3.	magnets	34.336		
22. 1. 4.	supplemental heating systems	0.000		
22. 1. 5.	primary structure & support	12.251		
22. 1. 6.	reactor vacuum systems(unless integral elsewhere)	16.409		
22. 1. 7.	power supply, switching & energy storage	48.616		
22. 1. 8.	impurity control	2.519		
22. 1. 9.	direct energy conversion system	0.000		
22. 1.10.	ecrh breakdown system	2.015		
22. 1.	reactor equipment	128.819		
23.	turbine plant equipment	224.190		
24.	electric plant equipment	113.006		
25.	miscellaneous plant equipment	41.831		
26.	special materials	43.237		
90.	direct cost		1111.559	
91.	construction facilities, equipment & services (10%)		111.156	
92.	engineering & construction management services (8%)		88.925	
93.	other costs (5%)		55.578	
94.	interest during construction (IDC)		147.659	343.170
95.	escalation during construction (EDC)		0.000	211.918
99.	total cost		1514.877	1922.306

			constant	then-current
thermal power (MWth) = 3376.14	unit direct cost ($/kWe)	[90]=	1111.54	1111.54
gross electric power (MWe) = 1215.41	unit base cost ($/kWe)	[93]=	1367.20	1367.20
net electric power (MWe) = 1000.01	unit total cost ($/kWe)	[99]=	1514.86	1922.28
1/recirculating power fraction QE= 5.64	capital return (mills/kWeh)	=	22.79	43.37
plant availibility factor = 0.76	O&M (2.0%) (mills/kWeh)	[40-47,51]=	4.11	5.25
construction= 5 yr: constant then-current	B/FW replacement (mills/kWeh)	[50]=	1.00	1.28
fIDC= 0.108 0.251	deuterium fuel (mills/kWeh)	[02]=	0.03	0.03
fEDC= 0.000 0.155	COE (mills/kWeh)	=	27.93	49.93

TABLE B-VII (Cont)

reversed-field pinch reactor calculations	
plasma parameters	
minor plasma radius (m)	0.705
major plasma radius (m)	3.879
plasma aspect ratio	5.500
plasma current (MA)	17.731
toroidal current density (MA/m2)	11.345
plasma density (1.0e20/m3)	6.278
plasma temperature (keV)	10.000
lawson parameter (1.0e20 s/m3)	1.600
energy confinement time (s)	0.255
lawson parameter * t2 (1.0e22 s keV2/m3)	1.600
alcator coefficient (1.0e-21)	0.000
poloidal beta	0.200
theta parameter	1.450
reversal parameter	0.200
plasma/first-wall radius	0.947
streaming parameter (1.0e-14 A m)	1.807
plasma ohmic dissipation during burn (MW)	22.698
poloidal field quantities	
coil thickness (m)	0.354
average minor radius of coil (m)	1.785
mass of coil (tonne)	705.333
magnetic field level at the coil (T)	1.987
magnetic field level at the plasma surface (T)	5.028
poloidal coil current (MA)	23.649
poloidal current density (MA/m2)	5.966
maximum energy stored in coil (MJ)	1167.577
ohmic dissipation during burn (MW)	88.428
volumetric heating during burn (MW/m3)	0.915
toroidal field quantities	
coil thickness (m)	0.088
average minor radius of coil (m)	1.564
mass of coil (tonne)	153.087
initial toroidal bias field (T)	3.214
reversed-toroidal field during the burn (T)	0.656
maximum energy stored in the coil (MJ)	769.622
toroidal current density (MA/m2)	5.966
ohmic dissipation during burn (MW)	19.193
volumetric heating during burn (MW/m3)	0.915
engineering summary	
ohmic q-value, qt	25.907
total thermal power (MW)	3376.142
14.1-mev neutron loading (MW/m2)	18.724
14.1-mev blanket multiplication	1.330
2.45-mev neutron loading (MW/m2)	0.000
2.45-mev blanket multiplication	0.000
first-wall radius (m)	0.745
minor radius of system (m)	1.961
FPC (FW/B/S/C) mass (tonne)	1063.396
system power density (MWt/m3)	11.462
FPC (FW/B/S/C) mass (tonne)	1063.396
system power density (MWt/m3)	11.462
mass utilization (tonne/MWt)	0.315
specific net power (MWe/tonne)	0.940
blanket thickness (m)	0.775
mass of first wall/blanket (tonne)	42.833

REFERENCES FOR APPENDIX B

1. S. C. Schulte, T. L. Wilke, and J. R. Young, "Fusion Reactor Design Studies--Standard Accounts for Cost Estimates," Battelle (Pacific Northwest Laboratory) report PNL-2648 (May 1978).

2. S. C. Schulte, W. E. Bickford, C. E. Willingham, S. K. Ghose, and M. G. Walker, "Fusion Reactor Design Studies-Standard Cost Estimating Rules," Battelle (Pacific Northwest Laboratory) report PNL-2987 (May 1979).

3. D. L. Phung, "A Method for Estimating Escalation and Interest during Construction (EDC and IDC)," Proc. 2nd Miami Int. Conf. on Alternative Energy Sources (December 10-13, 1979).

4. W. R. Hamilton, D. C. Keith, and S. L. Thomson, "Cost Accounting System for Fusion Studies," Fusion Engineering Design Center draft document (1985).

5. J. G. Delene, G. R. Smolen, H. I. Bowers, and M. L. Myers, "Nuclear Energy Cost Data Base," USDOE report DOE/NE-0044/2 (March 1984).

6. United Engineers and Constructors Inc., "Pressurized Water Reactor Plant," U.S.A.E.C. report 1230, Vol. 1 (June 1972).

7. A. A. Hollis, "An Analysis of the Estimated Capital Cost of a Fusion Reactor," AERE Harwell Laboratory report AERE-R.9933 (June 1981).

8. B. Badger, G. L. Kulcinski, R. W. Conn, C. W. Maynard, K. Audenaerde, H. Avci, et al., "Tokamak Engineering Test Reactor," University of Wisconsin report UWFDM-191 (1977).

9. TFCX Design Team, "Cost Summary Addendum to the Preconceptual Design Report," Princeton Plasma Physics Laboratory report A-Axxx-8407-010 (July 5, 1984).

10. K. I. Thomassen (principal investigator), "Conceptual Engineering Design of a One-GJ Fast Discharging Homopolar Machine for the Reference Theta-Pinch Fusion Reactor," Electric Power Research Institute report ER-246, Project 469 (August 1976).

11. R. E. Stillwagon, "Design Studies of Reversible Energy Storage and Transfer Systems for the Reference Theta-Pinch Reactor," Westinghouse report E.M. 4620 (September 1974).

12. R. L. Hagenson and R. A. Krakowski, "Compact Reversed-Field Pinch Reactors (CRFPR): Sensitivity Study and Design Point Determination," Los Alamos National Laboratory report LA-9389-MS (July 1982).

13. C. C. Baker, M. A. Abdou, R. M. Arons, A. E. Bolon, C. D. Boley, J. N. Brooks, et al., "Starfire--A Commercial Tokamak Fusion Power Plant Study," Argonne National Laboratory report ANL/FPP-80-1 (September 1980).

14. C. G. Bathke, D. J. Dudziak, R. A. Krakowski, W. B. Ard, D. A. Bowers, J. W. Davis, et al., "The Elmo Bumpy Torus Reactor and Power Plant Conceptual Design," Los Alamos National Laboratory report LA-8882-MS (August 1981).

15. B. Badger, I. N. Sviatoslavsky, S. W. VanSciver, G. L. Kulcinski, G. A. Emmert, D. T. Anderson, et al., "UWTOR-M: a Conceptual Modular Stellarator Power Reactor," University of Wisconsin report UWFDM-550 (October 1982).

16. K. Evans, Jr., "A Tokamak Reactor Cost Model Based on Starfire/Wildcat Costing," Argonne National Laboratory report ANL/FPP/TM-168 (March 1983).

17. J. Sheffield, R. A. Dory, S. M. Cohn, J. G. Delene, L. Parsly, D. E. T. F. Ashby, and W.T. Reiersen, "Cost Assessment of a Generic Magnetic Fusion Reactor," Oak Ridge National Laboratory report ORNL/TM-9311 (1984).

18. B. G. Logan, C. D. Henning, G. A. Carlson, R. W. Werner, D. E. Baldwin, W. L. Barr, et al., "MARS Mirror Advanced Reactor Study Final Report," Lawrence Livermore National Laboratory report UCRL-53480 (July 1984).

19. R. L. Hagenson, R. A. Krakowski, C. G. Bathke, R. L. Miller, M. J. Embrechts, N. M. Schnurr, et al., "Compact Reversed-Field Pinch Reactors (CRFPR): Preliminary Engineering Considerations," Los Alamos National Laboratory report LA-10200-MS (August 1984).

20. R. L. Reid, R. J. Barrett, T. G. Brown, G. E. Corker, R. J. Hooper, S. S. Kalsi, et al., "The Tokamak Systems Code," Oak Ridge National Laboratory report ORNL/FEDC-84/9 (March 1985).

*U.S. GOVERNMENT PRINTING OFFICE: 1985-0-576-034/20120

Printed in the United States of America
Available from
National Technical Information Service
US Department of Commerce
5285 Port Royal Road
Springfield, VA 22161

Microfiche (A01)

Page Range	NTIS Price Code	Page Range	NTIS Price Code	Page Range	NTIS Price Code	Page Range	NTIS Price Code
001-025	A02	151-175	A08	301-325	A14	451-475	A20
026-050	A03	176-200	A09	326-350	A15	476-500	A21
051-075	A04	201-225	A10	351-375	A16	501-525	A22
076-100	A05	226-250	A11	376-400	A17	526-550	A23
101-125	A06	251-275	A12	401-425	A18	551-575	A24
126-150	A07	276-300	A13	426-450	A19	576-600	A25
						601-up*	A99

*Contact NTIS for a price quote.